Spectra and variability of accreting black holes

Using X-ray observations

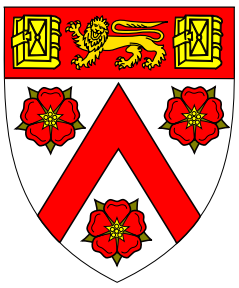

Douglas John Keith Buisson

Supervisor: Prof. A.C. Fabian

Institute of Astronomy
University of Cambridge

This dissertation is submitted for the degree of
Doctor of Philosophy

Trinity College July 2019

Declaration

This dissertation is the result of my own work and includes nothing which is the outcome of work done in collaboration except as declared in the Preface and specified in the text.

It is not substantially the same as any that I have submitted, or, is being concurrently submitted for a degree or diploma or other qualification at the University of Cambridge or any other University or similar institution except as declared in the Preface and specified in the text. I further state that no substantial part of my dissertation has already been submitted, or, is being concurrently submitted for any such degree, diploma or other qualification at the University of Cambridge or any other University or similar institution except as declared in the Preface and specified in the text.

It does not exceed 60,000 words, including summary/abstract, tables, footnotes and appendices, but excluding table of contents, photographs, diagrams, figure captions, list of figures/diagrams, list of abbreviations/acronyms, bibliography and acknowledgements.

Several chapters are based on published work:

- Chapter 2: 'Ultraviolet and X-ray variability of active galactic nuclei with Swift'

  Buisson, D. J K.; Lohfink, A. M.; Alston, W. N.; Fabian, A. C. (2017) MNRAS 464,3194

- Chapter 3: 'Is there a UV/X-ray connection in IRAS 13224–3089?'

  Buisson, D. J. K.; Lohfink, A. M.; Alston, W. N.; Cackett, E. M.; Chiang, C.-Y.; Dauser, T.; De Marco, B.; Fabian, A. C.; Gallo, L. C.; García, J. A.; Jiang, J.; Kara, E.; Middleton, M. J.; Miniutti, G.; Parker, M. L.; Pinto, C.; Uttley, P.; Walton, D. J.; Wilkins, D. R. (2018a) MNRAS 475, 2306

- Chapter 4: 'NuSTAR observations of Mrk 766: distinguishing reflection from absorption'

Buisson, D. J. K.; Parker, M. L.; Kara, E.; Vasudevan, R. V.; Lohfink, A. M.; Pinto, C.; Fabian, A. C.; Ballantyne, D. R.; Boggs, S. E.; Christensen, F. E.; Craig, W. W.; Farrah, D.; Hailey, C. J.; Harrison, F. A.; Ricci, C.; Stern, D.; Walton, D. J.; Zhang, W. W. (2018b) MNRAS 480, 3689

- Chapter 5: 'Coronal temperatures of the AGN ESO 103–035 and IGR 2124.7+5058 from NuSTAR observations'

  Buisson, D. J K.; Fabian, A. C.; Lohfink, A. M. (2018c) MNRAS 481, 4419

- Chapter 6: 'MAXI J1820+070 with *NuSTAR* I. An increase in variability frequency but a stable reflection spectrum: coronal properties and implications for the inner disc in black hole binaries'

  Buisson, D. J. K.; Fabian, A. C.; Barret, D.; Fürst, F.; Gandhi, P.; García, J. A.; Kara, E.; Madsen, K. K.; Miller, J. M.; Parker, M. L.; Shaw, A. W.; Tomsick, J. A.; Walton, D. J. (2019) MNRAS 490, 1350

Douglas John Keith Buisson
July 2019

Summary

Spectra and variability of accreting black holes

Douglas John Keith Buisson

In this thesis, we present various results concerning the structure of matter close to black holes when they are actively accreting. The two components (apart from the black hole itself) most relevant to this work are the accretion disc and X-ray emitting corona. We use various methods to help determine their location, properties and relation to each other.

In chapters 2 and 3, we consider how thermal emission from the accretion disc is affected by the coronal emission. Chapter 2 presents an analysis of a sample of supermassive black hole (SMBH) sources, showing that in many of these sources, variability in the accretion disc emission is driven by heating from the central source. Chapter 3 presents results from a dedicated campaign on a particularly X-ray variable object, IRAS 13324–3809, which however does not show disc variability in response to X-ray variations. We discuss potential reasons for this.

Chapters 4 and 5 consider what we can learn about accreting black holes from their X-ray spectra. Chapter 4 describes the use of X-rays which reflect from the disc to study properties of the disc such as its innermost extent (governed in part by the black hole spin) and ionisation state. Chapter 5 analyses hard X-ray spectra of two sources, including the electron temperature of the corona, and considers the physical process which could produce the observed temperature.

Finally, in chapter 6, we use a number of the techniques utilised previously to perform an in-depth study of the recent outburst from the stellar-remnant black hole in the MAXI 1820+070 X-ray binary system in our own Galaxy. As they are much smaller, such systems can show far more drastic state changes on observable timescales than SMBH can; the reasons for these state changes are not yet fully explained. The reflected emission shows that the disc extends close to the black hole, which has not been universally accepted in the state observed here. That the reflecting disc extends so close to the black hole also constrains the possible causes of characteristic timescales (QPOs) in the variability.

Table of contents

List of figures

List of tables

Chapter 1

Introduction

1.1 Black holes

The non-Euclidean geometry of Einstein's general relativity allows the possibility of some region of spacetime from which no future-pointing worldlines emerge. From this region, nothing could escape so it would be black and its edge would form a horizon beyond which no event could be observed.

The first exact solution of the Einstein equations which contains an event horizon was found soon after their proposal by Schwarzschild (1916). This was derived in the context of the gravitational field of a point mass.

While the Schwarzschild solution is the unique spherically symmetric vacuum solution (Birkhoff and Langer, 1923; Jebsen, 1921), generalisations allow for electromagnetic charge (Jeffery, 1921; Nordström, 1918; Reissner, 1916) or angular momentum (Kerr, 1963) or both (Newman et al., 1965).

Indeed, black holes carry only mass, angular momentum and electric charge (in the absence of magnetic monopoles), which has been shown for several restricted cases (Carter, 1971; Israel, 1967, 1968) and is believed to hold generally. This is known as the no-hair conjecture. In an astrophysical context, electric charge is expected to neutralise quickly, leaving only mass and angular momentum as relevant properties. The mass (M) acts as a simple scaling; distances around different black holes may be compared using the dimemsionless radius $r = R/r_{[}\mathrm{g}$, where $r_\mathrm{g} = GM/c^2$ is the graviational radius (using Newton's Gravitational constant, G, and the speed of light, c). The relative angular momentum ($\mathbf{J}$) may also be rescaled to be dimensionless, giving the spin parameter

$$a_\mathrm{BH} = \frac{|\mathbf{J}|c}{GM^2}$$

which is well-behaved for $|a| < 1$. For $|a_{\rm BH}| \geq 1$, the solution includes a naked singularity, which is viewed as unphysical (the cosmic censorship hypothesis) since such singularities pose potential problems for determinism in general relativity. Where there is some other reference frame for angular momentum (typically an accretion disc around the black hole), $a_{\rm BH}$ may be generalised

$$a = \pm a_{\rm BH}$$

to describe the relative sense of the angular momenta of the components: $a > 0$ is used when considering a black hole with angular momentum matching surrounding material (prograde) and $a < 0$ when these are counter-rotating (retrograde).

1.1.1 Detection of black holes

While direct emission from black holes (Hawking, 1974) is currently believed to be negligible in an astrophysical context, there are now several observational methods by which the presence of black holes has been inferred. Each of these relies upon the need to concentrate more mass in a small region than can be done without forming a black hole. Most recently, mm VLBI has been used to detect a ring structure in the centre of M87 which is characteristic of strongly lensed emission around a black hole (Event Horizon Telescope Collaboration et al., 2019). An equivalent black hole at the centre of the Milky Way had previously been implied by the orbits of stars around Sgr A* (Gillessen et al., 2009). The detection of gravitational waves (Abbott et al., 2016) shows the presence of much smaller compact objects, as had the orbital motions in the system containing Cyg X-1 (Bolton, 1972; Webster and Murdin, 1972).

The least direct but longest established method of detecting black holes is from the emission from material being accreted by the black hole. Many galaxies show luminous, rapidly variable point sources in their centres. Causality arguments imply that the size of the emitting region is at most around the light travel distance in the time for these variations to happen. This implies a very small size; the only realistic scenario to produce such high power (capable of varying coherently) in this space is matter being accreted onto a black hole (Lynden-Bell, 1964, 1969; Salpeter, 1964).

Currently, the black holes detected in the universe are of two types: supermassive black holes at the centres of galaxies, usually detected when they are actively accreting; and stellar mass black holes, detected when they accrete from a companion, emitting photons, or merge with a companion, emitting gravitational waves.

Active galactic nuclei

The powerful emission in the centres of some galaxies implies the presence of a central black hole in these galaxies. The strong correlations between inferred black hole mass and host galaxy properties (e.g Ferrarese and Merritt, 2000; Kormendy and Richstone, 1995; Magorrian et al., 1998) shows that the growth of the central black hole is closely linked to that of the galaxy (e.g. Kormendy and Ho, 2013) through some process termed feedback (Silk and Rees, 1998). These correlations, along with the number density of AGN, suggest that every galaxy contains a SMBH which goes through accretion phases (Beckmann and Shrader, 2012).

X-ray binaries

Many, possibly even a majority of, stars are found in binaries. When a star in such a system evolves into a compact object, and if this does not eject it from the binary, the companion star provides a source of matter which may be accreted onto the compact object, producing X-rays, hence X-ray binaries (XRBs), (e.g. reviews by Belloni, 2010; Fender, 2010; Remillard and McClintock, 2006). The relative mass of the companion star to the compact object determines the available means of mass transfer. If the companion star is of lower mass (in a LMXB), then it may fill its Roche lobe as it evolves. Any further increase in size will lead to material escaping the region bound to the companion; some of this will feed the compact object. Where the companion star is of higher mass (in a HMXB), such Roche lobe overflow would be unstable so in such systems the compact object is fed from the stellar wind of the companion.

One phenomenon which is observed in XRBs but not AGN is state changes: XRB outbursts consist of Compton-dominated (hard state) and thermal-dominated (soft state) phases, with rapid changes between them (e.g. Remillard and McClintock, 2006). The lack of observed state changes in AGN may be due to the difference in black hole mass: changes in AGN are much slower, so long-timescale changes in XRBs are unobservable in AGN. If accretion processes are equivalent (apart from scaling relations) across the mass range, as seems to be the case in some respects (e.g McHardy, 2010), then XRBs provide complementary information on the accretion process to AGN.

1.1.2 Accreting black holes

Black holes may be inferred from the energy given off by matter which accretes in the gravitational well of the black hole. Understanding this process is the primary subject of this thesis.

When matter gets close to the black hole, its angular momentum will cause it to become rotationally supported. Further infall requires that this material lose angular momentum, allowing it to orbit progressively closer to the black hole, forming a disc. The standard model for this disc is due to Shakura and Sunyaev (1973) (modified for relativistic effects by Novikov and Thorne 1973). Matter at each radius is in Keplerian motion, which leads to a velocity gradient with radius. Viscosity in the disc then allows matter to lose energy and be transferred to closer orbits (some outer matter must also be accelerated onto more distant orbits, but this need only be a small amount and may be counteracted by a supply of new gas). This leads to net inward transport of matter and outward transport of angular momentum, along with the release of significant energy.

The viscosity which allows matter and angular momentum transport is not molecular viscosity, as this is far too small; it is thought to be due to turbulence induced by magnetic fields through the Magneto-Rotational Instability (MRI Balbus and Hawley, 1991, 1992; Blaes, 2014). The viscosity (ν) in the disc is prescribed to be proportional to pressure (P), $\nu = \alpha P$, hence these discs may be referred to as α-discs.

The gravitational potential energy released in accretion must be transferred to some other form; commonly, it is emitted as photons with a thermal spectrum at each radius. The temperature (T) depends on radius (r) as

$$T^4(r) = \frac{3GM_{\rm BH}\dot{M}}{8\pi\sigma r^3}\left(1-\sqrt{\frac{R_{\rm in}}{r}}\right) \tag{1.1}$$

Where G is the Gravitational constant; $M_{\rm BH}$ is the black hole mass; $\dot{M}$ is the accretion rate; σ is the Stefan-Boltzmann constant; and $R_{\rm in}$ is the inner radius of the disc. When the blackbody from each radius is summed across the whole disc, this temperature profile produces a spectrum which is Rayleigh-Jeans-like at low frequency, Wien-like at high frequency and has a powerlaw middle section with $\nu f(\nu) \propto \nu^{4/3}$. This spectrum – particularly the middle and high frequency sections – is known as a disc-blackbody; it is responsible for the 'big blue bump' of AGN and dominates emission in the soft state of XRBs.

This thin disc model is not applicable to all accretion flows. At high accretion rate, the radiation pressure from the photons which are released by accretion is sufficient to balance the attraction from gravity. In the spherical case, this occurs at

$$L_{\rm Edd} = \frac{4\pi GM_{\rm BH}m_{\rm p}c}{\sigma_{\rm e}} \simeq 1.3\times10^{38}\left(\frac{M}{M_\odot}\right)\,{\rm erg\,s^{-1}}, \tag{1.2}$$

($m_{\rm p}$ is the proton mass; $\sigma_{\rm e}$ is the Thomson scattering cross section; and $M_\odot$ is the Solar mass) known as the Eddington luminosity. In the case of an originally disc-like geometry, outflows

are expected to be driven out in the solid angle away from the disc plane. This is referred to as the supercritical case in Shakura and Sunyaev (1973). Such outflows have been detected in various sources, including both AGN and binaries (e.g. Pinto et al., 2016; Tombesi et al., 2010), and in AGN are a potential source of feedback (e.g. Fabian et al., 2012; Nardini et al., 2015). Conversely, at low accretion rates, the density may be too low for material to emit the released energy before it is advected into the black hole, an advection dominated or radiatively inefficient accretion flow. This can explain at least some XRB hard states (e.g. Courvoisier, 2013), but the question of how high an accretion rate is needed for the disc to form is not settled (e.g. García et al., 2015).

Another effect of accretion is that the angular momentum of the accreted material affects the spin of the black hole. For a disc aligned with the spin axis of the black hole, the accreted gas rapidly leads to maximal spin (Bardeen, 1970), however photons from the disc impart a counteracting torque, setting a limit of $a \simeq 0.998$ (Thorne, 1974). This means that the spin of a black hole contains a record of its accretion history (combined with its merger history): black holes which have experienced prolonged accretion with consistent direction of angular momentum will have high spin, while black holes which have undergone more chaotic accretion will have low spin (Volonteri et al., 2005).

1.2 X-ray emission from black hole accretion

This work is principally concerned with studies of the X-ray emission (and its effects on emission in other wavebands) of accretion systems around black holes. The temperatures in the accretion discs of stellar mass black holes are high enough (when the majority of the accretion power is emitted thermally) for their thermal emission to reach the X-ray band but most X-ray emission is from (moderately, with optical depth $\tau \leq$ a few) optically thin plasma producing a non-thermal spectrum from Compton scattering. In AGN, this typically provides a significant fraction ($\sim 5-10\%$) of the bolometric luminosity (In XRBs, the proportion depends on the state). The material which produces these X-rays is referred to as the corona (analogously to the Solar corona) but its exact location and constituents are not yet fully understood.

1.2.1 X-ray coronae

The corona is a region of hot plasma which emits through inverse-Compton scattering of photons from the disc (Haardt and Maraschi, 1991, 1993; Merloni and Fabian, 2003). The spectrum may therefore be approximated by a powerlaw (e.g. Mushotzky et al., 1980) up to

energies corresponding to the temperature of the plasma, where emission rolls over. The high energy cut-off is commonly approximated by exponential suppression, but physical models for Comptonised emission are also available (Coppi, 2000; Farinelli et al., 2008; Lamb and Sanford, 1979; Sunyaev and Titarchuk, 1980; Titarchuk, 1994; Zdziarski et al., 1996; Życki et al., 1999).

Hard X-ray observations have shown that the plasma temperature is typically around $20-200\,\mathrm{keV}$ both for AGN and XRBs (Ricci et al., 2017) and that objects accreting at a higher rate tend to have lower temperatures (Ricci et al., 2018). The mechanism which regulates the temperature is not yet confirmed; one recent suggestion is that it is the effect of pair production at high radiative compactness (Fabian et al., 2015, see Chapter 5).

Several methods show that the corona is also physically compact compared to the accretion system, typically $\lesssim 10r_{\mathrm{g}}$ in size: microlensing (Chartas et al., 2012; Dai et al., 2010); variability (De Marco et al., 2013, 2011; Kara et al., 2016b, 2014a; Reis and Miller, 2013); and reflection spectra (e.g. Parker et al., 2014b; Wilkins et al., 2016; Wilkins and Fabian, 2011, 2012). The location of the corona is not fully determined, but the small size provides some justification for the common approximation of a point source on the spin axis. Clearly, the corona cannot actually be infinitesimal in size and indeed there is evidence for changing coronal extent (Kara et al., 2019; Wilkins et al., 2016; Wilkins and Gallo, 2015).

1.2.2 Reprocessed X-rays

The observed spectrum of most sources is not just a simple Comptonised continuum; instead, several other components are also seen.

Reflection

Where the primary X-rays encounter a cloud of gas, they interact in a variety of scattering, fluorescence and similar processes so the resulting reflected X-rays have a characteristic spectrum including many atomic lines and the Compton hump at around $20-50\,\mathrm{keV}$ (e.g. George and Fabian, 1991; Lightman and White, 1988; Ross and Fabian, 1993).

Much of the solid angle seen from the corona is intercepted by the disc, so this is a major source of reflection. The high velocities and strong gravity near the centre of the disc lead to strong blurring of the reflected emission so lines are strongly blurred (e.g. Tanaka et al., 1995); this blurring can be used to infer properties of the system, Section 1.2.4.

Soft excess

Early soft X-ray measurements showed that emission at $\lesssim 2\,\mathrm{keV}$ is often stronger than expected based on extrapolating the powerlaw from higher energies; this became known as the soft excess. It is not yet confirmed whether this is from an additional region of Comptonisation (e.g. Dewangan et al., 2007) or is part of the reflection spectrum (e.g Crummy et al., 2006).

Absorption

All of these emission components are viewed through some amount of gas, which may supply significant absorption. Firstly, neutral absorption from our own Galaxy often has a notable effect and for AGN this can be supplemented by the outer regions of the host galaxy. Further absorption which is intrinsic to the accretion system (or at least strongly affected by it) can also be present. AGN often show mildly ionised warm absorbers (e.g. Halpern, 1984; Lee et al., 2001; Sako et al., 2001) which are photoionised by the flux from accretion. Warm absorbers are often mildly outflowing but absorption is also seen by highly ionised, mildly relativistic ($v \sim 0.1 - 0.3c$) gas, known as UFOs (e.g. Parker et al., 2017b; Tombesi et al., 2010).

An example spectrum including these components is shown in Figure 1.1.

1.2.3 Measurements of black hole parameters

Mass is typically measured from the orbital motion of surrounding material, either galactic gas or a binary companion. X-ray binaries have a binary companion and the changing Doppler shift of the companion's spectral lines can be used to determine parameters of the binary orbit, including the black hole mass. For AGN, the most reliable method is from reverberation mapping, where a monitoring campaign allows measurement of the size (through light-travel delays) and velocity (through the line width induced by Doppler shifts) of gas in the broad line region. These can then be used to calculate the enclosed (black hole) mass (Blandford and McKee, 1982; Peterson, 2008). Where a galaxy contains a nuclear water maser, VLBI observations can similarly be used to calculate the mass (e.g. Miyoshi et al., 1995). Alternatively, scaling relations between the black hole mass and properties of the host galaxy, such as those in Section 1.1.1 can be used, although these usually have larger systematic uncertainty.

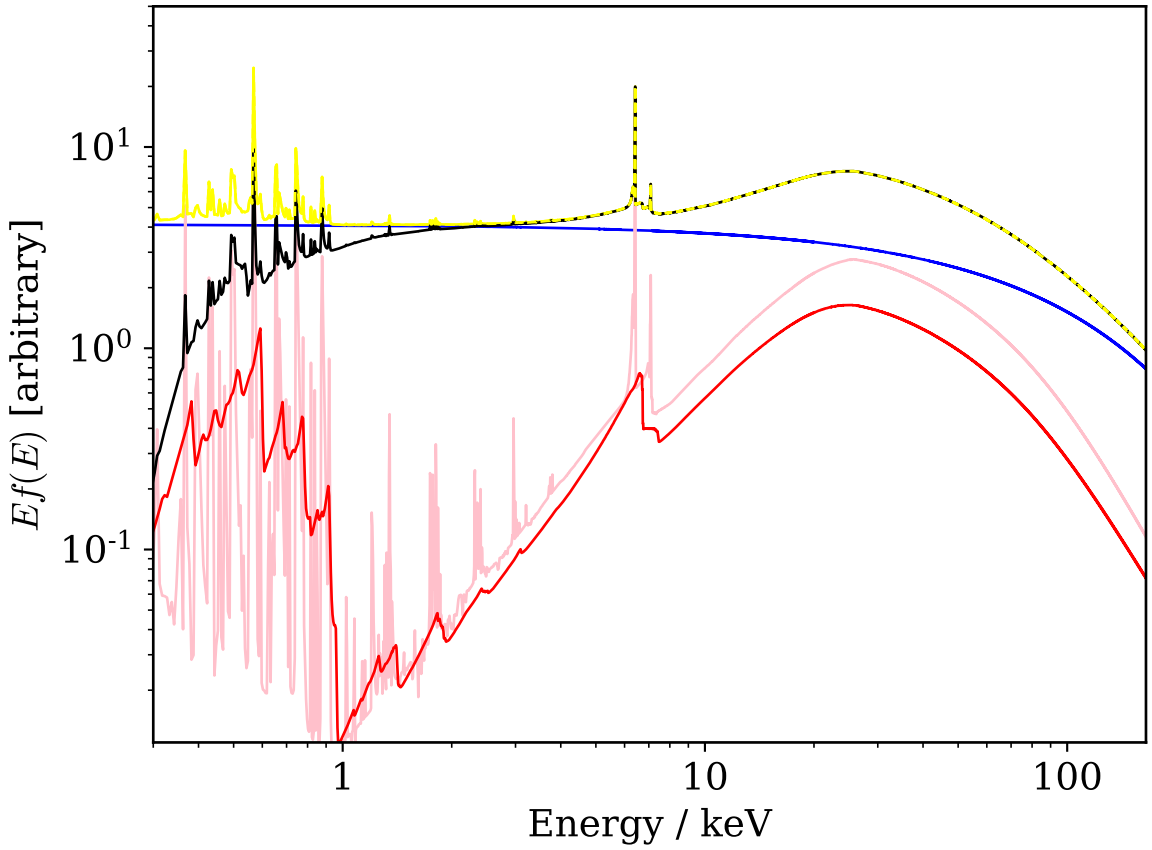

Fig. 1.1 Example X-ray spectrum of an AGN. Blue: Comptonised coronal continuum. Pink: Reflected emission from surrounding distant gas. Red: Relativistically blurred reflected emission from the inner accretion disc. Yellow: Sum of all components without absorption. Black: as observed after absorption from gas in the line of sight.

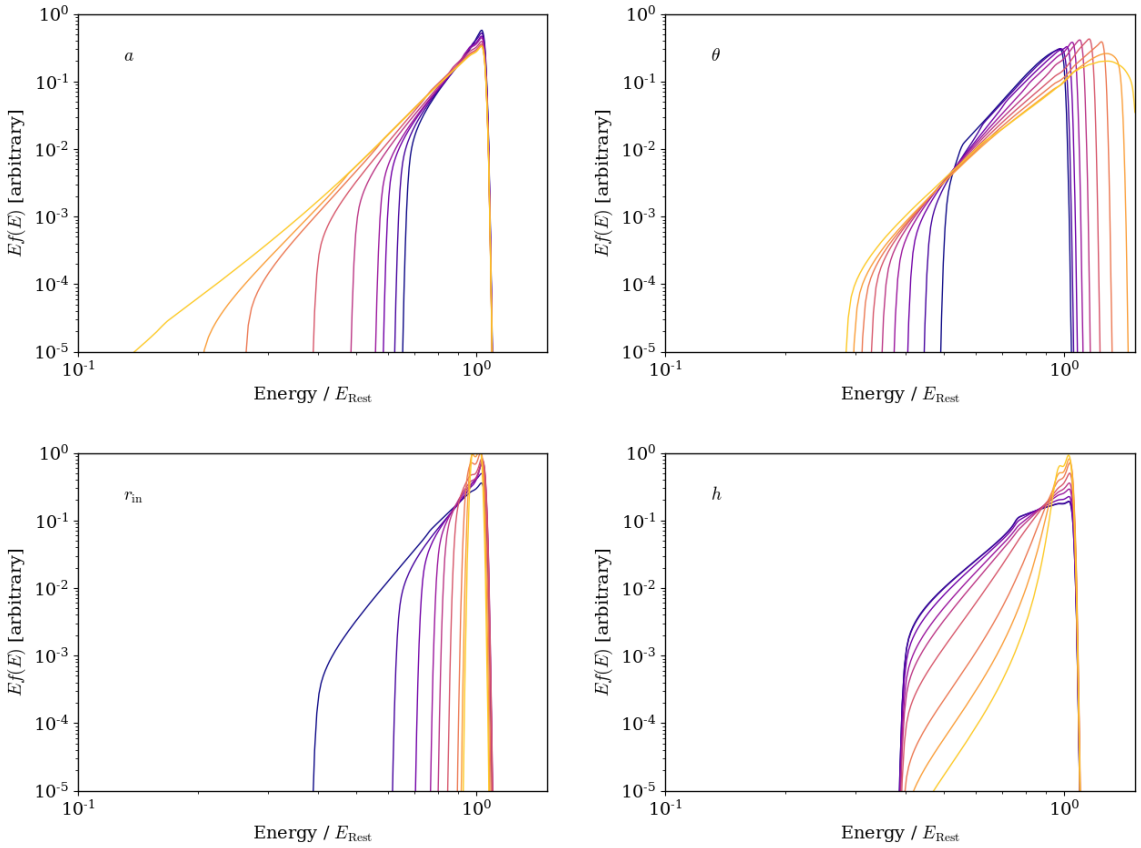

Fig. 1.2 Effect of varying various parameters on observed line profile. Bluer lines indicate a higher value of each parameter; more description of each parameter is given in the text.

1.2.4 Measurement of black hole spin

There are several ways to measure spin, usually relying on the change of stability and redshift of orbits at different radii with changes in spin. As spin increases, the event horizon shrinks from $2r_g$ to $1r_g$ and the innermost stable circular orbit (r_{ISCO}) shrinks more strongly from $6r_g$ to $1r_g$. The orbital velocity at each radius also changes.These differing gravitational redshifts and velocities at each orbit lead to different observed energies of any radiation that is emitted.

Line profiles

The effects of these energy shifts are most obvious on emission which originates with a single energy, i.e. atomic lines. Irradiation of the disc by the hard X-ray corona produces emission lines from the material in the surface of the rotating disc. The observed line profile then encodes the gravitational and Doppler shifts of the emitting material, which depend on the spin and other parameters.

The effects of some of the most significant parameters, as calculated by the `relxill` model (Dauser et al., 2010; García et al., 2014), are shown in Figure 1.2. This shows that the major effect of high spin is to increase the amount of red-shifted emission, since at high spin, stable circular orbits are present closer to the event horizon. As well as low spin, a narrower red wing can be produced by truncation of the accretion disc outside the ISCO (at r_{in}). The inclination (θ) of the system relative to the observer is the primary factor in determining the maximum observed blueshift. The relative emission at different disc radii also affects the shape of the line (more distant emission is observed closer to the rest energy). Provided the ionisation gradient across the disc is not extreme, emission is roughly proportional to illumination. The figure illustrates this for the case of illumination by a point source on the spin axis at various distances (h) from the black hole.

Continuum emission

The disc may also have significant observable thermal emission from its inner region; this emission is also affected by the spin. The range and distribution of observed temperatures can then be used to infer the spin.

The disc-blackbody (as described in Section 1.1.2) is essentially described by two parameters: the peak energy and total power (while this formula does not include relativistic effects, it turns out that these affect the spectral shape only subtly). However, rather more physical parameters determine the measurable parameters, so the physical parameters are necessarily degenerate. As well as spin, the spectrum is affected by the mass (M), accretion rate ($\dot{M}$), distance (D), inclination (θ) and hardening factor (f, which describes how the local disc emission differs from a true blackbody). The effect of each of these, as calculated by the `kerrbb` model (Li et al., 2005), is shown in Figure 1.3. The mass, distance and inclination can be determined from orbital dynamics of the binary system and modelling of the companion star, while the hardening factor is constrained theoretically (e.g. Davis and El-Abd, 2019). This then leaves spin and accretion rate as the two parameters determined by the disc spectrum.

The spin and inclination also change details of the spectral shape so these could in principle be determined independently with precise observations (Parker et al., 2019) but the magnitude of these effects may be smaller than the systematic errors from assuming emission is locally a perfect blackbody.

This method is only useful for low mass black holes which are emitting most of their power thermally, as for high masses, the disc emission peaks in the far UV (which is unobservable due to absorption by Galactic neutral hydrogen).

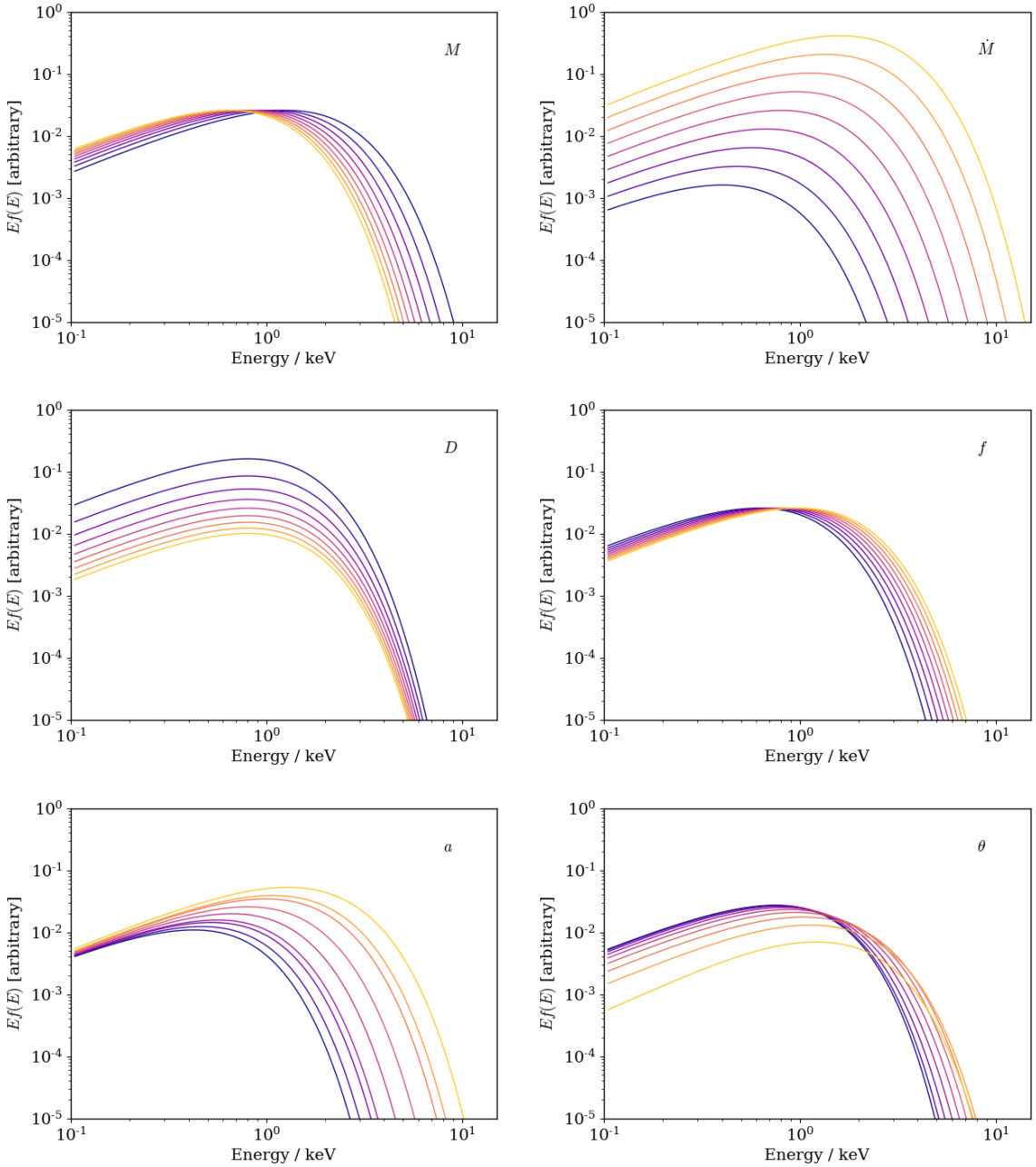

Fig. 1.3 Effect of varying parameters on observed disc spectrum. Bluer lines indicate a higher value of each parameter; more description of each parameter is given in the text.

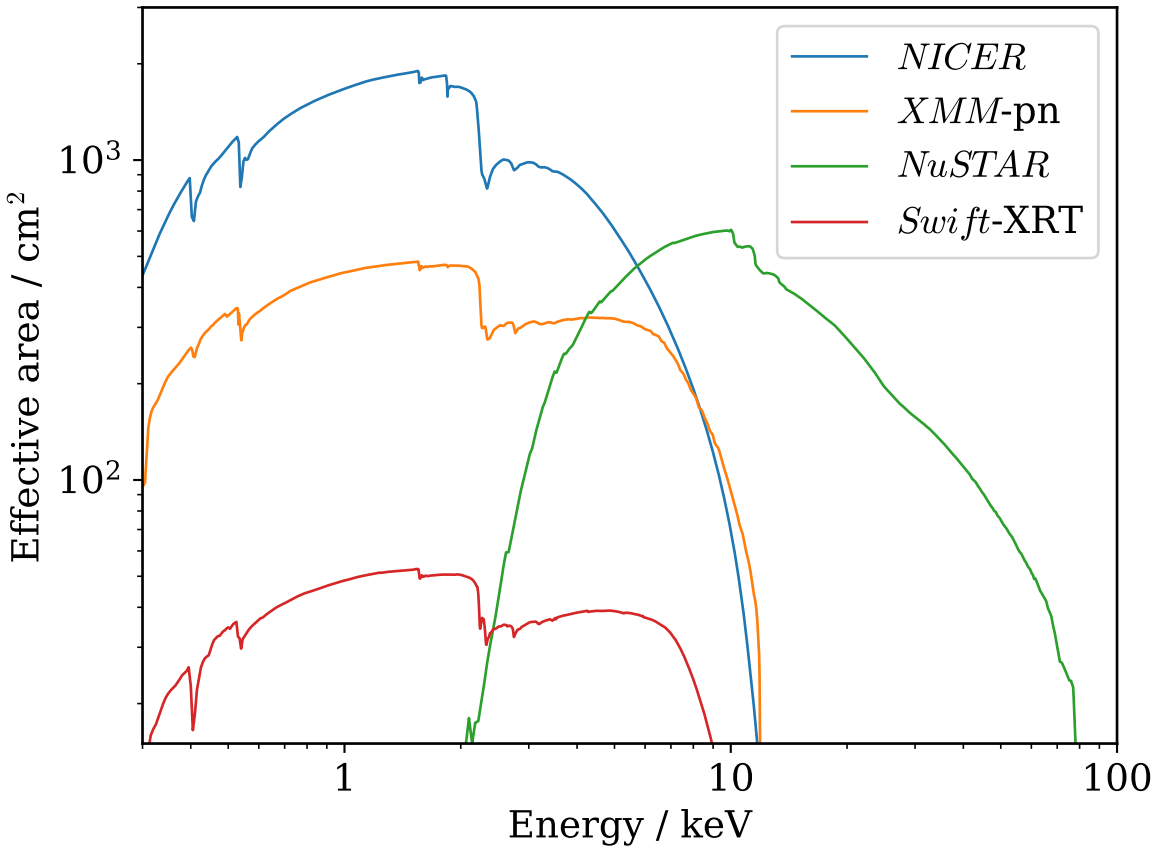

Fig. 1.4 Comparison of effective areas of major X-ray observatories.

1.3 X-ray observatories

Since X-rays are absorbed by the atmosphere, observations must be made by facilities onboard satellites (usually dedicated astronomy facilities but occasionally as part of larger projects such as the International Space Station, ISS). Various observatories are currently operational, each having slightly different capabilities driven by their primary science objectives. We describe in detail the instruments which are most heavily used in this work.

1.3.1 *XMM-Newton*

XMM-Newton (X-ray Multi-Mirror, Jansen et al. 2001) is ESA's current flagship X-ray mission and also has facilities for UV/optical observations. *XMM-Newton* has three similar co-aligned X-ray telescopes (hence Multi-Mirror) with identical mirror modules (Aschenbach, 2002; Gondoin et al., 1998a,b). Two of these also include a reflection grating assembly,

which diffracts around half of the incident photons onto the Reflection Grating Spectrometers (RGS, Brinkman et al., 1998; den Herder et al., 2001). The remaining non-dispersed photons are detected by the European Photon Imaging Camera (EPIC) MOS CCD detectors (Turner et al., 2001). In the third telescope, all of the flux is focussed onto a third EPIC detector, which uses pn CCDs (Strüder et al., 2001). Each EPIC camera operates over the $0.3-10\,\mathrm{keV}$ range; this covers from the lowest energies above Galactic absorption and high enough to include the iron Kα line at 6.4 keV. This can be used to measure the soft excess and warm absorbers as well as make spin measurements from the iron line. The RGS only operates up to $\sim 3\,\mathrm{keV}$, but at much higher resolution due to the dispersion from the gratings so provides detailed measurements of narrow lines in the soft band.

The last telescope onboard *XMM-Newton* is the Optical Monitor (OM, Mason et al., 2001). This is a 30 cm diameter Ritchey-Chretien telescope providing coverage in various filters from 170 to 650 nm. This provides simultaneous measurements of wavelengths with significant contribution from the disc, so is useful when determining the SED of AGN.

1.3.2 *NuSTAR*

NuSTAR (Harrison et al., 2013) is the leading observatory for hard ($> 10\,\mathrm{keV}$) X-rays, with innovations which provide major improvements over previous generation instruments in observations of either very bright or very faint sources. It is the first focussing telescope to operate at $\gtrsim 10\,\mathrm{keV}$. This greatly reduces the contribution from background so allows precise measurements of faint sources. Additionally, *NuSTAR* uses a triggered readout instead of a CCD, reducing the time over which pile-up can occur from the frame readout time to the trigger response time, which is short enough that pile-up is irrelevant for any astrophysical source. However, the dead-time before the detector is again sensitive limits throughput to around 400 detected counts/s. This asymptotic limit to the detected rate reduces the accuracy of flux measurements for very bright sources, but this effect is only significant at over 10 000 counts/s.

NuSTAR operates over $3-78\,\mathrm{keV}$, which in the context of accreting black holes provides simultaneous measurements of the iron Kα line and Compton hump and allows measurements of coronal temperatures in many sources.

1.3.3 *Swift*

The Neil Gehrels Swift Observatory (*Swift*) is a multi-wavelength mission principally designed to study gamma ray bursts; the high slew speed to achieve rapid follow-up of a gamma ray detection also makes *Swift* ideal for monitoring of other high-energy sources (as multiple

short observations can be made efficiently). The highest energy instrument on *Swift* is the Burst Alert Telescope (BAT), operating from $15-200$ keV with a wide field of view. The X-ray telescope (XRT) operates at similar energies to *XMM-Newton* but with only around 10% of the collecting area. The final science instrument is the Ultra-Violet and Optical Telescope (UVOT). This is derived from *XMM-Newton*-OM and uses flight spares from the OM as its optics. The available filters are also equivalent in wavelength while offering higher sensitivity, especially in the UV.

While the sensitivity of *Swift* is significantly lower in any given band than current class-leaders, the frequency with which multiple observations may be made is unparalleled, so *Swift* is uniquely suited to studying variability of multi-wavelength processes, such as relations between the disc and corona in AGN.

1.3.4 Others

Several other X-ray observatories provide (or recently provided) performance in complementary aspects of observing (the impact of these telescopes may be at least as significant as those described in more detail above; the distinction is based on their use in the following chapters).

Chandra (Weisskopf et al., 2002) covers a similar energy range to *XMM-Newton* and has higher spatial resolution, though at the expense of effective area and throughput. This means it is most useful for detection of very faint objects or observations of spatially extened objects (e.g. galaxy clusters).

Suzaku (Inoue, 2003; Mitsuda et al., 2007) was a Japanese mission which provided coverage from soft to very hard X-rays until its end-of-life in mid 2015. *Suzaku* included two functioning instruments, the X-ray imaging spectrometer (XIS, Koyama et al., 2007; Matsumoto et al., 2005) and Hard X-ray detector (HXD, Kokubun et al., 2004; Takahashi et al., 2007). The XIS consisted of four identical units, each similar to one of *XMM-Newton*'s X-ray telescopes. The HXD operated from 10 to 700 keV using two types of detector: silicon PIN diodes below 50 keV and GSO scintillators above. The intended primary isntrument was a calorimeter (Stahle et al., 2004) which would have provided imaging spectroscopy at much higher resolution (~ 6.5 eV FWHM) than other technologies but this suffered a failure before any science data could be taken. Despite this, the remaining instruments provided valuable data across an exceptionally broad X-ray band.

MAXI (Matsuoka et al., 2009) is an all sky monitor on the ISS operating from $2-20$ keV which is useful for early identification of transient outbursts.

The Neutron star Interior Composition ExploreR (*NICER* Gendreau et al., 2016) is a recent X-ray telescope designed to determine the mass-radius relation of neutron stars by

making measurements of their pulse profiles. The fast timing capability and high effective area this requires is also ideal for studying rapid changes in other bright sources and *NICER* has an extensive observatory programme taking observations of most X-ray binaries and many bright AGN.

1.4 Data analysis techniques

The instruments described in the previous section supply files describing a large number of photons, each tagged with a time and energy. This section describes the methods used or discussed in the rest of this work to extract meaningful information from the observed lists of photons. Since these are relatively standard techniques, we focus on practical reasons for and limitations of their use, rather than a rigorous statistical justification.

1.4.1 Spectral analysis

The high energy of X-ray radiation means that each photon deposits sufficient energy in a detector that it may be measured individually and its energy may be recovered well (typically to around $\pm 150\,\mathrm{eV}$). This means that any X-ray observation of a source generates a spectrum (of modest resolution); the information in this spectrum can be used to infer properties of the emitting object.

However, inferring the incident source flux spectrum from the detected counts spectrum is not trivial since the spectrum is distorted by variations in the effective area of the detector with photon energy (Figure 1.4) and blurred since photons of a given energy deposit a range of energies in the detector. The usual approach to accounting for this is to apply these effects (which are specific to each instrument) to each proposed souce flux spectrum to generate the expected counts spectrum. This is referred to as folding the spectrum through the instumental response. The response is provided by the instrument team and is usually divided into a component containing the effective area (Ancillary Response Function, ARF) and a component accounting for blurring effects (Redistribution Matrix Function, RMF). Any statistical tests are then performed by comparing the expected and observed counts spectra.

This provides a way to compare model spectra with the data but does not directly provide a representation of the information about the source spectrum provided by the data: plots of folded models and the data are distorted by the instrument response, while the models themselves are usually not unique. One way of representing the source spectrum is by ‘unfolding’ the observed counts to remove the effect of the detector response. The unfolded spectrum is produced by multiplying a given model flux spectrum by the ratio of the detected

counts to the expected counts (each as a function of energy) from the model spectrum. If the model spectrum matches the true spectrum, the ratio should only differ from one by the noise in the observation and the unfolded spectrum will match the input flux spectrum, as would be expected. If the true spectrum is different to the model used, this should be accounted for by the ratio between detected and expected counts, and the unfolded spectrum should still represent the true flux spectrum.

However, unfolding can be misleading in two principal ways. Firstly, it does not remove the blurring of features in the data but does show unblurred feartures in the unfolded spectrum: the chosen model may include features as narrow as a single detector bin, which can be much narrower than the energy resolution of the spectrum. The unfolded spectrum will then contain this narrow feature. This will appear as a clear and obvious feature even where the blurred version (seen in the actual data) is subtle and could be explained by other deviations. For this reason, unfolding spectra should be done with smooth models rather than a detailed fit of the data. The model should still have a similar shape to the observed spectrum; typically a powerlaw which is constant in νF_ν is a suitable canonical shape. Secondly, features in the spectrum around rapid changes in the detector effective area (such as the gold edge at $\sim 2.2\,\mathrm{keV}$, see Figure 1.4) may appear to occur in otherwise simple regions of the spectrum. When viewed in the counts spectrum, the change in effective area is apparent and these features are more easily assigned to limitations in the calibration (these regions are hardest to calibrate), while they may appear source related when viewed in an unfolded spectrum. This effect is difficult to remove and is best accounted for by a careful understanding of the detector calibration.

Due to the complexity of modern X-ray instruments, many ancillary values are involved in calculating the expected detected (counts) spectrum from a model source (flux) spectrum so this is commonly done with black-box software packages, of which several are available. The most commonly used is XSPEC (Arnaud, 1996), which uses very concise input commands, allowing efficient interactive use. An alternative, the Interactive Spectral Interpretation System (ISIS, Houck and Denicola, 2000) is built on the S-Lang scripting language, allowing straightforward implementation of more complex analysis. This package is used for the majority of this work.

Also available is SPEX (Kaastra et al., 1996), which includes fast photoionisation calculations, but is not used here.

As well as converting models from physical to detector units, these packages run a number of statistical tests which show whether a model is a good description of a dataset and what are plausible ranges for any parameters. These are generically referred to as fitting. The traditional, and still most common, approach, is to find the model which minimises a

'fit statistic' which encodes the difference between the model and the data. If this is small enough, the model is deemed acceptable and the range of parameters which give a fit statistic within a certain difference of the best-fit value are found. These ranges are the confidence intervals of acceptable parameters, to the chosen confidence interval (which determines the difference in fit statistic between the best fit and the edge of the confidence interval). Most analysis uses χ^2 minimisation since often the intrinsically Poisson-distributed photon counts can be approximated as Gaussian, provided there are enough photons in each data bin analysed (detector channels may be grouped together to allow this). Where insufficient photons are present (without binning to levels which would unacceptably degrade the spectral resolution), Cash statistics may be used (Cash, 1979). This treats the Poisson nature of the photon distribution exactly but the properties of the resulting statistics are less well studied. Various methods are implemented; the default (and almost universally used) being Levenberg-Marquardt (e.g. Bevington and Robinson, 1992). This method converges quickly but can get stuck in local minima. For fitting with more corrugated χ^2 spaces, slower but more robust algorithms can be used.

A more powerful way to determine ranges of parameters which fit well is Markov chain Monte-Carlo (MCMC). This has several advantages over simple minimization of a fit statistic but is significantly more computationally expensive. Firstly, the resulting chains (subject to having suitable priors) provide a direct estimate of the probability distribution of each parameter; this is usually a more relevant quantity than the range of reasonable values to expect given that the best-fit model is correct. This estimate of the probability distribution also automatically includes errorbars (credible intervals) to any level, the shape (e.g. asymmetry, multimodality) of resulting distributions and the shape of degeneracies between parameters. Determining all these from grids of fit statistics would be even more computationally expensive.

1.5 Variability analysis

The flux released by the accretion process is also observed to vary in time and this provides further information on the mechanisms involved. There are various ways in which information about the nature of the variability may be extracted from the raw lightcurves. These methods are commonly divided into time-domain and Fourier-domain methods. In time-domain methods, statistics are calculated directly from the flux at each time, while in Fourier-domain methods, a Fourier transform is first applied to the lightcurves, separating fast and slow (high and low frequency) changes in the lightcurves.

1.5.1 Time domain

The simplest variability property is the amount of variability. The observed variance (S^2) will have a contribution from measurement uncertainties ($\sigma_{\rm err}$) as well as intrinsic variability. An estimator of the intrinsic variability is the excess variance (Vaughan et al., 2003a),

$$\sigma_{\rm XS}^2 = S^2 - \bar{\sigma_{\rm err}^2} \tag{1.3}$$

which may also be viewed as its fractional amplitude (Edelson et al., 1990)

$$F_{\rm Var} = \sqrt{\frac{S^2 - \bar{\sigma_{\rm err}^2}}{\bar{x}^2}} \tag{1.4}$$

Where two lightcurves ($A(t), B(t)$, for example in different energy bands) have been measured, relations between them may also be investigated. They can be compared by testing the extent to which they vary together in the same way that any pair of sets of values may vary together, or be correlated,

$$r^2 = \frac{{\rm Cov}(A(t), B(t))^2}{{\rm Var}(A(t)){\rm Var}(B(t))} \tag{1.5}$$

Additionally, time series are located in time; this provides further information on how the series relate, for example if changes in one series are reflected some time later in another. This is expressed as the cross-correlation function (CCF, or auto-correlation function, ACF, if $A = B$),

$$CCF(\tau) = \frac{{\rm Cov}(A(t), B(t+\tau))}{\sqrt{{\rm Var}(A(t)){\rm Var}(B(t))}} \tag{1.6}$$

Typically, astronomical lightcurves do not consist of equispaced measurements due to the constraints of observatory operations, Sun avoidance etc. (and where equispaced data are available, Fourier methods may be more powerful). Therefore, some adjustment is required to account for the different spacings in the data, which may also differ between the two lightcurves which are to be compared.

If both lightcurves are generally well-covered, it is reasonable to simply interpolate each lightcurve onto a regular grid of times and calculate the CCF as before (producing the ICCF). Where the sparsity or irregularity of each lightcurve is more significant, interpolation will not give a reliable estimate of the true lightcurve so methods relying on the measured values

should be used. This is typically done with the discrete cross-correlation function (DCF, Edelson et al., 1990)

$$DCF(\tau) = \frac{\langle (A_i - \bar{A})(B_j - \bar{B}) \rangle_{|t_i - t_j - \tau| < \varepsilon}}{\sqrt{\mathrm{Var}(A(t))\mathrm{Var}(B(t))}} \tag{1.7}$$

Here, the average across all points of a given offset, τ, is replaced by the average across offsets within a given range around τ.

Any of these variants of the cross-correlation function may be used to show the relation between the processes responsible for producing the flux in each lightcurve: a peak at a given lag, τ, shows the difference in time between variations in the two lightcurves. This time difference can be attributed to the time taken for the signal which determines the changes (e.g. a photon flux) to propagate between the two regions (e.g. the light travel time). Hence distances between the two regions can be inferred.

The measured DCF depends on how the times of observations correspond to the variability timescales of the lightcurve; once observations are sparse and irregular, it is hard to determine analytically how each observation contributes to the DCF. Therefore, errorbars on quantities derived from the DCF (such as time lags) are usually calculated by bootstrapping; details of the method implemented are given at the point in the text where this is used.

1.5.2 Fourier domain

The variability in a process can also occur rapdily or slowly; a convenient way to express this (since it has many convenient mathematical properties) is through the Fourier transform:

$$\tilde{A}(f) = \int_{-\infty}^{\infty} A(t) e^{-i2\pi ft} \mathrm{dt} \tag{1.8}$$

or in discretised form, as applicable to observations of a lightcurve:

$$\tilde{A}(f) = \sum_{t \in T} A(t) e^{-i2\pi ft} \tag{1.9}$$

where T is the set of measured times in the lightcurve.

While this calculation can be made for any f and T, it is usual to use equispaced $T = \{0, t, 2t, ..., (N-1)t\}$ and $f = \{-1/2t + 1/Nt, -1/2t + 2/Nt, ..., 1/2t\}$ since this is invertible and the resulting $\tilde{A}(f)$ are statistically independent. Further, for real $A(t)$ (as is the case for lightcurves), $\tilde{A}(-f) = \tilde{A}^*(f)$, so the full information is carried in the positive frequency components.

Since a set of complex numbers is no easier to interpret than a lightcurve, various products are produced from combinations of Fourier transforms of one or more lightcurves. These typically separate the amount from the relative time of any variability. Each complex $\tilde{A}(f)$ may be considered in its polar form, $a(f)e^{i\phi(f)}$, with a and ϕ real. a is then the amplitude (amount) of variability at a given frequency and ϕ is the phase (delay in time). This phase is usually with respect to the (arbitrary) start of the measured lightcurve, so only phase differences have physical meaning.

The power spectrum $P(f) = \tilde{A}(f)\tilde{A}^*(f) = a^2(f)$ (where * denotes the complex conjugate) isolates the magnitude of the variability at each frequency. This can be smooth if there are no specific timescales on which variability occurs most strongly, or have peaks if variability occurs at particular frequencies. These can be very sharp (e.g. spin period of a neutron star, resonant frequency of a pipe) or somewhat broadened (e.g. precession of a gas disc, resonant frequency of a soft cavity).

There is significant scatter in a power spectrum taken from a single lightcurve. Using a longer lightcurve does not improve this as it generates a power spectrum with more points over a wider range of frequencies. Instead, the scatter is reduced by splitting a lightcurve into many sections and averaging over at least each section and sometimes also adjacent frequencies. The power spectrum is then

$$P(f_i) = \frac{1}{MN} \sum_{n=1}^{N} \sum_{Mi \leq j < M(i+1)} \tilde{A_n}(f_j) \tilde{A_n}^*(f_j) \tag{1.10}$$

Provided MN is large enough, the errors on such power spectra (or other products) may be approximated as Gaussian; typically, 50 is considered sufficient (Vaughan et al., 2003a).

Another common product of Fourier analysis is lags between different lightcurves. The phase lag $\Delta\phi(f) = \phi_A - \phi_B$ is taken from the Fourier transforms (e.g. Nowak et al., 1999) and converted to a time lag as

$$\Delta t(f) = \frac{\Delta\phi(f)}{2\pi f} \tag{1.11}$$

Higher order products may also be constructed; for example the bispectrum,

$$B(f_1, f_2) = \tilde{A}(f_1)\tilde{A}(f_2)\tilde{A}^*(f_1 + f_2) \tag{1.12}$$

which can be used to study connections between different components of variability (e.g. Arur and Maccarone, 2019; Maccarone and Coppi, 2002; Maccarone and Schnittman, 2005).

1.6 This thesis

In this work, we present a number of results on different aspects of the accretion system. We begin by considering the effect of emission from the central regions on outer regions of the disc, through variable heating (Chapter 2). In Chapter 3, we show that the correlated variability this would be expected to cause is not always seen.

Chapter 4 describes how a broadband X-ray spectrum can be used to distinguish between different models for the spectral shape.

In Chapter 5, we consider properties of the X-ray corona itself, in particular the temperature and possible reasons for the temperature. Chapter 6 explores the evolution of the corona during an outburst of an X-ray binary and how this compares with the inner radius of the disc.

Finally, we provide brief conclusions and consider possible future directions in Chapter 7.

Chapter 2

Ultraviolet and X-ray variability of active galactic nuclei with *Swift*

Abstract

We analyse a sample of 21 active galactic nuclei (AGN) using data from the Swift satellite to study the variability properties of the population in the X-ray, UV and optical band. We find that the variable part of the UV-optical emission has a spectrum consistent with a powerlaw, with an average index of -2.2 ± 0.1, as would be expected from central illumination of a thin disc (index of $-7/3$). We also calculate the slope of a powerlaw from UV to X-ray variable emission, $\alpha_{\mathrm{OX,Var}}$; the average for this sample is $\alpha_{\mathrm{OX,Var}} = -1.06 \pm 0.04$. The anticorrelation of α_{OX} with the UV luminosity, L_{UV}, previously found in the average emission is also present in the variable part: $\alpha_{\mathrm{OX,Var}} = (-0.18 \pm 0.08) \log(L_{\nu,\mathrm{Var}}(2500\,\text{Å})) + (3.9 \pm 2.3)$. Correlated variability between the emission in X-rays and UV is detected significantly for 9 of the 21 sources. All these cases are consistent with the UV lagging the X-rays, as would be seen if the correlated UV variations were produced by the reprocessing of X-ray emission. The observed UV lags are tentatively longer than expected for a standard thin disc.

2.1 Introduction

The structure of AGN is difficult to determine in part because their small size means they cannot be resolved by current instruments. Fortunately, this small size implies a short light-crossing time and hence AGN emission can vary on observable time-scales. Observations of variations in the emission from AGN have shown that they do indeed vary on all time-scales and at all wavelengths probed. The nature of these variations may be used to infer properties of the structure of AGN.

Our fundamental picture of this structure is that the central regions of AGN comprise an accretion disc principally emitting thermally in UV (Pringle, 1981) and a central hot corona which Compton upscatters some of these photons to X-rays (Haardt and Maraschi, 1991). A fraction of the X-rays are then emitted back towards the disc, and heat it, increasing its UV emission (Lightman and White, 1988). In these two ways, the X-ray and UV emission are linked and studying the details of the interaction can retrieve information about the nature of the UV and X-ray emitting regions.

The variability of the emission is strongest and occurs over the shortest time-scales at high energies (Mushotzky et al., 1993), indicating that the hard X-rays are produced on the smallest scales. X-ray variability studies have become a field of their own, mapping the innermost regions around the black hole (e.g. Alston et al., 2014; Fabian et al., 2009; Kara et al., 2016a; McHardy, 2013; Uttley et al., 2014; Vaughan et al., 2011). UV and optical measurements over longer time-scales form the basis for studies at longer wavelengths (e.g. Cackett et al., 2007; Cameron et al., 2012), allowing a larger region of the accretion flow to be probed. The relation of the two bands is also studied (e.g. review by Gaskell and Klimek, 2003).

While variability studies do their part in enhancing our understanding of the innermost regions of AGN, studying the time-averaged emission in great detail also provides crucial information. The time-averaged UV spectra of AGN (e.g. Francis et al., 1991; Schneider et al., 1991; Shull et al., 2012; Telfer et al., 2002; Vanden Berk et al., 2001) have been measured for many different samples and wavelength ranges. When the continuum is fit with a powerlaw, $F_\lambda \propto \lambda^\alpha$, the quasars of the Sloane Digital Sky Survey (SDSS) have $\alpha = -1.56$ over $1300 - 5000$ Å (Vanden Berk et al., 2001). This is softer than the spectrum of a thin accretion disc ($\alpha = -7/3$, Shakura and Sunyaev (1973)), although the variable part of the spectrum of NGC 7469 has been found to be consistent with that value (Collier et al., 1999). The difference from the theoretical value may be influenced by the strength of obscuration by dust and gas in the UV band (e.g. Meléndez et al., 2011), the presence of strong emission lines (e.g. Krolik and Kallman, 1988) and host starlight (e.g. Bentz et al., 2009, 2006). Cackett et al. (2007) study optical AGN spectra and derive the reddening values necessary for the difference spectra to match a thin disc spectrum. Their reddening values match those from the flux-flux or Balmer decrement method, indicating that the variable spectrum is indeed shaped like that of a thin disc. Softer spectra are found at shorter wavelengths: α is -1.32 ± 0.14 over $1200 - 1750$ Å and -0.59 ± 0.21 over $550 - 1000$ Å (both Shull et al., 2012), suggesting the presence of a turn over at wavelengths probing the highest temperatures in the disc. The high-energy cut-off in the coolest sources may also redden the average spectral index at longer wavelengths.

When the mean UV emission is compared with that of the X-rays, the power is found to be tightly correlated: the X-ray luminosity scales as $L_\mathrm{X} \propto L_\mathrm{UV}^k$ with $k = 0.5 - 0.8$ (e.g. Lusso and Risaliti, 2016; Steffen et al., 2006; Vignali et al., 2003) which results in the UV (2500 Å) to X-ray (2 keV) slope, α_OX, being anticorrelated with luminosity: $\alpha_\mathrm{OX} = a \log L_\mathrm{UV} + \mathrm{const}$, $-0.2 \lesssim a \lesssim -0.1$ (Just et al., 2007; Strateva et al., 2005; Vagnetti et al., 2010). This relation suggests that the processes producing the UV and X-ray radiation are closely related, as would be expected for an accretion disc–corona system.

The link between the X-ray and different UV bands can also be studied by comparing their correlation for a given source across time. Lags between changes in each band are interpreted as being due to the light travel time between the regions responsible for the emission in the different bands and hence the distances between them can be inferred.

Such lags have been sought in various sources (e.g. Maoz et al., 2000; Shemmer et al., 2001) and compared to the predictions for a steady state accretion disc (Shakura and Sunyaev, 1973). Where lags are found, they often disagree with thin disc theory, usually showing a longer lag than expected.

Before precision cosmology provided a largely unquestioned value of $H_0 \simeq 70\,\mathrm{km\,s^{-1}\,Mpc^{-1}}$, the luminosity of a standard disc was used to provide a distance modulus and hence H_0 (Collier et al., 1999). However, the disc sizes from the measured lags implied $H_0 = 42 \pm 9\,\mathrm{km\,s^{-1}\,Mpc^{-1}}$ (Collier et al., 1999) or $H_0 = 44 \pm 5\,\mathrm{km\,s^{-1}\,Mpc^{-1}}$ (Cackett et al., 2007), so the disc is not as bright as is expected for its size. Other studies also find deviations from a standard disc. For example, studies of NGC 5548 by Edelson et al. (2015) and Fausnaugh et al. (2016) describe the disc as larger than expected for its mass and accretion rate. Similarly, Troyer et al. (2016) and Lira et al. (2015) find the best fitting accretion rate, $\dot{M}$, is unreasonably high for a standard disc model in NGC 6814 and MCG-6-30-15 respectively. The longer lags being associated with a larger disc than expected is corroborated by quasar microlensing observations, which find emitting regions a factor of a few ($2-3$, Chartas et al. (2016); ~ 4, Morgan et al. (2010)) larger than predicted.

However, a larger emitting region may not be the whole answer, as longer lags are not always found: McHardy et al. (2016) study the low mass AGN NGC 4395 ($3.6 \times 10^5 M_\odot$) and find lags which are not markedly different from standard thin disc theory.

Despite the lags often being longer than expected, the lag-wavelength relation found by these studies in the UV to IR bands is usually consistent with the predicted $\tau \propto \lambda^{4/3}$ for a standard accretion disc.

Lags have also been sought in the short time-scale variability within an X-ray observation with simultaneous UV monitoring. Smith and Vaughan (2007) analyse *XMM* observations of 8 sources but find no significant correlations. Arévalo et al. (2005) find the UV emission leading the X-rays by $\sim 160\,\mathrm{ksec}$ (1.9 days) in a 430 ksec observation, although this lag is a large fraction of the observation length.

These studies of lags in individual sources have shown that, at least for some sources, the reprocessing of X-ray radiation does not behave as expected for a centrally illuminated thin disc. A study of many sources has the potential to show what proportion of sources has a longer lag and whether this correlates with other AGN properties.

The *Swift* satellite (Gehrels et al., 2004), principally designed for the detection of GRBs, is ideal for such broadband variability analysis: it has detectors for X-rays (Burrows et al., 2005) and ultraviolet/optical emission from 1700–6000 Å (Roming et al., 2005). Since it has been operating for more than a decade, many AGN lightcurves covering time-scales of several years are available.

Here, the amount of variability in the UV and X-rays and the time differences between them are analysed for a sample of AGN to determine properties of AGN as a population. Emission from the V-band to X-rays is included to consider a large extent of the accretion disc.

The choice of sources and observations and the reduction of data is described in Section 2.2. The methods and results of the analysis are described in Section 2.3. In particular, the UV variability is considered in Section 2.3.1 and the X-ray in Section 2.3.2. The bands are compared in terms of power in Section 2.3.3 and time lags are explored in Section 2.3.4. These results are interpreted in Section 2.4. Comments on individual sources are given in Section 2.5.

2.2 Observations and Data Reduction

Our sample consists of all those AGN from the CAIXA sample (Bianchi et al., 2009) with at least 20 *Swift* observations by September 2015. CAIXA comprises all unobscured radio-quiet AGN with public targeted *XMM-Newton* observations as of March 2007. The radio-loud AGN 3C 120 was also included to test whether radio-loud AGN have grossly different properties and the Seyfert 1 galaxy Zw 229–15 was included as a large number of *Swift* observations was present in the archive. This provides 21 sources, shown in Table 2.1 along with their mass and reddening.

Our analysis uses the data from both telescopes on board of *Swift* (Gehrels et al., 2004): the UV (UVOT, Roming et al., 2005) as well as the X-ray (XRT, Burrows et al., 2005) telescope.

The X-ray light curves used in this work were produced using the automatic pipeline of the UK Swift Science Data Centre (Evans et al., 2009, 2007). Light curves were produced with a resolution of one bin per observation in 8 fine energy bands (0.3–0.6 keV, 0.6–0.9 keV, 0.9–1.2 keV, 1.2–1.5 keV, 1.5–3.0 keV, 3.0–5.0 keV, 5.0–7.0 keV, 7.0–10 keV)and the broader bands 0.3–10 keV, 0.3–1.5 keV and 1.5–10 keV. For our analysis we used the default grade selection. When converting counts to flux, we correct for Galactic absorption using values from the LAB survey (Kalberla et al., 2005).

Table 2.1 List of sources in our sample, with number of observations, black hole mass and reddening values for each object

Source	Number of Observations	UV bands with ≥ 10 Observations	$\log_{10}(M_{\rm BH})$	Ref.	$E(B-V)$ (Galactic)	$E(B-V)$ (Intrinsic)	Ref.
NGC 5548	744	6	$7.59^{+0.24}_{-0.21}$	P	0.0171	0.152	G
MRK 335	339	6	$7.23^{+0.04}_{-0.04}$	B	0.0307	0.00	C
NGC 7469	224	6	$6.96^{+0.05}_{-0.05}$	B	0.0591	0.09	C
FAIRALL 9	168	6	$8.41^{+0.11}_{-0.09}$	P	0.0223	0	N
1H 0707-495	119	1	$6.72^{+0.5}_{-0.5}$	Pa	0.0816	0	N
MCG–6-30-15	105	1	$6.7^{+0.1}_{-0.2}$	P	0.0521	0.54	Wa
MRK 766	100	6	$6.82^{+0.05}_{-0.06}$	P	0.0169	0.613	G
ARK 120	90	2	$8.18^{+0.05}_{-0.06}$	P	0.1094	0.04	C
IRAS 13224–3809	70	1	$6.76^{+0.5}_{-0.5}$	Z	0.0601	0.628	Po
PG 1211+143	68	6	$8.17^{+0.11}_{-0.15}$	P	0.0293	0	G
NGC 4051	59	1	$6.13^{+0.12}_{-0.16}$	P	0.011	0.12	Wi
NGC 3516	58	1	$7.40^{+0.04}_{-0.06}$	B	0.0359	0.15	C
MRK 1383	35	2	$9.01^{+0.11}_{-0.07}$	B	0.0275	0	N
PG 1247+267	33	1	$8.91^{+0.15}_{-0.17}$	T	0.0112	0	N
H 0557–385	28	1	7^{+1}_{-1}	A	0.0375	0.511	Ki
MRK 509	27	3	$8.05^{+0.04}_{-0.04}$	B	0.0493	0.11	C
MRK 841	26	6	$7.88^{+0.1}_{-0.1}$	V	0.0255	0	Wi
PDS 456	22	2	$8.91^{+0.5}_{-0.5}$	Z	0.4450	0	N
IC 4329A	20	6	$8.34^{+0.3}_{-0.3}$	M	0.0501	0.98	M
3C 120	71	5	$7.75^{+0.04}_{-0.04}$	B	0.2558	0.05	H
Zw 229–15	71	1	$6.91^{+0.08}_{-0.12}$	B	0.0615	0	N

A: Ashton et al. (2006), B: Bentz and Katz (2015), M: Markowitz (2009), P: Peterson et al. (2004), Pa: Pan et al. (2016), T: Trevese et al. (2014), V: Vestergaard (2002), Z: Zhou and Wang (2005).
C: Cackett et al. (2007), G: Grupe et al. (2010), H: Hjorth et al. (1995), Ki: Kishimoto et al. (2011), M: Marziani et al. (1992), N: No value found in literature – $E(B-V)=0$ assumed, Po: Polletta and Courvoisier (1999), Wi: Winter et al. (2010), Wa: Ward et al. (1987)

The UVOT observations were taken in different filters (*V*: 5440 Å, *B*: 4390 Å, *U*: 3450 Å, *W1*: 2510 Å, *M2*: 2170 Å, *W2*: 1880 Å) and we reduce each filter individually for each observation. We started our UVOT reduction from the level II image files, performing photometry with the tool `uvotsource`. To obtain the source counts, we assumed a circular source region with a 5 arcsec radius and a, also circular, background region with a 15 arcsec radius. Some areas of the UVOT detector have shown spuriously low fluxes (Edelson et al., 2015), so we excluded observations where the source region overlaps these bad areas. Count rates were converted to fluxes for each source using calibration factors from Poole et al. (2008).

Where necessary, the UV emission for each source was dereddened using the idl tools `ccmunred` (Cardelli et al., 1989; O'Donnell, 1994) for Galactic dust and `mszdst`[1] for host absorption, with the extinction law from the LMC (Pei, 1992).

UV/optical fluxes include a significant contribution from the host galaxy. Removing this component is difficult and requires high resolution images of the host galaxy. Here, we avoid the problem by using methods which are not affected by the additional constant host flux.

The luminosity distance was calculated with $H_0 = 70\,\mathrm{kms}^{-1}\,\mathrm{Mpc}^{-1}$. The relative luminosities are not sensitive to cosmological parameters since all sources apart from PG1247+267 ($z = 2.038$) are at low redshift ($z \ll 1$).

2.3 Results

2.3.1 UV variability

We initially consider the variability of the 6 *Swift* UV/optical bands.

Presence of variability

To characterise the variability of the luminosity in each band, the intrinsic variability was estimated as the error-corrected rms variability, $L_{\mathrm{Var}} = \sqrt{\sigma^2 - \bar{\varepsilon^2}}$ (Edelson et al., 2002; Nandra et al., 1997a), where σ is the measured standard deviation of the luminosity measurements from the observations and ($\bar{\varepsilon^2}$) is their mean square error. We only consider UV bands with at least 10 data points to remove lightcurves where the uncertainty would be excessively dominated by the stochastic variations due to sampling.

X-ray studies usually consider the fractional (rms) variablity, $F_{\mathrm{Var}} = L_{\mathrm{Var}}/\bar{L}$ (although this is usually calculated directly from the measured count rates), where $\bar{L}$ is the mean of the measured lightcurve, to avoid the effects of absorption. Absorption is a multiplicative

[1] https://heasarc.gsfc.nasa.gov/xanadu/xspec/models/dust.html

effect which changes $L_{\rm Var}$ and $\bar{L}$ by the same factor, so their ratio is unchanged. In the UV, host galaxy contamination is a more significant problem, so $\bar{L}$ from the AGN alone is not precisely known. This constant addition to the measured $\bar{L}$ has no effect on the variance of the lightcurve. Hence, we prefer the absolute luminosity variance. The standard deviation (rms variability) is preferred to the variance because of its more familiar dimension.

We define a source as variable if this variable luminosity, $L_{\rm Var}$, is larger than its associated error. The approximate error in the lightcurve variability is given by equation (2.1) (Vaughan et al., 2003a, eq. 11), where N is the number of datapoints.

$$\mathrm{err}(L_{\rm Var}^2) = \frac{1}{\sqrt{N}}\sqrt{\left(\sqrt{2}\bar{\varepsilon^2}\right)^2 + \left(2\sqrt{\bar{\varepsilon^2}}L_{\rm Var}\right)^2} \tag{2.1}$$

We assess the variability for each source and band separately. In four bands out of 90 with sufficient data (≥ 10 points) to calculate variability (IC 4329A *B*, *W2*; MRK 766 *M2*; PDS 456 *W1*), the error was greater than the measured variability. Since the measured variability is subject to random variations depending on when a source is observed, a varying source may by chance be observed when it varies little. Since there is no reason to expect this small fraction of bands to not be varying, these bands were not excluded from further analysis to avoid biasing results towards observations which happened to catch higher variability.

UV variability spectra

For 12 sources, $L_{\rm Var}$ measurements exist in at least 2 wavebands; for these, we produced a spectrum of this variable component of the emission ($L_{\lambda,\rm Var}$). The variable UV spectrum of Fairall 9, which is typical of the sample, is shown in Fig. 2.1, fitted with a powerlaw. Spectra of the whole sample are shown in Appendix A.2.

To characterise the shape of the spectrum, the spectrum of variable luminosity was fitted with a powerlaw, $L_{\lambda,\rm Var} \propto \lambda^{\alpha}$. We performed a chi-square minimisation with `mpfit` in IDL in the logarithmic domain. The wavelengths of each band were taken as the nominal central value. Errors of the luminosity variability were estimated from equation (2.1). Values for α are given in Table 2.2.

In most sources, the powerlaw provides a good fit; however, for 3C 120, Mrk 766 and PG 1211+143 the reduced χ^2 value is unacceptably high. Exploring the reasons for this, we find that in Mrk 766, the *W2* measurement is much higher than would be expected from extrapolating a powerlaw fitted to the remaining values. Since for Mrk 766 the *W2* band has a large number of samples from 2012-13 which are not taken in the other filters, the W2 variability measurement may be increased by the difference in variability in the different epochs. In PG1211+143, the *U*-band is somewhat higher than expected and the *M2* much

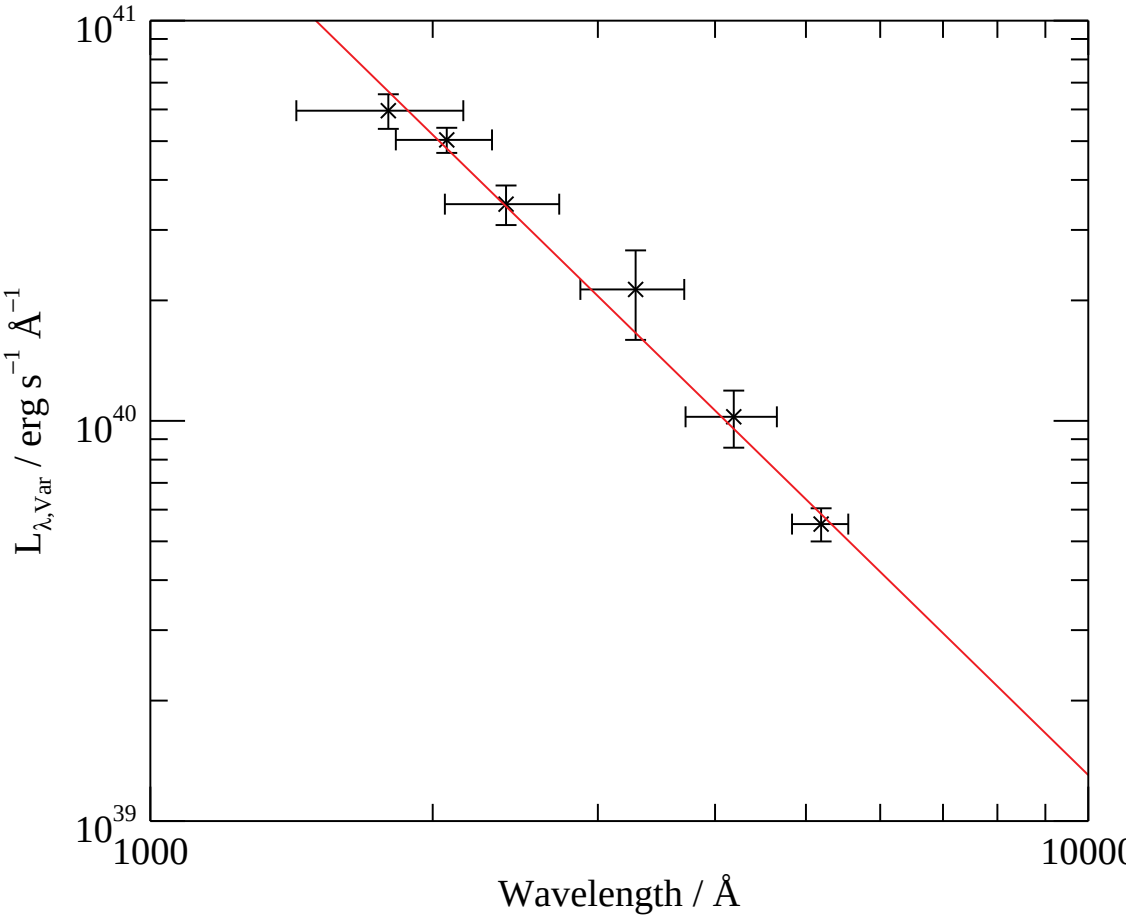

Fig. 2.1 The spectrum of the variable UV emission of Fairall 9, along with the best-fitting powerlaw, $\alpha = -2.29 \pm 0.10$.

Table 2.2 Index of powerlaw fit to variable part of UV spectrum, with 1σ errors. Most sources are consistent with $-2 > \alpha > -2.33$, as predicted for a thin accretion disc

Source	Index, α	$\chi^2_{\rm red}$	d.o.f.
3C 120	-2.21 ± 0.10	5.10	3
ARK 120	-2.41 ± 0.83	-	0
Fairall 9	-2.29 ± 0.10	0.94	4
IC 4329A	-3.14 ± 0.27	1.78	1
MRK 335	-2.27 ± 0.11	2.14	4
MRK 509	-1.96 ± 2.41	0.04	1
MRK 766	-3.57 ± 0.09	34.31	4
MRK 841	-2.11 ± 0.16	0.59	4
MRK 1383	-2.81 ± 0.88	-	0
NGC 5548	-2.71 ± 0.07	0.67	4
NGC 7469	-3.13 ± 0.39	1.65	3
PG 1211+143	-2.01 ± 0.15	9.90	4

lower. In 3C 120, the *U* and *M2*-bands are both higher than the fit. Since these sources show scatter rather than curvature, it is possible that the errors have been underestimated.

From the fits, we find an average slope of $\alpha = -2.6 \pm 0.8$. For all sources apart from IC 4329A, MRK 766, NGC 5548 and NGC 7469, the index is consistent with $\alpha = -2$ to -2.33, as predicted by Davis et al. (2007) for a thin accretion disc. The variable spectrum of NGC 5548 has also been measured by Edelson et al. (2015) with a subset of the data used here, finding $\alpha = -1.98 \pm 0.20$ assuming no intrinsic reddening (this is consistent with our value before dereddening). For IC 4329A and Mrk 766, the intrinsic reddening is strong (Table 2.1), so the uncertainty in the reddening may allow their indices to be consistent with $\alpha = -2$ to -2.33. Collier et al. (1999) also measured the variable spectrum of NGC 7469, finding an index consistent with $\alpha = -2.33$.

For the sources with $E(B-V) \leq 0.05$ and excluding those sources with very large uncertainties ($\Delta\alpha > 0.75$), the average index is $\alpha = -2.21 \pm 0.13$. We consider this our best estimate of the slope.

In order to investigate the nature of the variability on different time-scales and ensure that the non-uniformly sampled lightcurves do not bias the results based on the different time-scales sampled in different observations, the lightcurves were also split into sections of different lengths. The index of the variable spectrum was calculated in the same way as for the full lightcurve. For each section length, we calculate the average index of all sections. For Fairall 9, which has enough data to split on many time-scales, Fig. 2.2 shows the spectral index as a function of section length. The index converges towards the value calculated from the full lightcurve as the section length increases, which justifies the use of the full lightcurve.

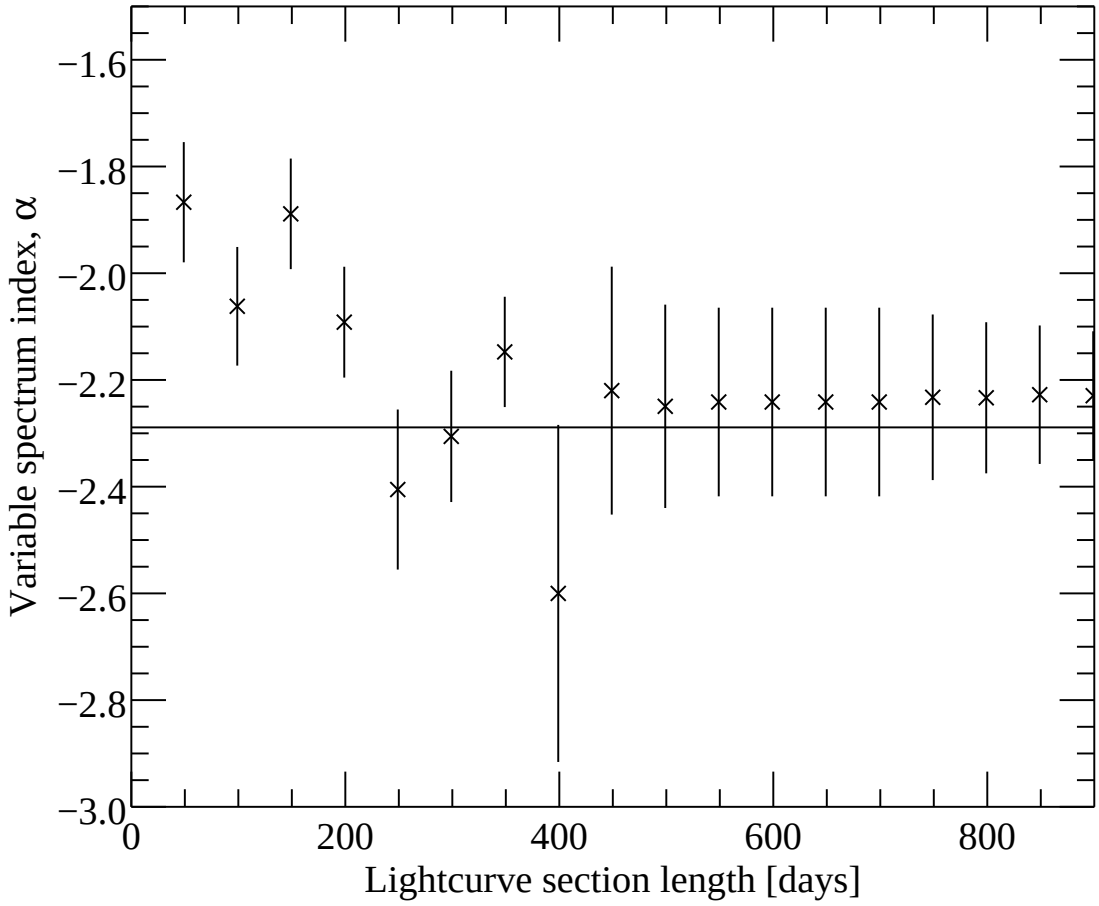

Fig. 2.2 Plot of index of variable spectrum of Fairall 9 against duration of lightcurve used to calculate variability. The index shown at each timescale is the average over all sections of given length. The horizontal line shows the value for the full lightcurve. The index appears to converge to the value measured from the full lightcurve as section length increases.

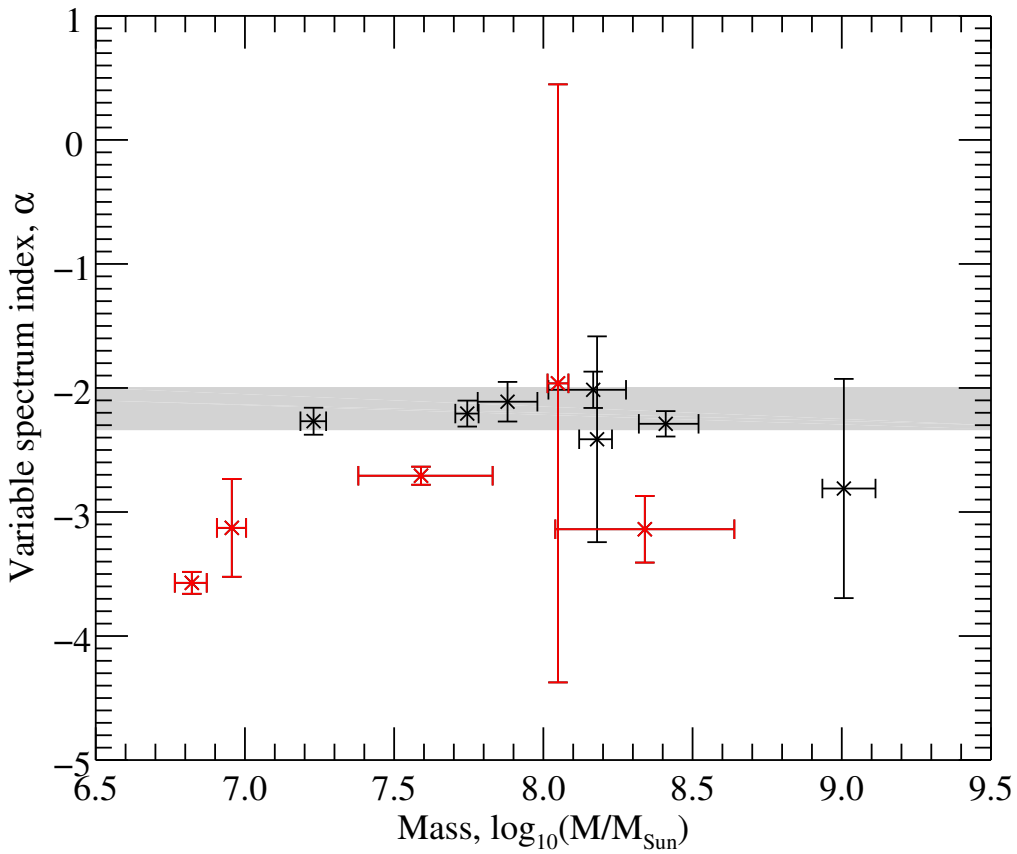

Fig. 2.3 Plot of spectral index of variable emission against black hole mass. Most sources are consistent with an index of $-2 > \alpha > -2.33$ (indicated by the shaded region), as predicted for a thin accretion disc. Those sources with a steeper spectrum tend to have been the most dereddened: sources with $E(B-V)_{\rm int} > 0.05$ are shown in red. No correlation with mass is apparent ($r = 0.36$).

Finally, we consider how the spectra of variable power depend on black hole mass. Plotting the spectral indices, α, of the variable part of the spectrum against mass (Fig. 2.3) shows no clear correlation ($r = 0.36$). Fig. 2.4 shows the variable luminosity in each UV band against black hole mass, $M_{\rm BH}$. Sources with observations in all 6 bands are shown in black and the remaining sources in grey. It is apparent that $L_{\rm Var}$ increases with mass. While the black points show a tight correlation, this is a selection effect: the power is also dependent on the Eddington ratio and, for this subsample, the Eddington ratio smoothly decreases with mass (Table 2.4). This flattens the observed correlation so the slope of the relationship is not meaningful. The effect of scattered Eddington ratios can be seen in the greater scatter when including the remaining sources (grey points). The correlations between $M_{\rm BH}$ and $L_{\rm Var}$ seen

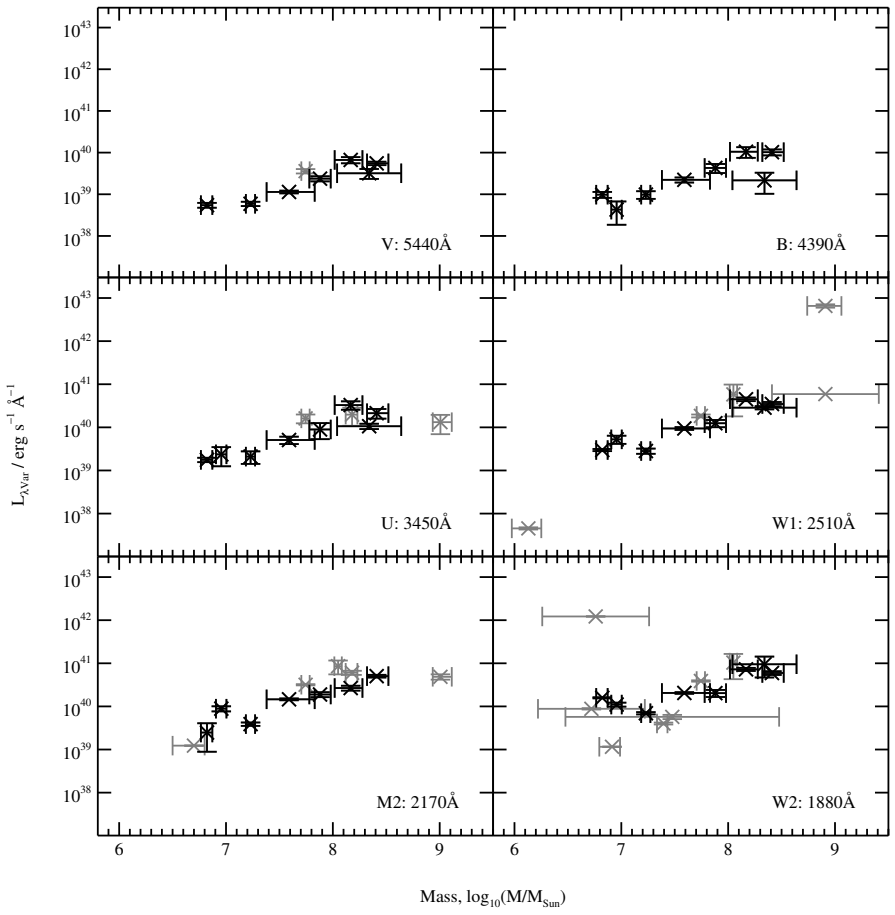

Fig. 2.4 Plot of variable luminosity, $L_{\rm Var}$, against black hole mass in each waveband. Sources in black are observed in all bands, other sources are in grey.

in the black points do show that the scaling with mass is consistent between the different bands, as would be expected if the spectral shape is constant.

2.3.2 X-ray Variability

To compare the variability of the thermal disc emission with that of the coronal emission, we also calculated the variable luminosity, $L_{\rm var}$, in the 8 X-ray bands. Due to the stronger variability in the X-ray lightcurves, the analytic formula for the error (as used for the UV variability) is less reliable (Vaughan et al., 2003a), so we estimated the error in the excess variance due to measurement error from simulated lightcurves. To do this, we simulated lightcurves by adding values from a Gaussian with the same width as the error on each observation to the measured lightcurve and used the distribution of excess variance from 20000 realisations to estimate 1σ and 2σ confidence intervals. As the error is comparable to

the measured value in some sources, we converted the confidence limits from variance to rms directly, as in Poutanen et al. (2008), rather than using differential error propagation.

The variable X-ray luminosity spectra this produces are shown alongside the UV variable spectra in Appendix A.2. The X-ray variable spectra look superficially similar in shape to the mean spectra of their respective sources.

To quantify the differences between the mean and variable spectra, we fitted powerlaws to the hard (1.5-10 keV) X-ray band for each source. For consistency with other X-ray measurements, we use the photon index defined as $N(E) \propto E^{-\Gamma}$ (note that this converts from the wavelength spectral index as $\Gamma = \alpha_X + 3$). These photon indices, Γ_{Var}, are compared to the indices of the mean spectra over the same band, Γ_{Avg}, in Fig. 2.5. This shows that the two indices are well correlated ($r = 0.81$) and the variable spectra are softer than the average spectra over the 1.5-10 keV band. We estimate the relation between the variable and average indices with a linear function; the best fitting is $\Gamma_{Var} = (0.97 \pm 0.07)\Gamma_{Avg} + (0.36 \pm 0.08)$, compatible with a constant offset. Fitting for a constant offset gives $\Delta\Gamma = 0.28 \pm 0.02$ between average and variable index.

2.3.3 Comparison of UV and X-ray variable power

To help understand the interactions between the disc and corona, we compared the power of the variability in the X-ray ($L_{X,Var}$) and UV ($L_{UV,Var}$).

We first considered the variable power in the directly measured energy ranges, $0.3 - 10$ keV (X-ray) and $1500 - 5815$ Å (UV). The X-ray variability power was calculated from a direct sum over the power in each energy bin. Since the UV bands do not fully and evenly cover their overall wavelength range, we used a powerlaw fit to the datapoints integrated over the total range of the *Swift* filters. The variable power in the X-ray and UV is plotted in Fig. 2.6; this shows that the UV and X-ray power is broadly comparable. There is a strong correlation ($r = 0.74$) between the two quantities with the UV power increasing somewhat faster than the X-ray power. Approximating the relation with a powerlaw $L_{X,Var} \propto L_{UV,Var}^{\beta}$ gives a best fit of $\beta = 0.66 \pm 0.22$. This is consistent with the relationship between the average luminosities, for which $\beta = 0.72 \pm 0.01$ or 0.75 ± 0.06 have been found by Steffen et al. (2006) and Vignali et al. (2003) respectively.

We also consider the relative specific luminosity, using the definition of α_{OX} applied to the variable part of the emission. α_{OX} is the index of a powerlaw between the specific luminosity at 2500 Å and 2 keV (e.g. Vagnetti et al., 2010):

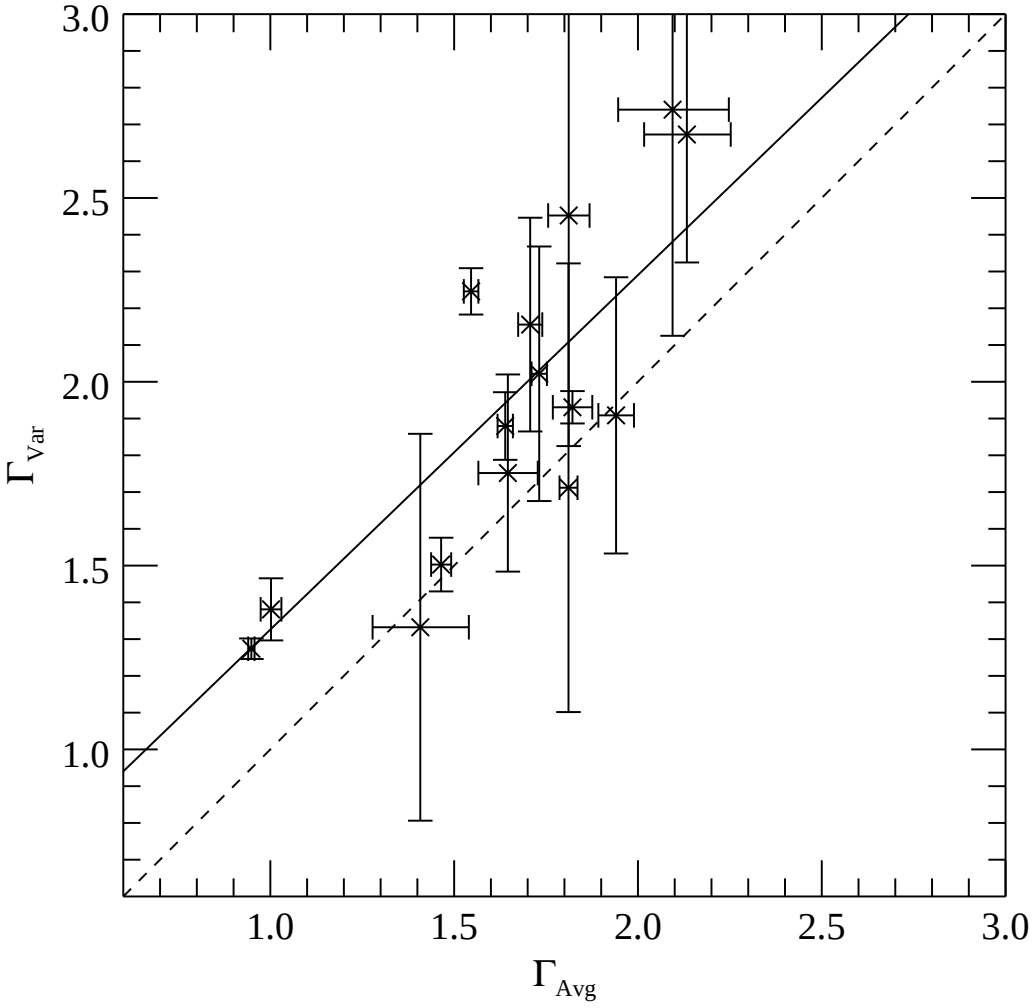

Fig. 2.5 Photon index (Γ) of powerlaw fit to average and variable parts of 1.5-10 keV X-ray spectra. Solid line: best fit; dashed line: equal variable and average indices. The variable part is usually softer than the average spectrum, with an average $\Delta\Gamma = 0.28 \pm 0.02$ (1σ error).

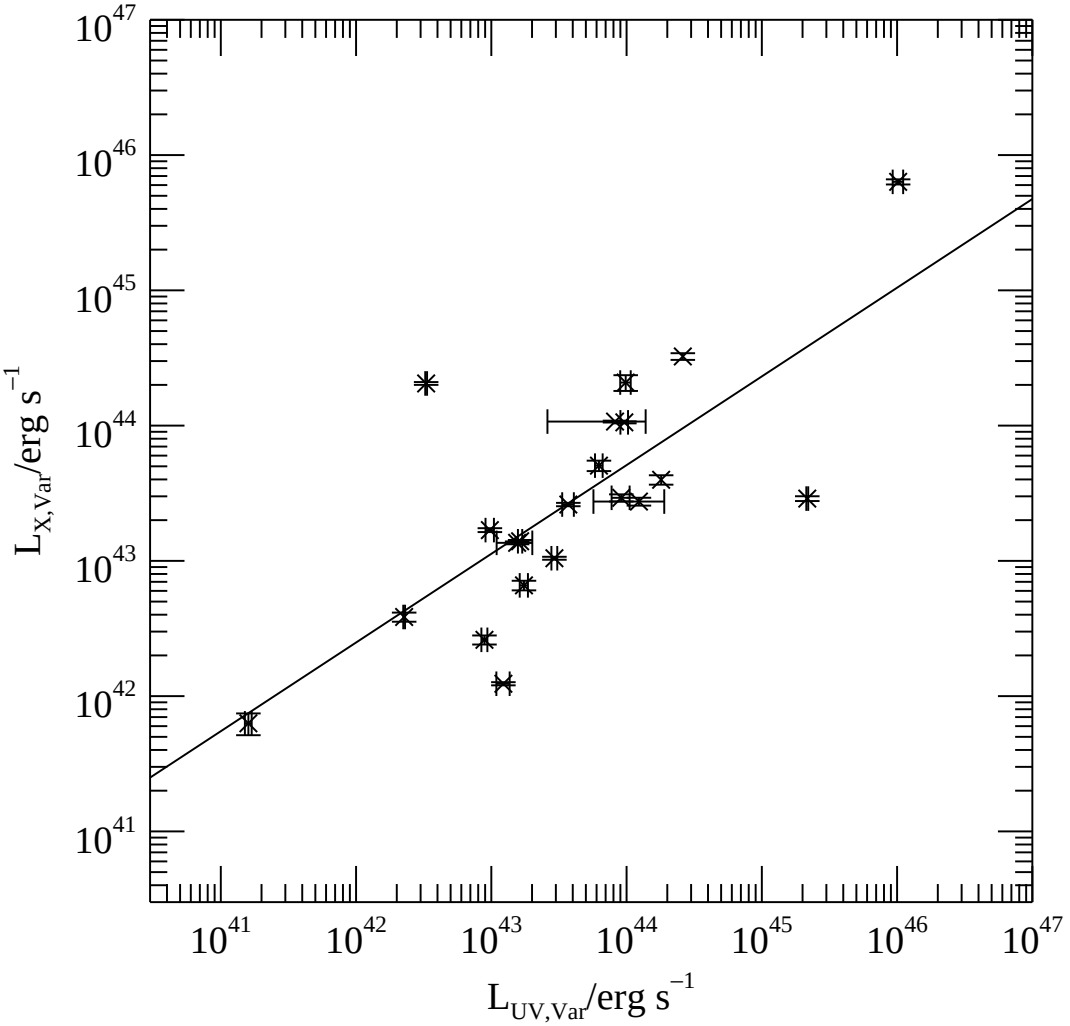

Fig. 2.6 Plot of total UV against X-Ray variable power in measured bands: UV: 1500 – 5815Å; X-ray: 0.3 – 10 keV. The line shows the best-fitting powerlaw, $L_{\mathrm{X,Var}} \propto L_{\mathrm{UV,Var}}^{0.66\pm0.22}$

$$\begin{aligned}\alpha_{\rm OX} &= \frac{\log(L_\nu(2\,{\rm keV})/L_\nu(2500\,\text{Å}))}{\log(\nu_{2\,{\rm keV}}/\nu_{2500\,\text{Å}})} \\ &= 0.3838\log\left(\frac{L_\nu(2\,{\rm keV})}{L_\nu(2500\,\text{Å})}\right)\end{aligned} \tag{2.2}$$

Here, we measure $\alpha_{\rm OX,Var}$ from the variable specific luminosities. The average is $\alpha_{\rm OX,Var} = -1.06 \pm 0.04$, which is flatter than some measurements of $\alpha_{\rm OX}$ measured from mean spectra of similarly bright sources (e.g. -1.32 ± 0.03, Steffen et al. 2006) but similar to values found in Xu (2011), which includes some sources which are in our sample. $\alpha_{\rm OX,Var}$ for each source is shown against specific variable UV luminosity at 2500 Å in Fig. 2.7. These are anticorrelated, $r = -0.73$, and the least-squares fit is

$$\alpha_{\rm OX,Var} = (-0.177 \pm 0.083)\log L_{\nu,{\rm Var}}(2500\,\text{Å}) + (3.88 \pm 2.33) \tag{2.3}$$

This relation has a slope within those found by previous authors for the mean spectrum, such as that by Gibson et al. (2008):

$$\alpha_{\rm OX} = (-0.217 \pm 0.036)\log L_{2500\,\text{Å}} + (5.075 \pm 1.118) \tag{2.4}$$

or the flatter relation found by Just et al. (2007):

$$\alpha_{\rm OX} = (-0.140 \pm 0.007)\log L_{2500\,\text{Å}} + (2.705 \pm 0.212) \tag{2.5}$$

Xu (2011) studied low-luminosity AGN and found:

$$\alpha_{\rm OX} = (-0.134 \pm 0.031)\log L_{2500\,\text{Å}} + (2.406 \pm 0.785) \tag{2.6}$$

Grupe et al. (2010) also analysed a sample of local ($z < 0.35$) sources with *Swift*, so provide the most similar reference sample:

$$\alpha_{\rm OX} = (-0.114 \pm 0.014)\log L_{2500\,\text{Å}} + (1.177 \pm 0.305) \tag{2.7}$$

However, Vagnetti et al. (2013) corrected for the galactic dilution in this sample and found:

$$\alpha_{\rm OX} = (-0.135 \pm 0.015)\log L_{2500\,\text{Å}} + (2.645 \pm 0.446) \tag{2.8}$$

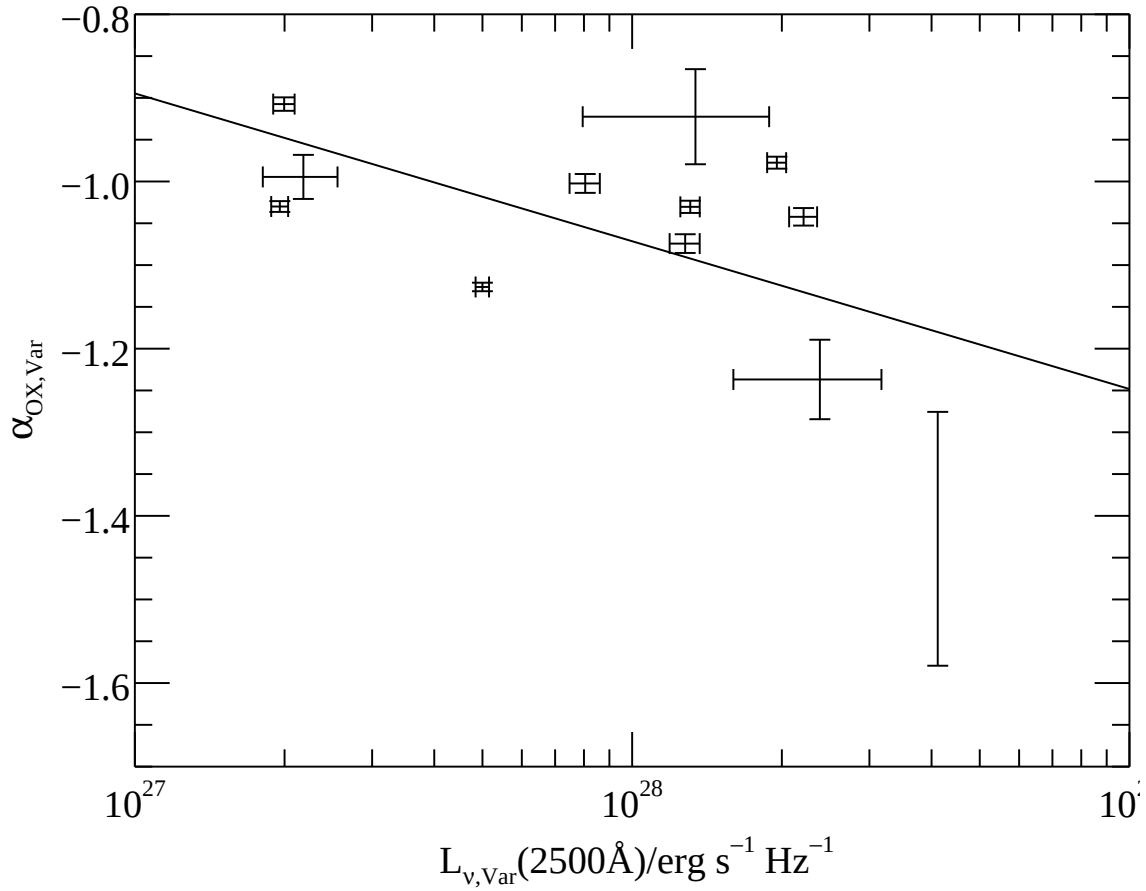

Fig. 2.7 Plot of $\alpha_{\mathrm{OX,Var}}$ against $L_{\nu,\mathrm{Var}}(2500\,\text{Å})$. The solid line shows the least squares fit, $\alpha_{\mathrm{OX,Var}} = (-0.177 \pm 0.083)\log L_{\nu,\mathrm{Var}}(2500\,\text{Å}) + (3.88 \pm 2.33)$.

While our value is within the range found by previous authors for the mean spectrum, the spread in indices from measurements of mean spectra is much larger than the error for a given sample and therefore a reliable comparison between the $\alpha_{\rm OX} - \log L_{2500\,\text{Å}}$ relations for the mean and variable parts of the spectra would require that both be calculated from the same sample and dataset.

2.3.4 Interband Lags

So far, we have only considered the amount of variability in each band. To investigate how the variability in different bands is related in time, we calculated the correlations between the different bands.

To look for correlated variability between the X-rays (0.3-10 keV) and each of the UV bands for each source, we used the discrete cross-correlation function (DCF) (Edelson and Krolik, 1988). The X-rays were chosen as the reference band since this is the only band which is measured for every source. Since the number and frequency of observations differs widely between sources, we grouped the DCF into lag bins by number of observation pairs rather than a fixed lag width. We chose 100 points as the minimum compatible with little apparent noise in the well-sampled sources. Before calculating the DCF, a 30 day half-width boxcar running mean was subtracted from the lightcurves to remove the effects of long-term variations and highlight the expected lags of a few days (Welsh, 1999).

To determine the significance of any correlations, we used the distribution of the DCFs from 10000 uncorrelated simulated lightcurves in each band. Using the method of Timmer and Koenig (1995), we produced lightcurves with the same power spectra as the real lightcurves and a resolution equal to the average observation length. We used X-ray power spectra from González-Martín and Vaughan (2012) and estimated UV power spectra by fitting a powerlaw to the periodogram of the *Swift* data. We added the rms-flux relation by taking the exponential of the lightcurves (Uttley et al., 2005). From these regular lightcurves, we extracted count measurements at points corresponding to the actual observation times and simulated observational noise by drawing the final simulated data from a Poisson distribution with mean equal to these count measurements. We calculated the DCF for each UV/X-ray pair and used the distribution of the DCFs at each lag value to estimate the 95% and 99% confidence intervals outside which a correlation is unlikely to be produced by random noise. This found significant (>99%) correlations in 9 sources out of the sample of 21. These sources either have more datapoints or a clear peak in the lightcurve, so the non-detection in the remaining sources is likely due to a lack of data quality rather than less intrinsic correlation. MCG–6-30-15 notably has many datapoints but no significant lag detection; see Section 2.5.3 for a detailed discussion.

Table 2.3 Lags of each UV band behind X-Rays, with 1σ errors.

Source	Band	Lag/days
3C 120	U	0.4 ± 4.5
	W2	-0.2 ± 2.3
ARK 120	U	2.4 ± 2.3
Fairall 9	V	4.2 ± 2.8
	B	2.7 ± 1.9
	U	3.1 ± 1.5
	W1	2.2 ± 1.0
	M2	1.7 ± 1.0
	W2	1.7 ± 0.8
IRAS 13224–3809	W2	6.4 ± 3.7
MRK 335	W2	0.0 ± 2.9
MRK 1383	M2	4.3 ± 8.5
NGC 3516	W2	1.6 ± 1.5
NGC 5548	V	2.0 ± 1.1
	B	1.5 ± 0.8
	U	1.4 ± 0.7
	W1	1.0 ± 0.7
	M2	0.8 ± 0.7
	W2	0.7 ± 0.5
NGC 7469	U	1.1 ± 1.0
	W1	-0.3 ± 1.2
	M2	1.3 ± 1.7
	W2	0.8 ± 0.7

Where a significant correlation was found, we estimated the potential lag between bands using the centroid of the DCF peak. To generate enough points to produce a smooth distribution to centroid, the X-ray lightcurve was linearly interpolated onto a finer grid ($\Delta t = 0.1$ days) and the ICCF of each UV band was measured against it (Gaskell and Peterson, 1987; Gaskell and Sparke, 1986). We used the centroid of the region with a correlation coefficient of at least 0.8 times the maximum value (e.g. Troyer et al., 2016).

Errors on the lag values obtained were estimated using subset selection/flux randomisation (Peterson et al., 2004, 1998). From 2000 realisations, we estimated 1σ errors by percentile.

Lag values are shown in Table 2.3. In all 9 sources, the UV bands are consistent with a lag behind the X-rays. For the two best measured sources, NGC 5548 and Fairall 9, the lower energy bands have a longer delay. For the remaining sources, the lags are not sufficiently well constrained to determine differences in lag between the different UV bands.

Table 2.4 X-ray luminosities and Eddington ratios for each source in the sample. $\dot{m}$ is calculated by converting $\log_{10}L_{2-10\,\mathrm{keV}}$ to a bolometric luminosity where κ is available. For the remaining sources, $\dot{m}$ is estimated from Γ_{Avg}.

Source	$\log_{10}L_{2-10\,\mathrm{keV}}/\mathrm{erg\,s^{-1}}$	κ	$\dot{m}$
1H 0707–495	41.90 ± 0.01		0.37
3C 120	44.09 ± 0.01	8.29	0.14
ARK 120	43.78 ± 0.02	25.0	0.08
Fairall 9	43.98 ± 0.01	10.5	0.03
H 0557–385	42.76 ± 0.02		0.02
IC 4329A	43.83 ± 0.01	14.8	0.04
IRAS 13224–3809	42.34 ± 0.06		0.68
IRAS 13349+2438	43.64 ± 0.05		0.07
MCG–6-30-15	42.65 ± 0.01	22.2	0.16
MRK 335	42.79 ± 0.01	102	0.30
MRK 509	43.97 ± 0.01	12.5	0.08
MRK 766	42.66 ± 0.01	70.5	0.39
MRK 841	43.48 ± 0.01	27.4	0.09
MRK 1383	44.07 ± 0.01	33.5	0.03
NGC 3516	42.58 ± 0.01	17.7	0.02
NGC 4051	41.03 ± 0.01	16.5	0.01
NGC 5548	43.25 ± 0.00	18.8	0.07
NGC 7469	43.06 ± 0.01	38.7	0.39
PDS 456	44.56 ± 0.01		0.24
PG 1211+143	43.55 ± 0.02	92	0.18
PG 1247+267	45.82 ± 0.04		0.22
Zw 229-15	42.56 ± 0.02		0.12

We compared these lags with the theoretical lags for a thin accretion disc around a black hole of the appropriate mass and accretion rate (Shakura and Sunyaev, 1973). To do so, we calculated the accretion rate in terms of the Eddington ratio, $\dot{m}$, derived from the average hard (2-10 keV) X-ray luminosity during the *Swift* monitoring. We used correction factors, κ, to convert from X-ray to bolometric luminosity based on the most recent measurement in Vasudevan and Fabian (2007, 2009); Vasudevan et al. (2010). Where a source does not have a value for κ in any of these papers, we estimated $\dot{m}$ from the average X-ray spectral index, Γ_{Avg}, using the relation from Shemmer et al. (2008). The resulting Eddington ratios are given in Table 2.4.

For each source, the lags and theoretical predictions (black lines) are plotted in Appendix A.4. The red lines indicate the 1σ uncertainties due to the mass and luminosity uncertainties but do not include uncertainties in κ.

The two best-measured sources, NGC 5548 and Fairall 9, both have lags slightly longer than the predicted values but each individual value is still consistent. The remaining sources do not have enough points of sufficient quality to determine inconsistencies as individuals.

To explore any potential global deviation from the lags expected for a thin accretion disc, the lags for each source were scaled to represent the accretion disc around a black hole with a common mass, $10^8 M_\odot$, and Eddington fraction, $\dot{m} = 0.1$. The lags were scaled by $\tau \sim R/c \sim \dot{m}^{1/3} M^{2/3}$ (Shakura and Sunyaev, 1973).

These scaled lags are plotted in Fig. 2.8, along with the expected lags for a thin accretion disc (red) and the best fitting size for the measured lags (blue). In each band, the average lag (corrected to the rest wavelength of the band) is shown in black. For every band, the measured lag is greater than the theoretical by an average factor of 1.3. However, the overall deviation is only 1.5σ.

2.4 Discussion

2.4.1 Summary of results

From our study of 21 AGN monitored by *Swift* over time-scales of several years in bands from optical through to X-ray, we find that:

- The UV variable spectra are consistent with a powerlaw. The average index is $\alpha = -2.21 \pm 0.13$.
- The amount of variable power increases with mass at the same rate for all UV bands.
- The UV variable luminosity and the index from UV to X-rays, $\alpha_{\rm OX}$, are anticorrelated: $\alpha_{\rm OX} = (-0.177 \pm 0.083) \log L_{\rm UV,Var} + (3.88 \pm 2.33)$
- The variable X-ray spectra are softer than the average spectra of their respective sources by $\Delta\Gamma = 0.28 \pm 0.06$.
- Significant correlations between X-ray and UV variability are detectable in 9 sources. The remaining sources are generally less well sampled and any correlated variability is too weak to detect with the current data.
- Every lag measurement is consistent with variations in the UV lagging behind the X-rays.

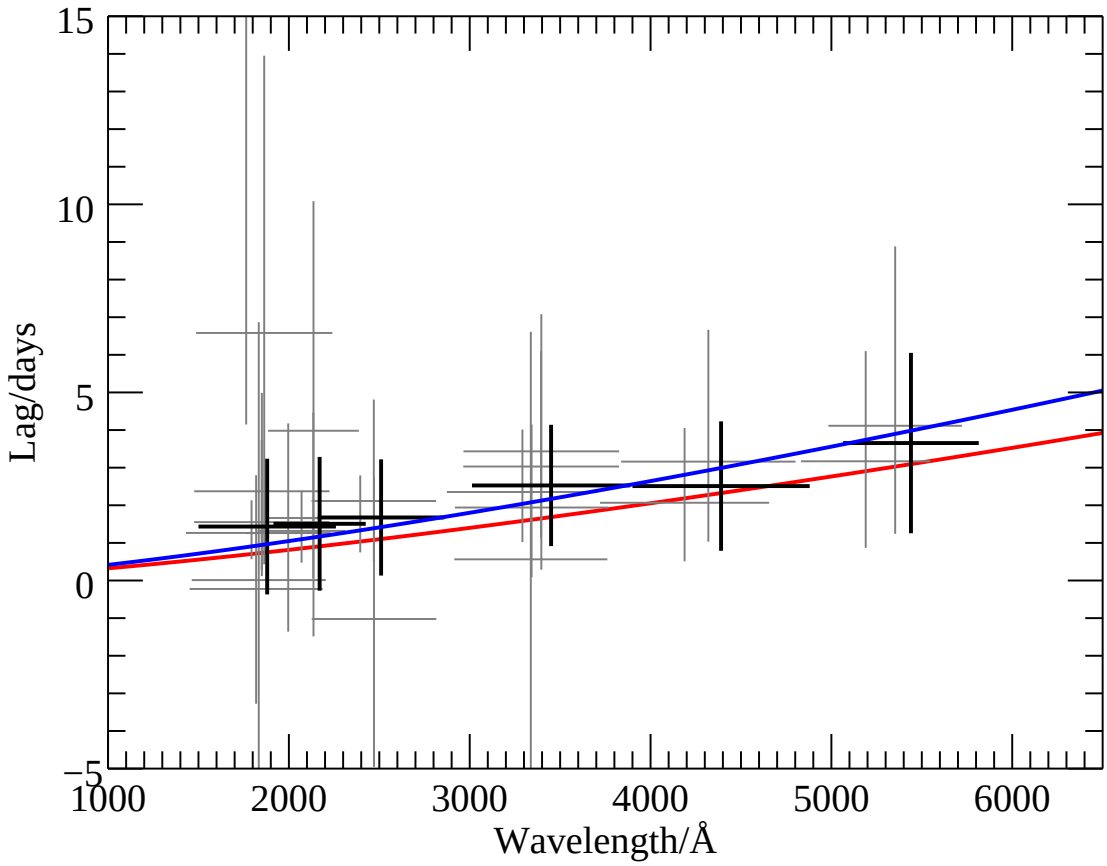

Fig. 2.8 Lags relative to X-rays for each source scaled to a black hole mass of $10^8 M_\odot$ and Eddington rate $\dot{m} = 0.1$. The red (lower) line shows the lags expected for a thin disc; the blue (upper) line shows the best fitting scaled lags.

2.4.2 Comparison with average spectra

In the unified AGN model (Antonucci, 1993; Urry and Padovani, 1995), the UV emission of AGN is principally from an accretion disc (Lynden-Bell, 1969) surrounding the central SMBH.

We can compare the indices of the variable spectra we measure with those of the average spectra, e.g. those by Shull et al. (2012) from *HST-COS* or Vanden Berk et al. (2001), who study quasar spectra over a more similar wavelength range ($1300-5000$ Å) to *Swift*. We find harder indices than either of these measurements. This may be due to our individual dereddening of the sources or there being more fractional variability at shorter wavelengths. An additional constant component which is cooler than the disc would make the total average nuclear spectrum appear redder than the variable part. The consistency of the variable spectra with a flat disc suggests that variable clouds obscuring the disc are unlikely to play a major role at the radii ($\sim 50-1000\,r_g$) probed here.

Contrastingly, we find that the variable X-ray spectra are softer than the average spectra. The X-ray variability is thought to come from fluctuations in the accretion rate in the innermost regions of the disc (e.g. Kelly et al., 2011; King et al., 2004; Lyubarskii, 1997; Zdziarski, 2005). The softer variable spectra are probably due to the shortest time-scale variations in the harder emission being averaged out across an observation. There may also be a contribution from the continuum varying more than the reflected part, which blurs out variations because it is produced over a larger region. Since the continuum is softer than the reflection it produces, the variable spectrum is softer.

Various groups (e.g. Gibson et al., 2008; Grupe et al., 2010; Just et al., 2007; Vagnetti et al., 2013, 2010) study the relationship between the UV and X-ray average luminosity and find an $\alpha_{\rm OX}$-$L_{\rm UV}$ anticorrelation: brighter UV sources have a lower $L_{\rm X,Avg}/L_{\rm UV,Avg}$. We find that this is also the case for the variable part of the emission. This means that the fractional variability of UV and X-ray emission behaves similarly between sources, suggesting a link between the two, as expected for an accretion disc and corona system.

2.4.3 Sources of variability

We find that our variable UV spectra are described well by a simple powerlaw. The indices are consistent with those expected for the emission from a disc heated by internal dissipation in the accretion process or by illumination by a central source.

To determine whether the variable UV spectral slope is the result of illumination or a variable accretion disc, we consider the expected time-scales of the two potential variability mechanisms. The shortest time-scales occur towards the centre of the disc, which are

principally probed by the higher energy bands. For our fiducial $10^8 M_\odot$ black hole, the shortest wavelength *W2*-band has a half light radius of $\sim 50 r_g$. The viscous time-scale at this radius is of the order of 1000 years, so variations in accretion rate due to viscous processes would not occur over the duration of our observations. However, the light-crossing time-scale, which governs variable illumination, is around 1 day and therefore consistent with these observations.

2.4.4 X-ray reprocessing

The variable X-ray emitting corona above the accretion disc directs some of its radiation towards the disc; this is seen both in X-ray reflection spectra (e.g. Tanaka et al., 1995) and X-ray reverberation (e.g. Alston et al., 2014; Fabian et al., 2009; Kara et al., 2016a). If some of this energy is absorbed by the disc, it will be re-emitted thermally in the UV (Lightman and White, 1988). This would suggest a connection between the UV and X-ray emission aside from the feeding of the corona with disc photons.

The correlation between X-ray and UV variability with the UV variations occurring after those in the X-rays in 9 of our sources strongly suggests that X-ray variations drive at least part of the UV variability in those objects. This could be explained by some of the UV variability being due to reprocessing of X-ray radiation.

We find that there is comparable variable power in the UV and X-ray bands that we measure. While this does not include all of the power in either band, it shows that the X-ray variations are sufficiently powerful to drive a significant component of the observed UV variability.

We also note that the X-rays have a level of steady emission: the minimum flux of a given source is typically around one third of the peak flux. If variable illumination is indeed producing notable changes in UV flux, the effect of steady illumination will also be a significant factor in the average flux of the disc.

Further support for the reprocessing scenario comes from the fact that of the 9 sources in which we detect correlated variability, 5 also have iron K reverberation lags (Kara et al., 2016a, 2013a,c). Two of the sources which have measured UV but not iron K lags, Fairall 9 and Ark 120, have relatively high black hole masses ($M_{\rm BH} = 8.41$ and 8.18 respectively) so the expected iron K lags become difficult to detect due to the length of an *XMM* orbit. Alternatively, the detection of only UV lags may be because the coronal emission is less focussed to the central regions in sources without iron K lags, so more coronal variable power is delivered to the outer regions of the disc which respond in UV. Equivalently, iron K reverberation is measured in 1H 0707–495 (Fabian et al., 2009; Kara et al., 2013b; Zoghbi et al., 2010), IC 4329A and PG 1211+143 (both Kara et al., 2016a) but we do not find

significant correlations, which may reflect a greater proportion of the coronal variability being focussed towards the central regions.

Some previous studies (e.g. Edelson et al., 2015; Shappee et al., 2014; Troyer et al., 2016) have found that the lags in the DCF are longer than the light travel time for a standard thin disc by a factor of a few. Our measurement of the average lag is not sufficiently precise to distinguish between a standard thin disc and these longer measurements. Even where lag times are incompatible with a standard thin disc, there are various explanations for this which still allow for X-ray reprocessing to occur. For example, the perceived disc lags can also be increased by UV emission from emission lines and the Balmer continuum (Korista and Goad, 2001). If these come from the larger BLR, the lags will appear longer. Dexter and Agol (2011) suggest that local fluctuations in the disc temperature allow hot regions to exist significantly further out than their average radius. These distant hot regions will increase the measured lags while maintaining a thin disc temperature profile on average.

However, the lightcurves are sometimes far from perfectly correlated (for example, the peak correlation coefficient for Fairall 9 is around 0.5), which suggests that at least one of the bands shows variations which do not affect the other. For example, relativistic light bending (Miniutti and Fabian, 2004) allows the disc to see different variability from a distant observer, particularly if the coronal geometry is changing. It is likely that there are also intrinsic fluctuations in the disc which add to the UV variable power. Variable reddening of the disc emission would also increase the observed UV variable power. The presence of some additional UV variability is supported by Uttley et al. (2003), who find more fractional variability in NGC 5548 in the optical (5100 Å) than X-rays in lightcurves binned on a 30 day time-scale.

We therefore conclude that X-ray reprocessing is likely to happen to some extent in all sources and that it is the origin of the observed UV/X-ray lags. However, X-ray reprocessing may not be the only driver of UV variability. Since the viscous time-scale is so much longer than the time-scale of the observed variations, any additional fluctuations must be governed by other processes such as magnetism.

2.5 UV/X-ray correlations in individual sources – comparison with previous results

2.5.1 1H0707–495

In agreement with our results, Robertson et al. (2015) did not find strong correlations between X-ray and W1 band variability in a 7 day long *XMM* observation, which they ascribe to a

particularly compact corona. They found low significance ($\sim 95\%$) UV leads, which we also find (at similarly low significance) in the longer lightcurves presented here. These could be due to upscattering of UV emission in the corona. Seemingly at odds with these findings, X-ray studies have found strong evidence of iron K and L reverberation lags (Fabian et al., 2009; Kara et al., 2013b; Zoghbi et al., 2010) and relativistic reflection (Dauser et al., 2012; Kara et al., 2015) in this source. However, the *Swift* monitoring includes a period where 1H0707–495 is in a very low state, and the X-ray reflection is concentrated towards the centre-most region of the disc due to illumination from a low corona ($\sim 2R_{\rm g}$) (Fabian et al., 2012). The most illuminated region ($\lesssim 10R_{\rm g}$) is smaller than the region ($\sim 500R_{\rm g}$) responsible for the bulk of the *W2*-band emission. This would make UV–X-ray lags hard to detect.

2.5.2 Fairall 9

We detect UV lags in all 6 bands, which are largely consistent with the expectations from a thin disc. Recondo-Gonzalez et al. (1997) find variability of up to a factor of 33 ± 4 in *IUE* data of the source, but the mean sampling interval of 96 days is too long to detect lags, giving an upper limit on the lag of 4298 Å behind 1400 Å of 80 days, consistent with our results of lag lengths of a few days. Lohfink et al. (2014) study 2.5 months of *Swift* monitoring and an *XMM* observation. They find correlated variability between UV-optical bands on all time-scales measured, down to the *Swift* sampling time. The additional data now available allow us to show that the longer wavelengths lag the shorter ones. They also find rapid UV flares in the *XMM* observation, with a lag behind the X-rays of $1-2$ hours at 2σ significance. We do not have sufficient sampling cadence to verify this result.

2.5.3 MCG–6-30-15

Despite the well-sampled *M2*-band lightcurve, we are unable to detect lags in MCG–6-30-15. Lira et al. (2015) studied long-term lightcurves in X-rays and optical/near-IR; they found only a weak correlation between X-rays and the *B*-band which does not put useful constraints on the lag. They do find correlations between different optical bands with longer wavelengths lagging shorter ones; these lags are consistent with a $\tau \propto \lambda^{4/3}$ relation but for a disc larger than expected by up to a factor of 4, indicating that weak reprocessing might be taking place. Arévalo et al. (2005) studied a ~ 5 day long *XMM* observation and found that the *U*-band emission leads the X-rays by $1.9^{+0.5}_{-0.8}$ days, as would be expected for X-rays which are produced by Compton upscattering of UV photons. We would expect to detect such a lag if it were present in the observations analysed here.

While a broad iron Kα line attributed to disc reflection has been detected in the mean X-ray spectrum (Fabian and Vaughan, 2003; Tanaka et al., 1995), Kara et al. (2014b) were unable to find an iron K lag despite having enough counts and variability. They suggest that some variability may be due to geometrical changes in the corona, which would not cause correlated changes in the iron K emission. Miller et al. (2008) suggest that the red wing of the iron line may be caused by complex absorption, which would not show an iron K lag. However, using high energy *NuSTAR* data, Marinucci et al. (2014) favour the relativistic reflection interpretation.

Rapid changes of the geometry of the source could explain the difficulty of detecting X-ray reverberation and reprocessing in the source despite the existence of reflection features in the spectrum.

2.5.4 Mrk 335

We detect a correlation between X-rays and the *W2*-band but only constrain the lag to 0 ± 2.9 days. Grupe et al. (2012) studied the first half of the *Swift* monitoring used here, finding strong variability but no significant correlation between the X-ray and UV flux. The additional *W2* measurements collected after 2012 allow for the detection of a significant correlation now. While we do not determine the direction of the lag, strong reflection (e.g. Parker et al., 2014b) indicates that the X-rays illuminate the disc, so some reprocessing is likely to occur and may well be the cause of the correlated variability.

2.5.5 Mrk 509

We do not detect a significant lag in Mrk 509. Since we have only 27 data points for Mrk 509, we would not expect to do so. Marshall et al. (2008) find the optical (*R*-band) flux leads the X-rays by 15 days in observations from *RXTE* and ground-based measurements by the SMARTS consortium. Mehdipour et al. (2011) find a correlation between disc and soft X-ray flux in *XMM* and *Swift* measurements, which they attribute to warm Comptonisation producing the soft excess. This interpretation agrees with Boissay et al. (2014), who study spectra from a large *XMM*/*INTEGRAL* campaign.

2.5.6 NGC 3516

We find a 1.6 ± 1.5 day lag of the *W2*-band behind the X-rays. Edelson et al. (2000) find no significant UV/X-ray correlation in a 3 day observation with *HST*, *RXTE* and *ASCA*. Such a short observation is unlikely to detect a lag of the length which we find. Maoz et al. (2002)

find a possible 100 day lag of the X-ray relative to the *R*-band but the correlation is not detected in a longer observation (Maoz et al., 2002). They suggest that this may be due to the initial section of the observation being at a higher flux level, in which the X-rays are dominated by a component of emission which does correlate with the UV but is less significant at lower fluxes. Noda et al. (2016) studied observations from *Suzaku* and Japanese ground-based telescopes. They found a correlation between the hard X-rays and the *B*-band with the X-rays lagging by $2.0^{+0.7}_{-0.6}$ days, which like our measurement is larger than expected for a thin disc.

2.5.7 NGC 4051

The *Swift* data for NGC 4051 are insufficient in number and frequency to measure the expected lags. While we find a formally significant correlation at 15 days lag, this corresponds to superposing the well sampled ends of the 35 day lightcurves with the unsampled middle of the lightcurve. Peterson et al. (2000) analysed 3 years of *RXTE* and ground-based observations and found that the long time-scale (>30 day) variability is correlated between optical and X-rays with a lag range of -106 to 68 days. Shemmer et al. (2003) found in 60 days of intensive *RXTE* monitoring that the DCF centroid showed a UV lead but that the peak may be at a lag, suggesting that both inward propagating fluctuations and X-ray reprocessing are responsible for some of the correlation. Alston et al. (2013) studied the UV/X-ray variability on short time-scales with *XMM* and found a 3 ks *W1*-band lag relative to the X-rays. The strength of correlation indicates that 25% of the UV variance is caused by X-rays. The lag is somewhat shorter than the ~ 0.2 day lag detected by Mason et al. (2002) with *XMM* in the same band at only 85% confidence. Breedt et al. (2010) correlated 12 years of *RXTE* observations with *u* to *I*-band measurements, finding that a $\lambda^{4/3}$ relation fits well and that the scaling, subject to significant uncertainties, is consistent with thin disc predictions. As well as lags of a few days, they find lags of ~ 40 days which they suggest may be due to the dusty torus which surrounds the inner regions.

2.5.8 NGC 5548

We find lags in all bands, increasing with wavelength and always longer than predicted for a thin disc, but consistent within the uncertainties. The *STORM* campaign has provided an extensive dataset from X-rays to IR: Edelson et al. (2015) measure the UV/X-ray lags against the Hubble 1315 Å band; and (Fausnaugh et al., 2016) extend the wavelength range to the *z*-band (~ 9160 Å). This finds that the lags are broadly consistent with $\tau \propto \lambda^{4/3}$ but that the disc radius is around 3 times the thin-disc prediction. This is in agreement with our

findings, which is expected as the majority of *Swift* data for NGC 5548 is part of the *STORM* campaign.

2.5.9 NGC 7469

We detect significant correlations in 4 UV bands. Our lag measurements are consistent with a thin disc but are poorly constrained. Studying the UV only, Wanders et al. (1997) find delays of UV lines and continuum behind the emission at 1315 Å. They find lags increasing with wavelength over 1315–1825 Å. Collier et al. (1998) find lags between 1315 Å and 4865,6962 Å. Kriss et al. (2000) use a *HST-FOS* spectrum over 1150–3300 Å to better extract spectral bands which are less contaminated by line emission. These measurements of UV continuum lags find that the lags follow a $\lambda^{4/3}$ relation. Collier et al. (1999) use these lags to determine H_0; their value for $H_0 = 42 \pm 9\,\mathrm{km\,s^{-1}\,Mpc^{-1}}$ is lower than is now accepted, corresponding to the lags being longer than expected. However, Nandra et al. (1998) find a 4 day UV (1315 Å) lead relative to the X-rays. This could indicate that UV upscattering and X-ray reprocessing are both responsible for some of the correlations.

2.5.10 PG 1211+143

We find peaks in the DCF at 0 ± 5 days, consistent with previous findings, but these are not significant at the 99% level. Bachev et al. (2009) studied the first section of *Swift* observations, along with ground-based photometry down to *I*-band. They found lags compatible with a $\lambda^{4/3}$ relation at approximately twice the expected lag. Papadakis et al. (2016) also analyse the first *Swift* section of this dataset but find that the UVOT measurements are consistent with constant flux. Lobban et al. (2016) studied the second section of *Swift* observations along with *XMM-PN/OM* data, finding marginally significant X-ray/UV correlations with lags $\lesssim 1$ day.

2.6 Conclusions

We have presented a variability analysis of archival *Swift* data from AGN monitoring.

We find that essentially all bands vary and that the variable part of the UV emission has a spectrum consistent with that of the thermal emission from dissipation in an accretion disc or central illumination of a flat disc. The time-scales of variability and lags of UV relative to X-ray variability show that the latter is principally responsible.

The variable power in sources with heavier black holes is higher. The variable UV power increases faster than the variable X-ray power, as is the case for the average emission.

The X-ray and UV variations are significantly correlated in 9 sources; the data for the remaining sources are not sufficient to detect a correlation. All measurements of correlated X-ray/UV variability are consistent with the UV lagging the X-rays. We associate this with the reprocessing of X-rays on the accretion disc.

Chapter 3

Is there a UV/X-ray connection in IRAS 13224–3809?

Abstract

We present results from the optical, ultraviolet and X-ray monitoring of the NLS1 galaxy IRAS 13224–3809 taken with *Swift* and *XMM-Newton* during 2016. IRAS 13224–3809 is the most variable bright AGN in the X-ray sky and shows strong X-ray reflection, implying that the X-rays strongly illuminate the inner disc. Therefore, it is a good candidate to study the relationship between coronal X-ray and disc UV emission. However, we find no correlation between the X-ray and UV flux over the available ~ 40 day monitoring, despite the presence of strong X-ray variability and the variable part of the UV spectrum being consistent with irradiation of a standard thin disc. This means either that the X-ray flux which irradiates the UV emitting outer disc does not correlate with the X-ray flux in our line of sight and/or that another process drives the majority of the UV variability. The former case may be due to changes in coronal geometry, absorption or scattering between the corona and the disc.

3.1 Introduction

AGN are the most luminous persistent point sources in the Sky in the optical to X-ray bands. They have a significant impact on galaxy evolution and are therefore of great interest for study. Since AGN are unresolved with current instruments in the X-ray band, their structure must be inferred from properties of their spectra or the variability of their emission.

A significant fraction of their bolometric luminosity is emitted in the X-ray band from a small region known as the corona (Haardt and Maraschi, 1993; Merloni and Fabian, 2003). Microlensing (Chartas et al., 2012; Dai et al., 2010) and timing (De Marco et al., 2013, 2011; Kara et al., 2016b, 2014a; Reis and Miller, 2013) results show that this is often smaller than $10r_g$ in size. Much of the X-ray power from the corona is directed towards the accretion disc, as seen in reflection features in the X-ray spectrum (Fabian and Ross, 2010; Tanaka et al., 1995).

Additional evidence that the X-ray emission affects the disc is that variations in X-ray and optical fluxes are often seen to be correlated (e.g. Alston et al., 2013; Buisson et al., 2017; Edelson et al., 2015; Fausnaugh et al., 2016; Gliozzi et al., 2017; Lobban et al., 2017;

Shappee et al., 2014). Where the optical emission lags the X-rays, this is often interpreted as heating of the disc by the additional X-ray flux directed towards the disc (Lightman and White, 1988). In some cases (e.g. Edelson et al., 2017; Troyer et al., 2016), the lags are longer than predicted for a standard thin disc (Shakura and Sunyaev, 1973) and the X-ray lightcurve does not always match the inferred driving lightcurve (Starkey et al., 2017). This may be explained by a larger disc or an additional stage of reprocessing (Edelson et al., 2017; Gardner and Done, 2017). There is also now good evidence that diffuse continuum emission from the broad line region can also contribute significantly to the lags, which needs to be accounted for (Cackett et al., 2017; McHardy et al., 2018). Sometimes, the optical emission is found to lead the X-ray emission (Arévalo et al., 2005), which is interpreted as Compton upscattering of the optical photons to X-rays (Haardt and Maraschi, 1991) or the propagation of fluctuation inwards through the disc (Arévalo and Uttley, 2006; Lyubarskii, 1997). However, sometimes no correlation is found (e.g. Robertson et al., 2015). Continued study of optical to X-ray variability in more sources has the potential to provide more information on why correlations are seen only in some sources.

The narrow line Seyfert 1 (NLS1) galaxy IRAS 13224–3809 ($z = 0.066$, $M_{\rm BH} = 10^6 - 10^7\,{\rm M}_\odot$, Zhou and Wang 2005) is the most variable AGN in X-rays, often showing changes in X-ray flux by a factor of 50 on timescales of less than one hour (Boller et al., 1997; Dewangan et al., 2002; Fabian et al., 2013). Its X-ray spectrum shows a soft continuum with strong relativistic reflection and soft excess (Chiang et al., 2015; Fabian et al., 2013; Ponti et al., 2010, Jiang et al. submitted). The soft X-ray continuum suggests that IRAS 13224–3809 is accreting at a high Eddington fraction ($\dot{m} \simeq 0.7$ using the relation from Shemmer et al. 2008). It shows little X-ray obscuration, although the recent *XMM-Newton* observations have allowed the detection of an Ultra-Fast Outflow (UFO) which is observed only at low X-ray flux (Parker et al., 2017a,b). Previous studies show that IRAS 13224–3809 has little absorption in the UV and that the CIV emission line is asymmetric and blueshifted (Leighly, 2004; Leighly and Moore, 2004), which may indicate an outflow out of the line of sight.

The strong X-ray variability and reflection suggest strong variable heating of the disc, so IRAS 13224–3809 is an ideal candidate to study UV/X-ray relations. The source is a member of the sample studied in Buisson et al. (2017) to find UV/X-ray relations. This work found a marginally significant (2σ confidence) lag of *UM2*-band (~ 2170 Å) behind X-ray emission, suggesting that X-ray reprocessing may occur in this source. Here, we present the results from the Optical Monitor of the recent 1.5 Ms *XMM-Newton* observing campaign of IRAS 13224–3809, along with associated *Swift* monitoring (50 ks XRT exposure over the period 7$^{\rm th}$ July to 14$^{\rm th}$ August 2016).

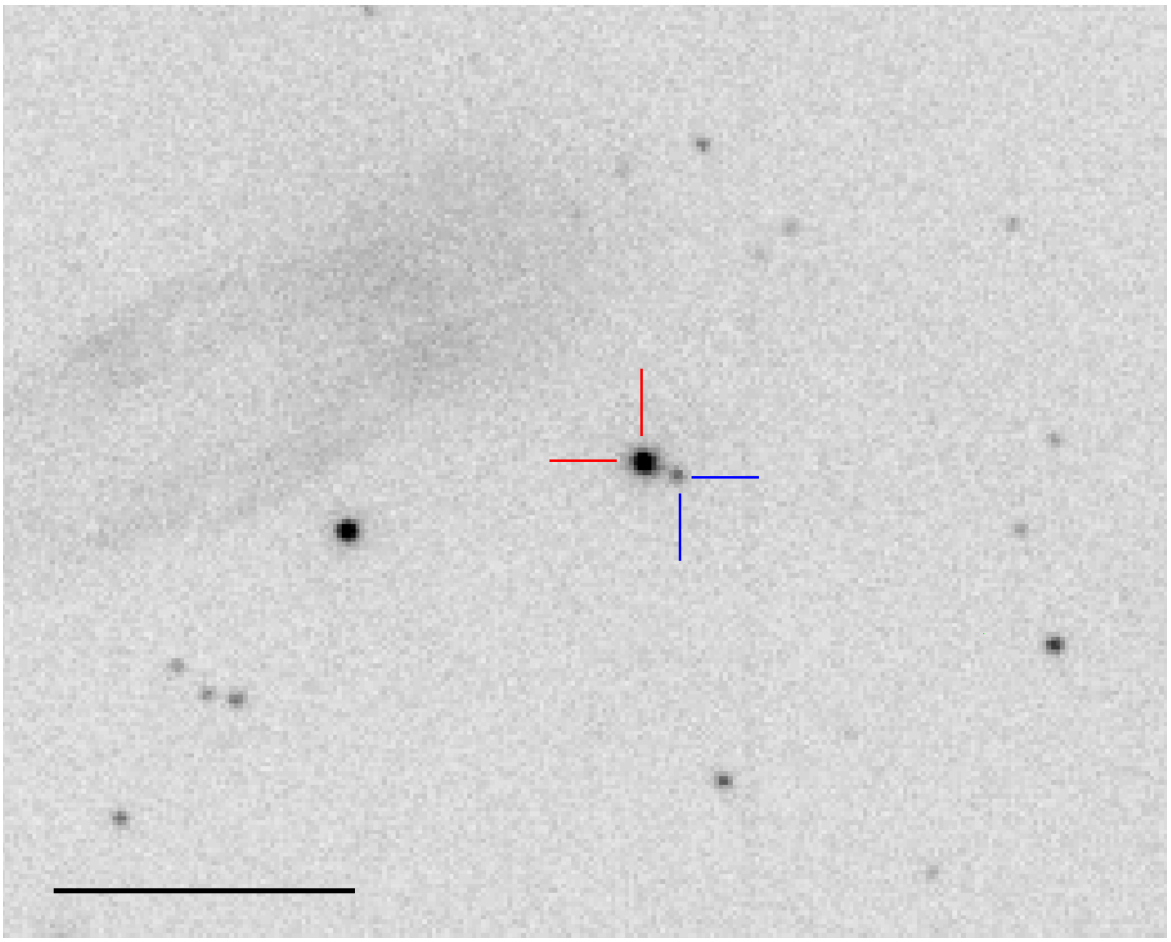

Fig. 3.1 Image from *XMM-Newton*-OM showing IRAS 13224–3809 (red, left) and nearby secondary source (blue, right). The scalebar indicates 1 arcmin.

The increase in data now available allows us to study more of its properties. The additional *Swift* monitoring allows us to measure the optical/UV variable spectrum and the extensive *XMM-Newton* coverage provides constraints on the short timescale UV/X-ray relation.

3.2 Observations and Data Reduction

3.2.1 *XMM-Newton*

We use *XMM-Newton* (Jansen et al., 2001) data from the recent very large programme (P.I. Fabian) dedicated to monitoring IRAS 13224–3809, with observations from July to August 2016. Here, we consider X-ray lightcurves from the EPIC-pn (Strüder et al., 2001) instrument and ultraviolet lightcurves from the Optical Monitor (OM, Mason et al. 2001). To provide

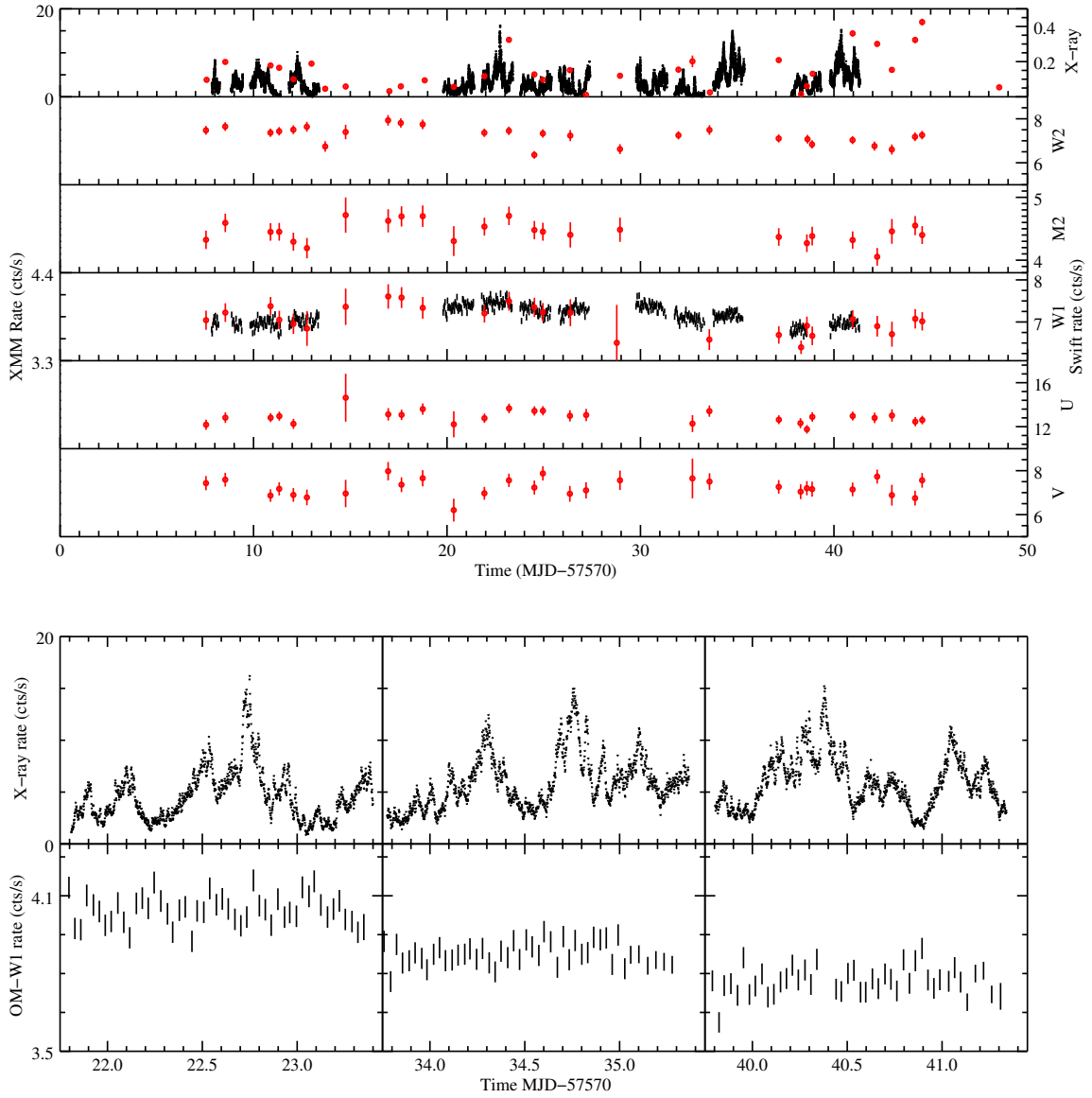

Fig. 3.2 Lightcurves of IRAS 13224–3809 from *XMM-Newton* (black) and *Swift* (red). Upper panels show, from top to bottom: X-rays ($0.3-10$ keV), *W2*-band, *M2*-band, *W1*-band, *U*-band, *V*-band. Note that the W1 filters of *Swift* and *XMM-Newton*, although plotted in the same panel, are not identical. Lower panels show detail of the X-ray and UV lightcurves of the three *XMM-Newton* orbits with the strongest X-ray peaks. There is no apparent response of the UV emission to the X-ray peaks.

continuous coverage, the OM observations were taken in the *W1*-band throughout and used a typical frametime of 2700 s.

The pn data were reduced using the standard task EPCHAIN, using a 50 arcsec circular source region and an annular background region comprising radii from 60–90 arcsec. Data were taken in Large Window mode, leading to mild pileup in the brightest X-ray states. While this may affect the detail of the X-ray spectra, the pile-up is too weak to have a significant impact on the work presented here (< 15 % flux loss at the lightcurve peaks). Additionally, since pile-up is roughly proportional to flux, any effect on correlation measurements is minor. Lightcurves were produced with EVSELECT and EPICLCCORR and rebinned to match the cadence of the OM frames.

The OM photometry of IRAS 13224–3809 is complicated by a nearby (7.5 arcsec separation) source (see Fig. 3.1) which causes the default execution of XMMEXTRACTOR to fail. We therefore take count rates directly from the images using the photometry tool IMEXAM from ZHTOOLS, extracting counts from within an aperture of radius 3 arcsec, using a nearby source-free circular region of radius 18 arcsec for background subtraction. We correct the count rates for deadtime and coincidence losses using the factors given by OMICHAIN. These corrections are between 1.043 and 1.049 for all points apart from one which is 1.029.

In 18 exposures, a count rate less than 0 is returned, which we exclude – the sky coordinates on these images are wrong (part of OBSID 0792180501). One further point in OBSID 0792180201 is unreasonably low (about 4 times less than neighbouring points) so it is also excluded. This leaves 524 good OM exposures.

We also produce a lightcurve of the nearby source to ensure that it does not affect our results. To minimise the effect of stray light from the edges of the PSF of IRAS 13224–3809, we use a 2 arcsec radius circular aperture. This shows that the nearby source is too faint and insufficiently variable to affect the lightcurves of IRAS 13224–3809: its flux is 10 % of IRAS 13224–3809 and its variability is consistent with Poisson noise.

3.2.2 *Swift*

Swift UVOT (Gehrels et al., 2004; Roming et al., 2005) lightcurves were extracted from level II image files using the tool UVOTSOURCE. We used a circular source region of 5 arcsec radius and a circular background region of 15 arcsec radius from a nearby source free area of the detector. We excluded exposures where the source region overlaps areas of the detector known to produce low count readings (Edelson et al., 2015). The good exposures are then summed across a whole observation. We converted count rates to fluxes using the conversion factors in Poole et al. (2008). UV fluxes were corrected for Galactic reddening using $E(B-V) = 0.0601$ (Kalberla et al., 2005). We use lightcurves from all UVOT filters

apart from the *B*-band, since the three observations available in this band are insufficient to produce reliable variability measurements.

Swift XRT (Burrows et al., 2005) lightcurves covering the $0.3-10$ keV energy band were produced using the online tool available on the UK *Swift* website[1] (Evans et al., 2009, 2007). The XRT was operated in PC mode. The source region is a circle of radius 1.2 arcmin. The background region is an annulus with radii from 2.3 to 7 arcmin (with point sources removed).

The lightcurves from all instruments are shown in Fig. 3.2.

Except where noted, errors are given at the 1-σ level.

3.3 Results

3.3.1 Mean SED

We show the mean SED of IRAS 13224-3809 in Fig. 3.3. The UV points show the mean flux across the full *Swift* lightcurve; the X-ray points show the mean *XMM-Newton* spectrum from Jiang et al. (2018). We characterise the UV spectrum with a powerlaw of the form $f_\lambda \propto \lambda^\alpha$ and exclude the *V*-band since Vanden Berk et al. (2001) show that there is a strong break in powerlaw index at around 5000 Å, blueward of the *V*-band. This gives $\alpha = -1.2 \pm 0.1$, slightly softer than the mean quasar spectrum ($\alpha = -1.56$) found in Vanden Berk et al. (2001), suggesting that there is some contribution from the host galaxy.

From the simultaneous optical to X-ray SED, we can estimate the bolometric luminosity. We approximate the intrinsic AGN emission as a thin disc (for the UV, black in Fig. 3.3) plus a hot blackbody (for the X-ray soft excess, green) and a powerlaw (for the hard X-ray component, blue). The hot blackbody and powerlaw are directly fit to the X-ray data excluding the reflection dominated region above 3 keV; we do not attempt to fit the reflection here since its contribution is small compared to the uncertainty in the disc flux. The disc normalisation is set by assuming that the flux from the highest energy UV band is entirely due to the disc. There is likely to be some host galaxy contamination but this is unlikely to be significant compred to the uncertainty due to the temperature: the host is not visible in the UV image and the observed variability shows that there is significant AGN contribution. The principal source of uncertainty is the disc temperature, which is poorly constrained as the cut-off lies in the unobserved extreme UV; we take the lower limit as measured from the RMS spectrum (see Sec. 3.3.2) and take the upper limit as being where the disc emission becomes too great to be consistent with the observed X-ray emission. This gives a bolometric

[1] http://www.swift.ac.uk/user_objects/

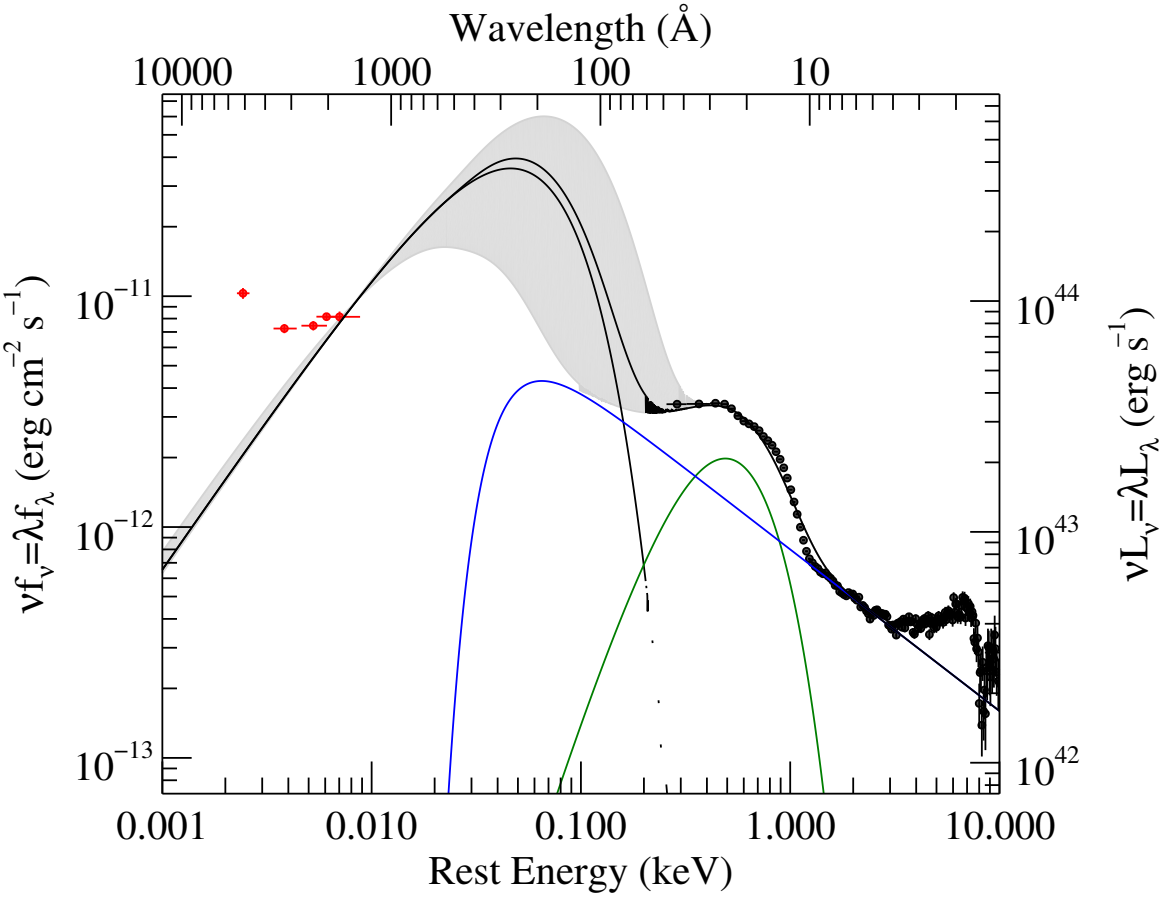

Fig. 3.3 Mean SED of IRAS 13224–3809. Optical/UV points (red) are from *Swift*-UVOT (and do not have the contribution from the host galaxy subtracted); X-ray points (black) are from *XMM-Newton*-pn (Jiang et al., 2018). The grey region indicates the range of SED models used to derive the bolometric luminosity (see text for details). The components of the model are: the disc (black); a blackbody accounting for the soft X-ray excess (green); and a powerlaw for the hard X-ray emission (blue). The contribution to the hard ($\gtrsim 3$ keV) X-ray emission from reflection is not accounted for but is insignificant.

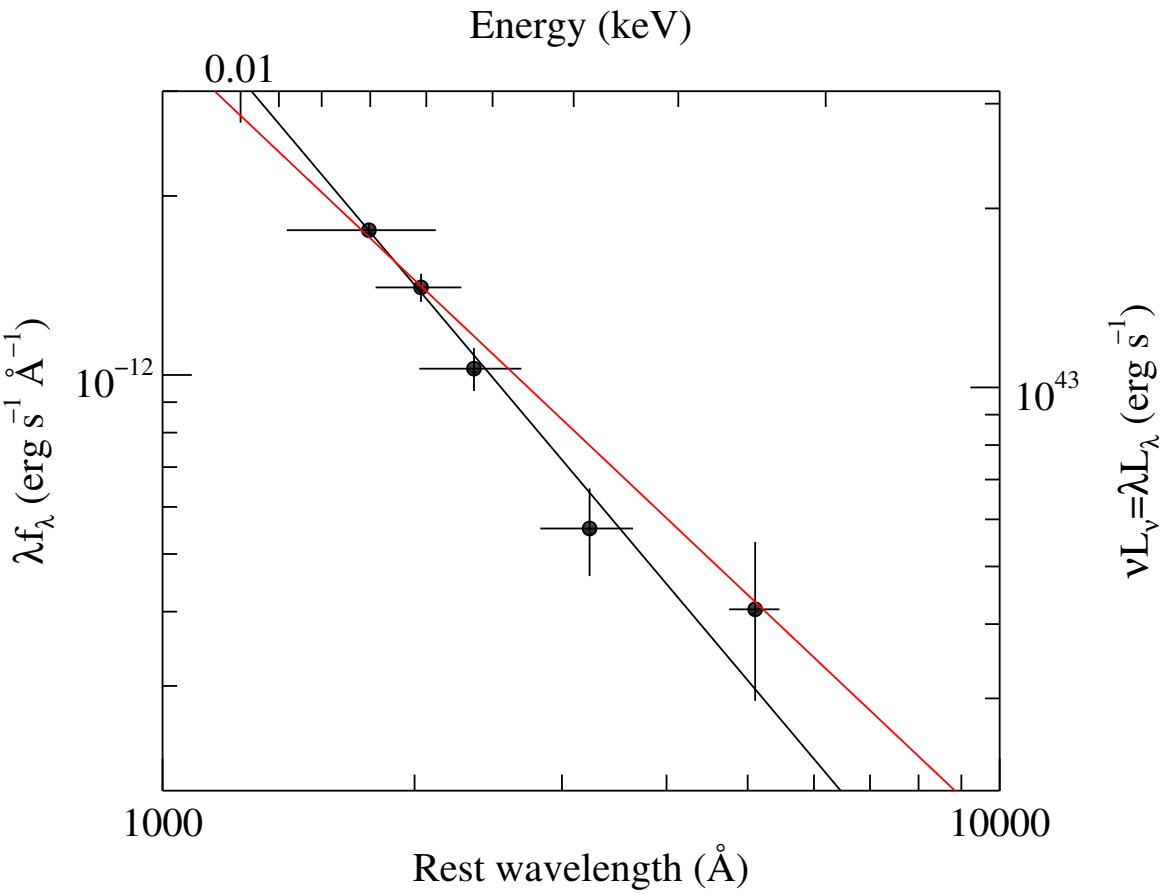

Fig. 3.4 RMS spectrum from *Swift*-UVOT data. The black line shows a powerlaw fit, with index $\alpha = -2.67 \pm 0.15$. The red line has the index expected of a thin disc, $\alpha = -2.33$. Errors in wavelength represent the half maximum of the filters.

luminosity range of $4 \times 10^{44} - 1.3 \times 10^{45}$ erg s^{-1}. For $M_{\rm BH} = 10^6 - 10^7\,{\rm M}_\odot$, this implies an Eddington fraction $\dot{m} = 0.3 - 10$. While this is not a strong constraint (due largely to the poorly-determined black hole mass), a high Eddington fraction is widely regarded as typical of NLS1s and agrees well with estimates of the Eddington fraction from other methods, such as $\dot{m} \simeq 0.7$ using the $\Gamma - \dot{m}$ relation of Shemmer et al. (2008).

We also consider the relative X-ray and UV power, using the standard measure $\alpha_{\rm OX}$ (e.g. Vagnetti et al., 2010). This gives $\alpha_{\rm OX} = -1.46$, which is compatible with (though at the X-ray weak end of) values found by various authors who have presented a $L_{\rm UV} - \alpha_{\rm OX}$ relation ($\alpha_{\rm OX} = -1.18$, Gibson et al. 2008; $\alpha_{\rm OX} = -1.31$, Grupe et al. 2010; $\alpha_{\rm OX} = -1.46$, Xu 2011).

Table 3.1 Fits to the PSD of the *XMM-Newton*-OM lightcurve with a powerlaw plus noise model, $P(f) = \alpha(f/10^{-4}\,\mathrm{Hz})^{\beta} + C$.

Model	Norm (α)	Index (β)	Noise (C)	χ^2/(d.o.f.)
Fixed noise	0.13 ± 0.06	-1.3 ± 0.3	0.557	5.68/5
Fixed index	0.040 ± 0.013	-2.0	0.61 ± 0.05	8.10/5
Free	0.70 ± 0.050	-0.5 ± 0.1	< 0.35	2.45/4

3.3.2 *Swift* variable UV spectrum

To characterise the emission of the innermost regions, we study the variable part of the UV spectrum to avoid contamination by the host galaxy.

We characterise the variable part of the spectrum with the error corrected RMS flux variability, $f_{\lambda,\mathrm{Var}} = \sqrt{\sigma^2 - \bar{\varepsilon}^2}$ (Edelson et al., 2002; Nandra et al., 1997a) as in Buisson et al. (2017), taking the measured standard deviation, σ, and mean square error, $\bar{\varepsilon}^2$, from the whole lightcurve. Errors on this quantity are given by $\mathrm{err}(f^2_{\lambda,\mathrm{Var}}) = \frac{1}{\sqrt{N}}\sqrt{\left(\sqrt{2}\bar{\varepsilon^2}\right)^2 + \left(2\sqrt{\bar{\varepsilon^2}} f_{\lambda,\mathrm{Var}}\right)^2 \bar{x}^2}$ (Vaughan et al., 2003a).

The spectrum this produces (Fig. 3.4) is consistent ($\chi^2/\mathrm{d.o.f.} = 2.8/3$) with a powerlaw, $f_\lambda \propto \lambda^\alpha$, with index $\alpha = -2.67 \pm 0.15$ (or in frequency units, $f_\nu \propto \nu^\beta$, with $\beta = 0.67 \pm 0.15$). This is consistent at 2-σ with the expected index for the emission produced by irradiation of a thin disc ($\alpha = -2$ to –2.33, $\beta = 0$ to 0.33, Davis et al., 2007) and significantly flatter than the Rayleigh-Jeans tail of a single-temperature blackbody ($\alpha = -4$, $\beta = 2$).

Since the variability is expected to originate in a disc spectrum, we also test a powerlaw with an exponential cut-off representing the maximum temperature at the inner edge of the disc. This places an upper limit of 1440 Å on the cut-off (at 90% confidence), corresponding to a blackbody temperature of $\geq 10^5$ K. However, such a low cut-off requires a steeper powerlaw index, $\alpha = -4$. This limit to the temperature is less than that predicted for a standard disc (Shakura and Sunyaev, 1973), even for conservative parameters for IRAS 13224–3809 ($M_{\mathrm{BH}} = 10^7\,\mathrm{M}_\odot$, $\dot{m} = 0.1$), so the spectrum is consistent with the temperature of a standard disc.

3.3.3 Short timescale optical variability

While the UVOT lightcurve shows that IRAS 13224–3809 varies over the course of the observing campaign, we also seek to characterise that UV variability on shorter timescales with the *XMM-Newton*-OM data.

We calculate the average power spectral density (PSD, Vaughan et al. 2003a) of the optical monitor data over the whole observation. Since calculating the PSD requires an

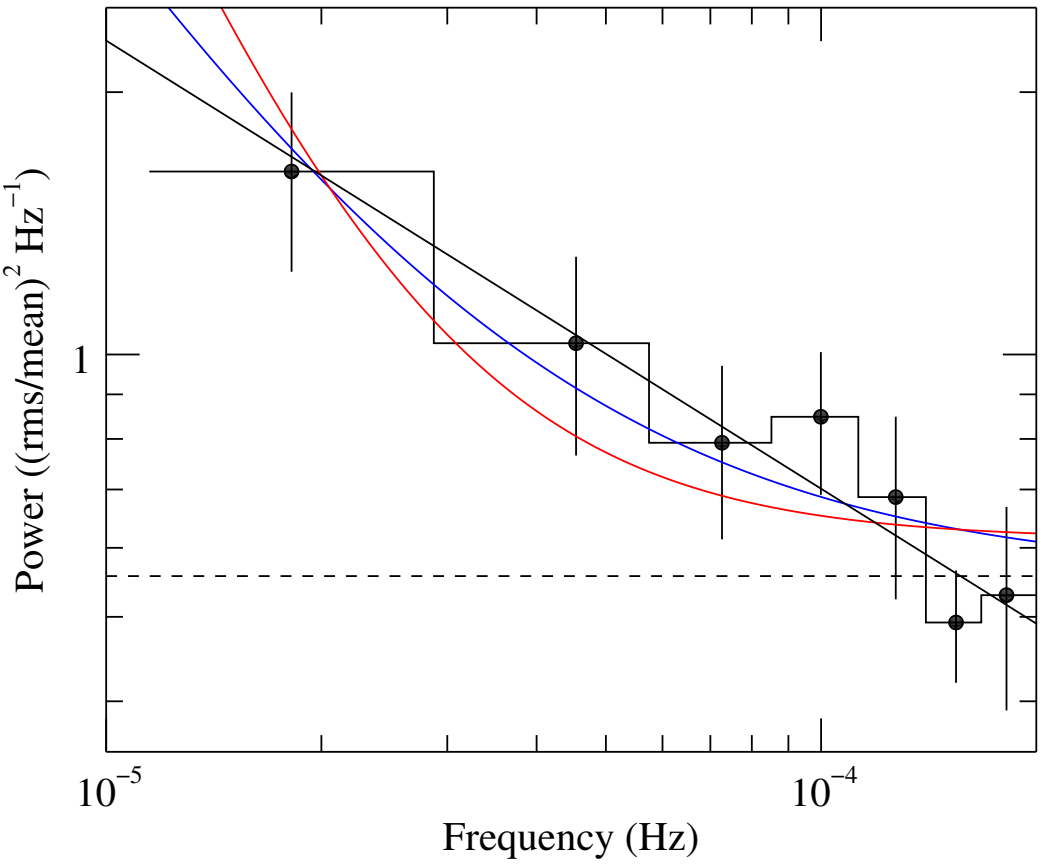

Fig. 3.5 PSD of optical monitor data. The estimated Poisson noise level is shown by the dashed line. Solid lines show fits with a powerlaw plus noise model, $P(f) = \alpha f^{\beta} + C$. Red: fixed index ($\beta$), free noise ($C$). Blue: free index, fixed noise. Black: both free. See Table 3.1 for full parameters.

evenly sampled time series, we split the observations where consecutive points are separated by more than 1.5 times the average. We then take sections of 120 ks and linearly interpolate onto a regular time grid. We calculate the periodogram for each section separately and average these into frequency bins containing at least 20 points to give the PSD. This is shown in Fig. 3.5. The expected Poisson noise level is calculated from equation A3 in Vaughan et al. (2003a) and shown as the dashed line in Fig. 3.5. We also fit the PSD with a sum of powerlaw red noise and Poisson white noise. The resulting parameters are shown in Table 3.1. The shape of the power spectrum is dependent on the assumptions made about Poisson noise, so we cannot simultaneously constrain the shape of the power spectrum and the level of Poisson noise, which only dominates at higher frequencies. Owing to the large uncertainties, there is insufficient statistical evidence to choose one model over another. We expect that fixing the Poisson noise to the calculated value gives the most reliable intrinsic PSD shape, $P(f) \propto f^{1.3\pm0.3}$. Independent of the exact model chosen, the UV PSD shows that the UV variability has the form of red noise on short timescales.

3.3.4 X-ray/UV correlation

To study the link between the emission from the accretion disc and coronal X-ray emission, we search for correlations between UV and X-ray flux in the *XMM-Newton* observations.

Initially, we produce a flux-flux plot (Fig. 3.6) to detect correlations between simultaneous X-ray and UV emission. This shows no strong correlation between the two bands, with Pearson coefficient $r = -0.02$ ($r = 0.025$ in the logarithmic domain) when using the full 0.3–10 keV band. When drawing lightcurves from uncorrelated red noise (from the same power spectra used for the DCF simulations presented below), a stronger correlation occurs with probability $p = 0.95$ (0.94). To determine whether the UV correlates with only the primary continuum (rather than the soft excess or reflected emission), we also consider the 2–4 keV band, which is dominated by the primary emission. This also shows no correlation ($r = -0.15$, $p = 0.61$; $r = -0.17$, $p = 0.60$ logarithmically) with the UV.

To test whether the lack of correlation seen in the flux-flux plot is due to a lag between X-ray and UV emission, we use the discrete cross-correlation function (DCF, Edelson and Krolik, 1988) from a single light curve of the whole observation so that timescales up to the full length of the observation are included.

To assess the significance of any correlations, we simulated 10 000 pairs of uncorrelated light curves and estimated 95 and 99% confidence intervals from the DCFs measured from these light curves. We used the method of Timmer and Koenig (1995) to generate light curves with appropriate red-noise power spectra. Since the shape of the UV PSD is poorly constrained, we use a simple power law with $P(f) \propto f^{-\alpha}$ with $\alpha = 2$ for the

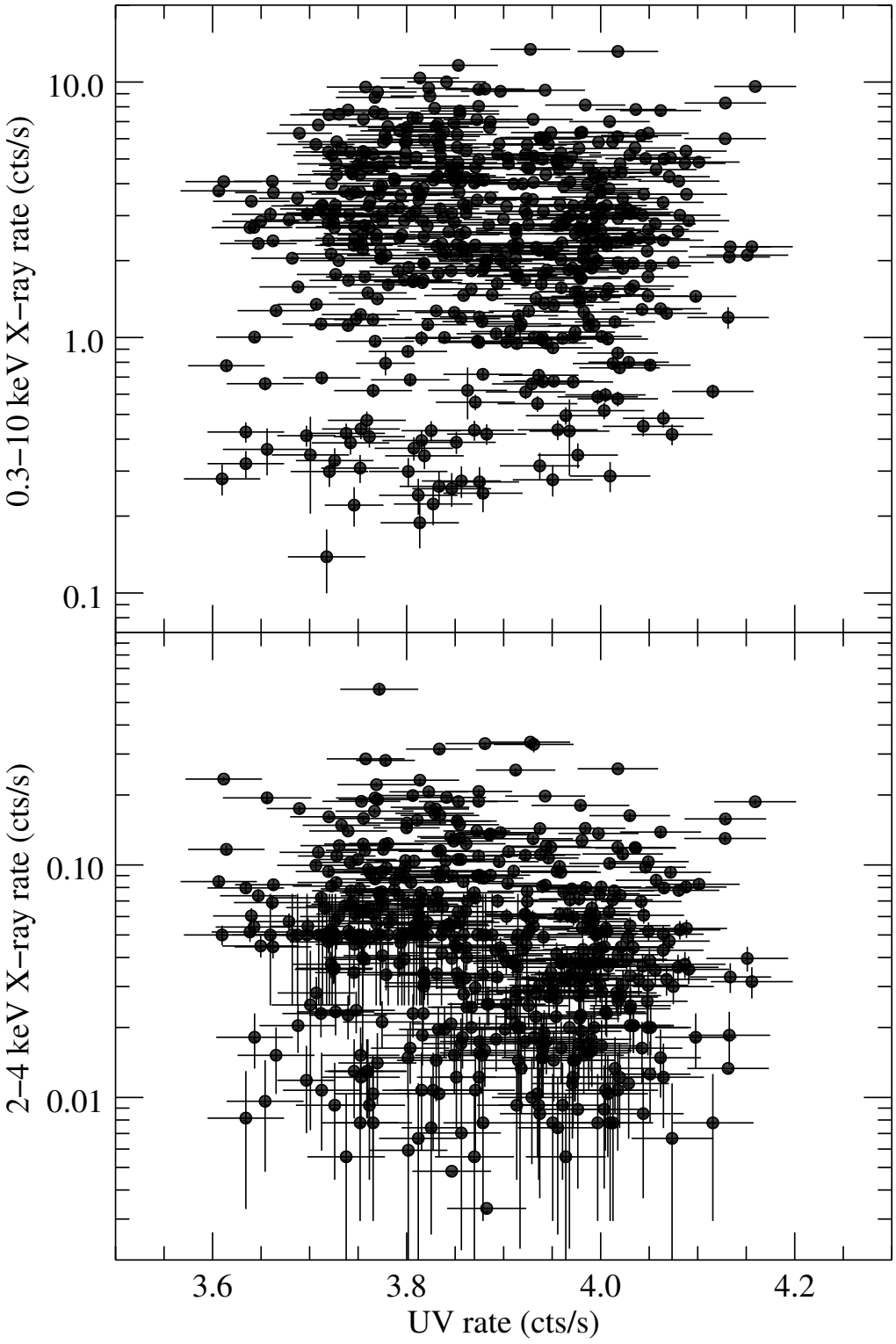

Fig. 3.6 Flux-flux plot of X-rays (top: 0.3–10 keV, full band; bottom: 2–4 keV, powerlaw dominated) against UV (*XMM*-OM *W1*, 2910 Å). No correlation between the two bands is apparent.

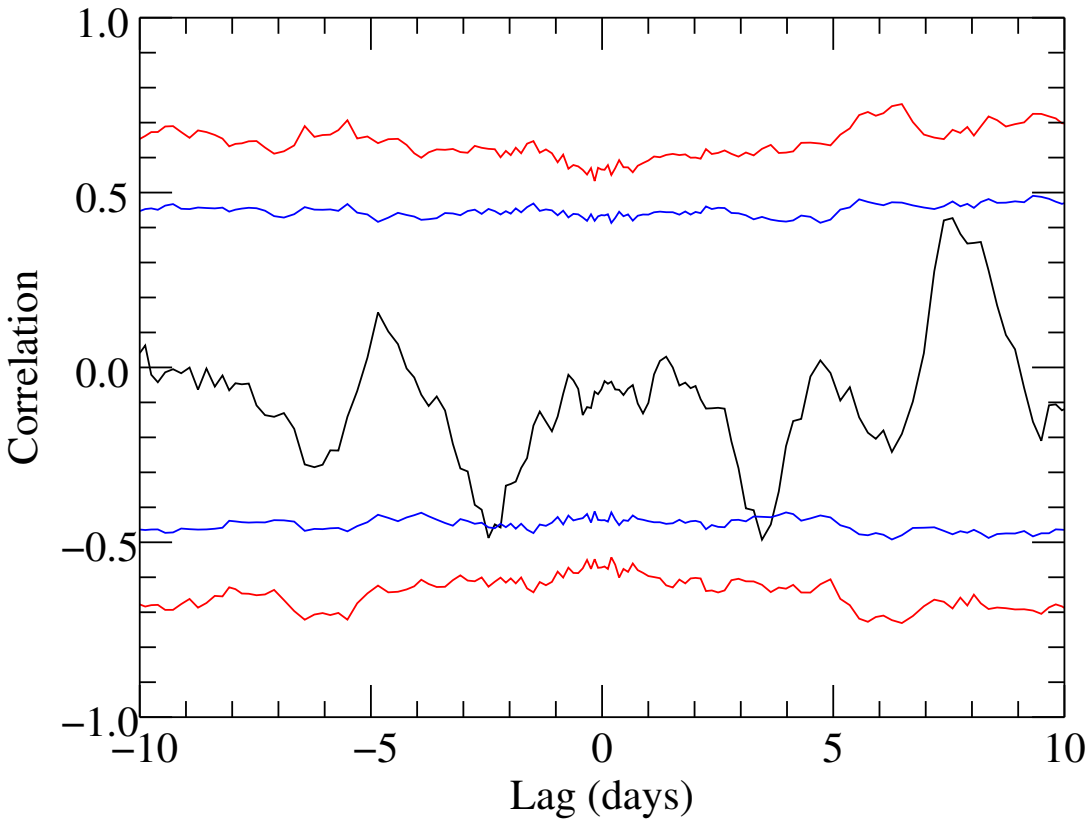

Fig. 3.7 DCF of X-rays (0.3–10 keV) against UV (*XMM*-OM *W1*, 2910 Å). Blue and Red lines indicate 95 and 99 % confidence intervals around 0 correlation.

UV. For the X-rays, we use a broken power law with $\alpha = 1.1$ and 2.22 below and above 6×10^{-5} Hz respectively for the X-rays (Alston et al, in prep.). We extract count rates at times corresponding to the real observations and draw our final simulated data from a Poisson distribution with mean equal to the simulated rates multiplied by the frame time.

The DCF is shown in Fig 3.7. There are no significant correlations between the X-ray and optical monitor data. Possible anticorrelations are detected at +3.5 and –2.5 days, although, since there is little physical motivation for such anticorrelations, these may be sampling artefacts due to the gaps between *XMM-Newton* orbits. A spurious detection is not unlikely as 5% of points are expected to lie outside the 95% confidence interval. To test whether only some components of the X-ray emission are correlated with the UV, we test different X-ray bands to isolate the soft excess and powerlaw components; this produces similar results so we show the full band to maximise signal.

3.4 Discussion

AGN almost universally show variability in their optical to X-ray spectra (e.g. Cackett et al., 2007; Ponti et al., 2012). Typically, the UV and X-ray emission are seen to correlate, with the UV often lagging the X-rays, indicative of reprocessing (e.g. Buisson et al., 2017; Edelson et al., 2015; McHardy et al., 2016).

We have found that for IRAS 13224–3809, the variability in the UV emission does not clearly correlate with variability observed in X-rays. This lack of correlation is unusual but not unique: for example, 1H 0707–495, which has a similar X-ray spectrum to IRAS 13224–3809 (Fabian et al., 2009), also shows no correlation between X-ray and UV emission (Robertson et al., 2015). While these non-detections use *XMM-Newton*-OM monitoring covering shorter timescales than are achievable with missions such as *Swift*, X-ray reprocessing should be detectable in the *XMM-Newton* campaigns: there is strong X-ray variability observed on timescales much shorter than the monitoring campaign. Indeed, UV/X-ray correlations have been detected with *XMM-Newton* for other sources (e.g. McHardy et al., 2016) and in shorter *Swift* campaigns (e.g. Edelson et al., 2017; McHardy et al., 2018; Pal and Naik, 2017). Additionally, AGN cover a wide range of black hole mass and the timescale for variability processes scales linearly with $M_{\rm BH}$. Therefore, timescales probed with *Swift* campaigns for large $M_{\rm BH}$ (e.g. FAIRALL 9, where correlations are observed Buisson et al., 2017; Lohfink et al., 2014) are equivalent to the timescales probed here, where the lower black hole mass means timescales are correspondingly shorter. Sources that do not show UV/X-ray correlations must have different emission to typical AGN in one or both of the UV and X-ray bands.

One possibility for the lack of UV/X-ray correlation is that there are significant sources of UV variability other than X-ray irradiation. This is likely to occur in some AGN as Uttley et al. (2003) found more fractional variability in the optical than X-ray emission in NGC 5548 (although in this case the optical and X-ray variability were correlated). One such source is the intrinsic disc fluctuations which propagate inwards to produce the X-ray variability. However, at the radii which produce the *W1*-band emission, the characteristic timescale of these fluctuations is much longer than the observations analysed here.

If the lack of correlation is due to an extra source of UV variability, the UV variability would be expected to be larger than in typical AGN. On timescales comparable to a night ($2 \times 10^{-5} - 2 \times 10^{-4}$ Hz), we find variability of 0.4 ± 0.1 %, consistent with Young et al. (1999), who found an upper limit on the optical variability of 1 % within a night. We can also make a direct comparison between the fractional variability of IRAS 13224–3809 and 1H 0707–495. Robertson et al. (2015) present the fractional variability of 1H 0707–495 in two sets of 4 continuous orbits. To compare the same timescales, we consider the 4 consecutive *XMM-Newton* orbits of IRAS 13224–3809 with OBSIDs 0780561501–0780561801 (other sections of consecutive orbits give similar results). This epoch has, in the *W1*-band, $F_{\rm Var} = 1.0 \pm 0.1$ %. These values are very similar to those of 1H 0707–495, being between the values for the two epochs presented in Robertson et al. (2015).

Therefore, both IRAS 13224–3809 and 1H 0707–495 show only modest UV variability, close to the average of 1.2% found by Smith and Vaughan (2007) for a sample of AGN measured with the optical monitor. The similarity of the UV variability in both these sources to sample averages (e.g. Grupe et al., 2010) may suggest that it is the nature of their X-ray rather than UV variability which prevents the detection of UV/X-ray correlations.

Despite the lack of UV/X-ray correlation, the variable part of the UV spectrum has the shape expected of an irradiated disc, as found for a number of other AGN in Buisson et al. (2017) (note that while IRAS 13224–3809 was included in this paper, the *Swift* data at the time of writing were insufficient to produce a RMS spectrum). This also suggests that the lack of UV/X-ray correlation may be due to unusual X-ray rather than UV emission. To further constrain the nature of the UV/optical emitting region, it would be desirable to study inter-band UV/optical lags, which are sometimes seen to match thin disc expectations even when X-ray lags do not (e.g. Edelson et al., 2017). However, the available *Swift* data are insufficient to constrain these lags.

For X-ray heating to be a plausible mechanism to drive the UV variability, there must be sufficient X-ray power to cause the observed changes in UV flux. To determine the regions responsible for *W1*-band emission in IRAS 13224–3809, we consider a thin disc (Shakura and Sunyaev, 1973) illuminated by a central X-ray source (Cackett et al., 2007).

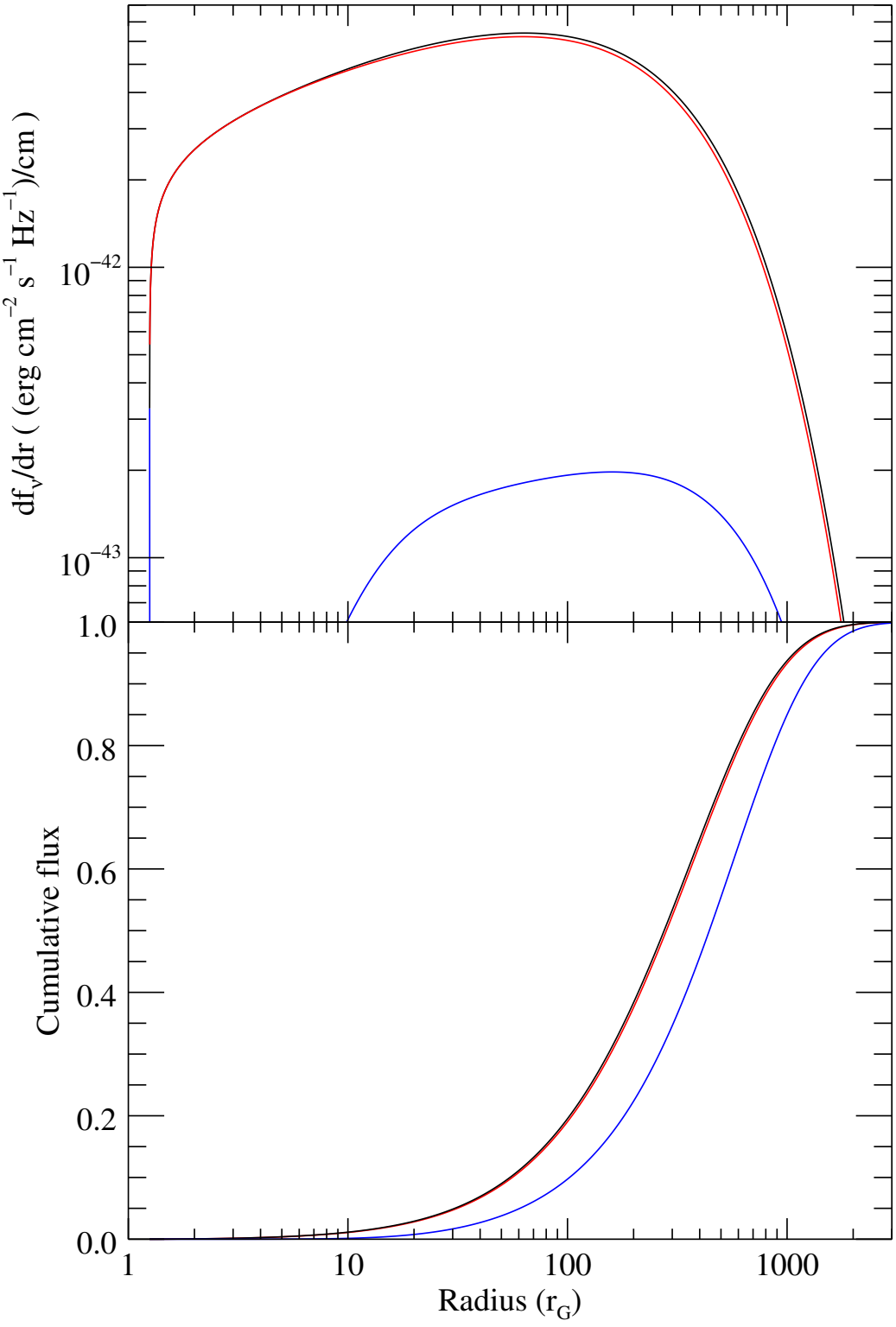

Fig. 3.8 Emission at the central wavelength of the *W1*-band from a standard disc with representative parameters for IRAS 13224–3809 (see text for details). Black: without X-ray irradiation. Red: with X-ray irradiation. Blue: Difference.

With sensible parameters for the mass ($M_{\rm BH} = 10^7\,{\rm M}_\odot$, Zhou and Wang 2005) and accretion rate ($\dot{m} = 0.7$, Buisson et al. 2017; Jiang et al. submitted), we show the radii responsible for the *W1*-band emission in Fig. 3.8. To demonstrate the potential effect of X-ray irradiation, we also test the same model illuminated by an isotropic point source (Cackett et al., 2007) at $10\,r_{\rm G}$ above the disc, with power $10^{44}\,{\rm erg\,s^{-1}}$ (based on the continuum model in Jiang et al., submitted). This shows that the majority of the flux in the *W1*-band is produced on scales of a few hundred $r_{\rm g}$. The change in flux due to heating occurs slightly further out, as more significant flux changes occur when disc material is heated to temperatures at which the material starts to emit in the *W1*-band. Integrating the flux density across the disc shows that the X-ray illumination changes the *W1*-band flux by $\nu F_\nu(W1) = 2.5 \times 10^{-13}\,{\rm erg\,s^{-1}}$. While there is significant uncertainty is some of these parameters, this shows that the effect of X-ray heating can be sufficiently powerful to drive a significant fraction of the observed UV changes.

One alternative model to explain deviations from the simple X-ray reprocessing scenario has been presented by Gardner and Done (2017), in which a thickened hot inner disc acts as an intermediate reprocessor between the X-ray and UV emission. This has been suggested as an explanation for the correlations seen in NGC 5548 (Gardner and Done, 2017) and NGC 4151 (Edelson et al., 2017). While an additional reprocessor does not remove all correlation between X-ray and UV flux, it significantly reduces the effect of fast X-ray variability on the UV emission. This could mean that X-ray/UV correlations are seen only on long timescales and the campaign presented here is too short to detect a correlation.

The UV variability we do observe could still be due to illumination from the X-ray source if the variability seen by the disc is different to that in our line of sight. Various effects may lead to different X-ray variability being observed by the disc, such as variable absorption between the disc and corona. IRAS13224–3809 must have some outflowing material, which may shield the disc from the corona, as a highly ionised variable UFO is observed (Parker et al., 2017b). While this outflow is too optically thin to have a significant effect on the transmission of X-ray flux, optically thicker material (denser or less ionised) may exist in the acceleration zone, out of the line of sight, between the corona and disc. It is also possible for there to be a weak extended region of the corona which, although producing little X-ray flux, is optically thick when viewed from close to the plane of the disc. Scattering in this extended corona could significantly change the flux from the main central corona to the disc relative to that in our line of sight. If such material is present and changes within the observing campaign (which is seen by Parker et al. (2017b) to occur in the highly ionised material) then the X-ray flux which reaches the *W1*-band emitting region of the disc may not correlate with the observed X-ray flux.

Alternatively, the changes in X-ray intensity received by the disc may be different to those observed if the geometry of the system changes (such as the corona moving up and down) for several reasons. Firstly, as the corona rises, it illuminates the disc from a less oblique angle, leading to stronger irradiation of the disc at constant coronal power. Additionally, if motion of coronal material is at relativistic speeds, changes of this motion will induce differences in the anisotropy of coronal emission due to special relativistic beaming. General relativistic light bending also acts to focus light towards the black hole (Miniutti and Fabian, 2004; Wilkins et al., 2016). While this principally affects the innermost regions, small effects in the outer regions may further complicate the observed variability. A combination of these effects along with changes in the intrinsic coronal power could lead to removal of the correlation between observed coronal power and UV emission from disc heating. The interpretation of the lack of correlation as being due to variable coronal geometry also fits with the relatively large X-ray variability of IRAS 13224–3809: if other sources have a more stable coronal geometry, they will be observed to have both weaker X-ray variability and stronger X-ray/UV correlation.

This interpretation could be tested with detailed mapping of the corona, such as in Wilkins and Fabian (2011); Wilkins and Gallo (2015). This would allow the X-ray irradiation of the disc to be measured rather than just the X-ray flux in the line of sight. However, mapping the corona on sufficiently short timescales is likely to require greater collecting area than is available with current missions.

3.5 Conclusions

We have shown that the X-ray and ultraviolet flux of the most X-ray variable bright AGN, IRAS 13224–3809, are not correlated on timescales of up to ~ 40 days. However, the variability of the UV spectrum matches that seen in other AGN that do show X-ray/UV correlations. The UV variability is much weaker than in the X-rays: the average *W1*-band fractional variability is $0.7 \pm 0.1\%$ over one *XMM-Newton* orbit and around 3% over 40 days, whereas the X-rays vary by more than a factor of ten on timescales of kiloseconds. This suggests that the X-ray variability viewed by the disc is different to that in our line of sight, which may be caused by changes in coronal geometry, absorption or scattering between the corona and outer disc.

Chapter 4

NuSTAR observations of Mrk 766: distinguishing reflection from absorption

Abstract

We present two new *NuSTAR* observations of the narrow line Seyfert 1 (NLS1) galaxy Mrk 766 and give constraints on the two scenarios previously proposed to explain its spectrum and that of other NLS1s: relativistic reflection and partial covering. The *NuSTAR* spectra show a strong hard (> 15 keV) X-ray excess, while simultaneous soft X-ray coverage of one of the observations provided by *XMM-Newton* constrains the ionised absorption in the source. The pure reflection model requires a black hole of high spin ($a > 0.92$) viewed at a moderate inclination ($i = 46^{+1}_{-4}{}^{\circ}$). The pure partial covering model requires extreme parameters: the cut-off of the primary continuum is very low (22^{+7}_{-5} keV) in one observation and the intrinsic X-ray emission must provide a large fraction (75%) of the bolometric luminosity. Allowing a hybrid model with both partial covering and reflection provides more reasonable absorption parameters and relaxes the constraints on reflection parameters. The fractional variability reduces around the iron K band and at high energies including the Compton hump, suggesting that the reflected emission is less variable than the continuum.

4.1 Introduction

A common feature of the X-ray spectra of many non-jetted active galactic nuclei (AGN) is the hard excess, a strong increase in flux above ~ 15 keV. This was first detected in stacked spectra from *Ginga* (Pounds et al., 1990) and measured for individual sources with *BeppoSAX* (Perola et al., 2002). Prior to the launch of *NuSTAR*, detailed measurements had only been made in a handful of AGN, using *Swift*-BAT or the *Suzaku* PIN detector, which were interpreted either as evidence of Compton thick absorption (Risaliti et al., 2009; Turner et al., 2009) or the Compton hump of reflected emission (Walton et al., 2010). X-ray reflection (George and Fabian, 1991; Lightman and White, 1988) occurs when the primary X-ray source, known as the corona, illuminates the accretion disc or other relatively cold material such as the torus. This illumination triggers the emission of fluorescent lines at low energies and is scattered into a 'Compton hump' at high energies. When the reflection spectrum originates from the parts of the accretion disc close to the innermost stable circular

orbit (ISCO) of the black hole, the narrow features are blurred out by relativistic effects (Fabian et al., 1989; Laor, 1991).

Since the launch of *NuSTAR* (Harrison et al., 2013), the Compton hump has been more definitively detected in many AGN (Baloković et al., 2015; Brenneman et al., 2014; Kara et al., 2015; Marinucci et al., 2014; Parker et al., 2014b; Risaliti et al., 2013; Walton et al., 2014). The sensitivity of *NuSTAR* at high energies means that it can be used to differentiate between reflection and absorption models for the hard excess (e.g. Vasudevan et al., 2014).

One object which has had both these processes proposed to explain its spectrum is Mrk 766. Mrk 766 is a nearby ($z = 0.013$) narrow line Seyfert 1 (NLS1) galaxy. NLS1s are thought to be rapidly accreting ($\dot{m} \sim 0.01 - 1$), relatively low mass (typically $M_{\rm BH} \sim 10^6 - 10^7 M_{\odot}$) AGN, and are distinguished by narrow optical Balmer lines, weak [O III] and strong Fe II emission (see review by Komossa, 2008). In the X-ray band, NLS1s are spectrally soft, and are thus easily detected by low energy instruments. They frequently show complex, rapid variability and non-trivial spectral shapes, so are of great interest for study. The supermassive black hole in the nucleus of Mrk 766 has a mass of 1–6$\times 10^6 M_{\odot}$ (Bentz et al., 2009, 2010) and the host is a barred spiral galaxy. Spectrally, the evidence for a relativistically-broadened iron Kα line in Mrk 766 is tentative. A broad line was claimed with *ASCA* by Nandra et al. (1997b). However, later analysis of a more sensitive *XMM-Newton* spectrum by Pounds et al. (2003) showed that the line profile could instead be described by ionized reflection alone, with no need for relativistic blurring. Based on *XMM-Newton* and *Suzaku* observations of Mrk 766, Miller et al. (2007) and Turner et al. (2007) proposed a model where the bulk of the spectral variability is due to variations in multiple complex (partially-covering, ionized) absorbing zones. A recent re-analysis of the archival *XMM-Newton* data by Liebmann et al. (2014) showed that the spectra and variability could be well described by a composite model, containing both partial-covering absorption and relativistic reflection.

More robust evidence for the presence of relativistic reflection in Mrk 766 comes from the detection of a reverberation lag (De Marco et al., 2013; Emmanoulopoulos et al., 2011), thought to be caused by the time delay induced in the reflected signal due to the light travel time from the corona to the disc. Emmanoulopoulos et al. (2011) found almost identical reverberation lags in Mrk 766 and MCG–6-30-15, the first source in which a broad iron Kα line was discovered (Tanaka et al., 1995). Mrk 766 is included in the sample of objects studied by Emmanoulopoulos et al. (2014), who found that by modelling the time lag spectra they could precisely determine the mass ($M_{\rm BH} = 1.6^{+1.4}_{-1.2} \times 10^6 M_{\odot}$) and constrain other physical parameters (e.g. the dimensionless spin, $a > 0.56$). The discovery of iron K lags in some sources (e.g. Kara et al., 2016b, 2013d; Zoghbi et al., 2012), which have so far only

Table 4.1 List of *NuSTAR* observations of Mrk 766 and associated simultaneous X-ray observations.

Telescope	OBSID	Start time	Observation length/ks
NuSTAR	60101022002	2015-01-24T12:31	90.2
Swift-XRT	00080076002	2015-01-25T00:08	4.9
NuSTAR	60001048002	2015-07-05T22:24	23.6
XMM-EPIC	0763790401	2015-07-05T17:26	28.2

been explained by invoking relativistic reflection, have reinforced the interpretation of these high-frequency time lags as originating from reverberation close to the black hole. However, iron K reverberation lags have not yet been detected in Mrk 766 (Kara et al., 2016b).

In this paper, we present the results of recent *NuSTAR* observations of Mrk 766, where we examine the hard X-ray spectrum using the sensitivity and high-energy spectral resolution of *NuSTAR* to enable us to constrain the different physical models for the hard excess. The observations and methods of data reduction are presented in Section 6.2; results of the analysis are given in Section 6.3; these results are discussed in Section 6.4; and conclusions are made in Section 6.5.

4.2 Observations and Data Reduction

Mrk 766 has been observed twice by *NuSTAR*: for 90 ks starting on 2015 Jan 24 and for 23 ks starting on 2015 July 5. The first observation had a simultaneous *Swift* snapshot and the second was taken jointly with *XMM-Newton* (see Table 6.1).

The *NuSTAR* data were reduced using the *NuSTAR* data analysis software (NuSTARDAS) version 1.4.1, and CALDB version 20140414. We extracted cleaned event files using the NUPIPELINE command, and spectral products using the NUPRODUCTS command, using 80 arcsec radius circular extraction regions for both source and background spectra. The background region was selected from a region on the same chip, uncontaminated with source photons or background sources.

The *Swift* data were reduced using the *Swift* XRT products generator, using the procedure described in Evans et al. (2009) to extract a spectrum.

The *XMM-Newton* data, taken in small window mode, were reduced according to the standard guidelines in the *XMM-Newton* User's Manual, using the *XMM-Newton* SCIENCE ANALYSIS SOFTWARE (SAS) version 14.0.0 as described in Vasudevan et al. (2013). The task EPCHAIN was used to reduce the data from the pn instrument. An annular source region

of outer radius 40 arcsec and inner radius 10 arcsec was used to extract a source spectrum to remove mild pileup (detected using the EPATPLOT tool), checking for nearby sources in the extraction region. Circular regions near the source were used to calculate the background. Additionally, the background light curves (between 10 and 12 keV) were inspected for flaring, and a comparison of source and background light curves in the same energy ranges was used to determine the portions of the observation in which the background was sufficiently low compared to the source (4 ks was lost to flaring); the subsequent spectra were generated from the usable portions of the observation. Response matrices and auxiliary files were generated using the tools RMFGEN and ARFGEN.

We use *XMM-Newton*-RGS data from the new observation and the highest and lowest flux archival observations (OBSIDs: 0304030101, 0304030301). We reduced the data with the standard *XMM-Newton* pipeline, RGSPROC. We use a source region including 95% of the PSF and background from outside 98% of the PSF (XPSFINCL=95 and XPSFEXCL=98). The two detectors were added for illustrative purposes only using RGSCOMBINE.

Spectra from all instruments were grouped to a signal to noise level of 5. Fits were made in ISIS Version 1.6.2-32 (Houck and Denicola, 2000); errors are given at the 90% level. We use the elemental abundances of Wilms et al. (2000) with cross sections from Verner et al. (1996).

4.3 Results

From the *NuSTAR* lightcurve (Fig. 4.1), we determine that long term flux variability is modest and no significant hardness variability is seen. It is therefore appropriate to fit average spectra of each observation. The *Swift* X-ray telescope (XRT) snapshot taken during the first *NuSTAR* observation (shown by the shaded region in Fig. 4.1) occurred at a flux level close to the average. Therefore, it is likely to be indicative of the average low energy spectrum over the whole observation.

We compare the *NuSTAR* observations with previous observations in Fig. 4.2. This shows that the new observations are close to the high flux end of the previously observed states of Mrk 766.

We begin our analysis by comparing all data for each of the new observations to a powerlaw with Galactic absorption (modelled with `tbnew`, Wilms et al. 2000). The residuals to a $\Gamma = 2$ powerlaw are shown in Fig. 4.3. This shows the spectrum is moderately soft, with a soft excess below 0.7 keV with a deficit above, and excesses at $5-7$ keV and $15-40$ keV.

The drop in flux at ~ 0.7 keV may be due to warm absorption features such as the OVII edge and the iron unresolved transition array (UTA). The excesses at $5-7$ keV and

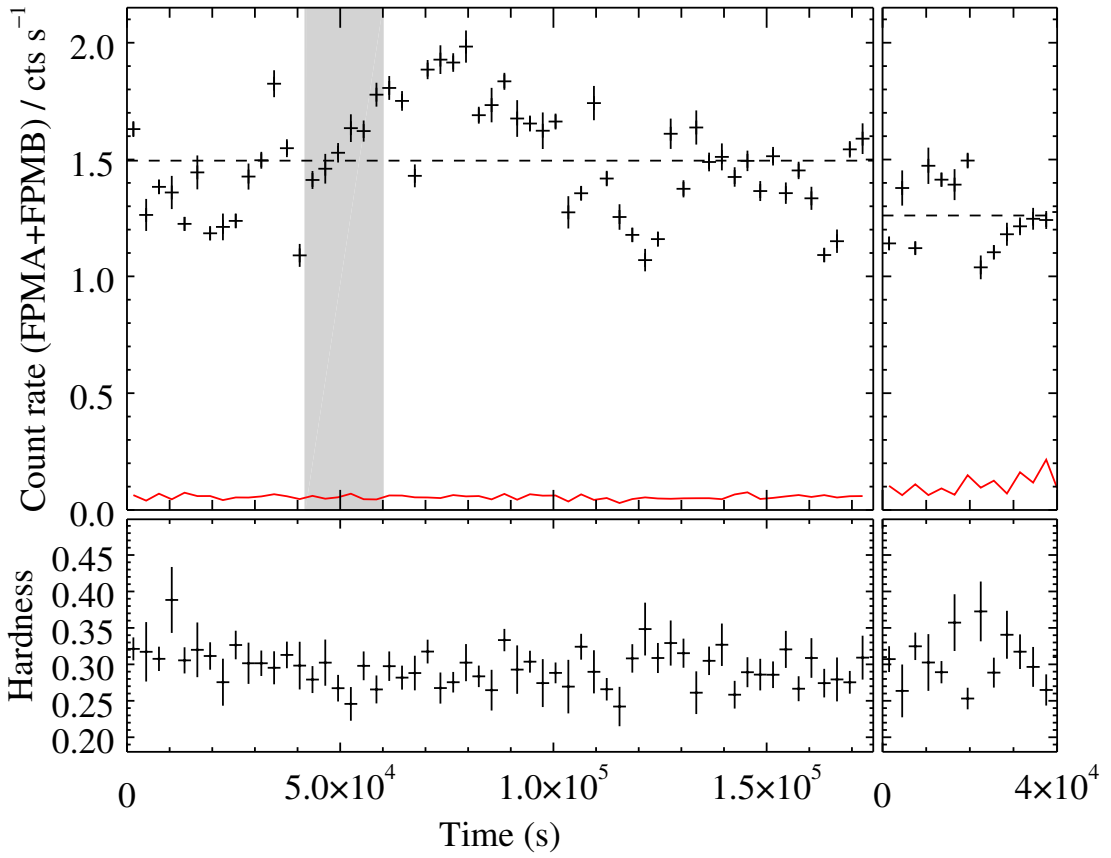

Fig. 4.1 Upper Panels: *NuSTAR* light curve with 3 ks bins. The gap between panels corresponds to $\sim$ 6 months. The background light curve is shown in red, and the time of the *Swift* XRT exposure by the shaded region. The dashed horizontal lines show the mean flux of each observation. Lower panels: 10–40/3–10 keV hardness ratio.

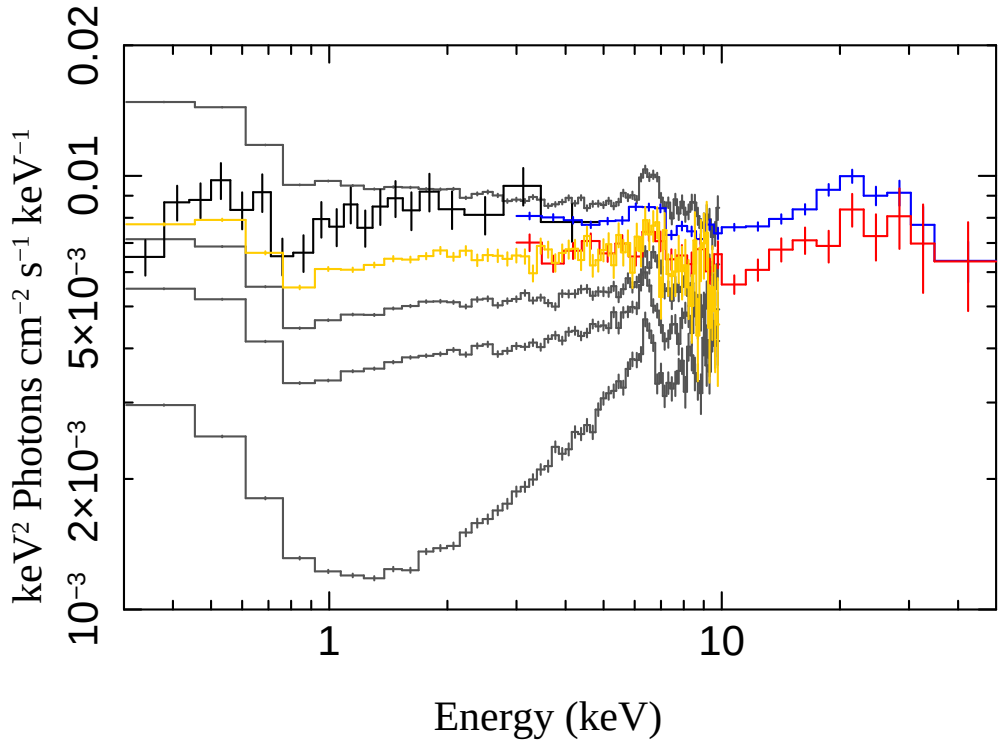

Fig. 4.2 Unfolded fluxes (to a $\Gamma = 2$ powerlaw) of the January (*NuSTAR*: blue, *Swift*: black) and July (*NuSTAR*: red, *XMM*: orange) observations, with a range of previous *XMM* (grey) observations (OBSIDs 0109141301, 0304030101, 0304030301 and 0304030401, see Giacchè et al. 2014; Miller et al. 2007 for detailed analysis). Spectra have been rebinned for plotting.

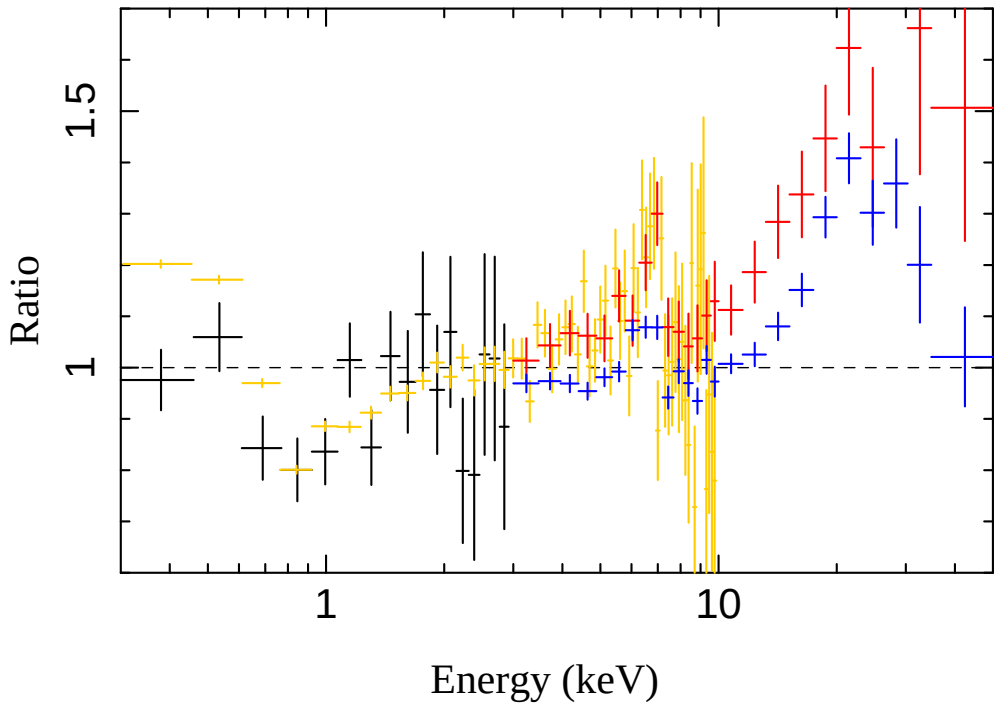

Fig. 4.3 Ratios of each observation to a $\Gamma = 2$ powerlaw with Galactic absorption: January *Swift* (black) and *NuSTAR* (blue); July *XMM-Newton*-pn (orange) and *NuSTAR* (red). Spectra have been rebinned for plotting.

$15-40$ keV are typical of emission from Fe K and Compton scattering due to reflection, but similar features can be produced by partial covering absorption reducing the flux at other energies. We therefore proceed by fitting detailed models of these processes to the spectra. Since different processes dominate the spectral features in the low and high energy data, we first consider each region separately, before combining these to give a consistent broadband picture.

4.3.1 High-energy fits – iron line and hard excess

To constrain the iron line and hard excess while minimising the effect of absorption, we initially fit the data above 3 keV. Since the *Swift* observation has little signal above 3 keV, we fit only the data from *NuSTAR* and *XMM*-pn. We fit the two observations separately.

In the reflection case, we find that distant reflection (modelled with `pexmon`, Magdziarz and Zdziarski 1995; Nandra et al. 2007) is insufficient to model the iron line (χ^2/d.o.f. $= 1682/1526 = 1.102$), leaving residuals around the narrow iron line (Fig. 4.4, inset), which suggest that the iron line is broadened. We test this by replacing the narrow iron line in `pexmon` with a broadened iron line, represented by a Gaussian with free width (`pexrav+zgauss`; `pexrav` is identical to `pexmon` without the Fe Kα emission line). This gives a significantly better fit, $\Delta\chi^2 = 46$ and 17 for one additional degree of freedom for the *Swift*/*NuSTAR* and *XMM-Newton*/*NuSTAR* observations respectively. Parameters of fits to this model are shown in Table 4.2. This shows significant width to the iron line, likely due to the orbital motion of material around the black hole.

Having shown that the iron line is broadened, we fit the spectrum with a reflection model that incorporates self-consistent relativistic blurring of the entire spectrum (`relxill`, Dauser et al. 2010; García et al. 2014). This provides a reasonably good fit and has no obvious residual features (χ^2/d.o.f. $= 1607/1518 = 1.059$, Figure 4.4). Further, we note that including distant reflection does not provide a significant improvement over relativistic reflection alone ($\Delta\chi^2 = 6$ for 2 additional degrees of freedom) and no physical parameters of the relativistic model change significantly. Hence, we present models including only relativistic reflection (Table 4.2).

These models show Mrk 766 as a source with slight relativistic blurring viewed at moderate inclination ($i = 42 \pm 3^\circ$ or $39^{+6}_{-3}{}^\circ$). Parameters such as the inclination, which are not expected to change within 6 months, are consistent between the two observations. The cut-off of the primary continuum is too high to measure.

It has also been suggested that the spectrum of Mrk 766 can be explained by partial covering absorption of the primary source (Miller et al., 2007; Turner et al., 2007). We model this with a cut-off power-law with a number of partially covering components, using the model

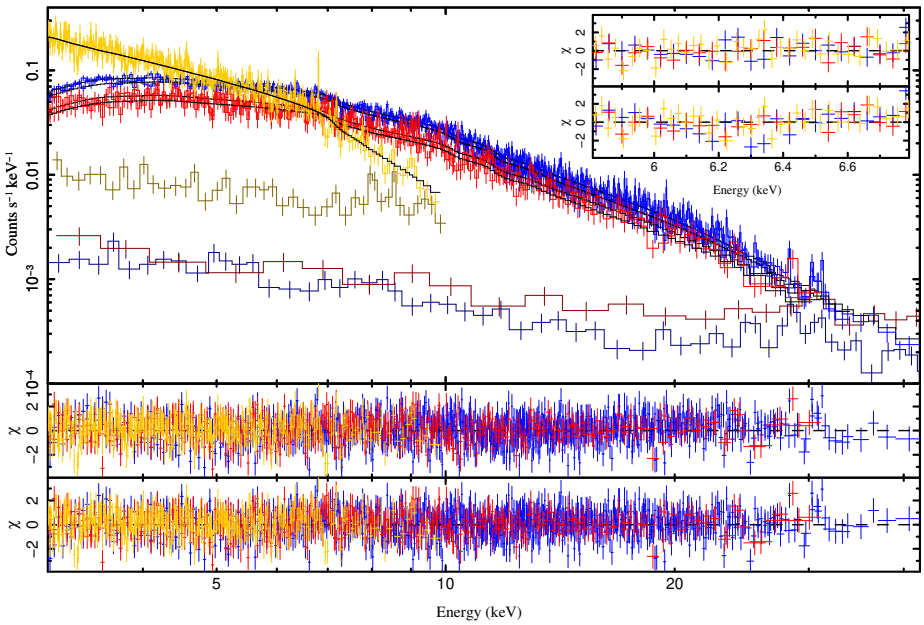

Fig. 4.4 Top panel: fits to *NuSTAR* and *XMM-Newton* data above 3 keV (the model shown is of relativistic reflection). *XMM-Newton* data in orange is simultaneous with the red (dimmer) *NuSTAR* data; the other *NuSTAR* observation is shown in blue. Backgrounds are shown in dark orange, red and blue respectively. Middle panel: residuals from relativistic reflection model. Lower panel: residuals from partial covering model. Inset: Residuals for reflection models over $5.8-6.8$ keV. Blurred reflection (upper inset) has smaller residuals around the iron K band than distant neutral reflection (lower inset): over $5.8-6.8$ keV, $\Delta\chi^2 = 18$.

`zpcfabs`. We find that a model with two components (χ^2/d.o.f. $= 1616/1522 = 1.062$) provides a similar quality fit to the reflection model. Having only one partial covering component gives a significantly worse fit to the data ($N_{\rm H} \sim 9 \times 10^{24}\,{\rm cm}^{-2}$, $f_{\rm cov} \sim 0.6$, χ^2/d.o.f. $= 1693/1526 = 1.110$, $\Delta\chi^2 = 77$ for 4 degrees of freedom) and three partial covering components gives insignificant improvement over 2 components ($\Delta\chi^2 = 8$ for 4 degrees of freedom).

The two-component fit requires a component of strong absorption ($N_{\rm H} > 5 \times 10^{24}\,{\rm cm}^{-2}$) in each observation and a low energy of the cut-off ($E_{\rm cut} = 27^{+20}_{-9}$ keV) in the *Swift*/*NuSTAR* observation, which has better high energy statistics due to the longer *NuSTAR* exposure.

4.3.2 Low-energy fits - warm absorption and emission

Warm absorption and emission are known to have an important effect on the spectrum of Mrk 766 in the soft band (e.g. Laha et al., 2014; Sako et al., 2003). To determine the nature of the gas which is responsible for these features, we begin by identifying features visually and with systematic line scans similar to those performed by for example Tombesi et al. (2010) and Pinto et al. (2016) with a phenomenological continuum (Fig. 4.6).

We use a broadband continuum model based on that of Branduardi-Raymont et al. (2001): a powerlaw with two broad lines. We then ensure that the local continuum is well-described with a cubic spline modification over the region ± 1 Å from the wavelength of interest. We measure line significance from the change in χ^2 when including an additional unresolved Gaussian at fixed wavelength, allowed to have positive or negative normalisation (one additional degree of freedom; the use of positive or negative normalisation in the same fit is needed to avoid the problems described in Protassov et al. 2002). We then scan the wavelength across the RGS range to find $\Delta\chi^2$ at each wavelength. We indicate approximate significance by estimating a critical $\Delta\chi^2_{\rm crit}$ for 95 % significance from the expected distribution of N independent trials each having a χ^2_1 distribution. We estimate the number, N of independent trials performed by the wavelength range tested divided by the instrumental resolution, $(\lambda_{\rm max} - \lambda_{\rm min})/{\rm d}\lambda = 450$. The global 95 % confidence interval (the solution $\Delta\chi^2_{\rm crit}$ to $P(\chi^2_1 < \Delta\chi^2_{\rm crit})^N = 0.95$) then corresponds to $\Delta\chi^2_{\rm crit} = 14.9$ (shown as the green line in Fig. 4.6). We note also that changing the estimate of the effective number of independent trials has only a small effect on the critical $\Delta\chi^2_{\rm crit}$: increasing or decreasing the number of trials by a factor of 2 changes the critical $\Delta\chi^2_{\rm crit}$ to 16.2 or 13.6 respectively.

Since the new observations show few features at high significance (the *XMM-Newton* RGS observation is relatively shallow – 37,000 counts in total across both detectors and orders), we are also guided by the sensitive archival *XMM-Newton* RGS spectra from the highest and lowest previously observed states (Fig. 4.5; pn spectra shown in Fig. 4.2). While the

Table 4.2 Fits to data from each observation above 3 keV. Parameters indicated with * are fixed. $R_{\rm Refl}$ indicates the reflection strength, where $R_{\rm Refl} = 1$ gives the reflection from material covering 2π steradians with an isotropic source.

Parameter	*Swift*/*NuSTAR*	*XMM-Newton*/*NuSTAR*
Reflection with broad Gaussian iron line		
Γ	$2.46^{+0.08}_{-0.08}$	2.31 ± 0.12
$E_{\rm cut}$/keV	> 440	> 310
$R_{\rm Refl}$	$3.5^{+1.0}_{-0.9}$	$2.1^{+1.2}_{-0.9}$
Line E /keV	6.4*	6.4*
Line σ /keV	$2.3^{+0.3}_{-0.4}$	$1.4^{+0.5}_{-0.7}$
χ^2/d.o.f.	$909.2/806 = 1.128$	$710.6/718 = 0.990$
Relativistic reflection		
Emissivity Index	< 4	> 4.3
a	Unconstrained	< 0.44
$i/^\circ$	42^{+3}_{-3}	39^{+6}_{-3}
Γ	$2.24^{+0.09}_{-0.05}$	$2.16^{+0.12}_{-0.08}$
$\log(\xi/{\rm erg\,cm\,s^{-1}})$	$1.8^{+0.4}_{-0.5}$	< 3.1
$A_{\rm Fe}$	$1.2^{+0.7}_{-0.3}$	$2.9^{+0.8}_{-1.4}$
$E_{\rm cut}$/keV	> 210	> 230
$R_{\rm Refl}$	$1.15^{+0.25}_{-0.20}$	$1.3^{+0.5}_{-0.4}$
χ^2/d.o.f.	$902.9/803 = 1.124$	$704.1/715 = 0.985$
Partial covering absorption		
$N_{\rm H}/{\rm cm^{-2}}$	$1.15 \pm 0.2 \times 10^{25}$	$7.1^{+2.6}_{-1.9} \times 10^{24}$
$f_{\rm Cov}$	$0.67^{+0.06}_{-0.07}$	$0.55^{+0.15}_{-0.11}$
$N_{\rm H}/{\rm cm^{-2}}$	$88^{+18}_{-15} \times 10^{23}$	$4^{+3}_{-2} \times 10^{23}$
$f_{\rm Cov}$	$0.45^{+0.06}_{-0.07}$	$0.37^{+0.10}_{-0.16}$
Γ	2.2 ± 0.15	$2.3^{+0.2}_{-0.4}$
$E_{\rm Cut}$/keV	27^{+20}_{-9}	110^{+390}_{-90}
χ^2/d.o.f.	$909.7/805 = 1.142$	$706.0/717 = 0.996$

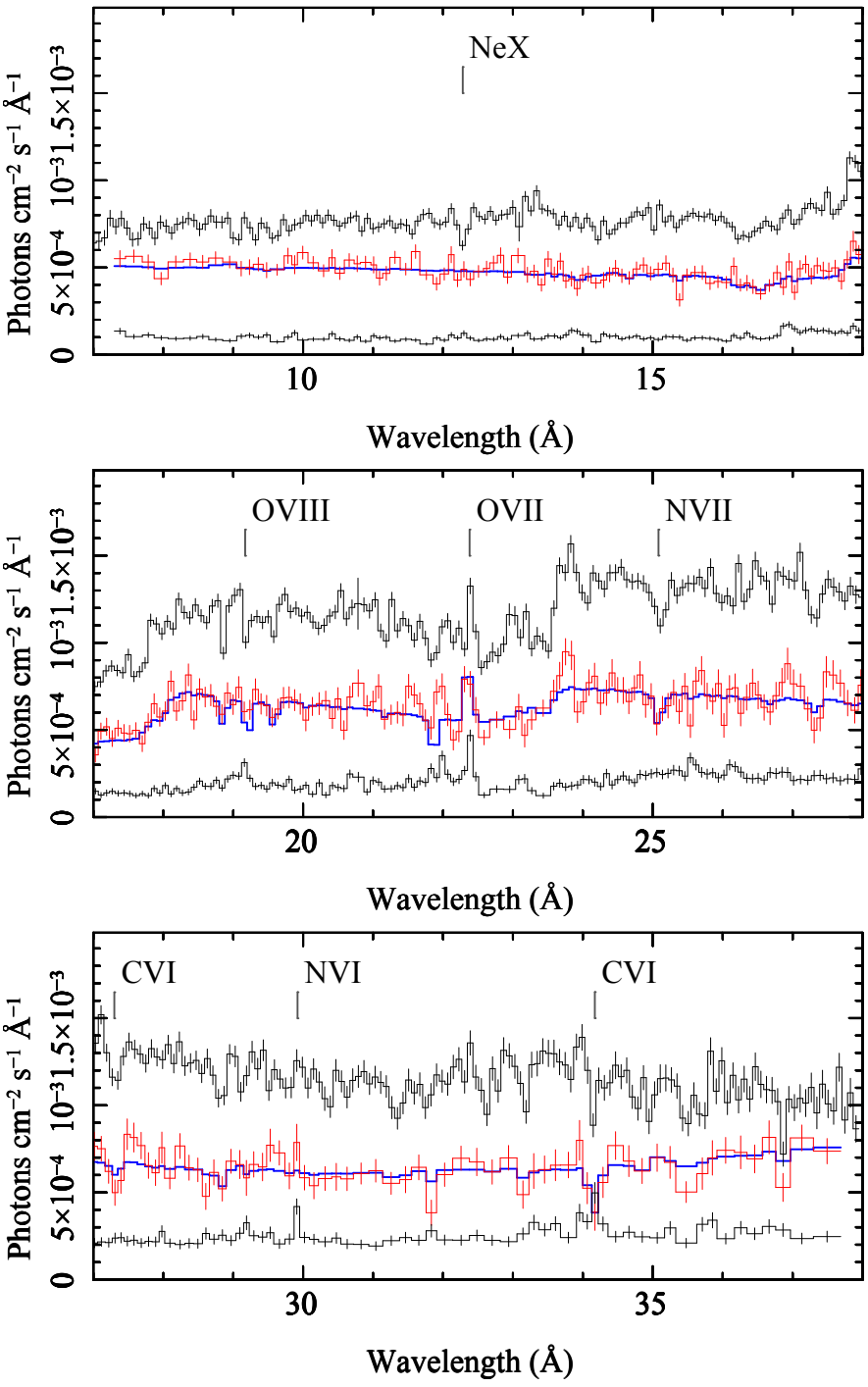

Fig. 4.5 RGS data from the new observation (red) and the highest and lowest archival flux states (black) unfolded to a constant model. Emission lines are clearly visible in the low state, while absorption features are present in the high state. The blue line shows a fit with absorption and emission components applied to a phenomenological continuum. Wavelengths are given in the observed frame and the range of each panel overlaps the next by 1 Å.

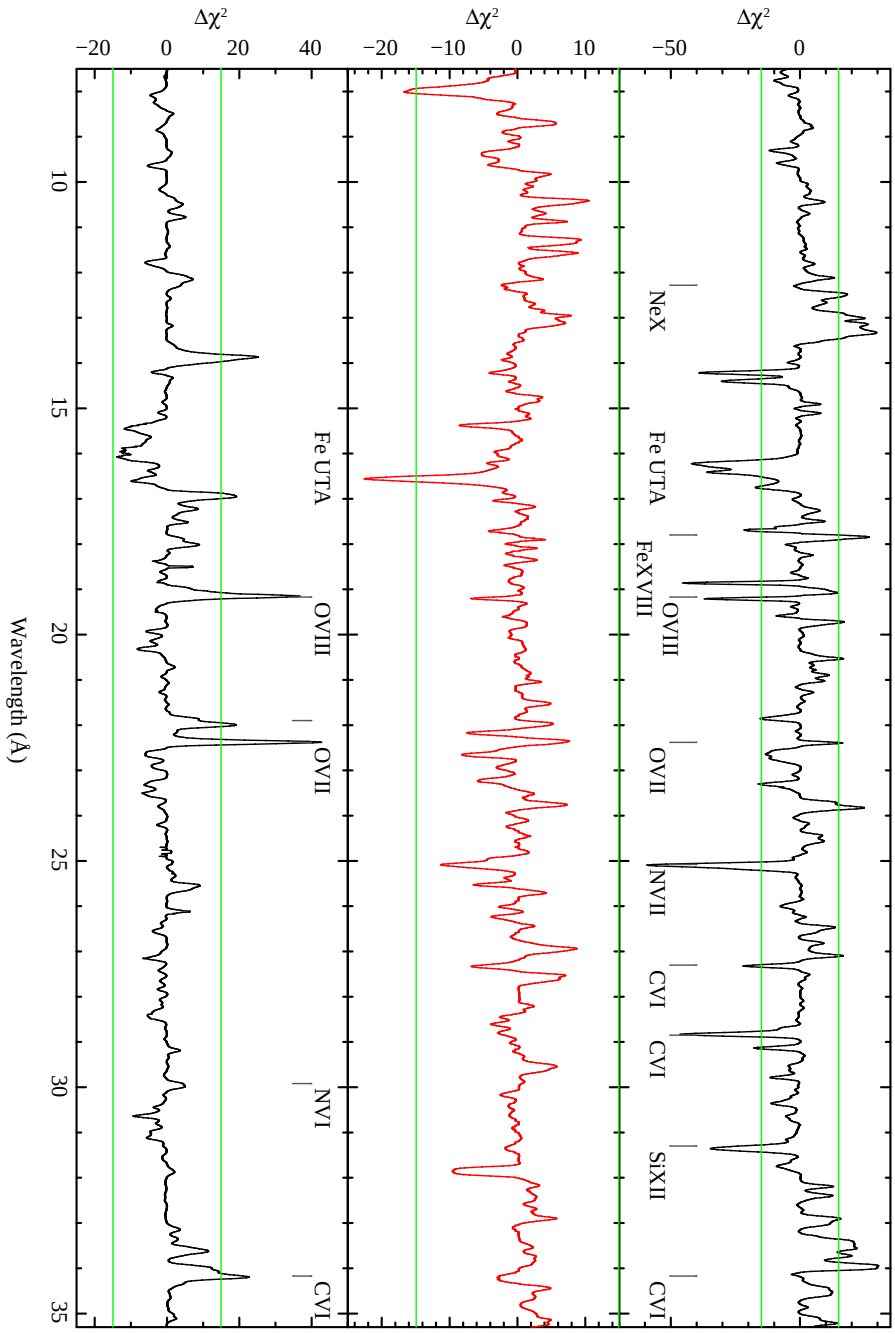

Fig. 4.6 Results of line scans to the new data (middle) as well as the highest (top) and lowest (bottom) flux archival observations. The green lines show the 95 % confidence interval for a blind search.

Table 4.3 Narrow features in archival RGS spectra. Line wavelengths and transition levels are values from the APEC database. Redshifts are given in the observer's frame (Mrk 766 is at $z = 0.0129$).

Low state – emission

Species		Rest wavelength/Å	Redshift
CVI	$2p^1 - 1s^1$	33.736	$0.0130^{+0.0008}_{-0.0021}$
NVI	$1s^1 2s^1 - 1s^2$	29.534	$0.0121^{+0.0009}_{-0.0004}$
OVII	$1s^1 2s^1 - 1s^2$	22.098	$0.0128^{+0.0006}_{-0.0006}$
OVIII	$2p^1 - 1s^1$	18.969	$0.0099^{+0.0012}_{-0.0010}$

High state – absorption

Species		Rest wavelength/Å	Redshift
NeX	$1s^1 - 2p^1$	12.134	$0.0126^{+0.0017}_{-0.0014}$
NVII	$1s^1 - 2p^1$	24.781	$0.0132^{+0.0009}_{-0.0031}$
CVI	$1s^1 - 4p^1$	26.990	$0.0124^{+0.0004}_{-0.0006}$
CVI	$1s^1 - 2p^1$	33.736	$0.0117^{+0.0005}_{-0.0004}$

absorbing material may not be identical in the *XMM-Newton* and *NuSTAR* exposures, the features found in the archival observations provide a guide from which to start modelling the latest data. Results of these line scans are shown in Fig. 4.6. Where a feature has a single most likely associated transition, we fit with a Gaussian to find the redshift of the feature. Results are shown in table 4.3. The lines are consistent with being unresolved.

The previous low-flux observation shows several emission lines (Table 4.3). The ionisation states of the observed lines suggest an ionisation parameter of $\log(\xi/\mathrm{erg\,cm\,s^{-1}}) \sim 1.5$. Warm emission in AGN is usually predominantly photoionised (e.g. Guainazzi and Bianchi, 2007) and the high strength of the OVII forbidden line relative to the corresponding recombination line in this case supports this. Most of the lines are consistent with being in the rest frame of Mrk 766, but the most highly ionised OVIII line is bluer, with a redshift corresponding to a projected outflow of $900^{+300}_{-350}\,\mathrm{km\,s^{-1}}$. We also note that the NVI line is larger than would be predicted based on Solar abundances. This is not unexpected as overly strong NVI lines have also been found in NGC 3516 (Turner et al., 2003).

In contrast, the high-flux spectrum principally shows absorption features (Table 4.3), with OVII the only previously identified emission line still seen in emission (the other emission lines are likely not visible due to their small equivalent width). Narrow features are present at wavelengths expected of CVI, NVII, and NeX.

Since detailed modelling of the warm absorber is not the primary focus of this work, we do not attempt to fit the archival observations but fit the new observations with photoionisation models including the detected features. We use the photoionisation model `XSTAR` (Kallman

and Bautista, 2001) and, for computational efficiency, fit using tables, which we compute for an appropriate region of parameter space.

Fitting the new observation with several warm-absorber components, we find that two ionisation states are sufficient (χ^2/d.o.f. $= 1040/982 = 1.06$). With only one rather than two absorbing components, the fit is significantly worse ($\Delta\chi^2 = 36$ for 2 fewer degrees of freedom), as the absorption around the iron unresolved transition array (UTA) region (~ 17 Å) is not sufficiently broad. Three absorbers provide insignificant improvement ($\Delta\chi^2 = 1.1$ for 2 additional degrees of freedom). It is likely that this two-component absorber represents a more complicated region of gas, but this parametrisation is sufficient to describe the absorber well enough to allow broadband continuum fitting.

When modelling the full dataset, we freeze the redshifts to appropriate values due to the large amount of low resolution data, which can drive the fitted redshift away from the values derived from the narrow RGS features. We fix the redshift of the warm absorbers to a value consistent with all the features observed in the high-flux spectrum, $z = 0.0118$. Since the OVIII line is not detected in the new observation, we model the line emission with a single component of photoionised gas at a redshift consistent with the OVII line.

4.3.3 Broadband fits

With a description of both the high-energy excesses and the warm absorber separately, we now perform a broadband fit to find a consistent model of the high and low energy features of the spectra. We include all data from *NuSTAR*, *Swift*, *XMM-Newton*-pn and *XMM-Newton*-RGS.

Reflection models

We first consider the reflection interpretation of the iron line and Compton hump. Combining the components found in each energy band results in a model of the form `TBnew* (warmabs(1) * warmabs(2) * relxill + photemis)`.

Fits to each observation separately are given in Table 4.4. The parameters are largely consistent with those found in the individual band models.

The *XMM-Newton*/*NuSTAR* observation shows evidence of more emission coming from very close to the black hole than the *Swift*/*NuSTAR* observation. This is reflected in the emissivity index and reflection fraction being higher, which can both be induced by light-bending of radiation from a corona close to the black hole (Miniutti and Fabian, 2004).

The *Swift*/*NuSTAR* observation does not constrain the black hole spin, whereas the *XMM-Newton*/*NuSTAR* observation prefers $a > 0.87$. The much stronger constraint in the *XMM-Newton*/*NuSTAR* observation is largely due to the much greater soft-band (<10 keV)

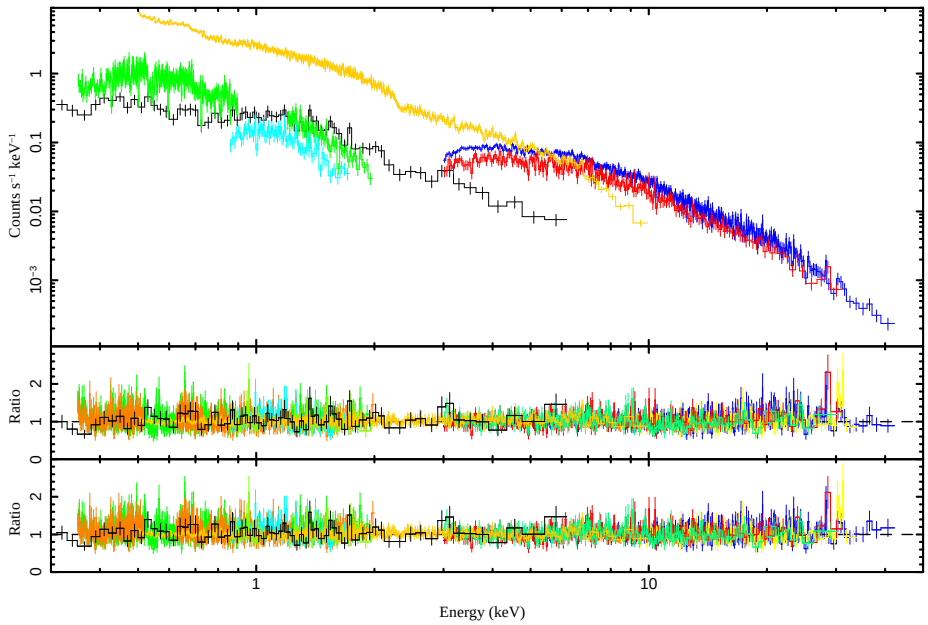

Fig. 4.7 Data and residuals of best fitting broadband models. Top: data; middle: residuals for reflection model; bottom: residuals for partial covering model.

signal from the *XMM-Newton* coverage. The remaining parameters of this observation also suggest that more emission is from the innermost region, which is most sensitive to the spin. The spin constraint from the *XMM-Newton*/*NuSTAR* observation is significantly higher than the fit to the high energy data only ($a < 0.43$). This is likely to be because the spin measurement is significantly influenced by the shape of the soft excess and not just the profile of the iron line; the inconsistency could be due to other factors influencing the soft excess (as was found in e.g. Parker et al., 2018), such as the hybrid model discussed later.

The iron abundance of the *XMM-Newton*/*NuSTAR* observation is also higher. Since the material in the disc is not expected to change in the 6 months between observations, this is likely to be due to degeneracy with other parameters. If the difference is real, it could be caused by a higher iron abundance in the inner region of the disc, which the higher emissivity index suggests provides more of the reflected component in this observation. However, the data presented here are insufficient to prove this.

The cut-off of the powerlaw is too high to be measured with the current dataset and our lower limits are well outside the observed bandpass. The stronger limit for the *Swift*/*NuSTAR* observation is due to its greater high-energy signal from the longer *NuSTAR* exposure.

In order to improve constraints on the parameters of the model which do not change over the 6 month interval between the two observations and increase physical self-consistency, we also perform a joint fit with these parameters – black hole spin, a, accretion disc inclination, i, and iron abundance, $A_{\rm Fe}$ – tied between the two observations. Since the *Swift* spectrum does not significantly constrain the parameters of the absorption and emission, we also tie these parameters between the two observations. This fit is shown in Table 4.4 and Fig 4.7. The model spectrum is shown in Fig. 4.8. The parameters of this fit are largely consistent with the fits to the individual observations. Differences are likely due to parameter degeneracies which are not evident in single-parameter confidence intervals.

Partial covering models

We also make a broadband fit with a partial covering model of the form `TBnew * zpcfabs(1) * zpcfabs(2) * (warmabs(1) * warmabs(2) * cutoffpl + photemis)`. Parameters for this model are given in Table 4.5; residuals are shown in Fig. 4.7 and model spectra in Fig. 4.8.

While this produces an acceptable fit to the spectrum, some parameters are not physically likely. In particular, the high-energy cut-off of 22^{+7}_{-5} keV in the *Swift*/*NuSTAR* observation is much lower than is typically found in AGN (e.g. Fabian et al., 2015; Lubiński et al., 2016) and below the lowest found so far with *NuSTAR* data (42 ± 3 keV in Ark 564, Kara et al. 2017). The time-averaged *Swift*-BAT spectrum does not show such a low cut-off energy (e.g.

Table 4.4 Parameters of fits to all data from each observation with reflection model (`TBnew * (warmabs(1) * warmabs(2) * relxill + photemis)`). Unconstrained parameters are allowed to vary within the ranges: $-0.998 < a < 0.998$; $1 < \log(\xi/\mathrm{erg\,cm\,s^{-1}}) < 2.5$; and $N_\mathrm{H}/\mathrm{cm^{-2}} < 5\times10^{22}$, indicated in the table by square brackets.

Component	Model	Parameter	Separate		Joint	
			Swift/*NuSTAR*	*XMM*/*NuSTAR*	*Swift*/*NuSTAR*	*XMM*/*NuSTAR*
Relativistic reflection	(`relxill`)	Norm	$1.3\pm0.1\times10^{-4}$	$9.9^{+0.1}_{-0.3}\times10^{-5}$	$1.24^{+0.06}_{-0.04}\times10^{-4}$	$9.85^{+0.04}_{-0.05}\times10^{-5}$
		Emissivity Index	$2.3^{+0.7}_{-0.5}$	$3.3^{+0.4}_{-0.2}$	2.4 ± 0.2	$4.5^{+1.1}_{-0.4}$
		a	Unconstrained	>0.87	>0.92	
		$\theta/^\circ$	47^{+8}_{-4}	36^{+1}_{-2}	46^{+1}_{-4}	
		Γ	$2.28^{+0.08}_{-0.06}$	$2.22^{+0.02}_{-0.01}$	$2.17^{+0.01}_{-0.02}$	2.23 ± 0.02
		$\log(\xi/\mathrm{erg\,cm\,s^{-1}})$	$1.7^{+0.3}_{-0.4}$	1.4 ± 0.2	$1.9^{+0.1}_{-0.1}$	$1.33^{+0.03}_{-0.15}$
		A_Fe	$1.0^{+0.8}_{-0.2}$	$2.7^{+0.7}_{-0.6}$	$2.9^{+0.7}_{-0.4}$	
		E_cut/keV	>290	>530	>510	>740
		R	$1.4^{+0.5}_{-0.3}$	$1.8^{+0.4}_{-0.3}$	$0.9^{+0.2}_{-0.1}$	2.1 ± 0.4
Ionised absorption	(`warmabs`)	$N_\mathrm{H}/\mathrm{cm^{-2}}$	$<4.7\times10^{21}$	$2.0^{+0.6}_{-0.4}\times10^{21}$	$1.8^{+0.5}_{-0.4}\times10^{21}$	
		$\log(\xi/\mathrm{erg\,cm\,s^{-1}})$	$[1-2.5]$	$1.96^{+0.07}_{-0.04}$	$1.97^{+0.07}_{-0.06}$	
		$N_\mathrm{H}/\mathrm{cm^{-2}}$	$<4.9\times10^{21}$	$2.0\pm0.3\times10^{21}$	$2.1^{+0.3}_{-0.2}\times10^{21}$	
		$\log(\xi/\mathrm{erg\,cm\,s^{-1}})$	$[1-2.5]$	$1.31^{+0.05}_{-0.04}$	1.29 ± 0.04	
Ionised emission	(`photemis`)	Norm	<0.047	$2.6^{+0.4}_{-2.1}\times10^{-4}$	$2.5^{+0.5}_{-1.9}\times10^{-4}$	
		$N_\mathrm{H}/\mathrm{cm^{-2}}$	$[<5\times10^{22}]$	$<5\times10^{21}$	$[<5\times10^{22}]$	
		$\log(\xi/\mathrm{erg\,cm\,s^{-1}})$	$[1-2.5]$	1.5 ± 0.1	1.5 ± 0.1	
Cross-calibration constant		FPMA/XRT	$1.15^{+0.10}_{-0.08}$	-	1.14 ± 0.03	
		FPMB/XRT	$1.14^{+0.09}_{-0.08}$	-	1.13 ± 0.03	
		RGS1 order 1/PN	-	1.00 ± 0.02	1.00 ± 0.02	
		RGS2 order 1/PN	-	1.01 ± 0.02	1.01 ± 0.02	
		RGS1 order 2/PN	-	0.99 ± 0.04	0.99 ± 0.04	
		RGS2 order 2/PN	-	0.97 ± 0.04	0.97 ± 0.04	
		FPMA/PN	-	$1.15^{+0.03}_{-0.02}$	$1.15^{+0.02}_{-0.03}$	
		FPMB/PN	-	$1.13^{+0.03}_{-0.02}$	$1.13^{+0.02}_{-0.03}$	
	χ^2 (bins)				990 (884)	2262 (2202)
	χ^2/d.o.f.		$974.7/866=1.13$	$2238/2180=1.03$	$3252/3056=1.06$	

Table 4.5 Parameters of fits to all data from each observation with partial covering model (`TBnew * zpcfabs(1) * zpcfabs(2) * (warmabs(1) * warmabs(2) * cutoffpl + photemis)`). Unconstrained parameters are allowed to vary within the ranges: $1 < \log(\xi/\mathrm{erg\,cm\,s^{-1}}) < 2.5$; and $N_\mathrm{H}/\mathrm{cm^{-2}} < 5\times10^{22}$, indicated in the table by square brackets.

Component	Model	Parameter	Separate		Joint	
			Swift/*NuSTAR*	*XMM*/*NuSTAR*	*Swift*/*NuSTAR*	*XMM*/*NuSTAR*
Partial covering absorber	(zpcfabs)	$N_\mathrm{H}/\mathrm{cm^{-2}}$	$7.2^{+1.2}_{-1.1}\times10^{24}$	$5.5^{+1.3}_{-0.6}\times10^{24}$	$1.2^{+0.13}_{-0.1}\times10^{25}$	$5.2^{+1.2}_{-0.6}\times10^{24}$
		f_Cov	$0.64^{+0.03}_{-0.07}$	$0.51^{+0.05}_{-0.03}$	$0.69^{+0.05}_{-0.06}$	$0.51^{+0.05}_{-0.03}$
	(zpcfabs)	$N_\mathrm{H}/\mathrm{cm^{-2}}$	$6.2^{+0.7}_{-1.1}\times10^{23}$	$2.0^{+0}_{-0.2}\times10^{23}$	$1.0\pm0.15\times10^{24}$	$1.9^{+0}_{-0.2}\times10^{23}$
		f_Cov	$0.41^{+0.04}_{-0.03}$	$0.361^{+0}_{-0.003}$	0.43 ± 0.06	$0.356^{+0.018}_{-0.003}$
Primary cut-off powerlaw	(cutoffpl)	Norm	$0.052^{+0.014}_{-0.006}$	0.028 ± 0.001	0.06 ± 0.01	$0.0276^{+0.0001}_{-0.0023}$
		Γ	$2.14^{+0.10}_{-0.08}$	$2.33^{+0.02}_{-0.004}$	2.12 ± 0.06	2.33 ± 0.02
		E_Cut/keV	26^{+0}_{-6}	>190	22^{+7}_{-5}	>180
Ionised absorption	(warmabs)	$N_\mathrm{H}/\mathrm{cm^{-2}}$	$<8.8\times10^{21}$	$3.3^{+0}_{-0.2}\times10^{21}$	$3.16^{+0}_{-0.17}\times10^{21}$	
		$\log(\xi/\mathrm{erg\,cm\,s^{-1}})$	>1.2	$2.06^{+0.03}_{-0.05}$	$2.05^{+0.03}_{-0.05}$	
		$N_\mathrm{H}/\mathrm{cm^{-2}}$	$<4.6\times10^{21}$	$2.30^{+0}_{-0.06}\times10^{21}$	$2.29^{+0}_{-0.06}\times10^{21}$	
		$\log(\xi/\mathrm{erg\,cm\,s^{-1}})$	$[1-2.5]$	1.39 ± 0.03	$1.40^{+0.04}_{-0.05}$	
Ionised emission	(photemis)	Norm	$<1.1\times10^{-2}$	$3.4^{+0.6}_{-2.4}\times10^{-4}$	$1.6^{+0.3}_{-1.5}\times10^{-3}$	
		$N_\mathrm{H}/\mathrm{cm^{-2}}$	$[<5\times10^{22}]$	$<1.7\times10^{21}$	$<1.3\times10^{21}$	
		$\log(\xi/\mathrm{erg\,cm\,s^{-1}})$	>1.3	$1.55^{+0.07}_{-0.08}$	1.53 ± 0.08	
Cross-calibration constant		FPMA/XRT	$1.14^{+0.09}_{-0.08}$	-	$1.14^{+0.08}_{-0.05}$	
		FPMB/XRT	$1.13^{+0.09}_{-0.08}$	-	$1.13^{+0.08}_{-0.05}$	
		RGS1 order 1/PN	-	1.00 ± 0.02	0.96 ± 0.02	
		RGS2 order 1/PN	-	1.00 ± 0.02	0.95 ± 0.02	
		RGS1 order 2/PN	-	0.97 ± 0.04	0.92 ± 0.04	
		RGS2 order 2/PN	-	0.96 ± 0.04	0.93 ± 0.04	
		FPMA/PN	-	$1.12^{+0.02}_{-0.03}$	$1.12^{+0.02}_{-0.03}$	
		FMPB/PN	-	$1.10^{+0.02}_{-0.03}$	$1.10^{+0.02}_{-0.03}$	
	χ^2 (bins)				980 (884)	2339 (2202)
	χ^2/d.o.f.		$974.2/868 = 1.12$	$2297/2182 = 1.05$	$3319/3057 = 1.09$	

Ricci et al., 2017; Vasudevan et al., 2010), although the coronal temperature may change with time. This is corroborated by the low cut-off not being present in the *XMM-Newton*/*NuSTAR* observation, which is detected only up to 35 keV, below the far side of the Compton hump. Forcing the cut-off to be at least 100 keV results in a significantly worse fit ($\Delta\chi^2 = 18.5$ for one degree of freedom). The low cut-off value may be due to curvature from the high-energy side of the Compton hump being accounted for by an artificially low cut-off energy. A high column density component ($N_{\rm H} = 1.2^{+0.13}_{-0.1} \times 10^{25}\,{\rm cm}^{-2}$) is then required to produce the low-energy side of the Compton hump.

The large absorbing column density also implies a high unabsorbed luminosity: $L_{0.5-10\,{\rm keV}} = 7.5 \times 10^{43}\,{\rm erg\,s}^{-1}$ for the *Swift*/*NuSTAR* observation. This is not compatible with the bolometric luminosity of $10^{44}\,{\rm erg\,s}^{-1}$ found by SED fitting (Vasudevan et al., 2010) which must also include significant intrinsic disc emission.

Hybrid models

Further to the extreme scenarios in which only reflection or only absorption are responsible for the spectrum of Mrk 766, we consider a model which includes both of these effects. We use a model of the form `TBnew * zpcfabs(1) * (warmabs(1) * warmabs(2) * relxill + photemis)`. Due to the potential for strong degeneracy between the two possible causes (relativistic emission and partial covering absorption) for the spectral shape, we use Monte-Carlo methods to sample the parameter space. We use the XSPEC_EMCEE code[1]. We use 600 walkers and take probability densities from 10000 iterations after the chain has converged. Results are shown in table 4.6 and Fig. 4.9.

Note that we have shown the χ^2 value from direct minimisation for comparison with other models; the parameters from the two methods are consistent.

The reflection parameters found are largely consistent with those found for the pure reflection case, with less strict confidence limits. The iron abundance is somewhat lower, being slightly closer to Solar, and the reflection fraction of the *XMM-Newton*/*NuSTAR* observation is closer to unity. The constraint on the spin is significantly weaker. The parameters of the absorption are much less extreme than the pure partial covering model. We now find solutions with column densities $N_{\rm H} \simeq 10^{22-23}\,{\rm cm}^{-2}$, which is more reasonable given the lack of a strong narrow iron line, which would be expected with the higher columns required for the pure partial covering model. In general, the hybrid model requires less extreme parameters than either reflection or partial covering alone.

[1] Written by Jeremy Sanders, based on the EMCEE package (Foreman-Mackey et al., 2013).

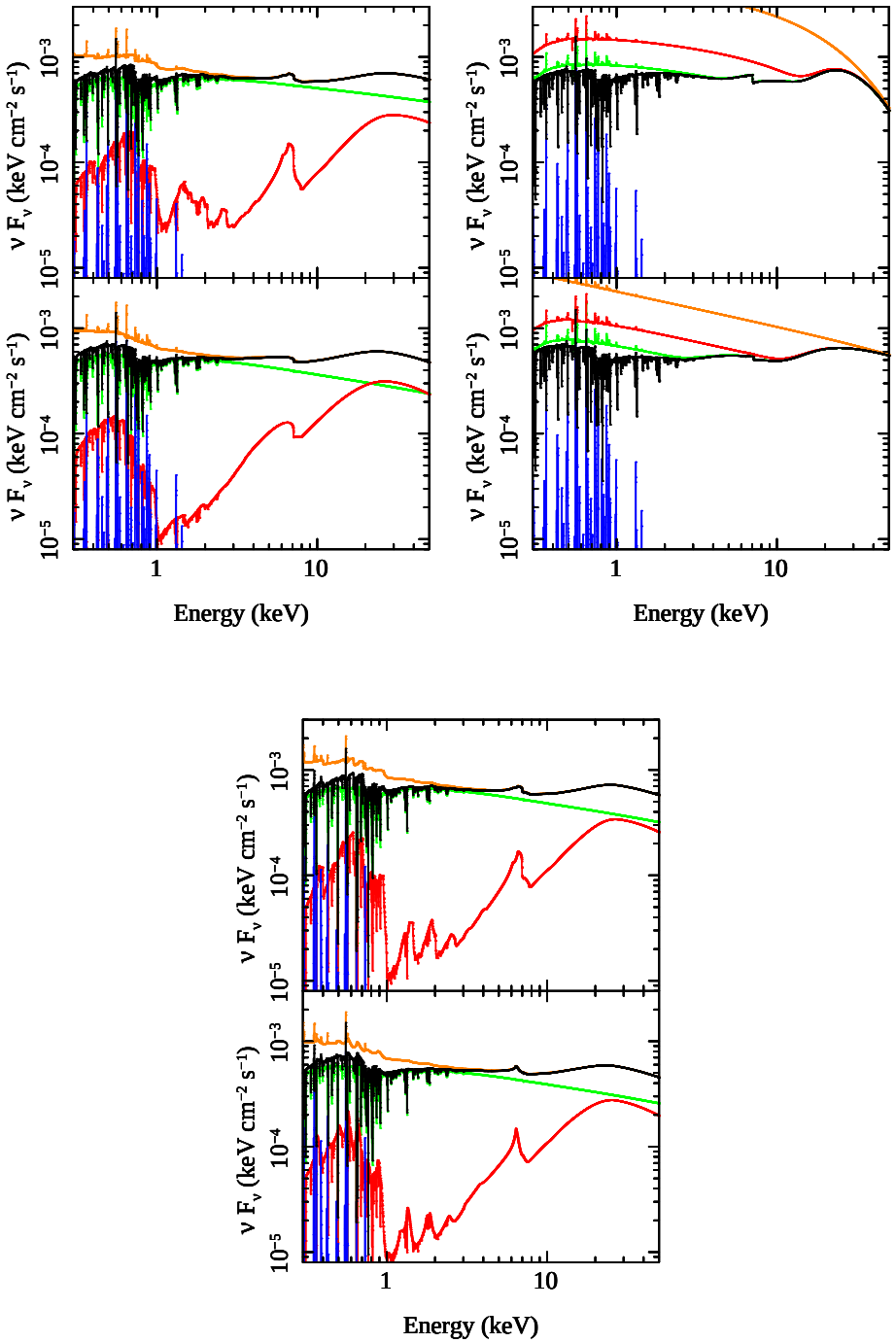

Fig. 4.8 Plot of models found for joint fit. Upper Left panels: reflection models; Upper Right panels: partial covering models; Lower panels: hybrid models. Top panels: *Swift*/*NuSTAR* observation; Bottom panels: *XMM-Newton*/*NuSTAR* observation. Black: total model; Orange: unabsorbed model; Blue: photoionised emission; Reflection/hybrid models: Green: powerlaw continuum; Red: reflected component. Partial covering models: Green: two partial covering components without ionised absorption; Red: one partial covering component.

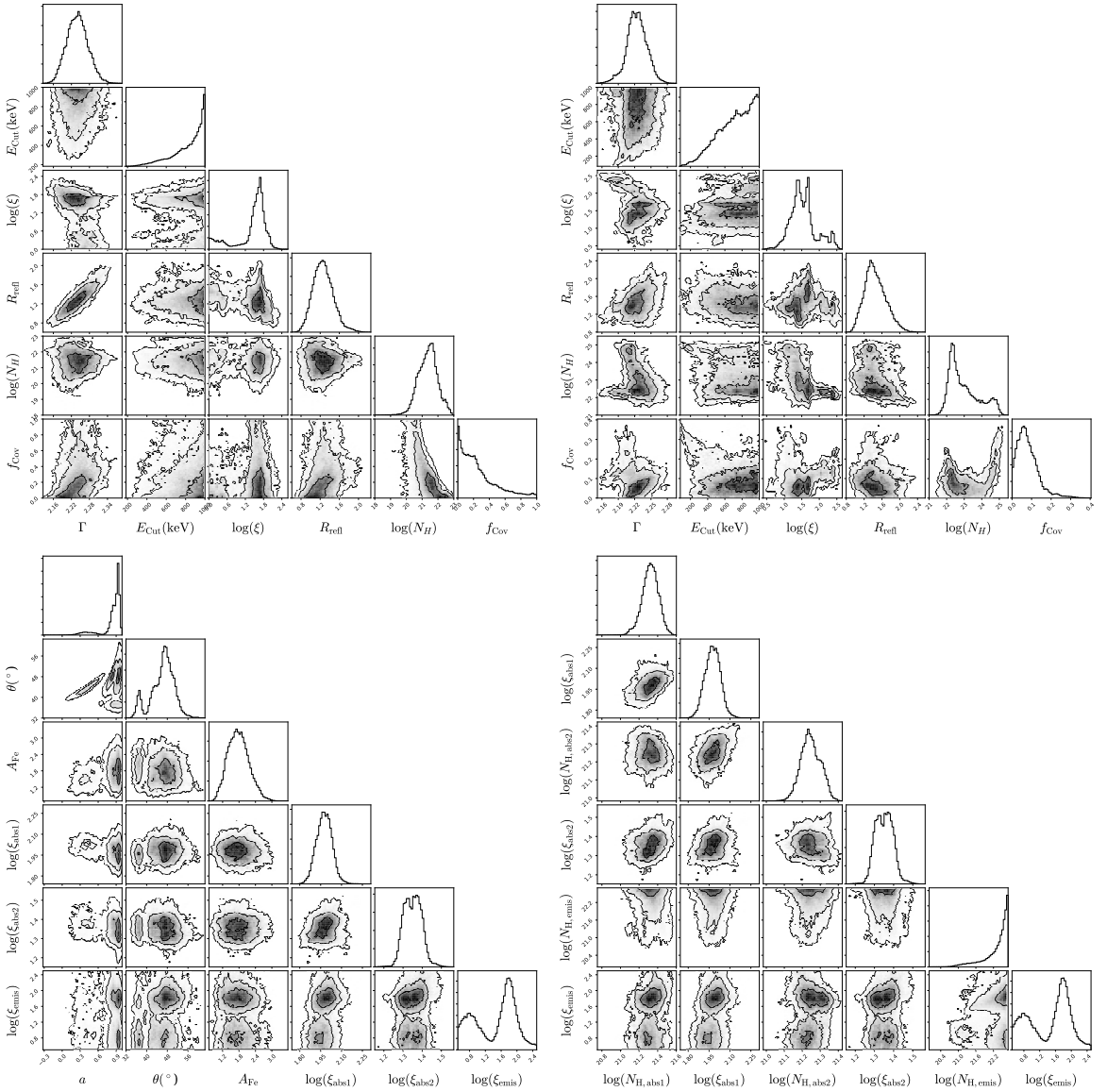

Fig. 4.9 Corner plots of MCMC parameter estimation for a hybrid model with reflection and partial covering. Parameters shown in each panel are: top left: *Swift*/*NuSTAR* observation; top right: *XMM-Newton*/*NuSTAR* observation; bottom left: parameters tied between observations; bottom right: warm absorption/emission. Column densities have units of cm^{-2}; ξ has units of $\mathrm{erg\,cm\,s}^{-1}$. Contours indicate 1,2, and 3σ intervals.

Table 4.6 Parameters of fits to all data from each observation with model including partial covering and reflection `TBnew * zpcfabs(1) * (warmabs(1) * warmabs(2) * relxill + photemis)`. Parameters given are the median of the posterior distribution; errors correspond to the central 90% of the MCMC posterior distribution. The χ^2 value refers to the value found by χ^2-minimisation. Unconstrained parameters are allowed to vary within the ranges: $1 < \log(\xi/\mathrm{erg\,cm\,s^{-1}}) < 2.5$; and $N_\mathrm{H}/\mathrm{cm}^{-2} < 5\times10^{22}$, indicated in the table by square brackets.

Component	Model	Parameter	Joint	
			Swift/*NuSTAR*	*XMM*/*NuSTAR*
Relativistic reflection	(`relxill`)	Norm	$1.30\pm0.04\times10^{-4}$	$1.02^{+0.06}_{-0.03}\times10^{-4}$
		Emissivity Index	$2.2^{+0.4}_{-0.6}$	$5.5^{+1.7}_{-1.0}$
		a	>0.4	
		θ	47^{+6}_{-10}	
		Γ	2.24 ± 0.06	2.22 ± 0.03
		$\log(\xi/\mathrm{erg\,cm\,s^{-1}})$	$1.6^{+0.4}_{-1.4}$	$1.5^{+0.8}_{-0.5}$
		A_Fe	$1.8^{+0.7}_{-0.6}$	
		E_cut	>490	>350
		R	$1.25^{+0.4}_{-0.3}$	$1.4^{+0.4}_{-0.3}$
Partial covering absorption	(`zpcfabs`)	$N_\mathrm{H}/\mathrm{cm}^{-2}$	$<2.3\times10^{22}$	$5^{+500}_{-1}\times10^{22}$
		f_Cov	<0.75	$0.07^{+0.12}_{-0.06}$
Ionised absorption	(`warmabs`)	$N_\mathrm{H}/\mathrm{cm}^{-2}$	$2.1^{+0.8}_{-0.6}\times10^{21}$	
		$\log(\xi/\mathrm{erg\,cm\,s^{-1}})$	1.98 ± 0.09	
		$N_\mathrm{H}/\mathrm{cm}^{-2}$	$1.8^{+0.4}_{-0.3}\times10^{21}$	
		$\log(\xi/\mathrm{erg\,cm\,s^{-1}})$	1.35 ± 0.07	
Ionised emission	(`photemis`)	Norm	$1.2^{+0.3}_{-0.8}\times10^{-5}$	
		$N_\mathrm{H}/\mathrm{cm}^{-2}$	$[<5\times10^{22}]$	
		$\log(\xi/\mathrm{erg\,cm\,s^{-1}})$	$1.6^{+0.5}_{-1.0}$	
	χ^2 (bins)		979 (884)	2267 (2202)
	χ^2/d.o.f.		$3246/3052 = 1.06$	

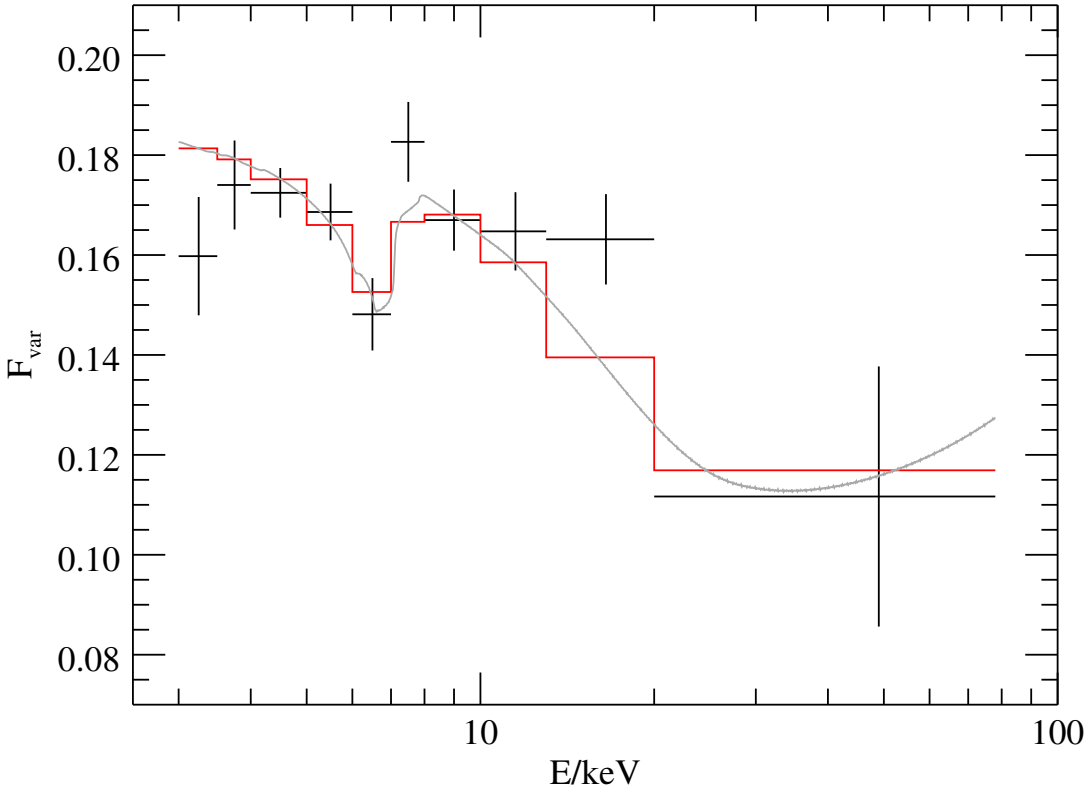

Fig. 4.10 The fractional excess variance for Mrk 766 computed using the entire light curve of the longer observation in time bins of 400 s. The variability drops in the iron K and Compton hump regions. This can be explained by a variable continuum and a constant reflection component (grey; binned to data resolution in red).

4.3.4 Variability

To characterize the rapid variability in this source, we compute the fractional excess variance in the *NuSTAR* spectrum, binned to 400 s, using the prescription in Edelson et al. (2002) with errors from the formula in Vaughan et al. (2003a). We use the fractional variability rather than Fourier methods owing to the former's insensitivity to the orbital gaps in *NuSTAR* observations (e.g. Nandra et al., 1997a). The shorter *XMM-Newton*/*NuSTAR* observation only has enough signal to produce two energy bins, which are broadly consistent with the results from the longer observation, so we only present detailed results from the longer observation here (Fig. 4.10).

The variability appears reduced in the $6-7$ keV band, the rest energy of iron K, and above 10 keV, where the Compton reflection hump provides significant flux in the mean

spectrum. Overall, the decrease in variability on short timescales appears to follow the profile of the relativistic reflection features, which suggests that the reflection component does not vary as much as the continuum emission in Mrk 766. This is reminiscent of previous spectral-timing results of MCG–6-30-15 that also showed that the continuum varies more than the ionised reflection (Fabian and Vaughan, 2003; Marinucci et al., 2014; Vaughan et al., 2003b). The increase in variability in the $7-8$ keV bin may be due to variable blueshifted absorption (Parker et al., 2017a; Risaliti et al., 2011).

We can test whether this $F_{\rm Var}$ spectrum is compatible with a variable continuum and less variable reflection by considering the extreme case in which the reflection is constant, so only the power law varies. Denoting the mean reflected flux as $f_{\rm R}(E)$, the mean continuum as $f_{\rm C}(E)$ and the variance as $\alpha^2 f_{\rm C}^2$ (i.e. the variability is a constant multiple of the continuum flux), the fractional variability is simply

$$F_{\rm Var}(E) = \alpha \frac{f_{\rm C}(E)}{f_{\rm C}(E) + f_{\rm R}(E)}.$$

Thus, higher α leads to higher $F_{\rm Var}$ while the shape of $F_{\rm Var}$ is set by the shape of the reflected spectrum, which we take from the fit to the mean spectrum. We may then substitute for the mean fluxes found in our fits to the mean spectrum and fit the observed $F_{\rm Var}(E)$ values (by χ^2-minimisation) to find α. This gives an acceptable fit, $\chi^2/\text{d.o.f.} = 16/9$, $p = 0.07$.

In the partial covering scenario, the > 20 keV bin shows intrinsic continuum variability (since there is little absorption at these energies) while the greater variability at lower energies is due to variable absorption strength or continuum pivoting. We do not attempt to fit this as covariance between different variability mechanisms rapidly introduces more free parameters than can be constrained by the available data.

4.4 Discussion

4.4.1 The reflection model

We note that the presence of distant cold reflection is not required in either observation. This may be due to the relativistic reflection already including a significant component of weakly blurred reflection from a low emissivity index (2.4 ± 0.2 in the *Swift*/*NuSTAR* observation). The lack of a distinct distant component could also be due to absorption reducing the X-ray flux to distant regions of the disc and to the torus, weakening the cold reflection. Since the warm absorber in our line of sight ($\sim 50^\circ$ from the disc plane) has only a small effect on the transmitted flux, this mechanism would require more absorption in the line of sight of

the outer disc and torus. Such absorption would also reduce the correlation between X-ray emission and reprocessing from the disc, consistent with the non-detection of correlated UV/X-ray lags in Buisson et al. (2017). The warm absorption also complicates the spectrum, increasing the uncertainty on the amount of cold reflection and so reducing the significance of any detection.

The lower limit on the cut-off of the primary continuum is higher than is typically found in AGN (Fabian et al., 2015; Lubiński et al., 2016). However, the limit presented here is far outside the *NuSTAR* bandpass so is strongly affected by the shape of the reflected part of the spectrum rather than being a direct measurement of the cut-off (García et al., 2015). Due to the complex absorption in Mrk 766, these features are harder to accurately isolate and so the cut-off may be significantly lower than the statistical limit presented here. The difference in curvature below the cut-off energy between a cut-off powerlaw and a true Comptonisation spectrum may also allow for a lower coronal temperature (Fürst et al., 2016b).

4.4.2 Comparison with a similar source, MCG–6-30-15

MCG–6-30-15 is a very well studied AGN with similar spectral appearance to Mrk 766 (and similar Principal Components of variability, Parker et al. 2015a); we therefore compare our interpretations with those found for MCG–6-30-15. Marinucci et al. (2014) study spectral variability in the available *NuSTAR* data, considering both reflection and partial covering models. The higher count rate of MCG–6-30-15 allows the observation to be cut into 11 sections. In the reflection interpretation, $a = 0.91^{+0.06}_{-0.07}$, $i = 33 \pm 3^{\circ}$, similar to values found here and in previous works for Mrk 766 (e.g. Branduardi-Raymont et al., 2001).

A detailed analysis of grating spectra of MCG–6-30-15 from RGS by Sako et al. (2003); Turner et al. (2004) and from *Chandra* by Holczer et al. (2010) shows two intrinsic absorption systems with distinct velocities, outflowing at 100 ± 50 and $1900 \pm 150\,\mathrm{km\,s^{-1}}$. The absorption considered in our model is comparable to the lower speed component (in our case with fixed outflow velocity of $350\,\mathrm{km\,s^{-1}}$ based on archival line positions) while the fast component in MCG–6-30-15 is too highly ionised ($\log(\xi/\mathrm{erg\,cm\,s^{-1}}) = 3.82 \pm 0.03$) to have a noticeable effect in the short RGS exposure studied here.

The slow component in MCG–6-30-15 has an ionisation parameter ranging from $\log(\xi/\mathrm{erg\,cm\,s^{-1}}) = -1.5$ to $\log(\xi/\mathrm{erg\,cm\,s^{-1}}) = 3.5$, while the two ionisations we consider have $\log(\xi/\mathrm{erg\,cm\,s^{-1}}) \sim 1.3$ and 1.9. Holczer et al. (2010) also find little gas with $0.5 < \log(\xi/\mathrm{erg\,cm\,s^{-1}}) < 1.5$ so our component with $\log(\xi/\mathrm{erg\,cm\,s^{-1}}) \sim 1.3$ may reflect a mixture of more and less ionised gas. This is plausible since the CCD spectra of MCG–6-30-15 may be described with a two-state warm absorber with ionisation parameters of $\log(\xi/\mathrm{erg\,cm\,s^{-1}}) \simeq 2$ and $\log(\xi/\mathrm{erg\,cm\,s^{-1}}) = 1.15 - 1.65$ (Marinucci et al., 2014).

Emmanoulopoulos et al. (2011) find soft lags in the X-ray light curves of both Mrk 766 and MCG–6-30-15 (as do Kara et al. 2014b), which are interpreted as arising from the delay of reflected emission. Parker et al. (2014a) study the variability of MCG–6-30-15 with Principal Component Analysis (PCA), finding that the variability is consistent with that expected from an intrinsically variable X-ray source with less variable relativistic reflection. This is corroborated by Miniutti et al. (2007), who calculate the RMS (fractional variability) spectrum of a *Suzaku* observation of MCG–6-30-15, which has a similar shape to the short timescale $F_{\rm Var}$ spectrum found here. This could arise from a vertically extended or two component corona, in which, due to strong light bending, the lower portion principally illuminates the disc while the upper region is responsible for the majority of the direct emission. This would also decorrelate the observed X-ray emission from any UV variability which is driven by disc heating, agreeing with the lack of correlation seen in these two sources (Buisson et al., 2017). In the observations presented here, Mrk 766 remains in a high state, so it is hard to find evidence of coronal extension from variability.

4.4.3 Distinguishing absorption from reflection

While variable partial covering absorption and reflection both provide acceptable fits to the data, the reflection model is favoured for the following reasons:

- the partial covering model gives a high unabsorbed luminosity ($L_{0.5-10\,\rm keV} = 7 \times 10^{43}\,\rm erg\,s^{-1}$), which is incompatible with previous directly integrated measurements of the bolometric luminosity (Vasudevan et al., 2010).
- the high-energy continuum cut-off of 22^{+7}_{-5} keV is very low in the partial covering model of the *Swift*/*NuSTAR* observation (although some recent *NuSTAR* observations have found low cut-offs in other sources, e.g. 53^{+11}_{-8} keV, Tortosa et al. 2017; 42 ± 3 keV, Kara et al. 2017);
- the PCA analysis in Parker et al. (2015a) shows that Mrk 766 varies in the same way as MCG–6-30-15, showing the behaviour of a source whose variability is explained well by relativistic reflection from a vertically extended corona;
- the fractional variability spectrum shows a clear dip in the shape of the iron line, as would be produced by a variable continuum and less variable reflection.

4.5 Conclusions

We have presented two new observations of Mrk 766 taken by *NuSTAR*, providing a detailed view of its hard X-ray spectrum. With simultaneous coverage in soft X-rays by *XMM-Newton* or *Swift*, we are able to exploit the high spectral resolution of *XMM-Newton*-RGS to take account of warm absorption and so produce better constraints on the broadband spectrum.

We can model the spectrum with reflection or partial covering to generate the iron K feature and Compton hump. In the reflection model, the system has a high spin black hole ($a > 0.92$) viewed at intermediate inclination ($i = 46^{+1}_{-2}\,^{\circ}$). The best-fitting partial covering model is questionable as it requires a very low cut-off energy and the intrinsic X-ray luminosity is high compared to the bolometric luminosity. A hybrid model including reflection and partial covering allows less extreme conditions for each component of the model.

Chapter 5

Coronal temperatures of the AGN ESO 103–035 and IGR 2124.7+5058 from *NuSTAR* observations

Abstract

We present measurements of the coronae of two AGN from hard X-ray observations made with *NuSTAR*: ESO 103–035, a moderately to highly obscured source with significant reflection; and IGR 2124.7+5058, a radio-loud source with a very hard spectrum. Using an exponentially cut-off powerlaw model for the coronal emission spectrum gives a high-energy cut-off of 100^{+90}_{-30} keV for ESO 103–035 and 80^{+11}_{-9} keV for IGR 2124.7+5058, within the typical range for AGN. Fitting with physical Comptonisation models shows that these correspond to a temperature of 22^{+19}_{-6} and 20^{+3}_{-2} keV respectively. These values are consistent with pair production limiting the coronal temperature.

5.1 Introduction

Active Galactic Nuclei (AGN) are powered by accretion onto a supermassive black hole (SMBH), converting gravitational potential energy to radiation across the electromagnetic spectrum. Due to the shape of the gravitational potential well, the majority of the energy is released in the innermost few gravitational radii ($r_g = GM_{\rm BH}/c^2$). Localised to this region is the X-ray emitting corona, which Compton scatters incident optical and UV photons to X-ray energies (e.g. Haardt and Maraschi, 1991) and is typically regarded as a region of electron pair plasma.

The X-ray spectrum of emission from the corona may be approximated by a powerlaw up to some cut-off energy where emission quickly rolls over (Rybicki and Lightman, 1979). The index of this powerlaw and the energy at which the cut-off occurs are then the primary observable characteristics from which conditions in the corona may be inferred.

Since the high-energy cut-off occurs when the electrons are no longer able to add energy to the photons in an interaction, its value is governed by the electron temperature (if the particles in the corona have a roughly thermal spectrum). If the cut-off is modelled as an exponential suppression of the emission ($N(E) \propto E^{-\Gamma} e^{-E/E_{\rm Cut}}$), the value inferred is around 2–3 times the temperature (Petrucci et al. 2001, where energy and temperature are expressed in the same units by $E = k_{\rm B}T$).

Table 5.1 List of observations of ESO 103–035 and IGR 2124.7+5058. Exposure is the mean good exposure per FPM, as used for spectral fitting.

ESO 103–035

Campaign	*NuSTAR*			*Swift*	
	OBSID	Start date	Exposure	*Swift* OBSIDs	Exposure
EGS	60061288002	2013-02-25	27.3	00080219001	6.7
Cycle 3	60301004002	2017-10-15	42.5	00088112001	1.9

IGR 2124.7+5058

Campaign	*NuSTAR*			*Swift*	
	OBSID	Start date	Exposure	*Swift* OBSIDs	Exposure
EGS	60061305002	2014-12-13	23.9	00080273001/2	6.8
Cycle 3	60301005002	2018-01-02	40.2	00088113001/2/3	4.0

The hard X-ray surveys performed by *INTEGRAL* (Malizia et al., 2014) and *Swift*-BAT (Ricci et al., 2017; Vasudevan et al., 2013) have shown that this cut-off is typically around a few hundred keV: Malizia et al. (2014) find a median of 128 keV and a standard devation of 46 keV; Ricci et al. (2017) find a median of 200 ± 29 keV. The cut-off energy also seems to decrease with Eddington rate (Ricci et al., 2018).

The mechanism by which the coronal temperature is regulated is, however, still an open question. One possibility is (electron) pair production in photon-photon collisions, the rate of which increases rapidly above a certain temperature. This provides many more particles to share the energy and so makes further temperature increase difficult (Bisnovatyi-Kogan et al., 1971; Guilbert et al., 1983; Svensson, 1982, 1984). This temperature then acts as an effective upper limit for the electron temperature. This possibility was explored in Fabian et al. (2015) and found to be reasonable: sources were seen to have temperatures close to the limit imposed by pair production.

Observations from *NuSTAR* (Harrison et al., 2013) are able to refine this picture: owing to its ability to focus hard (up to 78 keV) X-rays, *NuSTAR* allows more precise measurements to be made of dimmer sources with shorter observations. This increased signal also allows the effect of degeneracy between curvature due to the cut-off and due to reflection to be reduced.

Here, we present new studies of the coronae of two AGN, ESO 103–035 and IGR 2124.7+5058, from recent *NuSTAR* observations.

5.1.1 ESO 103–035

ESO 103–035 ($z = 0.013$) is an optical Seyfert 2 galaxy (Véron-Cetty and Véron, 2006) initially detected in X-rays with HEAO-A2 (Marshall et al., 1979; Phillips et al., 1979).

EXOSAT observations showed absorption with variability by almost a factor of 2 in column density over 90 days, from 1.7 to $1.0 \times 10^{23}\,\mathrm{cm}^{-2}$ (Warwick et al., 1988). ESO 103–035 was also observed with *BeppoSAX*, in October of 1996 and 1997 (Akylas et al., 2001; Wilkes et al., 2001), again finding significant absorption ($N_\mathrm{H} = 1.79 \pm 0.09 \times 10^{23}\,\mathrm{cm}^{-2}$) and also an iron-K emission line. Wilkes et al. (2001) additionally find an iron absorption edge and a low cut-off ($29 \pm 10\,\mathrm{keV}$).

Furthermore, the galaxy contains a nuclear maser source (Bennert et al., 2004) and the black hole mass has been estimated as $M_\mathrm{BH} = 10^{7.1\pm0.6}\,\mathrm{M}_\odot$ (Czerny et al., 2001).

The Galactic absorption column is modest, $N_\mathrm{H,Gal} = 4.56 - 6.81 \times 10^{20}$ (Kalberla et al., 2005), $6.42 - 7.86 \times 10^{20}\,\mathrm{cm}^{-2}$ (Dickey and Lockman, 1990).

5.1.2 IGR 2124.7+5058 (4C 50.55)

IGR J21247+5058 (4C 50.55, $z = 0.02$, Masetti et al. 2004) is a bright radio loud Seyfert 1 galaxy. Optical studies of this source have been challenging due to its alignment with a Galactic star (Masetti et al., 2004).

Several X-ray missions have observed IGR 2124.7+5058. Molina et al. (2007) analyse *XMM-Newton* data, finding significant absorption (up to $10^{23}\,\mathrm{cm}^{-2}$) and weak reflection. Combining the *XMM-Newton* data with *INTEGRAL* data constrains the high-energy cut-off to $E_\mathrm{Cut} = 100^{+55}_{-30}\,\mathrm{keV}$. The addition of *Swift*-BAT data refines this to $79^{+23}_{-15}\,\mathrm{keV}$.

Tazaki et al. (2010) apply Comptonisation models to *Suzaku* observations, finding $\tau_\mathrm{e} \sim 3$ and $kT_\mathrm{e} \sim 30\,\mathrm{keV}$. Their modelling of the Fe K-α line finds an inner disc radius $R_\mathrm{in} \sim 700\,r_\mathrm{g}$, which they explain by the inner disc being either truncated or covered by the corona. The flux is stable throughout most of the 170 ks observation but increases by 30 % below 10 keV in the last 20 keV.

IGR 2124.7+5058 is a radio-loud source, so it is possible that the X-ray spectrum includes a contribution from a jet. Tazaki et al. (2010) calculate the likely contribution based on the radio to gamma-ray SED and conclude that any contribution is between 10^{-4} and 10^{-1} of the X-ray power in observations of similar flux to those analysed here.

The Galactic absorption to IGR 2124.7+5058 is significant, being measured at $N_\mathrm{H,Gal} = 0.855 - 1.16 \times 10^{22}$ (Kalberla et al., 2005), $1.02 - 1.39 \times 10^{22}\,\mathrm{cm}^{-2}$ (Dickey and Lockman, 1990). Since the total absorption to IGR 2124.7+5058 is higher still and the redshift is low, differences in Galactic emission are degenerate with intrinsic absorption, so we fix Galactic absorption to $10^{22}\,\mathrm{cm}^{-2}$.

5.2 Observations and Data Reduction

There are two *NuSTAR* observations of each source, separated by several years; each observation has a simultaneous *Swift* snapshot (see Table 6.1). For each source, one observation was made as part of the *NuSTAR* Extragalactic Survey (EGS) and one as a Cycle 3 Guest Observer target; we therefore refer to the observations as 'EGS' and 'Cycle 3'.

We reduced the *NuSTAR* data with NuSTARDAS version 1.8.0 and CALDB version 20171002. We produced clean event files using NUPIPELINE, choosing filtering options for the SAA based on the online background reports. In each case the option which gave the greatest exposure while removing periods of elevated background was SAACALC=2 SAAMODE=OPTIMIZED TENTACLE=YES. Spectra and associated response files were produced using the NUPRODUCTS command, with a 60 arcsec radius circular source region and a 90 arcsec radius circular background region from a source free area of the same chip (the largest such region available).

The *Swift*-XRT data were reduced using the online *Swift*-XRT products generator[1], as described in Evans et al. (2009). We extracted the mean spectrum of the *Swift* observation(s) associated with each *NuSTAR* observation (see Table 6.1).

For ESO 103–035, the high absorption column means that the XRT data provide little signal below 3 keV (only one bin with the grouping used) and the greater effective area of *NuSTAR* means this data dominates above 3 keV, so we do not use XRT data in spectral fits of ESO 103–035.

We also compare with the *Swift*-BAT data of the sources. We use the spectra from the 105 month catalogue[2] (Oh et al., 2018) and light curves from the transient monitor[3] (Krimm et al., 2013).

Spectra from all instruments (apart from *Swift*-BAT) were grouped to a signal to noise level of 6. Fits were made in ISIS Version 1.6.2-42 (Houck and Denicola, 2000); errors are given at the 90% level. We use the elemental abundances of Wilms et al. (2000) with cross sections from Verner et al. (1996).

5.3 Results

We begin by producing a light curve and hardness ratio for each source (Fig. 5.1). While both sources have changed in flux between their two observations, the light curves show little variability within an observation for IGR 2124.7+5058 and moderate slow variability

[1] www.swift.ac.uk/user_objects
[2] swift.gsfc.nasa.gov/results/bs105mon/
[3] swift.gsfc.nasa.gov/results/transients/

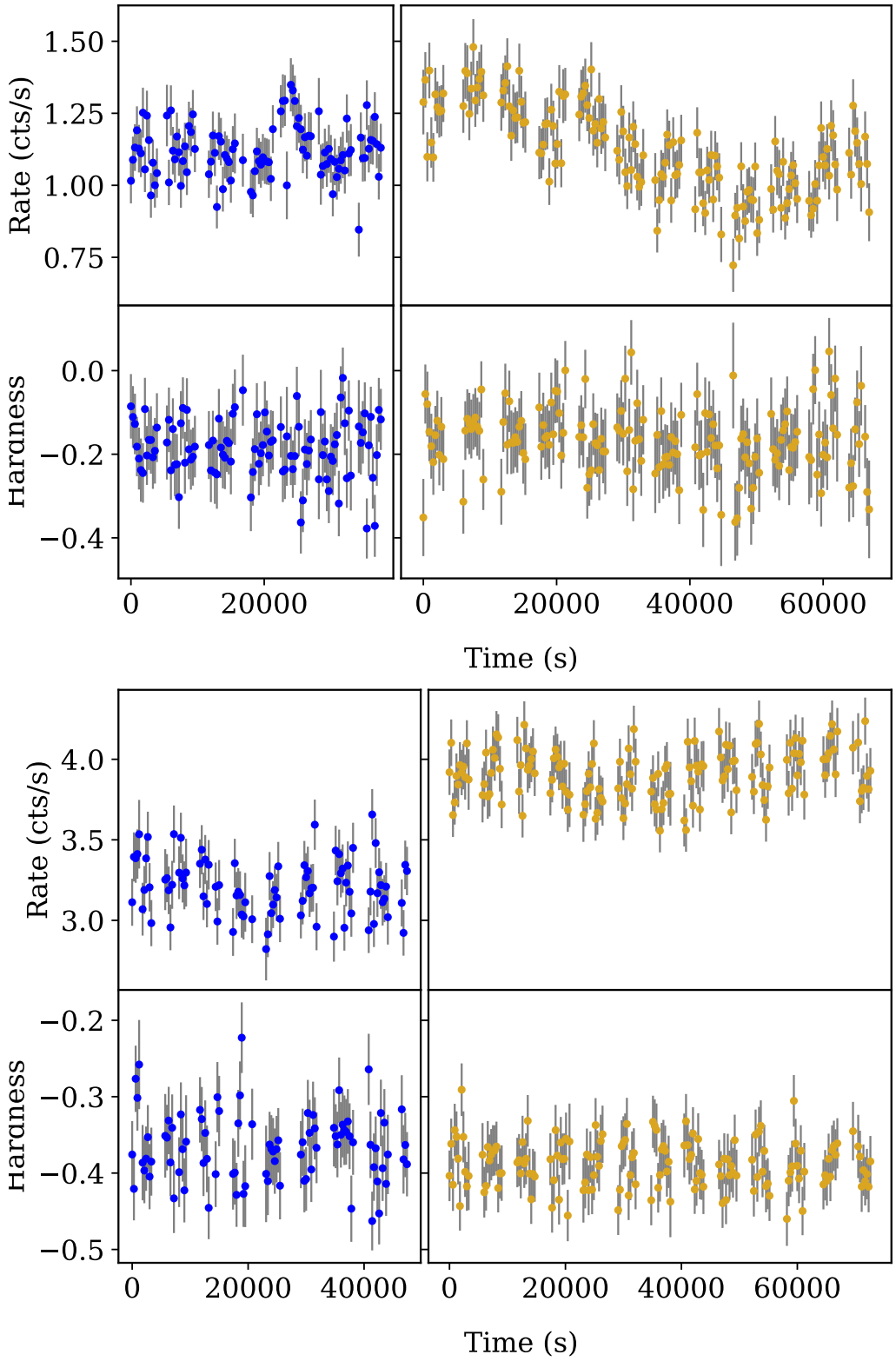

Fig. 5.1 *NuSTAR* (FPMA) light curve and hardness ratio with 300 s bins for ESO 103–035 (left) and IGR 2124.7+5058 (right). The first (blue) curve for each source shows the EGS observation, the second (yellow) cycle 3. The rate is given for $3-78$ keV. Hardness is defined as $(H-S)/(H+S)$, where H is $10-50$ keV rate and S is $3-10$ keV rate.

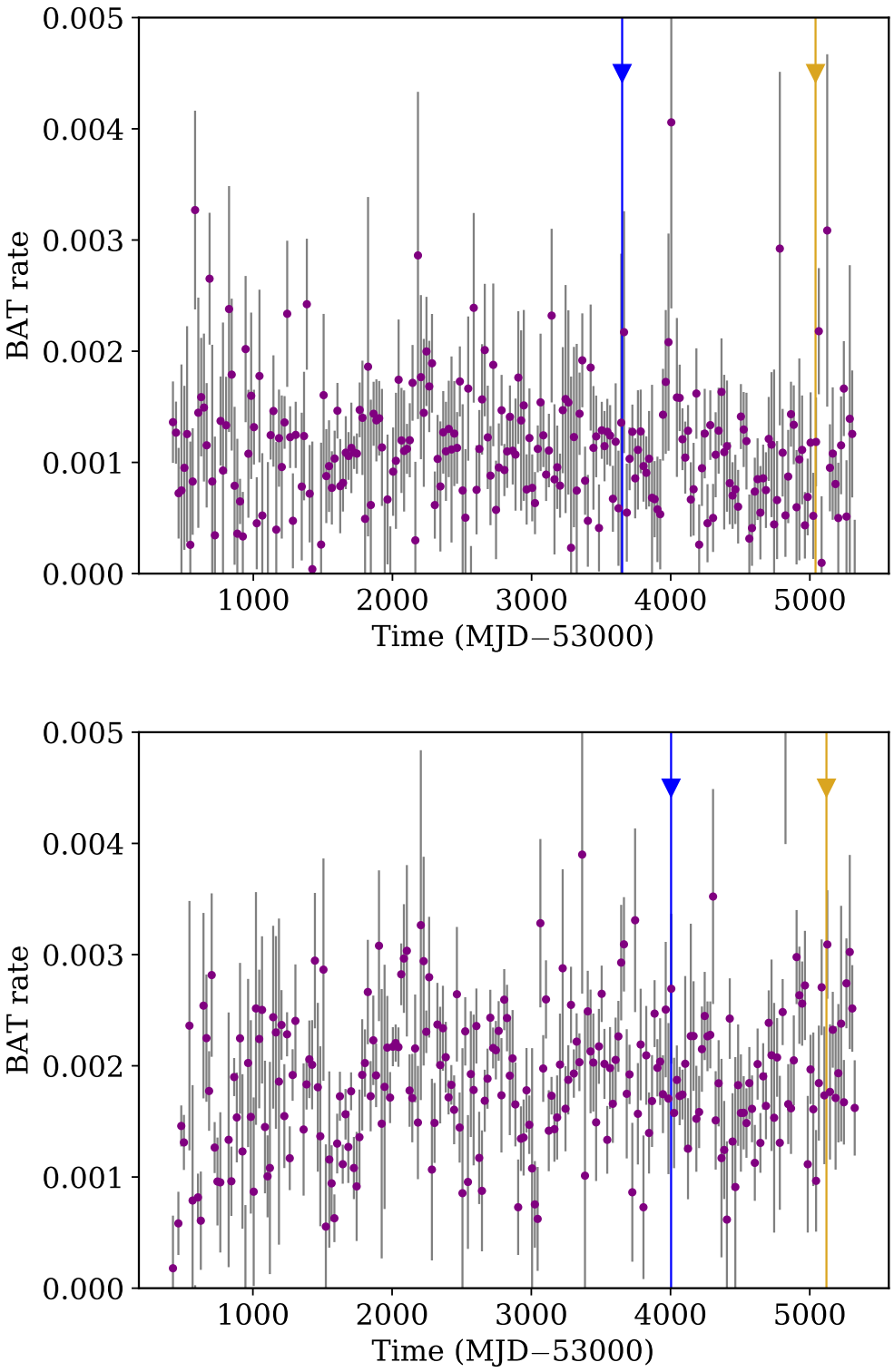

Fig. 5.2 *Swift*-BAT light curves of ESO 103–035 (left) and IGR 2124.7+5058 (right), binned to 20 days, with times of *NuSTAR* observations shown as vertical lines.

for ESO 103–035. Additionally, there is little change in hardness within any observation: each observation is consistent with constant hardness (χ^2/d.o.f = 84/99 and 147/157 for ESO 103–035; 89/86 and 121/144 for IGR 2124.7+5058). Therefore, we extract mean spectra from the whole of each observation of each source.

We show the spectra unfolded against a constant model ($\Gamma = 2$ powerlaw) in Fig. 5.3. Each source shows a hard spectrum with significant absorption. ESO 103–035 matches the long-term *Swift*-BAT spectrum well but IGR 2124.7+5058 exceeds the BAT flux by almost a factor of 2 at high energies (within the *NuSTAR* band). This higher flux is consistent with the variability in the long-term BAT light curve (Figure 5.2).

To show spectral features more clearly, we also plot the ratio of each spectrum to an absorbed powerlaw. Since this ratio is primarily for display, we fix the absorption to match the best-fit from detailed modelling performed later and fit for the power law normalisation and slope. Both sources show a drop in flux relative to the simple power law at high energies. ESO 103–035 shows a strong iron Kα line and Compton hump indicative of reflected emission, while IGR 2124.7+5058 shows these features only more weakly.

5.3.1 Spectral fitting

We begin with a model with components to account for all of the spectral features mentioned. We use (Z)TBABS (Wilms et al., 2000) for Galactic ($z = 0$) and intrinsic (matched to source redshift) absorption. We do not include the Galactic component for ESO 103–035 since this is insignificant compared to the intrinsic absorption. We initially use PEXMON to model the direct and reflected emission. This allows for a cut-off in direct coronal emission (modelled by an exponential cut-off) and reflection from neutral material with an iron-Kα line, calculated self-consistently for a given metallicity. We allow the coronal parameters (Γ and $E_{\rm Cut}$), reflection fraction and iron abundance to vary but freeze the inclination to the default value ($\theta = 60^\circ$).

This provides reasonable fits to each dataset (Tables 5.2,5.3). The iron abundance for IGR 2124.7+5058 is high ($>$ 12 times Solar), although such high abundances have been found in other AGN (e.g. Fabian et al., 2009; Ponti et al., 2010). This could occur if there is significant enrichment of the nuclear gas for example by supernovae from earlier generations of stars.

The cut-off energies, 130^{+450}_{-60} and 100^{+90}_{-30} keV for ESO 103–035 and 78^{+16}_{-12} and 80^{+11}_{-9} keV for IGR 2124.7+5058, are consistent between observations for both sources and in agreement with at least some previous observations (ESO 103–035: 57^{+18}_{-14} keV, Ricci et al. 2017; IGR 2124.7+5058: 79^{+23}_{-15} keV, Molina et al. 2007).

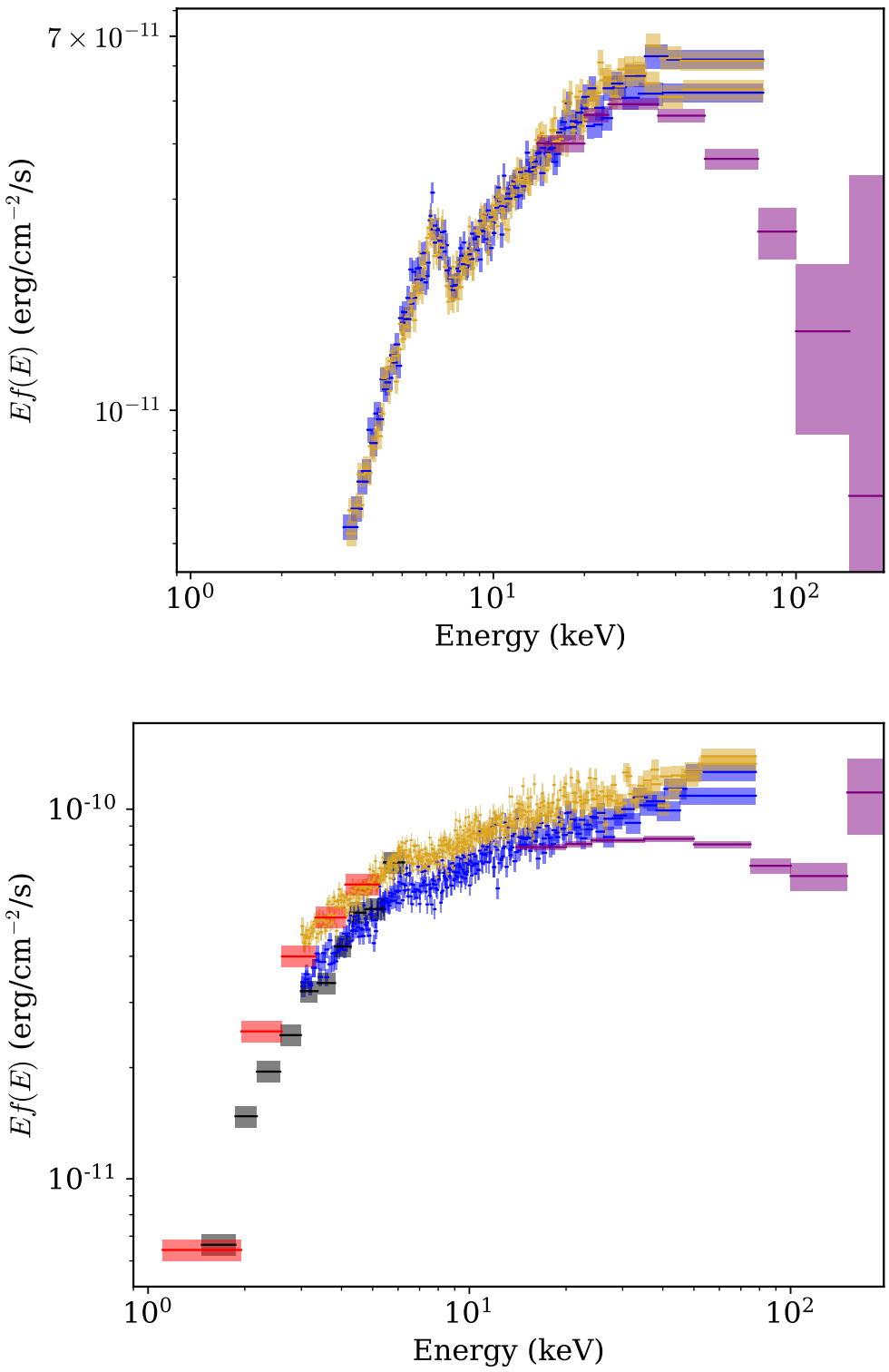

Fig. 5.3 Unfolded spectra of ESO 103–035 (top) and IGR 2124.7+5058 (bottom). Both sources have hard, absorbed spectra. ESO 103–035 shows similar hard-energy emission to the long-term average from *Swift*-BAT; IGR 2124.7+5058 is brighter and harder in the *NuSTAR* observations than the average. *Swift*-XRT (< 10 keV) is shown in black (EGS) and red (Cycle 3); *NuSTAR* ($3 - 78$ keV) in blue (EGS) and yellow (Cycle 3); and *Swift*-BAT ($15 - 200$ keV) in purple.

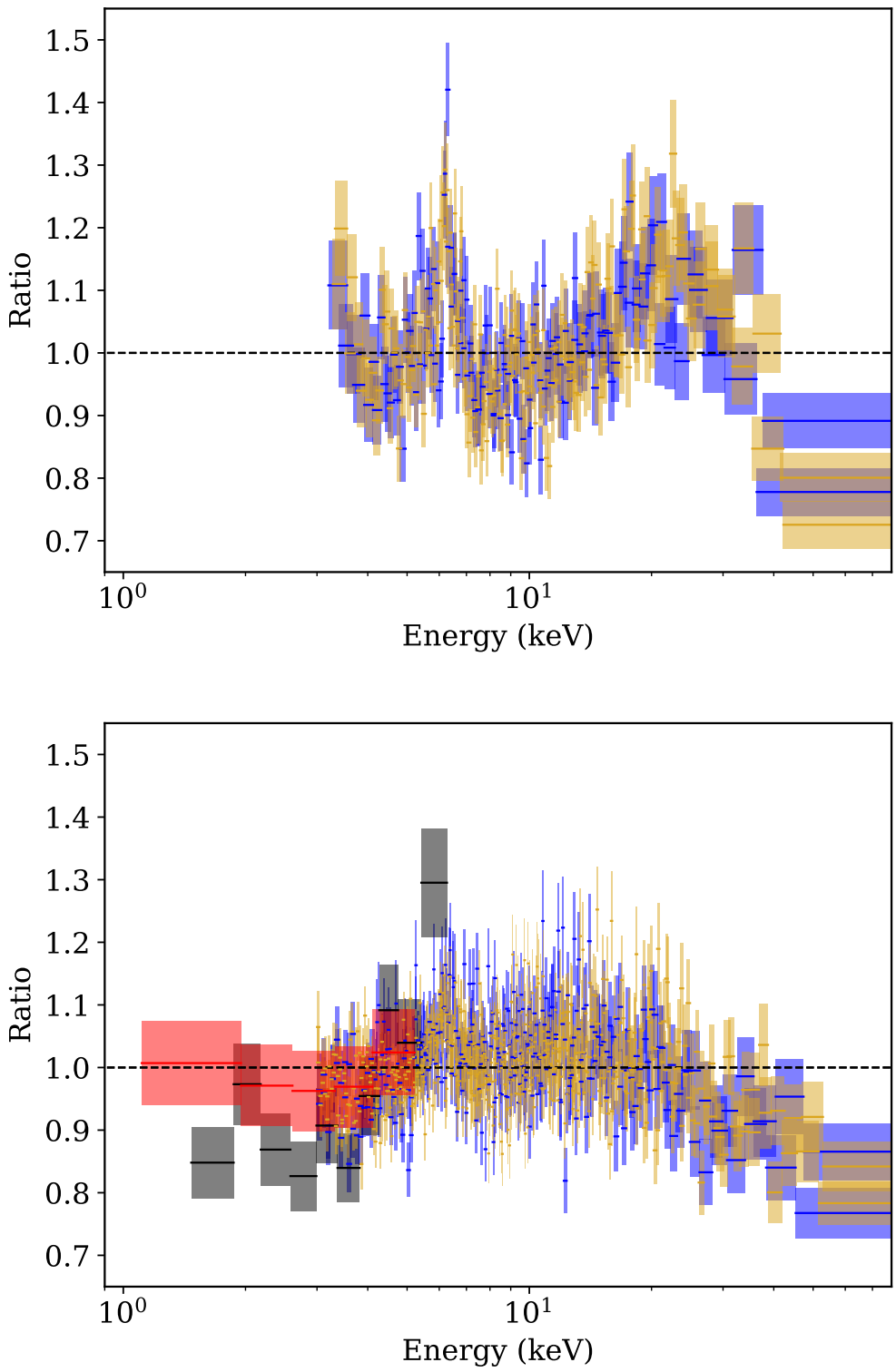

Fig. 5.4 Ratio of spectra of ESO 103–035 (top) and IGR 2124.7+5058 (bottom) to an absorbed powerlaw. For each source, the absorption is fixed to the best fit value from fits presented later and powerlaw parameters are fit to each observation separately. Both sources show a roll-over at high energies, while reflection features are stronger in ESO 103–035.

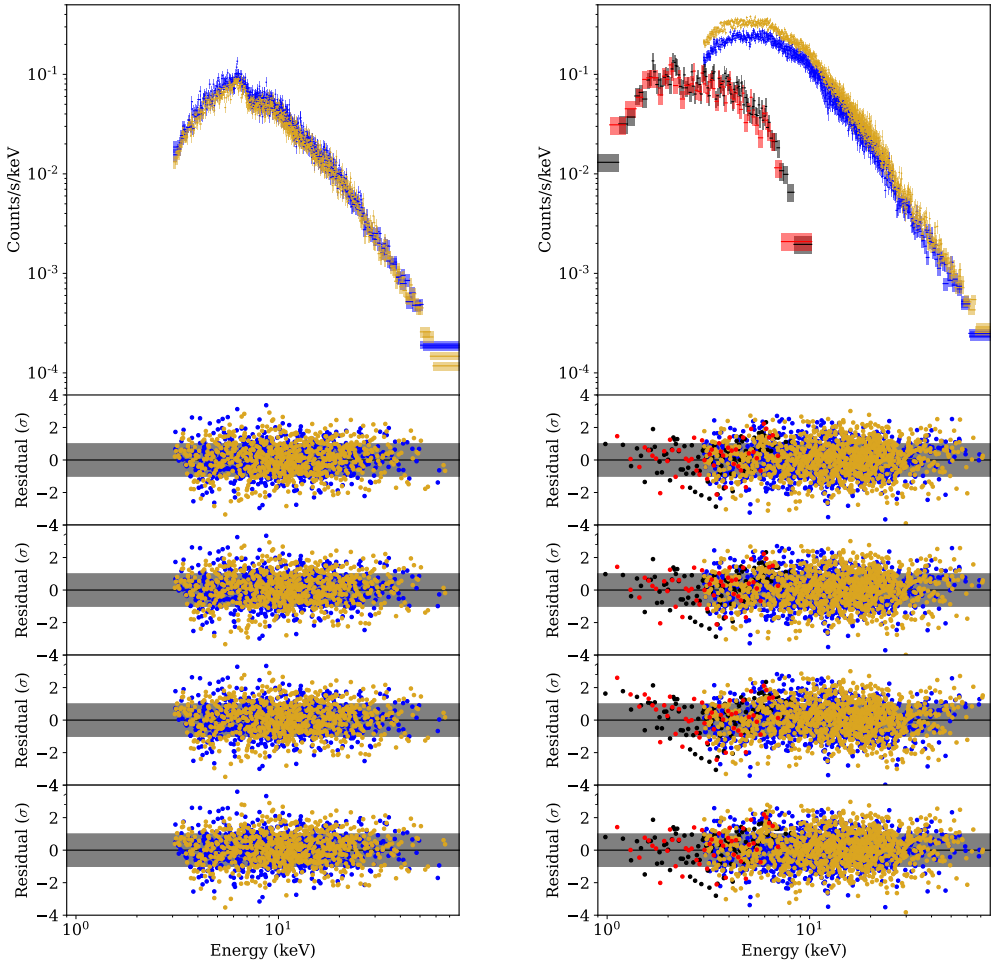

Fig. 5.5 Data and residuals of best fitting broadband models for ESO 103–035 (top) and IGR 2124.7+5058 (bottom). Top: data; lower: residuals to models: EGS in blue/black, Cycle 3 in red/yellow. From top to bottom: PEXMON, XILLVER, XILLVERCP, RELXILLCP.

Dataset	EGS			
Model	PEXMON	XILLVER	XILLVERCP	RELXILLCP
$N_{\rm H}/10^{22}{\rm cm}^{-2}$	$17.1^{+1.5}_{-1.4}$	$17.0^{+1.8}_{-1.6}$	$17.3^{+1.6}_{-1.3}$	$17.0^{+1.0}_{-1.6}$
Γ	$1.82^{+0.19}_{-0.16}$	$1.79^{+0.24}_{-0.16}$	$1.84^{+0.19}_{-0.10}$	$1.86^{+0.13}_{-0.16}$
$E_{\rm Cut}$/keV	130^{+450}_{-60}	110^{+340}_{-40}	-	-
$kT_{\rm e}$/keV	-	-	> 17	> 20
$A_{\rm Fe}/A_{\rm Fe,\odot}$	$0.8^{+0.4}_{-0.3}$	$1.1^{+1}_{-0.5}$	$1.5^{+1.6}_{-0.9}$	< 7
$R_{\rm Refl}$	$1.1^{+0.5}_{-0.3}$	$0.8^{+0.4}_{-0.2}$	$0.7^{+0.6}_{-0.2}$	$0.8^{+0.2}_{-0.5}$
$\theta/^\circ$	-	-	-	< 17
$C_{\rm FPMB/FPMA}$	$1.06^{+0.018}_{-0.018}$	$1.06^{+0.018}_{-0.018}$	$1.06^{+0.018}_{-0.018}$	$1.06^{+0.018}_{-0.018}$
χ^2/d.o.f.	634/645	635/645	636/645	638/642
	0.98	0.98	0.99	0.99
Dataset	Cycle 3			
Model	PEXMON	XILLVER	XILLVERCP	RELXILLCP
$N_{\rm H}/10^{22}{\rm cm}^{-2}$	$15.6^{+1.2}_{-1.2}$	$15^{+1.4}_{-1.3}$	$16.4^{+1.2}_{-0.9}$	$16^{+1.0}_{-1.1}$
Γ	$1.71^{+0.15}_{-0.13}$	$1.73^{+0.22}_{-0.15}$	$1.82^{+0.16}_{-0.08}$	$1.76^{+0.07}_{-0.08}$
$E_{\rm Cut}$/keV	100^{+90}_{-30}	100^{+160}_{-30}	-	-
$kT_{\rm e}$/keV	-	-	27^{+200}_{-9}	22^{+19}_{-6}
$A_{\rm Fe}/A_{\rm Fe,\odot}$	$0.8^{+0.3}_{-0.2}$	$0.9^{+0.5}_{-0.3}$	$1.0^{+0.8}_{-0.4}$	$2.0^{+2.0}_{-1.1}$
$R_{\rm Refl}$	$1.2^{+0.3}_{-0.3}$	$1.0^{+0.4}_{-0.2}$	$0.8^{+0.6}_{-0.2}$	$0.6^{+0.2}_{-0.2}$
$\theta/^\circ$	-	-	-	< 19
$C_{\rm FPMB/FPMA}$ $1.03^{+0.015}_{-0.015}$	$1.06^{+0.018}_{-0.018}$	$1.03^{+0.015}_{-0.015}$	$1.03^{+0.015}_{-0.015}$	$1.03^{+0.015}_{-0.015}$
χ^2/d.o.f.	768/778	775/778	759/778	743/775
	0.98	1.00	0.98	0.96

Table 5.2 Parameters of fits to ESO 103–035. Models are labelled by their primary component; each model also contains intrinsic absorption (with column density $N_{\rm H}$) and a cross-calibration constant between detectors ($C_{\rm FPMB/FPMA}$).

Dataset	EGS		
Model	PEXMON	XILLVER	XILLVERCP
$N_{\rm H}/10^{22}{\rm cm}^{-2}$	$1.45^{+0.15}_{-0.15}$	$1.45^{+0.15}_{-0.15}$	$1.8^{+0.2}_{-0.2}$
Γ	$1.53^{+0.03}_{-0.03}$	$1.52^{+0.03}_{-0.03}$	$1.72^{+0.01}_{-0.01}$
$E_{\rm Cut}$/keV	78^{+16}_{-12}	73^{+13}_{-10}	-
$kT_{\rm e}$/keV	-	-	19^{+3}_{-2}
$A_{\rm Fe}/A_{\rm Fe,\odot}$	> 12	>6.5	>7.9
$R_{\rm Refl}$	$0.06^{+0.02}_{-0.02}$	$0.065^{+0.025}_{-0.025}$	$0.05^{+0.025}_{-0.025}$
$C_{\rm FPMB/FPMA}$	$1.02^{+0.01}_{-0.01}$	$1.02^{+0.01}_{-0.01}$	$1.02^{+0.01}_{-0.01}$
$C_{\rm XRT/FPMA}$	$0.83^{+0.03}_{-0.03}$	$0.83^{+0.03}_{-0.03}$	$0.83^{+0.03}_{-0.03}$
χ^2/d.o.f.	1007/961	1010/961	1067/961
	1.05	1.05	1.11
Dataset	Cycle 3		
Model	PEXMON	XILLVER	XILLVERCP
$N_{\rm H}/10^{22}{\rm cm}^{-2}$	$1.2^{+0.2}_{-0.2}$	$1.2^{+0.2}_{-0.2}$	$1.8^{+0.2}_{-0.2}$
Γ	$1.59^{+0.01}_{-0.02}$	$1.59^{+0.02}_{-0.02}$	$1.76^{+0.01}_{-0.01}$
$E_{\rm Cut}$/keV	80^{+11}_{-9}	82^{+12}_{-9}	-
$kT_{\rm e}$/keV	-	-	20^{+3}_{-2}
$A_{\rm Fe}/A_{\rm Fe,\odot}$	> 12	$10^{+0}_{-4.5}$	> 8.3
$R_{\rm Refl}$	$0.25^{+0.06}_{-0.05}$	$0.07^{+0.02}_{-0.02}$	$0.06^{+0.02}_{-0.02}$
$C_{\rm FPMB/FPMA}$	$1.02^{+0.01}_{-0.01}$	$1.02^{+0.01}_{-0.01}$	$1.02^{+0.01}_{-0.01}$
$C_{\rm XRT/FPMA}$	$0.83^{+0.05}_{-0.04}$	$0.83^{+0.05}_{-0.04}$	$0.86^{+0.05}_{-0.04}$
χ^2/d.o.f.	1290/1189	1291/1189	1340/1189
	1.09	1.09	1.13

Table 5.3 Parameters of fits to IGR 2124.7+5058. Models are labelled by their primary emission component; each model also contains Galactic absorption (with $N_{\rm H} = 10^{22}\,{\rm cm}^{-2}$) intrinsic absorption (with column density $N_{\rm H}$) and cross-calibration constants between detectors ($C_{\rm FPMB/FPMA}$, $C_{\rm XRT/FPMA}$).

The powerlaw indices are all relatively hard. IGR 2124.7+5058 in particular has a very hard spectrum ($\Gamma = 1.53 \pm 0.03$ and 1.52 ± 0.03) but not harder than has been found previously for this source ($\Gamma = 1.5$, Molina et al., 2007).

The sources differ markedly in their reflection fractions. While ESO 103–035 has a reflection fraction around 1, as expected from illumination of a disc by an isotropic source away from strong relativistic effects, IGR 2124.7+5058 has much weaker reflection ($R_{\rm Refl} = 0.06 \pm 0.02$ and $0.25^{+0.06}_{-0.05}$). Since IGR 2124.7+5058 has a jet, this would fit with a scenario in which coronal material in IGR 2124.7+5058 is the outflowing base of this jet and hence beamed away from the disc. Such a model has been proposed to explain the variability of Mrk 335 (Wilkins and Gallo, 2015) and the relationship between radio Eddington luminosity and X-ray reflection fraction (King et al., 2017).

The cross-calibration between *NuSTAR* and *Swift*-XRT is slightly below that expected from IACHEC calibration observations (Madsen et al., 2017) but not unreasonable when allowing for source variability.

There is inevitably some degeneracy between curvature due to the high-energy cut-off and due to reflection. To quantify this, we calculate confidence contours in the cut-off/reflection fraction plane (Figure 5.6). This shows (particularly for ESO 103–035) the expected degeneracy, in that the fit has either a lower cut-off energy or a higher reflection fraction. However, in each case both parameters are still constrained (though only weakly for the shallowest, ESO 103–035 EGS, observation).

To test the effect of different models, we perform a similar fit with the XILLVER model (García et al., 2013), which has a more detailed model for the reflected spectrum. We fit for the same parameters as the PEXMON model and fix the additional ionisation parameter $\log(\xi/\mathrm{erg\,cm\,s^{-1}}) = 0$ to best match the neutral PEXMON reflection. This recovers very similar parameters (Tables 5.2 and 5.3).

Comptonisation models

Having determined the shape of the high-energy roll-over phenomenologically, we now fit with physical Comptonisation models to obtain a direct constraint on the electron temperature.

We use the XILLVERCP model so that the reflected component is calculated self-consistently with the illuminating Comptonised continuum, which is generated with the NTHCOMP model (Zdziarski et al., 1996; Życki et al., 1999). We again allow equivalent parameters to our previous models to be free. Fits to this model are given in Tables 5.2,5.3. Most parameters are similar to those found for the previous models, but the fits to IGR 2124.7+5058 have a significantly softer photon index ($\Gamma = 1.72 \pm 0.01$ rather than 1.52 ± 0.03).

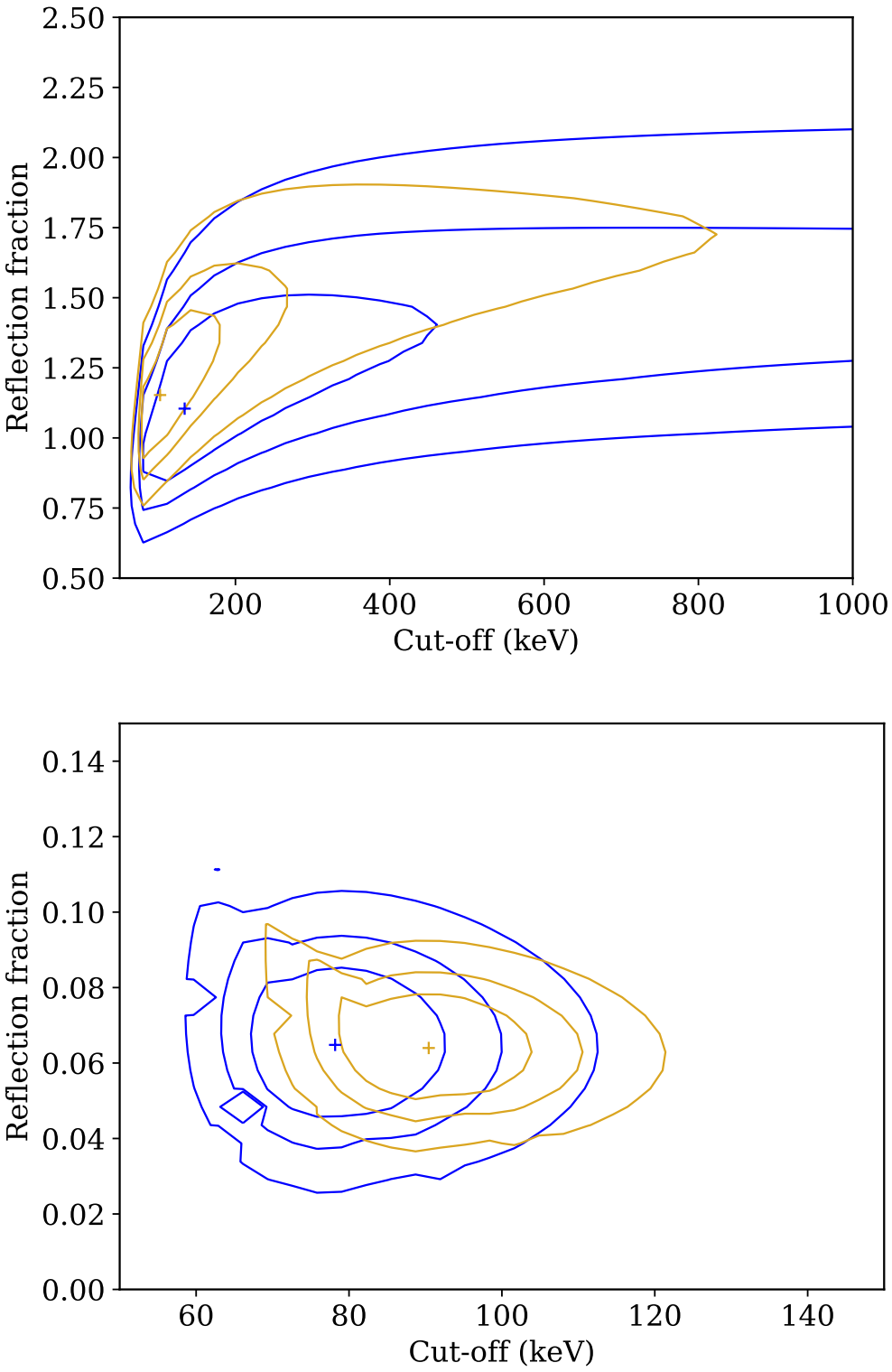

Fig. 5.6 Contour plots of cut-off energy against reflection fraction for ESO 103–035 (left) and IGR 2124.7+5058 (right). The best fit is indicated by a cross, contours are shown at 1σ, 90% and 3σ confidence. Loci for EGS data are shown in blue, Cycle 3 in yellow. Despite some degeneracy between reflection strength and cut-off energy, both parameters are constrained.

The electron temperatures for ESO 103–035 are consistent with the expectation of a factor of $2-3$ lower than the cut-off energy (Petrucci et al., 2001). For IGR 2124.7+5058, this difference is slightly larger (around a factor of 4, though we note that the fit quality for IGR 2124.7+5058 is not perfect). This could be due to the difference in shape of the reflected component (but this would be expected to have a larger effect in ESO 103–035, which has stronger reflection) or because the difference between $E_{\rm Cut}$ and $kT_{\rm e}$ becomes larger at high optical depth, which corresponds to a harder spectrum (Petrucci et al., 2001).

Alternative models

While the fit for ESO 103–035 is formally acceptable, residuals are apparent around the iron line. Therefore, we also test a model with relativistically blurred reflection, using RELXILLCP (Dauser et al., 2010; García et al., 2014). For the Cycle 3 observation, this gives a somewhat better fit, $\Delta\chi^2 = 15$ and shows only weak blurring ($R_{\rm in} > 7R_{\rm ISCO}$). For the EGS observation, there is minimal improvement and parameters are consistent with the least blurring available to the model. Parameters of the Comptonised continuum are consistent with the unblurred model. For completeness, we also fit this model to the observations of IGR 2124.7+5058 but this does not provide a significant improvement.

We also consider a jet component in IGR 2124.7+5058: while Tazaki et al. (2010) estimate the contribution of a jet component to be subdominant, it is possible that even a small contribution has an effect on the more sensitive *NuSTAR* spectra presented here or that the jet emission has increased to a more significant level. Therefore, we also consider a model including a jet component approximated by a hard ($\Gamma < 1.5$) power law. This reduces the best-fit value of the coronal temperature, as the high-energy coronal emission is replaced by the jet; the exact value depends on the index assumed for the jet component. If allowing any value of jet power, our coronal temperature measurement could then be seen as an upper limit. However, a strong jet component requires a > 78 keV flux far above the *Swift*-BAT value so would require a highly variable jet. We therefore note this possible effect of jet emission but do not pursue the quantitative effect further.

5.3.2 Comparison to other sources

We compare the temperature and compactness of the coronae of ESO 103–035 and IGR 2124.7+5058 with that found for other sources by Fabian et al. (2015). Using the formulae in Fabian et al. (2015), we calculate compactness, ℓ, and electron temperature, $kT_{\rm e}$ for each observation. We take the required values of coronal luminosity and high-energy cut-off from the PEXMON fit, since this is the most commonly used model in fits to the other sources in the sample.

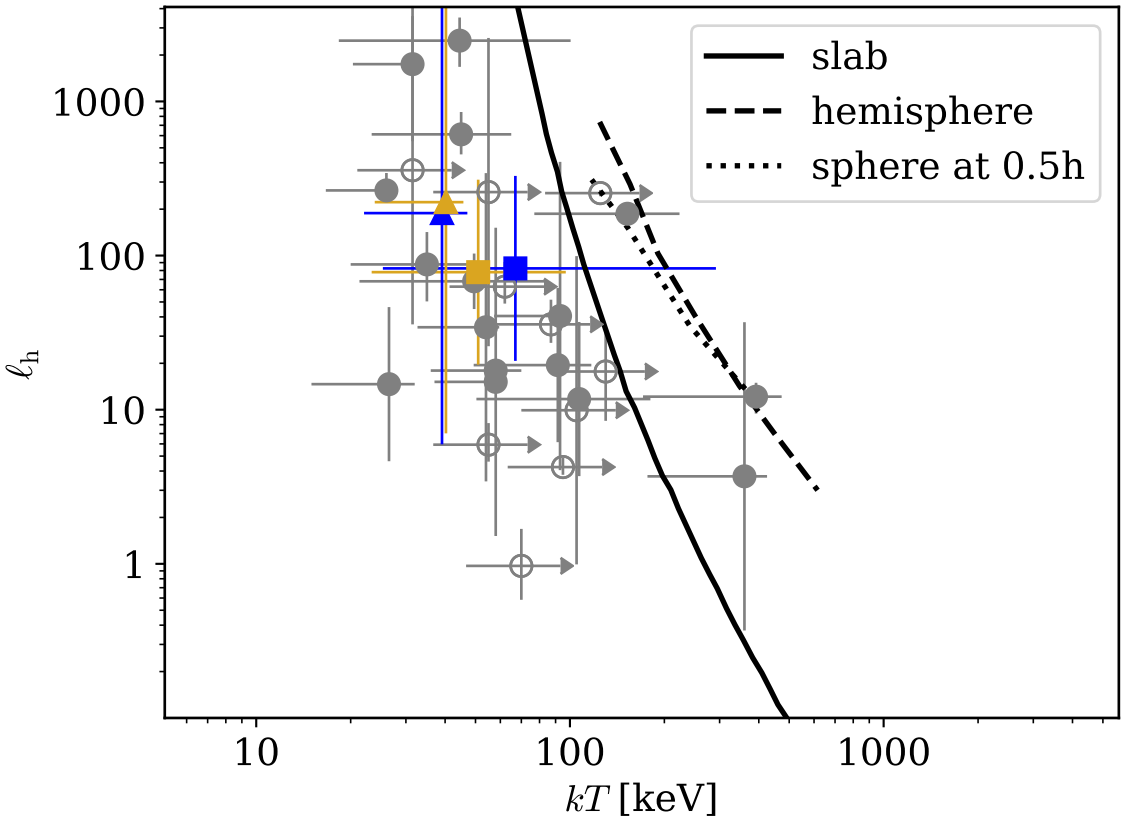

Fig. 5.7 Plot of coronal compactness (ℓ) against temperature (T). Sources from Fabian et al. (2015) are shown by grey circles, IGR 2124.7+5058 by triangles and ESO 103–035 by squares. For ESO 103–035 and IGR 2124.7+5058, EGS data is shown in blue and Cycle 3 in yellow. The limits due to pair production in various geometries are shown by the lines described in the legend; details on their calculation can be found in Fabian et al. (2015).

Using values from the other models gives similar results. Since we have no strong constraint on the coronal size, we follow Fabian et al. (2015) in using a fiducial value of $10r_g$. For ESO 103–035 we use the mass estimate of Czerny et al. (2001), $M_{BH} = 10^{7.1\pm0.6}\,M_\odot$, and $M_{BH} = 10^{7.5\pm1.5}\,M_\odot$ This constraint in the $\ell - T$ plane is shown in Figure 5.7. Both sources have temperatures below the limit imposed by the pair thermostat and within the typical range of other sources of similar compactness. The upper limits for IGR 2124.7+5058 are significantly below the pair thermostat limit; this may indicate that some of the electrons in the corona have a non-thermal energy distribution (Fabian et al., 2017), as might the better description by an exponential roll-over than a thermal Comptonisation model.

5.4 Discussion

We have presented new hard X-ray spectra of two AGN made by *NuSTAR* and compared the coronal parameters found with the predictions of the pair thermostat for coronal temperature regulation.

Both sources have features which differ from the simplest typical AGN, which often formed the basis for the first round of *NuSTAR* observations. ESO 103–035 has strong and variable obscuration ($\sim 1.7 \pm 0.2 \times 20^{23}$ cm^{-2} here, previously $1.0 - 1.7 \times 10^{23}$ cm^{-2}, Warwick et al. 1988) and IGR 2124.7+5058 has both a very hard spectrum ($\Gamma \sim 1.5$) and significant radio emission (Combi et al., 2005; Ribo et al., 2004). The strong obscuration makes measuring other spectral properties harder as their effects must be separated from features of obscuration. Since *NuSTAR* has good sensitivity up to high energies, we can still constrain features including the high-energy cut-off (which principally affects the spectrum at higher energies than obscuration) although to a lesser extent than might be possible with similarly deep observations of unobscured sources. Despite their idiosyncrasies, both sources show coronal temperatures within the typical range for AGN (see Figure 5.7). This could indicate a controlled means of temperature regulation independent of the wider AGN environment, such as the pair thermostat discussed here. The apparent normality of sources which are in other ways unusual also provides a wider pool of AGN of which to take future coronal measurements.

Significant results on coronal properties have been based on large samples of low signal-to-noise spectra made with non-focussing instruments such as *INTEGRAL* and *Swift*-BAT. The more sensitive *NuSTAR* spectra now available present an opportunity to cross-check results from previous instruments. The coronal temperature of ESO 103–035 agrees with that found from *Swift*-BAT (Ricci et al., 2017) and that of IGR 2124.7+5058 agrees with *INTEGRAL* (Malizia et al., 2014). This is promising for the robustness of results such as the decrease of cut-off energy with increasing Eddington rate (Ricci et al., 2018) derived from such spectra.

We have also considered possible means of temperature regulation and found that both sources lie in the region of the $\ell - T$ plane allowed by the pair thermostat. The position relative to the annihilation limit is consistent with pair annihilation being an important means of regulation of the coronal temperature. Furthermore, IGR 2124.7+5058 has a temperature significantly below that implied by the pair thermostat. This could be due to the electron population including a non-thermal component, which tends to lower the limiting temperature (Fabian et al., 2017).

It is also possible that the compactness presented here is an under-estimate. Firstly, the $10r_{\rm g}$ size is a relatively high value: AGN coronae have often been found to be significantly

smaller (e.g. Parker et al., 2014b), although this is usually accompanied by strong relativistic reflection. Secondly, the corona may have a highly inhomogeneous flux-density: it may composed of many much smaller regions of higher compactness within the overall $\sim 10r_{\rm g}$ extent. Both these effects would move the points upwards, closer to the pair-production limit.

Chapter 6

An increase in variability frequency but a stable reflection spectrum: implications for the inner disc in black hole binaries

Abstract

MAXI J1820+070 (optical counterpart ASASSN-18ey) is a stellar mass black hole candidate discovered through its recent very bright outburst. The low extinction column and long duration at high flux allow detailed measurements of the accretion process to be made. In this work, we compare the evolution of X-ray spectral and timing properties through the initial hard state of the outburst. We show that the inner accretion disc, as measured by relativistic reflection, remains steady throughout this period of the outburst. Nevertheless, subtle spectral variability is observed, which is well explained by a change in coronal geometry. However, characteristic features of the temporal variability – low-frequency roll-over and QPO frequency – increase drastically in frequency, as the outburst proceeds. This suggests that the variability timescales are governed by coronal conditions rather than solely by the inner disc radius. We also find a strong correlation between X-ray luminosity and coronal temperature. This can be explained by electron pair production with a changing effective radius and a non-thermal electron fraction of $\sim 20\%$.

6.1 Introduction

Accretion of matter produces variability on all timescales. This variability shows interesting features lasting as long as the complete accretion of the matter and as short as the shortest light-crossing times associated with the system. In black hole binaries (BHBs), accretion occurs onto a particularly compact object, so timescales are correspondingly short and accretion episodes can evolve quickly (compared to, for example, active galactic nuclei, AGN). BHBs are therefore ideal laboratories for observations of processes which would occur on unreasonably long timescales in other accreting sources.

X-ray emission from BHBs occurs principally in two accretion states (along with some additional transitional states), commonly referred to as soft and hard (e.g. review by Remillard and McClintock, 2006). In the soft state, emission is dominated by pseudo-blackbody thermal emission from the disc (Novikov and Thorne, 1973; Shakura and Sunyaev, 1973), which extends to the innermost stable circular orbit (ISCO, Gierliński and Done, 2004; Steiner et al.,

2010). Contrastingly, hard state emission is dominated by coronal emission produced by inverse-Compton scattering in a cloud of hot electrons (Sunyaev and Truemper, 1979; Thorne and Price, 1975), which has a spectrum approximated by a powerlaw with a high-energy cut-off.

A complete understanding of the physical changes between these two states is not yet well known: in particular, the nature of the inner disc during the hard state is still not agreed upon. In some models, the disc is truncated and the accreting material forms a hot inner flow with high ionisation, which produces the Comptonised spectrum (Done et al., 2007; Esin et al., 1997; Gilfanov, 2010). However, this is sometimes at odds with the inner radius measured spectrally, which is often small (Park et al., 2004; Parker et al., 2015b; Reis et al., 2013). In this case, the central part of the disc is cool and dense enough to reflect but only emits a small fraction of the energy released by accretion thermally (Reis et al., 2010), as energy is extracted magnetically to power a corona positioned above the disc, possibly as the base of a jet (e.g. Fabian et al., 2012; Markoff et al., 2005).

X-ray emission from BHBs also shows fast variability on many timescales. Often, specific frequencies show stronger variability, known as Quasi Periodic Oscillations (QPOs; e.g. van der Klis 2006). These QPOs give characteristic timescales to the system's variability, so can be used to infer physical properties when combined with theoretical models for their production.

QPOs can be divided into various classes; the primary distinction being between high-frequency (HF, $\sim 10 - 10^3$ Hz) and low-frequency (LF, $\sim 10^{-2} - 10$ Hz) QPOs. Low-frequency QPOs are further divided into subtypes depending on their coherence and the strength of different harmonics (Homan et al., 2001; Remillard et al., 2002; Wijnands et al., 1999). Unfortunately, there is not yet an accepted explanation for the production of any of the classes of QPOs. In the hot inner flow model, the boundary between the disc and the hot inner flow provides a possible source of QPOs. The inner flow can undergo Lense-Thirring precession, with frequencies similar to those seen in low-frequency QPOs (Ingram and Done, 2011; Ingram et al., 2009; Stella et al., 1999).

New observations of bright sources with the new generation of telescopes have the potential to resolve these questions.

6.1.1 MAXI J1820+070

MAXI J1820+070 is a recently discovered transient source, which is likely to be a black hole binary system. The optical counterpart to MAXI J1820+070, ASASSN-18ey, was detected by the All-Sky Automated Search for SuperNovae (Shappee et al., 2014) on 2018 March 3, several days before the announcement of the X-ray source (Kawamuro et al., 2018) and their

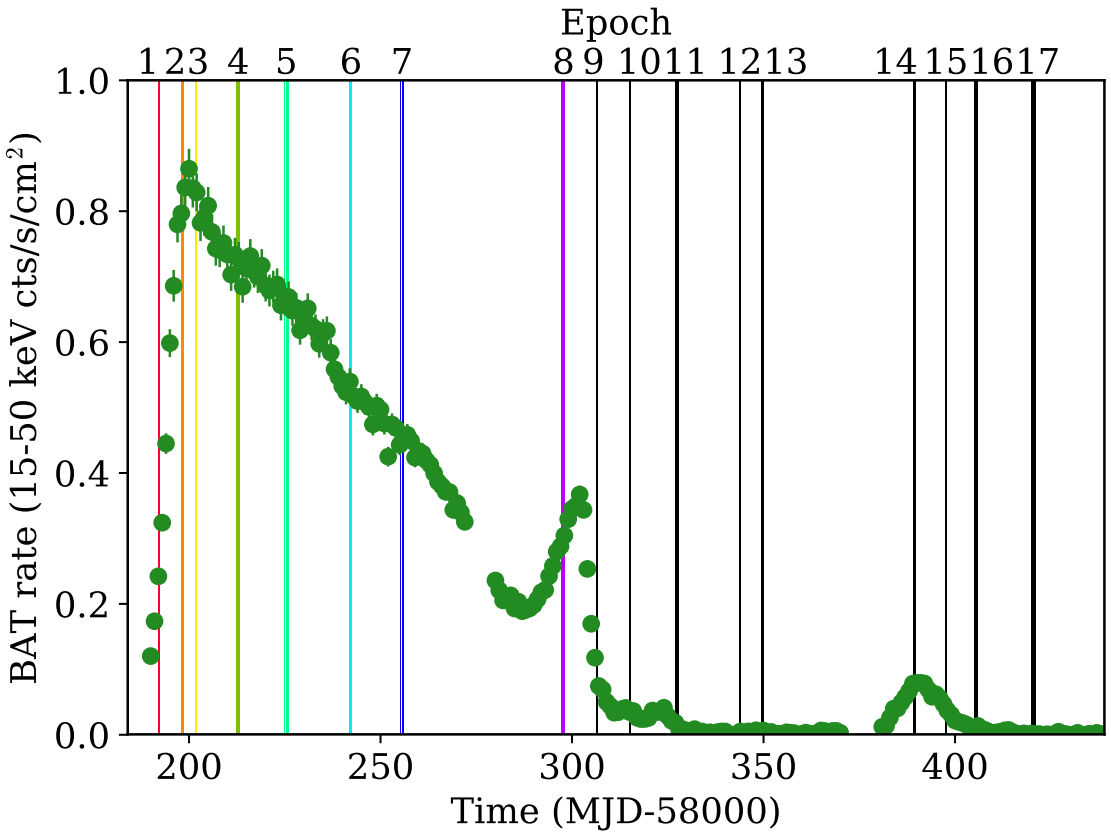

Fig. 6.1 Light curve of MAXI J1820+070 from *Swift*-BAT (green) with times of *NuSTAR* observations shown as vertical bars. Observations analysed here are in colour; later observations are in black

association was proposed (Denisenko, 2018) on 2018 March 11. The low extinction column and long outburst have allowed a wealth of data to be collected in many wavebands.

The X-ray outburst began with an initial fast rise (to MJD 58200) and slow decay (till around MJD 58290) across the full X-ray band; once the flux reached roughly one quarter of the peak, the source re-brightened substantially before the hard X-ray flux dropped dramatically (around MJD 58305) as the source transitioned into the soft state. After over 2 months in the soft state, the hard X-ray flux increased (from around MJD 58380) as the source re-entered the hard state before fading into quiescence. Figure 6.1 shows the hard ($15-50$ keV) X-ray light curve from the *Neil Gehrels Swift Observatory* Burst Alert Telescope (*Swift*-BAT) transient monitor (Gehrels et al., 2004; Krimm et al., 2013). Figure 6.2 shows a hardness-intensity diagram of the outburst from *Neutron star Interior Composition ExploreR* (*NICER*; Gendreau et al., 2016) data.

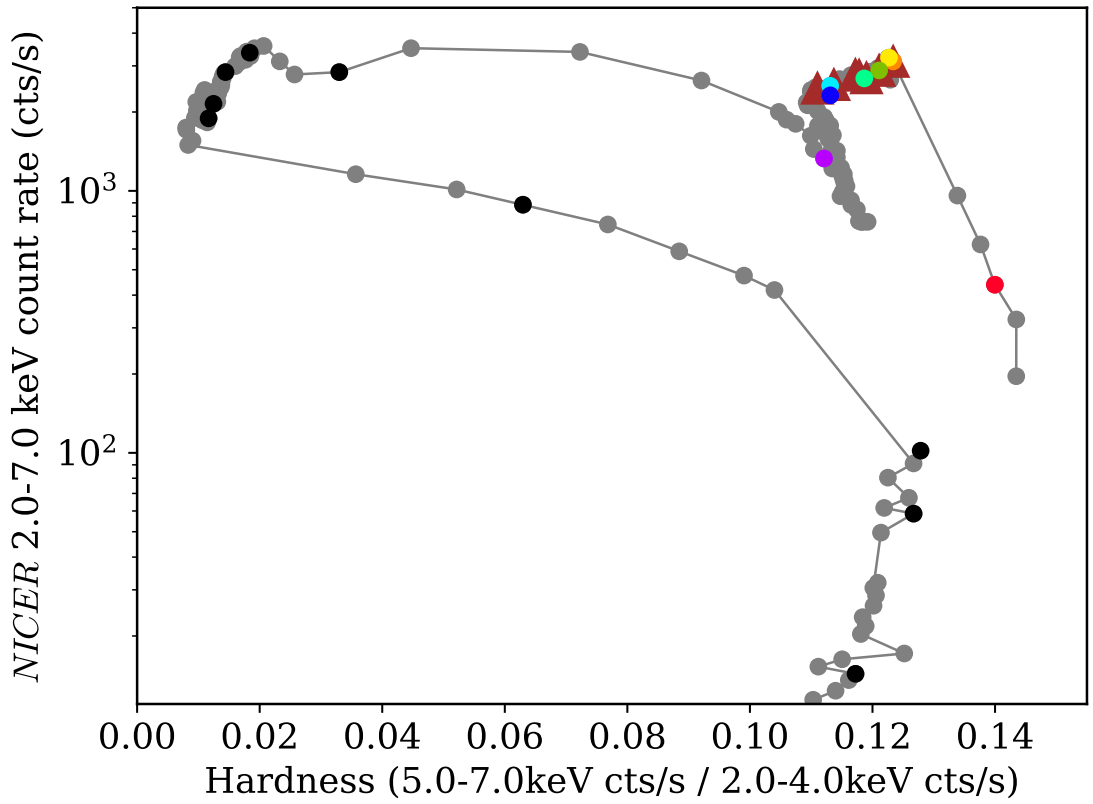

Fig. 6.2 Hardness-intensity diagram of MAXI J1820+070 from *NICER* data (grey). The day coincident with each *NuSTAR* observation is shown in the colour matching Figure 6.1. For comparison, the *NICER* observations analysed in Kara et al. (2019) are shown as brown triangles.

International Gamma Ray Astrophysics Laboratory (*INTEGRAL*; Winkler et al., 2003) observations show differences in the spectra between the rise and decay and a hard tail above the Compton cut-off, which may be from a jet (Roques and Jourdain, 2018). Combining *Monitor of All-sky X-ray Image* (*MAXI*; Matsuoka et al., 2009) with *Swift*-BAT data shows a typical photon index of $\Gamma \sim 1.5$ and an electron temperature of $kT_e \sim 50\,\mathrm{keV}$ (Shidatsu et al., 2018).

The start of the optical outburst preceded the X-ray by around 7 days; lightcurves and spectra show broad double peaked emission lines and variability in the outburst and pre-outburst emission, typical of low mass X-ray binaries (Tucker et al., 2018).

QPOs have been observed in the emission from MAXI J1820+070 in many wavebands, from optical (Fiori et al., 2018; Yu et al., 2018a,b; Zampieri et al., 2018) to hard X-ray (Mereminskiy et al., 2018). The frequency of these QPOs increases with time (Homan et al., 2018) during the first part of the outburst and, over the initial few *Nuclear Spectroscopic Telescope Array* (*NuSTAR*, Harrison et al., 2013) hard X-ray observations, this increase was suggested to be exponential with time (Buisson et al., 2018). Reverberation lags, differences in arrival time between direct coronal and reflected emission, have also been detected in the X-ray variability; these lags shorten as the variability frequencies increase, suggesting that the corona becomes more compact (Kara et al., 2019).

The distance to MAXI J1820+070 is still moderately uncertain. Among the first set of XRB distances to be derived directly from optical astrometry (rather than indirect photometric and spectroscopic methods), *Gaia* measurements of the system in quiescence give a parallax of 0.31 ± 0.11 milliarcsec, which corresponds to a distance of $3.5^{+2.2}_{-1.0}\,\mathrm{kpc}$ (Gandhi et al., 2018). This should be improved in the next *Gaia* data release, especially considering the long interval over which the source remained bright.

NuSTAR is the first X-ray telescope to focus hard ($\gtrsim 10\,\mathrm{keV}$) X-rays. It uses CdZnTe detectors with a triggered readout, allowing observations of bright sources to be free of pile-up which degrades conventionally read CCDs. These capabilities have allowed *NuSTAR* to perform several observations of MAXI J1820+070; the times of these are shown in Figure 6.1 as coloured vertical bands (these colours are used to indicate the same epoch throughout this work), showing that *NuSTAR* observations occurred during all of these stages of the outburst.

The accumulated dataset is vast and a full analysis is beyond the scope of a single work. Here, we focus on a comparison between the evolution of the spectral and timing properties during the initial hard state of the outburst. We summarise the data used in Section 6.2; present an overview of the outburst properties in Section 6.3.1 and describe details of power spectra in Section 6.3.2. We comment on possible interpretations of our findings in Section 6.4 and summarise in Section 6.5.

Table 6.1 List of *NuSTAR* observations of MAXI J1820+070. The observation length is significantly longer than the effective exposure due to deadtime, orbital and other gaps. Since pairs of observations are sometimes closely spaced, we divide the datasets into several Epochs for analysis purposes. Only epochs before the transition to the soft state are considered here.

OBSID	Start time	Observation length/ks	Count rate (incident cts/s)	Live fraction	Epoch	State
90401309002	2018-03-14T20:26:09	43.0	157	0.62	1	Hard
90401309004	2018-03-21T00:31:09	14.2	664	0.28	2	Hard
90401309006	2018-03-21T07:06:09	31.7	679	0.28	2	Hard
90401309008	2018-03-24T12:31:09	20.7	701	0.27	3	Hard
90401309010	2018-03-24T20:26:09	14.9	703	0.27	3	Hard
90401309012	2018-04-04T04:31:09	84.4	624	0.29	4	Hard
90401309013	2018-04-16T22:21:09	8.4	602	0.3	5	Hard
90401309014	2018-04-17T06:31:09	55.5	609	0.3	5	Hard
90401309016	2018-05-03T18:51:09	60.5	512	0.34	6	Hard
90401309018	2018-05-17T03:36:09	13.1	407	0.37	7	Hard
90401309019	2018-05-17T14:26:09	43.9	440	0.37	7	Hard
90401309021	2018-06-28T03:56:09	77.7	265	0.5	8	Hard
90401309023	2018-07-07T08:36:09	38.1	461	0.33	9	Soft
90401309025	2018-07-15T17:51:09	43.7	321	0.39	10	Soft
90401309027	2018-07-28T01:11:09	83.3	237	0.45	11	Soft
90401309029	2018-08-13T14:26:09	26.5	158	0.54	12	Soft
90401309031	2018-08-19T07:26:09	58.7	131	0.58	13	Soft
90401309033	2018-09-27T21:51:09	67.0	108	0.68	14	Hard
90401309035	2018-10-06T07:11:09	38.1	46	0.81	15	Hard
90401309037	2018-10-13T22:46:09	82.4	12	0.9	16	Hard
90401309039	2018-10-29T01:11:09	96.1	3	0.93	17	Hard

6.2 Observations and Data Reduction

We analyse data from all *NuSTAR* observations of MAXI J1820+070 before the transition to the soft state, as shown in Table 6.1. For data transfer reasons, some pseudo-continuous observation periods were divided into separate OBSIDs; we reduce these sections separately but treat them as a single observation for later analysis. We refer to different observations as epochs, numbered as in Table 6.1.

The data were reduced with the NUSTARDAS pipeline, version 1.8.0 and CALDB version 20171002. When filtering for passages through the South Atlantic Anomaly, `"saamode"` was set to `"strict"` and `"tentacle"` to `"yes"`. Following the recommendations of the *NuSTAR* team, we used the status expression `"STATUS==b0000xxx00xxxx000"` to avoid source photons being spuriously flagged as 'TEST' events due to the bright source. The source region was a circle of 60 arcsec radius centroided to the peak brightness. We also extracted a background from a circle of 60 arcsec radius from the area of the same chip with the lowest apparent source contamination. However, this background flux is negligible and source-dominated across the whole bandpass (for the observations analysed here). We group the FPMA data to a minimum signal to noise ratio of at least 50, which allows the use of χ^2 statistics, and group FPMB to the same energy bins to facilitate straightforward comparison of detectors.

To properly account for the loss of exposure due to dead-time and ensure all other instrumental effects are properly accounted for, we produce light curves using the NUPRODUCTS software, which includes the NULCCORR process. To fully account for dead-time, this requires that the light curve bin size is at least 1 s. When studying higher frequencies than this allows (> 0.5 Hz), we correct for dead-time using the HENDRICS package (Bachetti, 2015; Bachetti et al., 2015; Bachetti and Huppenkothen, 2018).

To indicate the magnitude of dead-time effects, mean incident count-rates and live fractions for each observation are also given in Table 6.1.

6.3 Results

6.3.1 Spectral analysis

Qualitative comparison

The spectrum from each epoch considered here is shown unfolded to a constant model in Figure 6.3. Apart from changes in hardness, this shows little evolution in spectral shape throughout the hard state. The spectra soften gradually till the second increase in flux (the

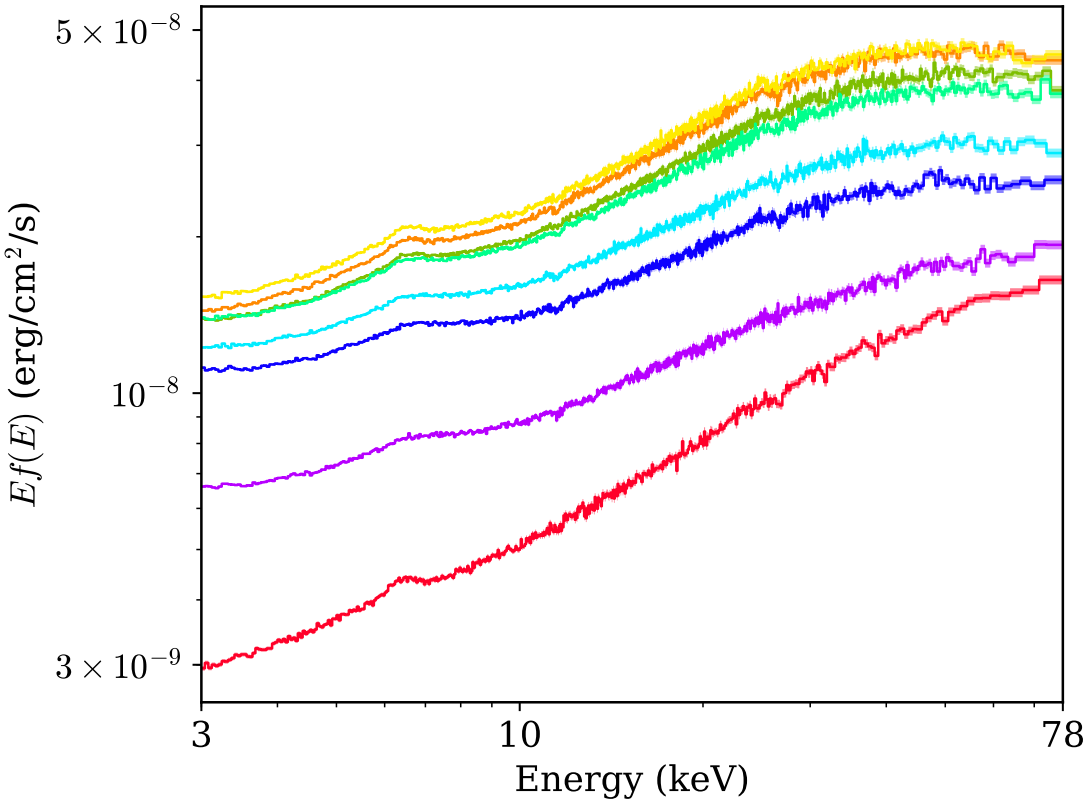

Fig. 6.3 Spectra of each *NuSTAR* observation, produced by unfolding the data to a constant model. FPMA and B have been combined for display purposes. The colour of each observation matches that in Figure 6.1. The source has almost constant spectral shape during the hard state, softening slowly through the initial outburst and re-hardening during the second rise.

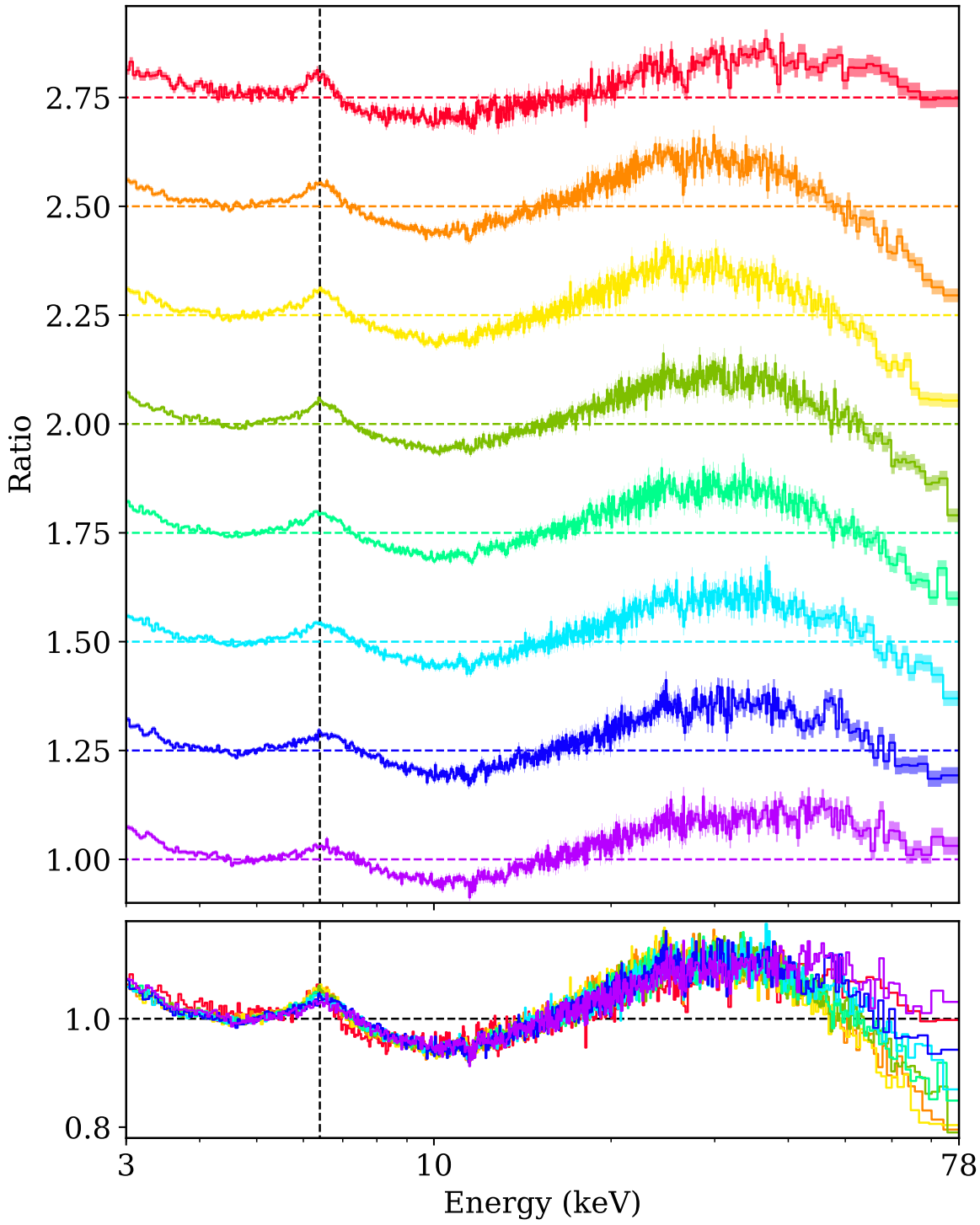

Fig. 6.4 Ratio of the mean spectrum of each epoch in the hard state to the best-fitting powerlaw. Time runs from top to bottom in the upper panel; successive epochs are offset by 0.25, as indicated by the dashed lines. All epochs are shown superimposed in the lower panel. The colour of each observation matches that in Figure 6.1. The vertical dashed line indicates the rest energy (6.4 keV) of the iron Kα line. The narrow core to the iron line weakens and (apart from the first epoch) the relative high-energy flux increases throughout the outburst. Features at $\sim$ 12 and 28 keV are calibration residuals.

last epoch in the hard state, Epoch 8, shown in purple), when a slight hardening is seen. To show spectral features more clearly, we also show the hard state spectra as a ratio to the best-fitting power law in Figure 6.4. This shows a broad (several keV wide) iron Kα emission line peaking around 6.5 keV and a Compton hump at $20-50$ keV, indicating the presence of relativistic reflection, as would be expected from an accretion disc extending close to a black hole (e.g. Fabian et al., 2000; Reynolds and Nowak, 2003). There is also a clear narrow core to the iron emission (although this is broadened by the 0.4 keV FWHM *NuSTAR* resolution). The broad component of the iron line appears remarkably stable throughout the outburst, while the relative strength of the narrow core reduces with time; this behaviour is also seen in observations by *NICER* (Kara et al., 2019). Additionally, the relative high energy flux increases during the outburst, possibly indicating an increase in coronal temperature. The relative high energy flux is also significantly greater during increases in broad band flux (the first and last hard-state spectra) than decreases.

Quantitative modelling

We model the hard X-ray emission as originating from a Comptonising corona illuminating a disc around a black hole. Owing to the availability of models, we make the standard geometrical approximation of a razor-thin (zero thickness), Keplerian disc. From the change in iron line profile, we deduce that the illumination of the outer disc (forming the narrow core) is changing, while the illumination of the inner disc (forming the broad component) varies less. Therefore, we require an extended, changing corona. We model this simply as two point sources on the spin axis at different heights above the disc (two instances of RELXILLLPCP, Dauser et al. 2010; García et al. 2014) with the upper point source inducing the majority of the narrow component of the reflection and the lower point source dominating the broad component. This is unlikely to be the true physical scenario (the true extension is likely continuous, especially once averaged over many dynamical times) but provides a representation with sufficient variable parameters to model the observed changes to the spectra while remaining computationally tractable.

The increase in flux at low energies relative to a simple powerlaw (see Figure 6.4) is greater than is present in the reflection in the RELXILLLPCP model (which uses XILLVER, García et al. 2013). This may be due to the disc having higher density than is used in (this version of) XILLVER, which has a proton density of $n = 10^{15}\,\mathrm{cm}^{-3}$ as appropriate for typical AGN (García et al., 2016). The higher density causes the reprocessed thermal continuum to move into the X-ray band (García et al., 2016; Jiang et al., 2019; Tomsick et al., 2018). A detailed analysis of this effect requires data at softer energies than are provided by *NuSTAR*

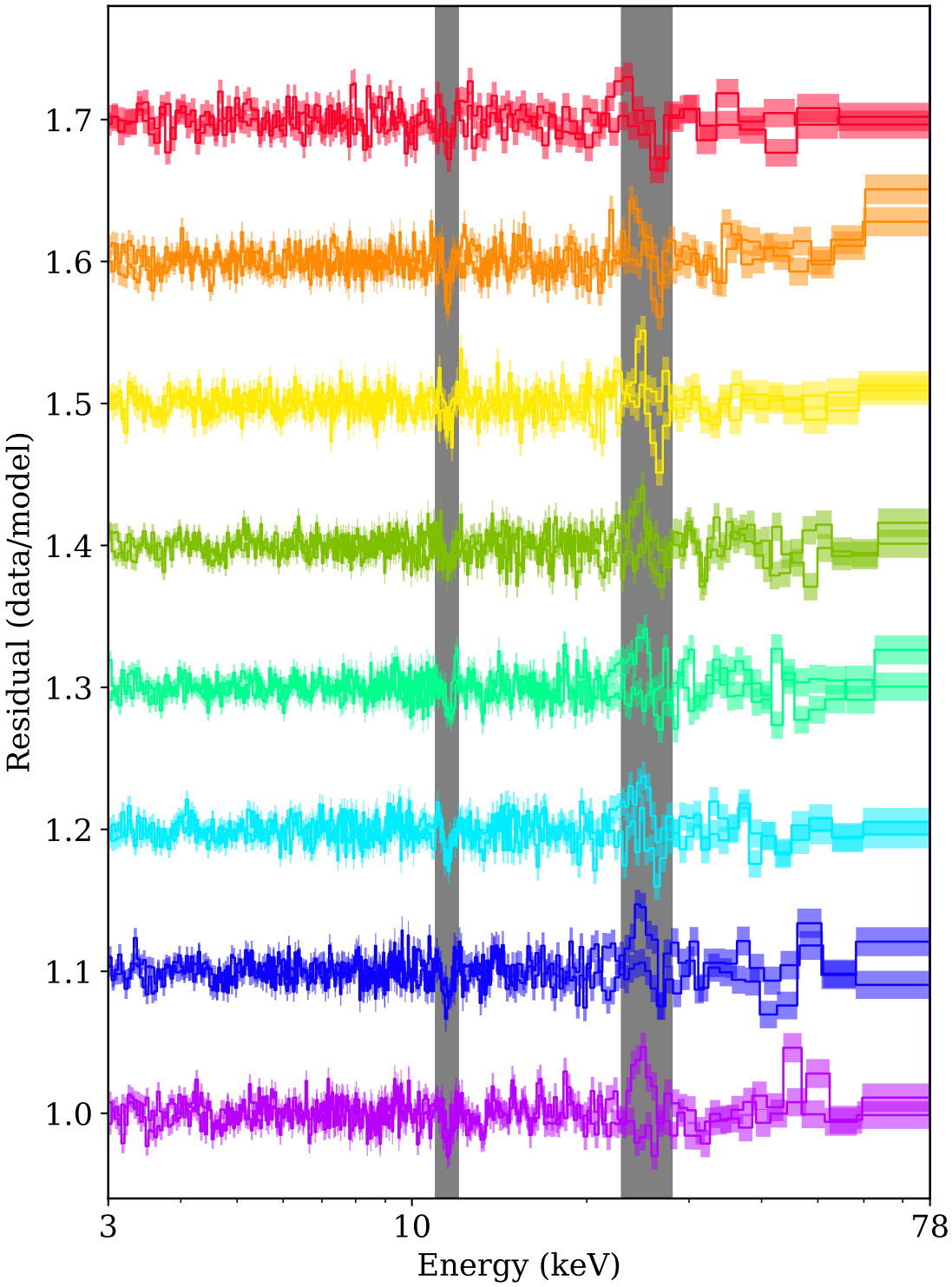

Fig. 6.5 Plot of ratio residuals to best-fit models for each spectrum. Successive spectra are offset by 0.1. The colour of each epoch matches that in Figure 6.1. Grey bands denote energy ranges which were ignored for fitting due to instrumental features.

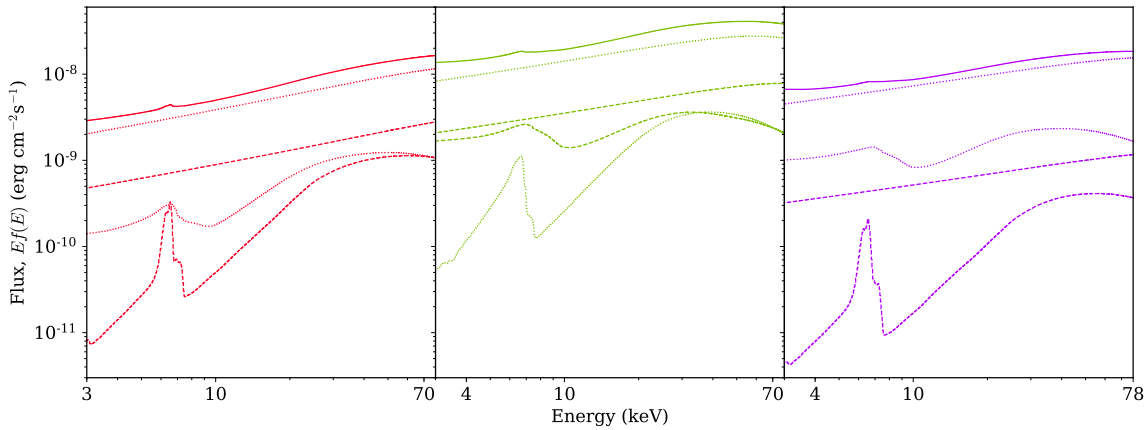

Fig. 6.6 Plot of best-fit models to Epochs 1, 4 and 8 (left to right). The colour of each epoch matches that in Figure 6.1. The upper line in each epoch is the total model; the contributions from the upper and lower corona are shown dashed and dotted respectively, each separated into their continuum and reflected components. The relative contribution from the narrow reflection component reduces in successive observations.

and will be considered in future work (Fabian et al. in prep.); here, we represent the additional soft flux with a DISKBB component.

We fit the data in ISIS (Houck and Denicola, 2000) version 1.6.2-41 across the full *NuSTAR* band, $3-78$ keV, excluding $11-12$ and $23-28$ keV due to sharp features which differ between FPMA and B, which we ascribe to instrumental effects (these energies correspond to more variable regions of the empirical correction factor, Madsen et al., 2015, figure 5). We give parameters in Table 6.3. Errorbars are given at the 90% level for 1 parameter of interest. Residuals are shown in Figure 6.5 and examples of the best-fitting models themselves are shown in Figure 6.6. The evolution of the parameters is shown in Figure 6.7.

Due to slight calibration differences between FPMA and FPMB, we allow different DISKBB parameters and photon indices (Γ) between modules. We find that the typical difference in photon index is similar to the uncertainty in the fit, with FPMB always requiring a slightly harder model, though the difference is less than the stated calibration level (Madsen et al., 2015). Similarly, FPMA always has a slightly hotter DISKBB component.

For self-consistency, we tie black hole parameters and disc parameters that cannot change quickly between the two RELXILLLPCP components. We also use the self-consistent reflection fraction (the reflection strength is calculated based on the coronal height, Dauser et al. 2016), so include the continuum contribution from both components. However, as well as the height, we allow the disc ionisation to differ between the two components. This can be justified in several ways. The different heights in the different components mean

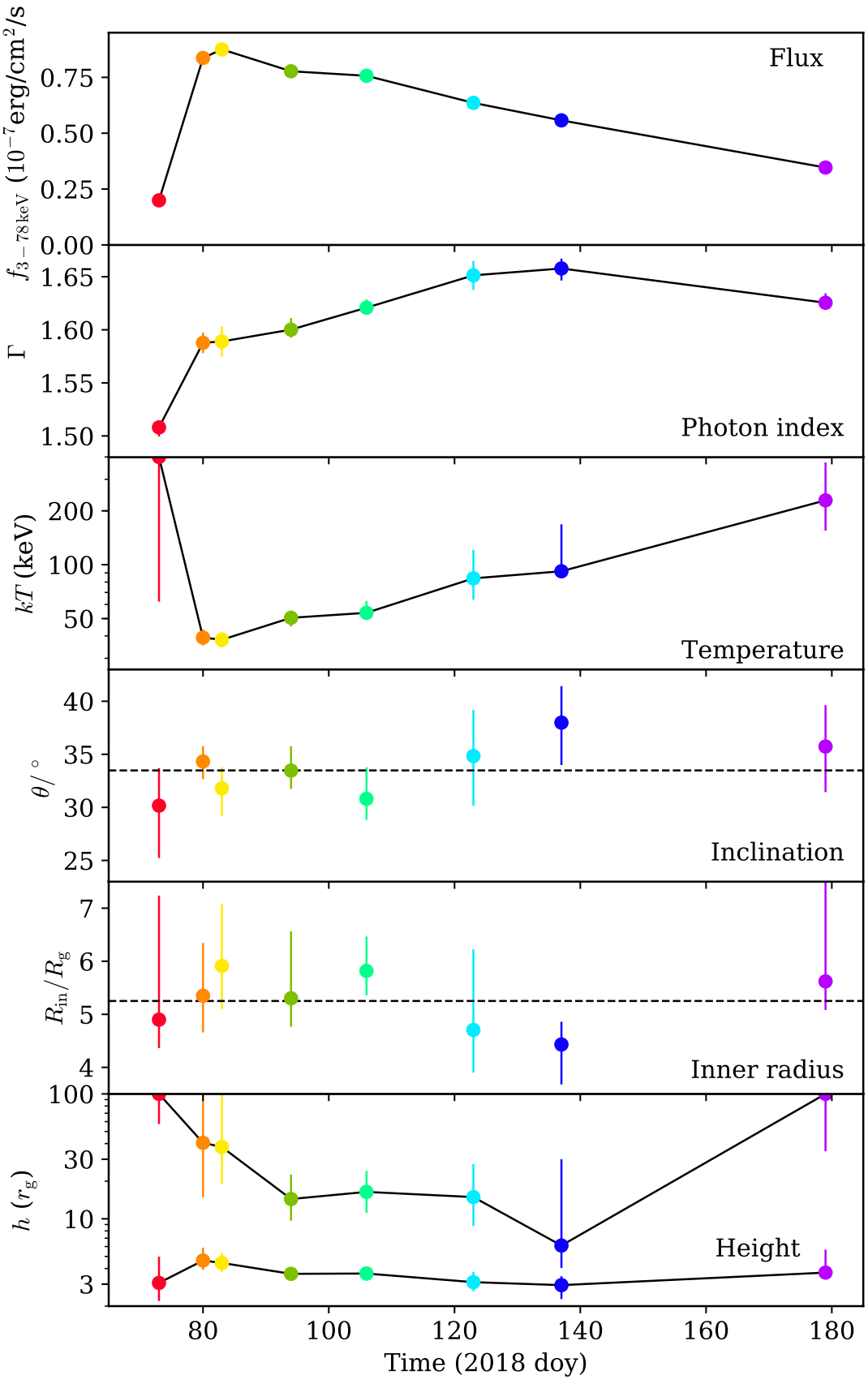

Fig. 6.7 Plot of key system parameters against time. Dashed horizontal lines indicate the weighted mean across epochs.

Table 6.2 Parameters of fits to MAXI J1820+070 in the hard state. The model is DISKBB+RELXILLLPCP(1)+RELXILLLPCP(2). Errors represent 90% confidence intervals.

Component	Model	Parameter	Epoch			
			1	2	3	4
Soft flux	DISKBB	$\mathrm{Norm}_{\mathrm{FPMA}}$	80^{+40}_{-50}	1000^{+800}_{-500}	1000^{+700}_{-500}	1500^{+900}_{-500}
		kT_{FPMA}/keV	0.8 ± 0.1	$0.68^{+0.08}_{-0.05}$	$0.7^{+0.08}_{-0.07}$	0.64 ± 0.05
	DISKBB	$\mathrm{Norm}_{\mathrm{FPMB}}$	300^{+100}_{-300}	1500^{+2500}_{-900}	2000^{+4000}_{-1000}	4000^{+3000}_{-2000}
		kT_{FPMB}/keV	$0.6^{+0.3}_{-0.2}$	$0.6^{+0.09}_{-0.06}$	$0.58^{+0.09}_{-0.08}$	$0.53^{+0.05}_{-0.06}$
Compton continuum	RELXILLLPCP(1/2)	$\mathrm{Norm}_{\mathrm{FPMA}}$	$0.24^{+37.25}_{-0.07}$	$0.28^{+0.08}_{-0.06}$	$0.32^{+0.07}_{-0.06}$	$0.41^{+0.04}_{-0.08}$
		$C_{\mathrm{FPMB/FPMA}}$	1.023 ± 0.01	1.03 ± 0.002	1.031 ± 0.002	1.029 ± 0.002
		Γ_{FPMA}	$1.508^{+0.005}_{-0.009}$	$1.588^{+0.009}_{-0.01}$	$1.59^{+0.01}_{-0.02}$	$1.6^{+0.011}_{-0.007}$
		Γ_{FPMB}	$1.512^{+0.006}_{-0.008}$	$1.589^{+0.009}_{-0.015}$	1.59 ± 0.01	$1.602^{+0.011}_{-0.01}$
		kT/keV	400^{+0}_{-300}	39 ± 4	38^{+4}_{-3}	50 ± 5
Disc	RELXILLLPCP(1/2)	$R_{\mathrm{in}}/r_{\mathrm{g}}$	$4.9^{+2.3}_{-0.5}$	$5.4^{+0.9}_{-0.7}$	$5.9^{+1.2}_{-0.8}$	$5.3^{+1.3}_{-0.5}$
		θ/°	30^{+4}_{-5}	34^{+2}_{-1}	32^{+2}_{-3}	33^{+3}_{-1}
		$A_{\mathrm{Fe}}/A_{\mathrm{Fe},\odot}$	$4.0^{+0.9}_{-0.7}$	$5.3^{+2.0}_{-1.0}$	7^{+1}_{-2}	7^{+2}_{-1}
Lower reflection	RELXILLLPCP(1)	h/r_{g}	$3.1^{+1.9}_{-0.9}$	$4.6^{+1.3}_{-0.7}$	$4.4^{+0.9}_{-0.6}$	$3.63^{+0.07}_{-0.05}$
		$\log(\xi/\mathrm{erg\,cm\,s^{-1}})$	$3.08^{+0.14}_{-0.05}$	$1.9^{+0.4}_{-0.5}$	2.3 ± 0.3	$2.4^{+0.1}_{-2.4}$
Upper reflection	RELXILLLPCP(2)	h/r_{g}	100^{+0}_{-40}	40^{+60}_{-30}	40^{+60}_{-20}	14^{+9}_{-4}
		$\log(\xi/\mathrm{erg\,cm\,s^{-1}})$	0^{+2}_{-0}	3.9 ± 0.2	3.9 ± 0.1	$3.71^{+0.08}_{-0.25}$
χ^2/d.o.f.			676.7/624	957.5/895	890.1/864	1267.9/1037
			1.08	1.07	1.03	1.22
FPMA to FPMB comparison			1.09	1.1	1.0	1.24

Table 6.3 Continued: Parameters of fits to MAXI J1820+070 in the hard state. The model is DISKBB+RELXILLLPCP(1)+RELXILLLPCP(2). Errors represent 90% confidence intervals.

Component	Model	Parameter	Epoch			
			5	6	7	8
Soft flux	DISKBB	$\mathrm{Norm_{FPMA}}$	2600^{+2000}_{-700}	4000 ± 2000	5000^{+4000}_{-2000}	3000^{+2000}_{-1000}
		kT_{FPMA}/keV	$0.6^{+0.03}_{-0.05}$	0.56 ± 0.05	$0.53^{+0.04}_{-0.05}$	$0.53^{+-0.0}_{-0.02}$
	DISKBB	$\mathrm{Norm_{FPMB}}$	8000^{+13000}_{-4000}	6000^{+16000}_{-4000}	8000^{+14000}_{-4000}	2900^{+500}_{-1700}
		kT_{FPMB}/keV	0.48 ± 0.05	$0.48^{+0.09}_{-0.07}$	$0.47^{+0.05}_{-0.06}$	$0.5^{+0.06}_{-0.05}$
Compton continuum	RELXILLLPCP(1/2)	$\mathrm{Norm_{FPMA}}$	$0.38^{+0.11}_{-0.05}$	$0.4^{+0.3}_{-0.1}$	$0.35347^{+7e-05}_{-0.10446}$	$0.2535^{+0.0002}_{-0.0246}$
		$C_{\mathrm{FPMB/FPMA}}$	1.014 ± 0.002	1.016 ± 0.002	1.011 ± 0.002	$1.004^{+0.003}_{-0.004}$
		Γ_{FPMA}	$1.621^{+0.008}_{-0.006}$	1.65 ± 0.01	$1.658^{+0.009}_{-0.012}$	$1.626^{+0.008}_{-0.006}$
		Γ_{FPMB}	$1.623^{+0.008}_{-0.006}$	$1.65^{+0.02}_{-0.01}$	$1.658^{+0.009}_{-0.011}$	$1.63^{+0.004}_{-0.002}$
		kT/keV	54^{+9}_{-3}	80^{+40}_{-20}	92^{+76}_{-8}	230^{+140}_{-80}
Disc	RELXILLLPCP(1/2)	$R_{\mathrm{in}}/r_{\mathrm{g}}$	$5.8^{+0.7}_{-0.4}$	$4.7^{+1.5}_{-0.8}$	$4.4^{+0.5}_{-0.7}$	$5.6^{+2.6}_{-0.5}$
		θ/°	31^{+3}_{-2}	35^{+4}_{-5}	38^{+3}_{-4}	36^{+4}_{-5}
		$A_{\mathrm{Fe}}/A_{\mathrm{Fe},\odot}$	$5.0^{+3.7}_{-0.4}$	8^{+1}_{-3}	10^{+0}_{-4}	$6.0^{+1.3}_{-1.0}$
Lower reflection	RELXILLLPCP(1)	h/r_{g}	3.6 ± 0.4	$3.1^{+0.7}_{-0.5}$	2.9 ± 0.6	$3.7^{+2.0}_{-0.1}$
		$\log(\xi/\mathrm{erg\,cm\,s^{-1}})$	$1.7^{+0.8}_{-0.7}$	$2.1^{+0.4}_{-2.1}$	$2.1^{+0.7}_{-2.1}$	$3.48^{+0.14}_{-0.07}$
Upper reflection	RELXILLLPCP(2)	h/r_{g}	16^{+8}_{-5}	15^{+12}_{-6}	6^{+24}_{-2}	100^{+0}_{-70}
		$\log(\xi/\mathrm{erg\,cm\,s^{-1}})$	$3.49^{+0.29}_{-0.04}$	$3.8^{+0.1}_{-0.3}$	3.9 ± 0.1	$0.3^{+1.7}_{-0.3}$
χ^2/d.o.f.			1136.9/995	1033.7/909	936.3/849	1032.4/868
			1.14	1.14	1.1	1.19
FPMA to FPMB comparison			1.14	1.12	1.1	1.13

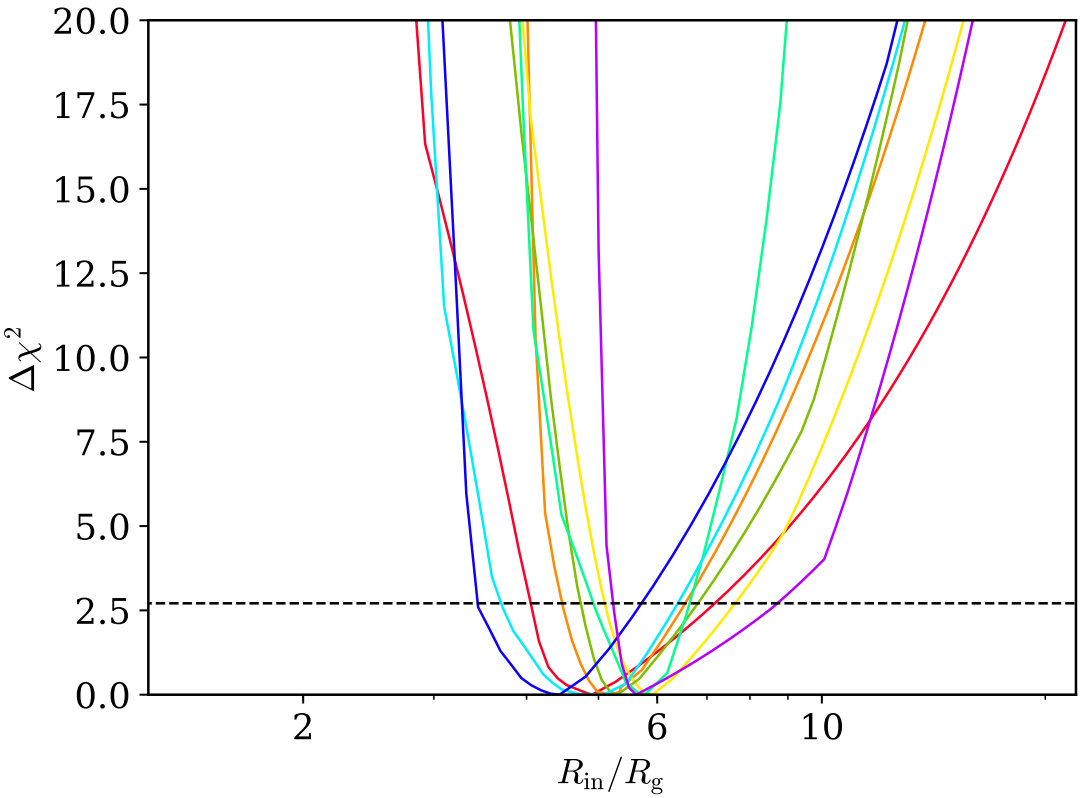

Fig. 6.8 Plot of constraint on inner disc radius, $R_{\rm in}$, in terms of change in fit statistic, $\Delta\chi^2$, for each epoch.

that they mostly illuminate different regions of the disc (the lower component principally illuminates the inner disc). Alternatively, the variability in the system could be such that the flux from different coronal regions is dominant at different times: the disc ionisation could also change with this such that the ionisation when the upper corona is dominant differs from that when the lower dominates. The resulting ionisation values often differ from the naïve expectation that the lower corona should illuminate a more ionised inner disc. For this to be taken as physical, either some variability allows the disc to be less ionised when emission from the lower corona is dominant or a density gradient allows the more strongly illuminated inner region to have lower ionisation. Alternatively, the relative ionisation values could be a modelling artefact; in this case, we can check the reliability of other parameters by tying both ionisation values together. Testing this on Epoch 4 data (which has the strongest signal) retrieves parameters which are similar to (and in particular the inner radius is consistent at the 90% level with) the values from the fits in Table 6.3.

Owing to the strong degeneracy between black hole spin and disc truncation, we fit for inner radius, $R_{\rm in}$, in a maximally spinning (dimensionless spin parameter $a = 0.998$) space-time. The resulting values show little spread around their weighted mean, $R_{\rm in} \sim 5.3\,r_{\rm g}$ ($r_{\rm g} = GM_{\rm BH}/c^2$), see Figure 6.8. If this radius is $R_{\rm ISCO}$, it implies a low spin black hole. A full estimate of the black hole spin, including low-energy data from *NICER*, will be presented in a forthcoming paper (Fabian et al., in prep.).

The iron abundance of the disc is found to be significantly higher than solar ($A_{\rm Fe} \sim 5A_{\rm Fe,\odot}$). This is not necessarily unexpected, since stars vary in metallicity, but the value found is likely to be an overestimate, particularly given the ubiquity of apparent super-solar iron abundances (García et al., 2018). The over-estimate could be due to a higher density disc (as predicted for stellar mass black holes, García et al. 2016; Svensson and Zdziarski 1994) which would show stronger iron lines at a given metallicity (García et al., 2016; Jiang et al., 2019; Tomsick et al., 2018). Additionally, high metallicity could occur if the supernova which formed the black hole polluted the surface of the companion with metal-rich material, which is now being accreted.

Many of these fits are formally poor, in the sense of having low null hypothesis probabilities. However, the statistical errors in the spectrum are comparable to the calibration precision of *NuSTAR* due to the extremely high signal in the datasets used here, so calibration differences between the detectors may lead to inflated χ^2 values. To give a guide to how significant this effect is, we also show the value:

$$\frac{(D_{\rm A} - M_A) - (D_{\rm B} - M_B)}{\sqrt{E_{\rm A}^2 + E_{\rm B}^2} \times \text{d.o.f.}}$$

where D_i, M_i, E_i are the data, model and error values respectively for detector i and d.o.f. is the number of degrees of freedom, i.e. the number of bins minus the 6 variables in our model which can differ between detectors (4 from two instances of DISKBB; the normalisation difference; and the difference in Γ). This is essentially a reduced χ^2 value testing that FPMA matches FPMB. All values are similar to the reduced χ^2 found for the respective source model, which justifies the fit quality of the source models.

Another way of determining the effects of calibration uncertainties is to add a systematic error to the measurement uncertainties; here, a systematic error of around 0.5% brings the reduced χ^2 to unity.

Various parameters (e.g. coronal temperature) change significantly between Epochs. How these changes are related, to each other and to properties of the rapid variability, is considered further in Section 6.3.3.

6.3.2 Variability analysis: power spectra

The timescales on which a source varies may be quantified with the Power Spectral Distribution (PSD, e.g. Priestley 1981)

$$P(f) = |A(f)|^2$$

where $A(f)$ is the Fourier transform of the flux at frequency f.

Initially, we produce periodograms from the full calibrated *NuSTAR* band ($3-78$ keV), using lightcurve segments of 1024 s with $0.0625\,\mathrm{s} = 1/16\,\mathrm{s}$ bins. We then produce PSDs from the average of all periodograms in an epoch, binning frequencies if necessary to ensure that each PSD data point is produced from at least 20 periodogram values (so that the error on the PSD value is approximately Gaussian). We estimate the size of the error of each PSD point from the variance of the periodogram values which produce it.

These PSDs are shown for each epoch in Figure 6.9. The low-frequency cut-off in power increases in break frequency as the outburst progresses. Additionally, a QPO is present close to the break frequency in each observation (although its detection is very marginal in the first); a further peak is present close to double the primary QPO frequency. These QPO frequencies also (with the exception of the final observation) increase with time.

We also test for changes in variability properties with energy by splitting each light curve into 5 energy bands (3-5, 5-6, 6-9, 9-13 and 13-78 keV) with approximately equal counts. This shows a similar PSD shape in each band and only a slight change in variability amplitude. Therefore, we consider only the full band PSDs here (a detailed analysis of the changes with energy will be presented as part of a future work).

Fitting

Power spectra of accreting black holes can typically be fit with the sum of several Lorentzians (Belloni et al., 2002; Olive et al., 1998). We fit such a model, typically using 5 Lorentzians (apart from Epochs 1 where only 3 are necessary, 4 where 6 are necessary and 7 where 4 are necessary), and including an additional constant (independent of frequency) component for the Poisson noise. We fit the two FPMs as separate datasets with the same source model but independent Poisson noise components.

We then use Markov-Chain Monte-Carlo methods to fit each of the PSDs, utilising the XSPEC_EMCEE implementation[1]. We use 150 walkers for 5000 steps after a burn in period of 1000 steps. For each parameter, we apply a simple uniform prior across a range determined by eye to encompass all reasonable values.

[1]Written by Jeremy Sanders, based on the EMCEE package (Foreman-Mackey et al., 2013).

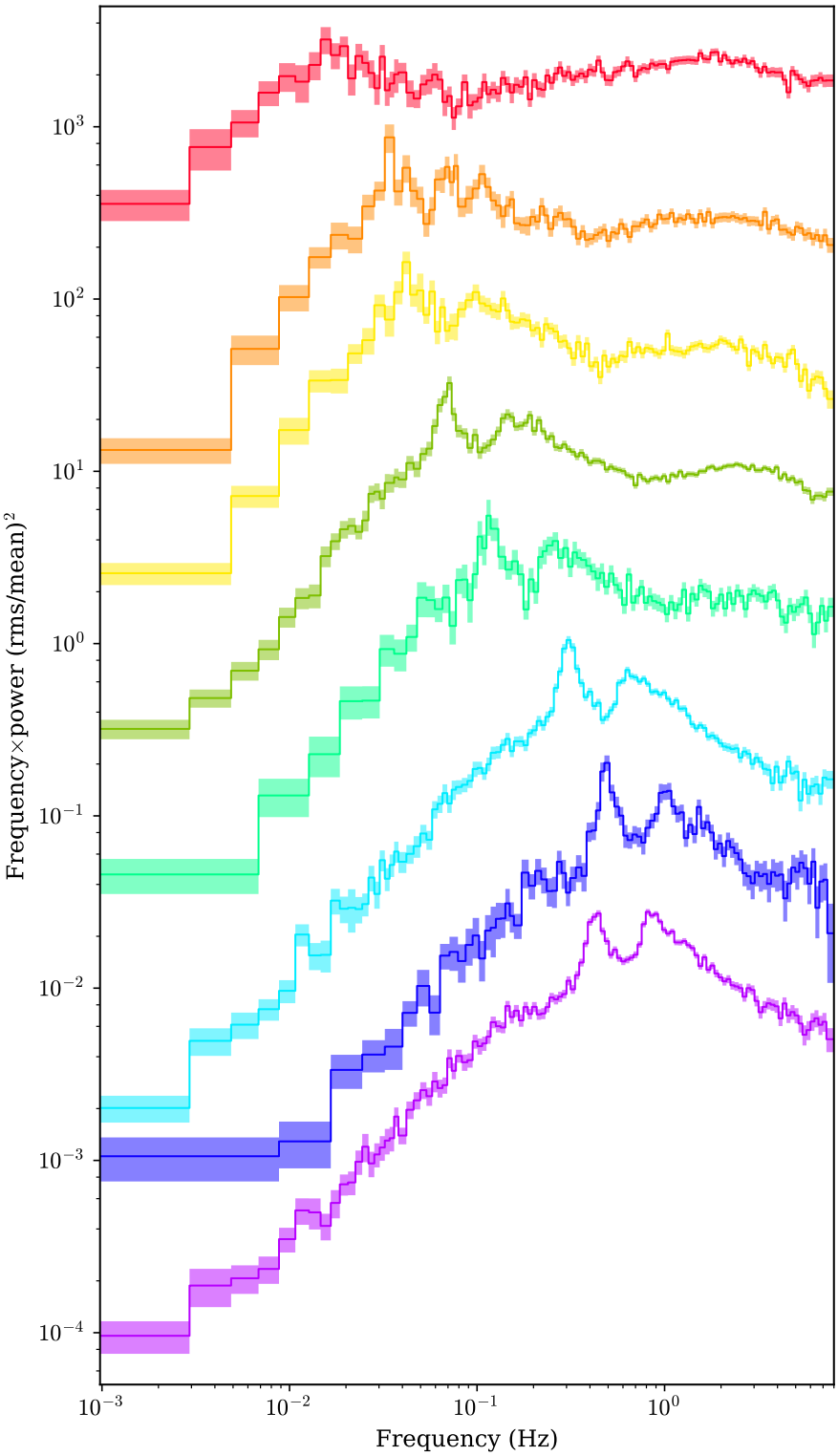

Fig. 6.9 PSDs of *NuSTAR* data, with the RMS normalisation. Successive PSDs are offset by a factor of 5. Poisson noise has been subtracted based on the best-fitting values and each PSD has been rebinned to a geometric progression of at least 1.05 for clarity. Frequencies of features in the PSD (QPO and low-frequency break) increase over the first section of the outburst. During the latter stages of the outburst, the variability decreases.

We then extract characteristic time scales to compare with spectral properties. We extract the QPO peak frequency ($\nu_{\rm peak} = \sqrt{\nu_0^2 + \sigma^2}$) by finding the narrow Lorentzian with the highest normalisation close to the visible QPO peak frequency (where the allowed range is determined by eye to exclude adjacent peaks). We define a Lorentzian as narrow based on the standard threshold, $Q > 2$, where $Q = \sigma/2\nu_0$ is the quality factor. We note that the low-frequency break follows the change in QPO frequency; due to the similar changes in each characteristic frequency and the complication in reliably extracting the low-frequency break from the multiple Lorenztian model, we do not consider the low-frequency break quantitatively.

6.3.3 Comparison of parameter evolution

We compare how key parameters evolve with respect to each other in Figure 6.10. This shows that the parameters are generally not simply related (in the sense of having a monotonic correlation) to each other. Parameters that do show simple correlations include: the upper and lower coronal heights; and the break and QPO frequencies. Since each of these pairs measure closely related properties, this provides little insight into how spectral and timing properties are linked so more detailed consideration is required.

Often, the first observation (red) does not agree with trends which are present in the rest of the data. This could be because the source was increasing in flux and accretion rate; therefore processes are being driven in a way which no longer occurs once the source has equilibrated and started to fade. The last observation also occurs during an increase in flux but can still follow trends since it is at the opposite end of any evolution.

Various models associate the inner disc radius with the characteristic scale which produces QPOs. We plot our measurements of QPO frequency and inner radius along with some models in Figure 6.11 (similarly to Fürst et al., 2016a). Firstly, relativistic effects introduce various precession frequencies. Of these, Lense-Thirring (nodal) precession is most likely to lie in the frequency range of LFQPOs (Stella and Vietri, 1998; Stella et al., 1999). Following Ingram et al. (2009), we plot the frequencies of a single particle and a hot flow extending to $R_{\rm ISCO}$ (we do not show a hot flow with the inner radius set by bending waves as this radius is always larger than our measurements). For illustration, we take a black hole mass $M_{\rm BH} = 100\,{\rm M}_\odot$ (a high mass is required to have low enough frequencies); a radial surface density profile ($\Sigma \propto r^{-\zeta}$) having $\zeta = 0$ to match simulations (Fragile et al., 2007); and choose $a = 0.3$ to give similar frequencies to those observed while not having the measured $R_{\rm in} < R_{\rm ISCO}$. Another possibility is an oscillation mode of the disc, such as the global normal disc oscillation discussed in Titarchuk and Osherovich (2000): an oscillation of the whole disc in the direction normal to the disc plane. We also plot this in Figure 6.11, again

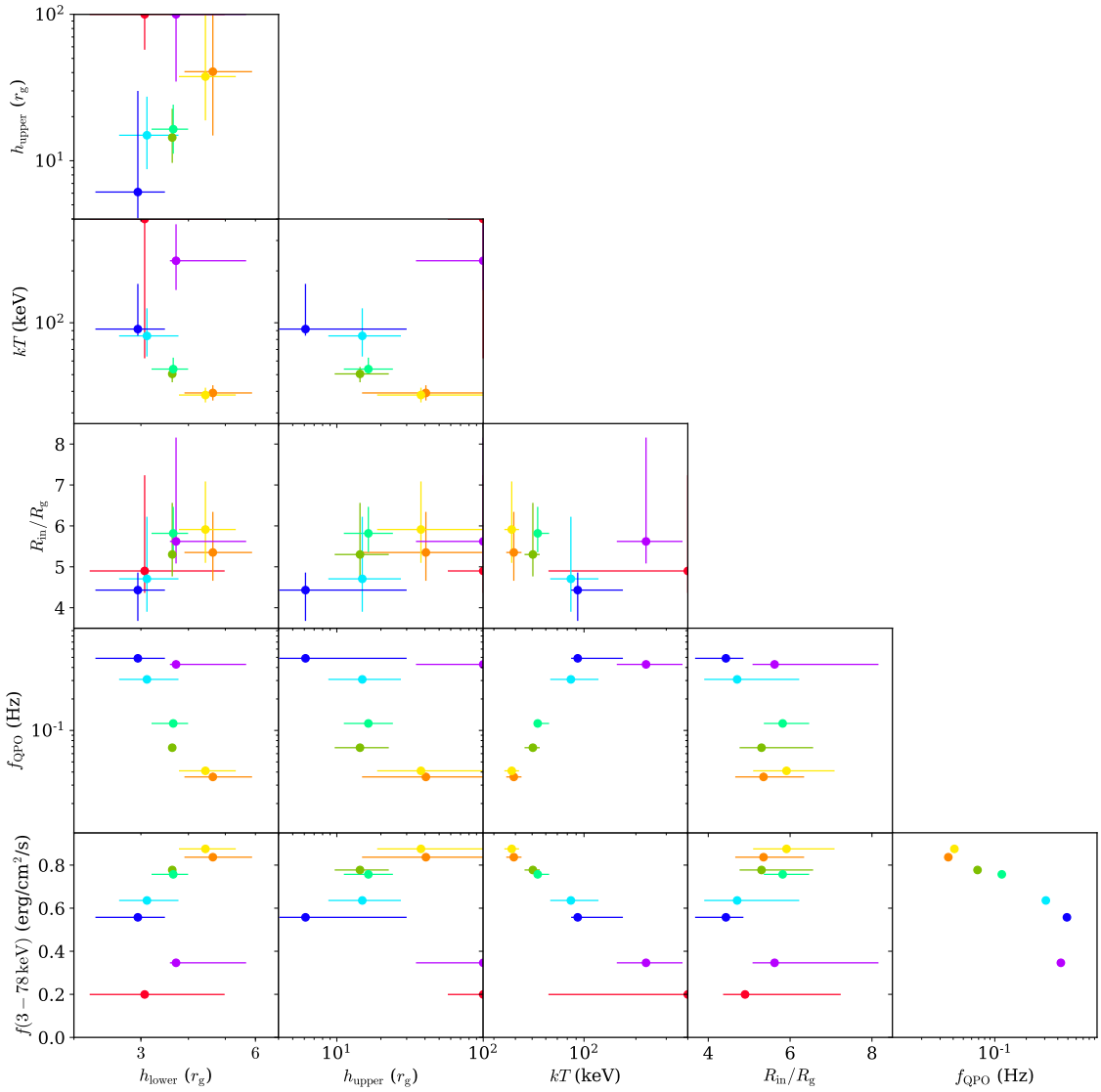

Fig. 6.10 Plot comparing evolution of different parameters. the colour of each epoch matches previous figures. Correlations are present between various parameters – see text for details.

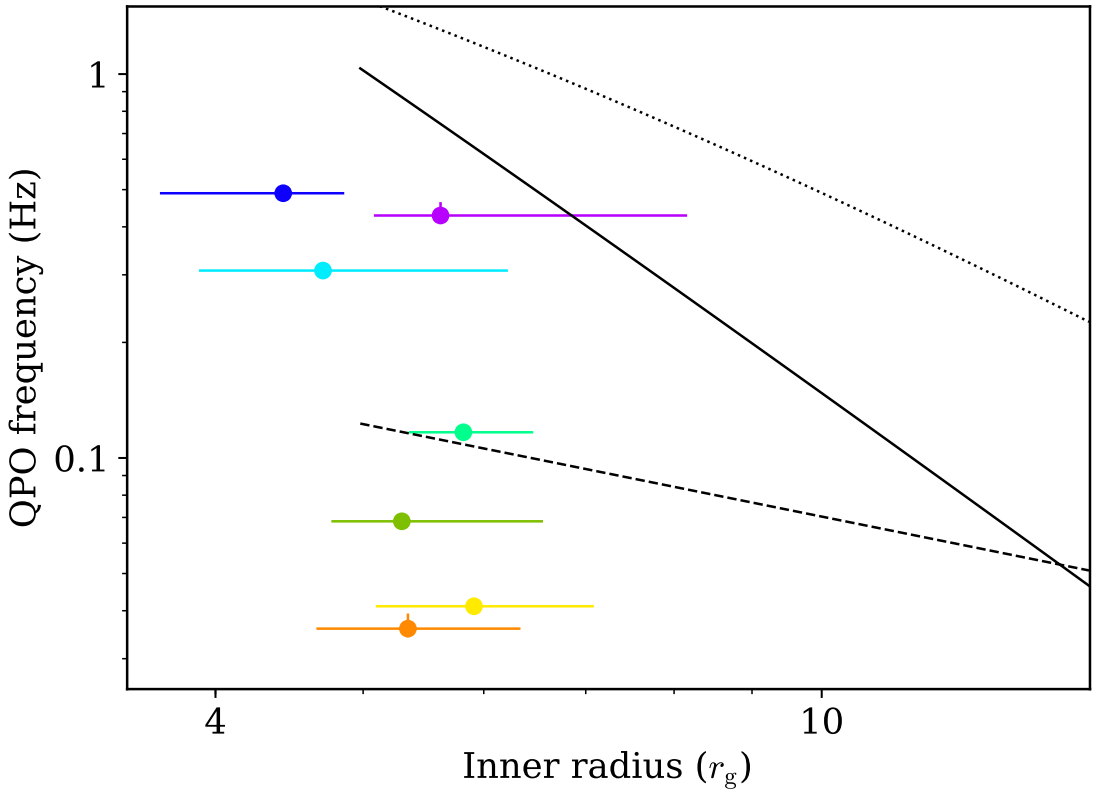

Fig. 6.11 Comparison of relation between inner radius and QPO frequency with various models. Solid: Lense-Thirring frequency of particle at $R_{\rm in}$. Dotted: solid-body precession of hot flow extending from $R_{\rm ISCO}$ to $R_{\rm in}$. Dashed: Global Normal Disk Oscillation (see text for details of each model). To reproduce the observed range of QPO frequencies, all these models require a significantly greater change in inner disc radius than is measured.

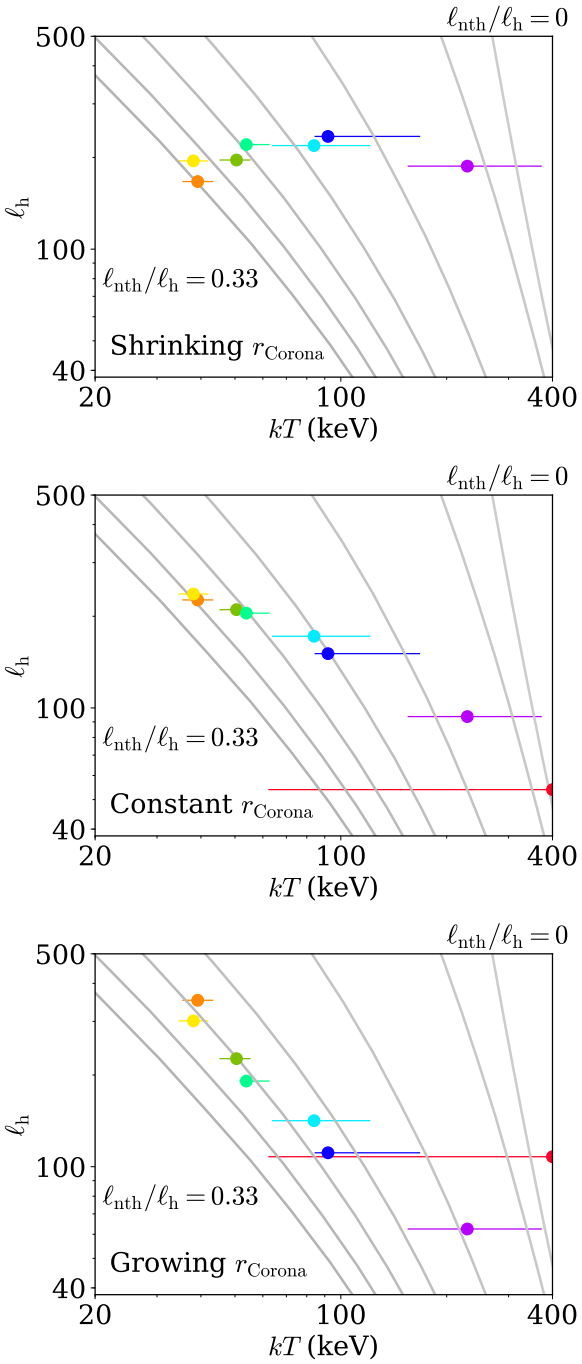

Fig. 6.12 Coronal compactness compared with coronal temperature at each epoch. Theoretical curves of constant non-thermal fraction(grey lines) are taken from Fabian et al. (2017); these have, from right to left, $\ell_{\rm nth}/\ell_{\rm h} = 0, 0.01, 0.09, 0.17, 0.23, 0.29, 0.33$. Data from each epoch have the same colours as other figures. Errors in $\ell_{\rm h}$ are dominated by the choice of coronal radius so error bars are not shown; instead, different choices are given in the different panels. The left hand panel uses a coronal radius decreasing linearly from $10r_{\rm g}$ to $5r_{\rm g}$; the centre panel uses a constant coronal radius of $10\,r_{\rm g}$; and the right hand panel uses a coronal radius which increases from $5\,r_{\rm g}$ to $15\,r_{\rm g}$ (see text).

taking $M_{\rm BH} = 100\,{\rm M}_{\odot}$ and choosing the outer disc radius, $r_{\rm out} = 10^4 r_{\rm g}$ to give reasonable frequencies. All of these models require a much greater change in inner radius than is measured to explain the range of QPO frequencies. Therefore, either some other process governs the frequency of QPOs or the inner radius of the reflecting material does not match the edge of the oscillating material.

The coronal temperature is higher at low flux. This could happen because pair production from photon collisions is regulating the temperature (Fabian et al., 2015; Svensson, 1984; Zdziarski, 1985): at higher fluxes, there are more photons, which allows sufficient pairs to be produced at lower temperatures. The presence of a non-thermal tail to the particle distribution also changes the critical temperature: a stronger non-thermal component further reduces the critical temperature (Fabian et al., 2017). We consider this in more detail by comparing the corona's radiative compactness with its electron temperature. We take electron temperatures from our fits and calculate the coronal compactness following the methodology of Fabian et al. (2015). We take the luminosity from the total direct flux of our best-fit models at a distance of 3.5 kpc. Calculation of the compactness also requires a radius; the coronal prescription used here (including contributions from two points) does not readily convert to an equivalent spherical size so we try several prescriptions. Firstly, we consider a fiducial $10r_{\rm g}$ size for all observations. We also consider the effect of a shrinking radius, as could be implied by the reduction in illumination of the outer disc with time. We reduce the radius linearly by epoch from $10r_{\rm g}$ to $5r_{\rm g}$, guided by the fractional change in the lag amplitudes from Kara et al. (2019) (since the lags are driven by the location of the majority of flux). We plot these measurements in Figure 6.12. The constant coronal size prescription gives a smooth trend but does not align with an obvious physical locus (such as constant non-thermal fraction, $\ell_{\rm nth}/\ell_{\rm h}$). The shrinking corona has an approximately constant compactness for all epochs after the peak (i.e. not the first epoch). With these size prescriptions, the non-thermal fraction is higher at high flux. We could instead assume consistent physical conditions within the corona, manifesting as a constant non-thermal fraction, and use this to infer a trend in effective coronal radius: increasing $r_{\rm Corona}$ from 5 to $15\,r_{\rm g}$ gives a roughly constant non-thermal fraction of around 20%. This would imply an anti-correlation between the vertical coronal extent and the effective coronal radius, so that the corona had changed shape from prolate or cylindrical to oblate. If this is the case and the QPO frequency is associated with coronal size, then the observed trend in QPO frequency would imply that the vertical, rather than horizontal, extent is the relevant dimension. We stress that these relations depend strongly on the assumed prescription for any change in coronal radius, so must be treated with caution.

The coronal temperature also correlates with QPO frequency. This could be explained by the QPO being associated with propagation of a wave across the corona, which travels faster in hotter plasma. However, this cannot be a complete explanation of the variability properties, since the first observation, where the QPO is not clearly detected, has a high temperature but low characteristic frequencies, such as the low-frequency break.

6.4 Further Discussion

We have described the evolution of the hard X-ray emission from the initial hard state of MAXI J1820+070. This is a powerful probe of the inner accretion system and our analysis shows a reflecting inner disc extending close to the ISCO of the central black hole throughout the hard state of the outburst. This is in stark contrast to the large change in variability timescale, which increases by a factor of around 30.

One important issue which is not yet fully resolved is when during an outburst the disc is truncated. Here, we have shown several observations in the hard state without strong disc truncation. To be consistent with observations of truncated discs at low accretion rate (Tomsick et al., 2009) this implies that the disc fills during the initial rise: most of the observations used here are at or after the peak of the outburst. This would imply that discs do eventually reach close to the ISCO regardless of hard/soft state, in this case showing bright hard state emission with a reflecting disc at or close to the ISCO; some emission can also occur early in the outburst before the disc has filled down to the ISCO.

QPOs are often found in the power spectra of X-ray binaries, though their origin is not yet fully understood. The luminosity changes are associated with the coronal powerlaw emission (Casella et al., 2004; Rodriguez et al., 2002) but most explanations invoke some link to the disc, as the disc possesses more accessible characteristic timescales, particularly those associated with the inner edge.

Our results show a change in QPO frequency without a significant change in disc inner radius (see also Fürst et al., 2016a; Xu et al., 2017), which is a challenge for models which rely on geometric (orbital or precession) timescales related to the inner edge of the disc. Since QPOs appear to have different observed properties depending on inclination (van den Eijnden et al., 2017), some geometric effects are likely; these could still occur but be linked to the frequency differently, such as jet precession, or indirectly, such as a coronal oscillation which is directed parallel to the plane of the disc.

There are other possible models for QPO production: it has also been suggested that feedback between coronal heating of the disc and increased seed photon rates could have resonant frequencies which manifest as QPOs.

Alternatively, the QPO could be generated directly by oscillations in the corona, such as a resonant mode of the constituent plasma. A simple prescription to describe this could be a sound wave passing across the corona. The frequency then scales as

$$\nu = A\frac{c_\mathrm{s}}{2d} \simeq A\frac{T_9^{1/2}}{d_2}\ \mathrm{Hz}$$

where c_s is the sound speed, $T = 10^9 T_9$ K is the temperature, $d = 100 d_2 r_\mathrm{g}$ is the distance across the corona and A is a constant factor. This would fit with the change in coronal extent and temperature implied by the spectral fitting – in the smaller, hotter corona, oscillations would have a higher frequency. More quantitatively, during the outburst the coronal height reduces by around a factor of 10 and the temperature increases by a factor of at least 4. This would increase the associated frequency by a factor of ~ 20, similar to the observed increase in QPO frequency. The average value of A for ν to match ν_QPO is then $\sim 1/30$ (taking $M_\mathrm{BH} = 10\,\mathrm{M}_\odot$). This factor could include contributions from the turnaround time at each end of the corona or from other physical processes. MHD calculations (Edwin and Roberts, 1983) show that magnetic fields affect the frequency of various modes of oscillation. Detailed calculations of expected values of A are beyond the scope of this work.

Any model for QPO production must also be able to explain the observed differences in the spectrum at different QPO phases (e.g. Ingram and van der Klis, 2015; Ingram et al., 2017, 2016). In particular, the energy of the centroid of the iron Kα line has been observed to oscillate twice per QPO cycle (Ingram et al., 2016). This can be qualitatively explained in the oscillating corona model if the putative wave travels up and down through a vertically extended corona, causing the coronal emission to occur, on average, from closer to and further from the disc. When very close to the disc, the corona will principally illuminate the innermost regions, which are strongly gravitationally redshifted so the centroid line energy will be low. At intermediate heights, the illumination will include the regions of the disc which are most strongly blueshifted so the centroid line energy will be high. At the highest heights, the illumination will include more of the distant disc where the line energy is less affected by Doppler boosting or gravitational redshift and the centroid line energy will reduce.

In this case, the peak values of the observed line energy would be similar, while one trough would be redshifted and one would be close to the rest energy. Additionally, the flux should be highest close to the line energy trough at rest energy, when there is least light bending of the coronal emission away from the observer (Miniutti and Fabian, 2004). Furthermore, the reflection fraction should be highest when the centroid line energy is lowest. We note that these features are also found in the reflection tomography of H 1743–322

presented in Ingram et al. (2017) for a precessing flow model of the QPO. Whether these modulations in line energy are also present in MAXI J1820+070 and whether such a coronal oscillation explains them quantitatively is beyond the scope of this work but should certainly be investigated in the future.

Remillard and McClintock (2006, figure 10) show that QPO frequency correlates with disc flux in hard/steep powerlaw intermediate states. The observations presented here have a weaker disc component which is not unambiguously detected but may be clearer at soft energies, so this could be investigated for example with *NICER*.

While the QPO is most dominant at high energies, it is also strongly detected in the 3-10 keV band, which is also covered by *NICER*. Owing to the more frequent coverage of MAXI J1820+070 by *NICER*, a more detailed analysis of the QPO progression can be made with this data.

The corona also shows changes in its mean properties: the temperature anti-correlates with flux. This has been observed in other individual XRBs (Joinet et al., 2008; Motta et al., 2009) and AGN (Lubiński et al., 2010). The coronal temperatures observed here are allowed by the pair thermostat, being below the pair-production limit which is observed to limit accreting sources as a population (Fabian et al., 2015). The lower temperatures than the pair limit can be explained by a deviation from a pure thermal distribution, which is expected as the cooling timescale is less than the collision timescale (Fabian et al., 2017). These considerations do not take sub-structure in the corona into account; this remains a potential caveat when estimating the coronal compactness from its total luminosity and size.

This paper covers only a small part of the data available on this outburst: further work on this and similar outbursts with the new generation of facilities now available will surely help to resolve these outstanding questions.

6.5 Conclusions

We have described the evolution of X-ray spectral and timing properties of the recent outburst of MAXI J1820+070 during the hard state. In particular:

- characteristic frequencies of the variability, QPO frequency and low-frequency cut-off, increase by a factor of ~ 30 during this outburst state;
- spectral features change subtly: the broad component of the iron line remains almost constant while the narrow core reduces with time;
- reflection modelling implies a small inner radius in all observations, consistent with the ISCO of a low to moderate spin black hole ($\sim 5.3 r_{\rm g}$);

- the change in the iron Kα line shape can be explained by coronal emission being more concentrated close to the black hole in later observations;
- the coronal temperature is higher at lower flux. It can be explained by pair-production if the effective radius of the corona grows with time and the non-thermal electron fraction is $\sim 20\%$;
- and the change in QPO frequency with stable $R_{\rm in}$ is hard to reconcile with hot inner disc precession models for QPOs. It is probably related to the temporal development of the corona.

Chapter 7

Conclusions

We have given various results concerning the structure of matter accreting onto black holes. In AGN, we have shown that variability in UV emission is often, but not always, caused by variations in flux from the central source.

We have demonstrated that the coronal temperature may be measured with *NuSTAR* even in sources with complications from other spectral components (e.g. strong absorption) and shown that these sources are consistent with the temperature being governed by the pair thermostat.

We have shown a constant, small inner radius in several observations of an X-ray binary in a bright hard state. This shows that a reflecting disc can exist close to the ISCO in the hard state. Additionally, we have shown a large change in QPO frequency during the same observations. Therefore, QPO frequency cannot be determined solely by disc inner radius.

7.1 Outlook

These findings may have demonstrated some relations between the disc and corona more clearly than previous work, but in doing so have opened further questions. Fortunately, there are many current and upcoming advances in technology which will allow for progress in understanding these additional complications.

It is becoming increasingly clear that not all AGN show the same relation between X-ray and UV variability. The long monitoring campaigns required mean that progress cannot be fast, but steady advances are being made. In particular, campaigns including spectroscopic UV measurements (Cackett et al., 2017) have now shown the importance of atomic processes in the length of UV lags. The archive of *Swift* monitoring programmes is now significantly larger than was available by the cut-off date for Chapter 2. This will allow the X-ray/UV

correlation strengths to be measured and compared for different types of sources, which should give further insight into why some sources do not show these correlations.

The origin of QPOs in X-ray binaries is another question which has been open for some time. New missions have the potential to resolve it: the recently-launched *NICER* instrument provides far greater throughput at CCD resolution ($R \sim 40$ at the iron Kα line) than has previously been available. This will allow studies of timing properties to separate different spectral components. Already, interesting results have been published, e.g. Kara et al. (2019). The large data archive which is accumulating will also allow comparison of different sources and different outbursts or stages of outbursts, which should further reduce the parameter space of possible solutions.

7.1.1 Future missions

The X-ray Imaging and Spectroscopy Mission (XRISM), due to be launched in 2021, will use a calorimeter (named Resolve) to provide higher spectral resolution around the iron line than has previously been available for a sustained mission. After various failures on previous missions, the calorimeter onboard *Hitomi* demonstrated their capabilities (Hitomi Collaboration et al., 2018, e.g.) but a spacecraft failure prevented collection of more than a brief interval of data. This will provide unprecedented spectral resolution with good collecting area at high energies (up to ~ 10 keV) which will allow clean separation of distant and blurred reflection and detailed measurements of high energy absorption lines from winds.

From the early 2030s, *Athena* will provide a vastly greater collecting area than current instruments. This will allow detailed measurements to be made of AGN at cosmological distances, showing how they change with the age of the universe.

Various other missions are currently planned or in a competitive selection process, including: *STROBE-X*; *Lynx*; *HEX-P*; and *AXIS*. Together, these cover all aspects and energy bands of X-ray astronomy so at least some areas are likely to be provided with even more advances in data quality.

References

Abbott, B. P., Abbott, R., Abbott, T. D., Abernathy, M. R., Acernese, F., Ackley, K., Adams, C., Adams, T., Addesso, P., Adhikari, R. X., and et al. (2016). Observation of Gravitational Waves from a Binary Black Hole Merger. *Physical Review Letters*, 116(6):061102.

Akylas, A., Georgantopoulos, I., and Comastri, A. (2001). BeppoSAX observations of the Seyfert 2 galaxies NGC 7172 and ESO 103-G35. *MNRAS*, 324:521–528.

Alston, W. N., Done, C., and Vaughan, S. (2014). X-ray time delays in the narrow line Seyfert 1 galaxy PG 1244+026. *MNRAS*, 439:1548–1555.

Alston, W. N., Vaughan, S., and Uttley, P. (2013). Ultraviolet and X-ray variability of NGC 4051 over 45 days with XMM-Newton and Swift. *MNRAS*, 429:75–84.

Antonucci, R. (1993). Unified models for active galactic nuclei and quasars. *ARAA*, 31:473–521.

Arévalo, P., Papadakis, I., Kuhlbrodt, B., and Brinkmann, W. (2005). X-ray to UV variability correlation in MCG-6-30-15. *AAP*, 430:435–442.

Arévalo, P. and Uttley, P. (2006). Investigating a fluctuating-accretion model for the spectral-timing properties of accreting black hole systems. *MNRAS*, 367:801–814.

Arnaud, K. A. (1996). XSPEC: The First Ten Years. In Jacoby, G. H. and Barnes, J., editors, *Astronomical Data Analysis Software and Systems V*, volume 101 of *Astronomical Society of the Pacific Conference Series*, page 17.

Arur, K. and Maccarone, T. J. (2019). Non-linear variability of quasi-periodic oscillations in GX 339-4. *MNRAS*, 486(3):3451–3458.

Aschenbach, B. (2002). In-orbit performance of the XMM-Newton x-ray telescopes: images and spectra. In Gorenstein, P. and Hoover, R. B., editors, *X-Ray Optics for Astronomy: Telescopes, Multilayers, Spectrometers, and Missions*, volume 4496 of *Society of Photo-Optical Instrumentation Engineers (SPIE) Conference Series*, pages 8–22.

Ashton, C. E., Page, M. J., Branduardi-Raymont, G., and Blustin, A. J. (2006). XMM-Newton observations of the Seyfert 1 AGN H0557-385. *MNRAS*, 366:521–528.

Bachetti, M. (2015). MaLTPyNT: Quick look timing analysis for NuSTAR data. Astrophysics Source Code Library.

Bachetti, M., Harrison, F. A., Cook, R., Tomsick, J., Schmid, C., Grefenstette, B. W., Barret, D., Boggs, S. E., Christensen, F. E., Craig, W. W., Fabian, A. C., Fürst, F., Gandhi, P., Hailey, C. J., Kara, E., Maccarone, T. J., Miller, J. M., Pottschmidt, K., Stern, D., Uttley, P., Walton, D. J., Wilms, J., and Zhang, W. W. (2015). No Time for Dead Time: Timing Analysis of Bright Black Hole Binaries with NuSTAR. *ApJ*, 800:109.

Bachetti, M. and Huppenkothen, D. (2018). No Time for Dead Time: Use the Fourier Amplitude Differences to Normalize Dead-time-affected Periodograms. *ApJL*, 853:L21.

Bachev, R., Grupe, D., Boeva, S., Ovcharov, E., Valcheva, A., Semkov, E., Georgiev, T., and Gallo, L. C. (2009). Studying X-ray reprocessing and continuum variability in quasars: PG 1211+143. *MNRAS*, 399:750–761.

Balbus, S. A. and Hawley, J. F. (1991). A Powerful Local Shear Instability in Weakly Magnetized Disks. I. Linear Analysis. *ApJ*, 376:214.

Balbus, S. A. and Hawley, J. F. (1992). A Powerful Local Shear Instability in Weakly Magnetized Disks. IV. Nonaxisymmetric Perturbations. *ApJ*, 400:610–621.

Baloković, M., Matt, G., Harrison, F. A., Zoghbi, A., Ballantyne, D. R., Boggs, S. E., Christensen, F. E., Craig, W. W., Esmerian, C. J., Fabian, A. C., Fürst, F., Hailey, C. J., Marinucci, A., Parker, M. L., Reynolds, C. S., Stern, D., Walton, D. J., and Zhang, W. W. (2015). Coronal Properties of the Seyfert 1.9 Galaxy MCG-05-23-016 Determined from Hard X-Ray Spectroscopy with NuSTAR. *ApJ*, 800:62.

Bardeen, J. M. (1970). Kerr Metric Black Holes. *Nature*, 226(5240):64–65.

Beckmann, V. and Shrader, C. R. (2012). *Active Galactic Nuclei*.

Belloni, T., Psaltis, D., and van der Klis, M. (2002). A Unified Description of the Timing Features of Accreting X-Ray Binaries. *ApJ*, 572:392–406.

Belloni, T. M. (2010). *States and Transitions in Black Hole Binaries*, volume 794, page 53.

Bennert, N., Schulz, H., and Henkel, C. (2004). Spectral characteristics of water mega-maser galaxies. II. <ASTROBJ>ESO 103-G035</ASTROBJ>, <ASTROBJ>TXS 2226-184</ASTROBJ>, and <ASTROBJ>IC 1481</ASTROBJ>. *AAP*, 419:127–137.

Bentz, M. C. and Katz, S. (2015). The AGN Black Hole Mass Database. *PASP*, 127:67–73.

Bentz, M. C., Peterson, B. M., Netzer, H., Pogge, R. W., and Vestergaard, M. (2009). The Radius-Luminosity Relationship for Active Galactic Nuclei: The Effect of Host-Galaxy Starlight on Luminosity Measurements. II. The Full Sample of Reverberation-Mapped AGNs. *ApJ*, 697:160–181.

Bentz, M. C., Peterson, B. M., Pogge, R. W., Vestergaard, M., and Onken, C. A. (2006). The Radius-Luminosity Relationship for Active Galactic Nuclei: The Effect of Host-Galaxy Starlight on Luminosity Measurements. *ApJ*, 644:133–142.

Bentz, M. C., Walsh, J. L., Barth, A. J., Yoshii, Y., Woo, J.-H., Wang, X., Treu, T., Thornton, C. E., Street, R. A., Steele, T. N., Silverman, J. M., Serduke, F. J. D., Sakata, Y., Minezaki, T., Malkan, M. A., Li, W., Lee, N., Hiner, K. D., Hidas, M. G., Greene, J. E., Gates, E. L., Ganeshalingam, M., Filippenko, A. V., Canalizo, G., Bennert, V. N., and Baliber, N. (2010). The Lick AGN Monitoring Project: Reverberation Mapping of Optical Hydrogen and Helium Recombination Lines. *ApJ*, 716:993–1011.

Bevington, P. R. and Robinson, D. K. (1992). *Data reduction and error analysis for the physical sciences*.

Bianchi, S., Guainazzi, M., Matt, G., Fonseca Bonilla, N., and Ponti, G. (2009). CAIXA: a catalogue of AGN in the XMM-Newton archive. I. Spectral analysis. *AAP*, 495:421–430.

Birkhoff, G. D. and Langer, R. E. (1923). *Relativity and modern physics*.

Bisnovatyi-Kogan, G. S., Zel'dovich, Y. B., and Syunyaev, R. A. (1971). Physical Processes in a Low-Density Relativistic Plasma. , 15:17.

Blaes, O. (2014). General Overview of Black Hole Accretion Theory. *SSR*, 183(1-4):21–41.

Blandford, R. D. and McKee, C. F. (1982). Reverberation mapping of the emission line regions of Seyfert galaxies and quasars. *ApJ*, 255:419–439.

Boissay, R., Paltani, S., Ponti, G., Bianchi, S., Cappi, M., Kaastra, J. S., Petrucci, P.-O., Arav, N., Branduardi-Raymont, G., Costantini, E., Ebrero, J., Kriss, G. A., Mehdipour, M., Pinto, C., and Steenbrugge, K. C. (2014). Multiwavelength campaign on Mrk 509. XIII. Testing ionized-reflection models on Mrk 509. *AAP*, 567:A44.

Boller, T., Brandt, W. N., Fabian, A. C., and Fink, H. H. (1997). ROSAT monitoring of persistent giant and rapid variability in the narrow-line Seyfert 1 galaxy IRAS 13224-3809. *MNRAS*, 289:393–405.

Bolton, C. T. (1972). Identification of Cygnus X-1 with HDE 226868. *Nature*, 235:271–273.

Branduardi-Raymont, G., Sako, M., Kahn, S. M., Brinkman, A. C., Kaastra, J. S., and Page, M. J. (2001). Soft X-ray emission lines from a relativistic accretion disk in <ASTROBJ>MCG -6-30-15</ASTROBJ> and <ASTROBJ>Mrk 766</ASTROBJ>. *AAP*, 365:L140–L145.

Breedt, E., McHardy, I. M., Arévalo, P., Uttley, P., Sergeev, S. G., Minezaki, T., Yoshii, Y., Sakata, Y., Lira, P., and Chesnok, N. G. (2010). Twelve years of X-ray and optical variability in the Seyfert galaxy NGC 4051. *MNRAS*, 403:605–619.

Brenneman, L. W., Madejski, G., Fuerst, F., Matt, G., Elvis, M., Harrison, F. A., Ballantyne, D. R., Boggs, S. E., Christensen, F. E., Craig, W. W., Fabian, A. C., Grefenstette, B. W., Hailey, C. J., Madsen, K. K., Marinucci, A., Rivers, E., Stern, D., Walton, D. J., and Zhang, W. W. (2014). The Broad-band X-Ray Spectrum of IC 4329A from a Joint NuSTAR/Suzaku Observation. *ApJ*, 788:61.

Brinkman, A., Aarts, H., den Boggende, A., Bootsma, T., Dubbeldam, L., den Herder, J., Kaastra, J., de Korte, P., van Leeuwen, B., Mewe, R., Paerels, F., de Vries, C., Cottam, J., Decker, T., Kahn, S., Rasmussen, A., Spodek, J., Branduardi-Raymont, G., Guttridge, P., Thomsen, K., Zehnder, A., and Guedel, M. (1998). The Reflection Grating Spectrometer onboard XMM. In *Science with XMM*, page 2.

Buisson, D., Fabian, A., Alston, W., Walton, D., Kara, E., Garcia, J., Homan, J., and Tomsick, J. (2018). Exponential increase in X-ray QPO frequency with time in MAXI J1820+070. *The Astronomer's Telegram*, 11578.

Buisson, D. J. K., Lohfink, A. M., Alston, W. N., and Fabian, A. C. (2017). Ultraviolet and X-ray variability of active galactic nuclei with Swift. *MNRAS*, 464:3194–3218.

Burrows, D. N., Hill, J. E., Nousek, J. A., Kennea, J. A., Wells, A., Osborne, J. P., Abbey, A. F., Beardmore, A., Mukerjee, K., Short, A. D. T., Chincarini, G., Campana, S., Citterio, O., Moretti, A., Pagani, C., Tagliaferri, G., Giommi, P., Capalbi, M., Tamburelli, F., Angelini, L., Cusumano, G., Bräuninger, H. W., Burkert, W., and Hartner, G. D. (2005). The Swift X-Ray Telescope. *SSR*, 120:165–195.

Cackett, E. M., Chiang, C.-Y., McHardy, I., Edelson, R., Goad, M. R., Horne, K., and Korista, K. T. (2017). Accretion disk reverberation with Hubble Space Telescope observations of NGC 4593: evidence for diffuse continuum lags. *ArXiv e-prints*.

Cackett, E. M., Horne, K., and Winkler, H. (2007). Testing thermal reprocessing in active galactic nuclei accretion discs. *MNRAS*, 380:669–682.

Cameron, D. T., McHardy, I., Dwelly, T., Breedt, E., Uttley, P., Lira, P., and Arevalo, P. (2012). Correlated X-ray/ultraviolet/optical variability in the very low mass AGN NGC 4395. *MNRAS*, 422:902–912.

Cardelli, J. A., Clayton, G. C., and Mathis, J. S. (1989). The relationship between infrared, optical, and ultraviolet extinction. *ApJ*, 345:245–256.

Carter, B. (1971). Axisymmetric Black Hole Has Only Two Degrees of Freedom. *Physical Review Letters*, 26:331–333.

Casella, P., Belloni, T., Homan, J., and Stella, L. (2004). A study of the low-frequency quasi-periodic oscillations in the X-ray light curves of the black hole candidate <ASTROBJ>XTE J1859+226</ASTROBJ>. *AAP*, 426:587–600.

Cash, W. (1979). Parameter estimation in astronomy through application of the likelihood ratio. *ApJ*, 228:939–947.

Chartas, G., Kochanek, C. S., Dai, X., Moore, D., Mosquera, A. M., and Blackburne, J. A. (2012). Revealing the Structure of an Accretion Disk through Energy-dependent X-Ray Microlensing. *ApJ*, 757:137.

Chartas, G., Rhea, C., Kochanek, C., Dai, X., Morgan, C., Blackburne, J., Chen, B., Mosquera, A., and MacLeod, C. (2016). Gravitational lensing size scales for quasars. *Astronomische Nachrichten*, 337:356.

Chiang, C.-Y., Walton, D. J., Fabian, A. C., Wilkins, D. R., and Gallo, L. C. (2015). Modelling the extreme X-ray spectrum of IRAS 13224-3809. *MNRAS*, 446:759–769.

Collier, S., Horne, K., Wanders, I., and Peterson, B. M. (1999). A new direct method for measuring the Hubble constant from reverberating accretion discs in active galaxies. *MNRAS*, 302:L24–L28.

Collier, S. J., Horne, K., Kaspi, S., Netzer, H., Peterson, B. M., Wanders, I., Alexander, T., Bertram, R., Comastri, A., Gaskell, C. M., Malkov, Y. F., Maoz, D., Mignoli, M., Pogge, R. W., Pronik, V. I., Sergeev, S. G., Snedden, S., Stirpe, G. M., Bochkarev, N. G., Burenkov, A. N., Shapovalova, A. I., and Wagner, R. M. (1998). Steps toward Determination of the Size and Structure of the Broad-Line Region in Active Galactic Nuclei. XIV. Intensive Optical Spectrophotometric Observations of NGC 7469. *ApJ*, 500:162–172.

Combi, J. A., Ribó, M., and Mirabel, I. F. (2005). On the Nature of the Unidentified X-ray/γ-ray Sources Igr J18027 1455 and Igr J21247+5058. , 297:385–391.

Coppi, P. S. (2000). EQPAIR: A Hybrid Thermal/Non-Thermal Model for the Spectra of X-Ray Binaries. In *AAS/High Energy Astrophysics Division #5*, volume 5 of *AAS/High Energy Astrophysics Division*, page 23.11.

Courvoisier, T. J. L. (2013). *High Energy Astrophysics*.

Crummy, J., Fabian, A. C., Gallo, L., and Ross, R. R. (2006). An explanation for the soft X-ray excess in active galactic nuclei. *MNRAS*, 365(4):1067–1081.

Czerny, B., Nikołajuk, M., Piasecki, M., and Kuraszkiewicz, J. (2001). Black hole masses from power density spectra: determinations and consequences. *MNRAS*, 325:865–874.

Dai, X., Kochanek, C. S., Chartas, G., Kozłowski, S., Morgan, C. W., Garmire, G., and Agol, E. (2010). The Sizes of the X-ray and Optical Emission Regions of RXJ 1131-1231. *ApJ*, 709:278–285.

Dauser, T., García, J., Walton, D. J., Eikmann, W., Kallman, T., McClintock, J., and Wilms, J. (2016). Normalizing a relativistic model of X-ray reflection. Definition of the reflection fraction and its implementation in relxill. *AAP*, 590:A76.

Dauser, T., Svoboda, J., Schartel, N., Wilms, J., Dovčiak, M., Ehle, M., Karas, V., Santos-Lleó, M., and Marshall, H. L. (2012). Spectral analysis of 1H 0707-495 with XMM-Newton. *MNRAS*, 422:1914–1921.

Dauser, T., Wilms, J., Reynolds, C. S., and Brenneman, L. W. (2010). Broad emission lines for a negatively spinning black hole. *MNRAS*, 409:1534–1540.

Davis, S. W. and El-Abd, S. (2019). Spectral Hardening in Black Hole Accretion: Giving Spectral Modelers an f. *ApJ*, 874:23.

Davis, S. W., Woo, J.-H., and Blaes, O. M. (2007). The UV Continuum of Quasars: Models and SDSS Spectral Slopes. *ApJ*, 668:682–698.

De Marco, B., Ponti, G., Cappi, M., Dadina, M., Uttley, P., Cackett, E. M., Fabian, A. C., and Miniutti, G. (2013). Discovery of a relation between black hole mass and soft X-ray time lags in active galactic nuclei. *MNRAS*, 431:2441–2452.

De Marco, B., Ponti, G., Uttley, P., Cappi, M., Dadina, M., Fabian, A. C., and Miniutti, G. (2011). PG 1211+143: probing high-frequency lags in a high-mass active galactic nucleus. *MNRAS*, 417:L98–L102.

den Herder, J. W., Brinkman, A. C., Kahn, S. M., Brand uardi-Raymont, G., Thomsen, K., Aarts, H., Audard, M., Bixler, J. V., den Boggende, A. J., Cottam, J., Decker, T., Dubbeldam, L., Erd, C., Goulooze, H., Güdel, M., Guttridge, P., Hailey, C. J., Janabi, K. A., Kaastra, J. S., de Korte, P. A. J., van Leeuwen, B. J., Mauche, C., McCalden, A. J., Mewe, R., Naber, A., Paerels, F. B., Peterson, J. R., Rasmussen, A. P., Rees, K., Sakelliou, I., Sako, M., Spodek, J., Stern, M., Tamura, T., Tandy, J., de Vries, C. P., Welch, S., and Zehnder, A. (2001). The Reflection Grating Spectrometer on board XMM-Newton. *AAP*, 365:L7–L17.

Denisenko, D. (2018). Optical follow-up of MAXI J1820+070 and possible identity with ASASSN-18ey. *The Astronomer's Telegram*, 11400.

Dewangan, G. C., Boller, T., Singh, K. P., and Leighly, K. M. (2002). A 10-day ASCA observation of the narrow-line Seyfert 1 galaxy IRAS 13224-3809. *AAP*, 390:65–80.

Dewangan, G. C., Griffiths, R. E., Dasgupta, S., and Rao, A. R. (2007). An Investigation of the Origin of Soft X-Ray Excess Emission from Ark 564 and Mrk 1044. *ApJ*, 671(2):1284–1296.

Dexter, J. and Agol, E. (2011). Quasar Accretion Disks are Strongly Inhomogeneous. *ApJL*, 727:L24.

Dickey, J. M. and Lockman, F. J. (1990). H I in the Galaxy. *ARAA*, 28:215–261.

Done, C., Gierliński, M., and Kubota, A. (2007). Modelling the behaviour of accretion flows in X-ray binaries. Everything you always wanted to know about accretion but were afraid to ask. *AAPR*, 15:1–66.

Edelson, R., Gelbord, J., Cackett, E., Connolly, S., Done, C., Fausnaugh, M., Gardner, E., Gehrels, N., Goad, M., Horne, K., McHardy, I., Peterson, B. M., Vaughan, S., Vestergaard, M., Breeveld, A., Barth, A. J., Bentz, M., Bottorff, M., Brandt, W. N., Crawford, S. M., Dalla Bontà, E., Emmanoulopoulos, D., Evans, P., Figuera Jaimes, R., Filippenko, A. V., Ferland, G., Grupe, D., Joner, M., Kennea, J., Korista, K. T., Krimm, H. A., Kriss, G., Leonard, D. C., Mathur, S., Netzer, H., Nousek, J., Page, K., Romero-Colmenero, E., Siegel, M., Starkey, D. A., Treu, T., Vogler, H. A., Winkler, H., and Zheng, W. (2017). Swift Monitoring of NGC 4151: Evidence for a Second X-Ray/UV Reprocessing. *ApJ*, 840:41.

Edelson, R., Gelbord, J. M., Horne, K., McHardy, I. M., Peterson, B. M., Arévalo, P., Breeveld, A. A., De Rosa, G., Evans, P. A., Goad, M. R., Kriss, G. A., Brandt, W. N., Gehrels, N., Grupe, D., Kennea, J. A., Kochanek, C. S., Nousek, J. A., Papadakis, I., Siegel, M., Starkey, D., Uttley, P., Vaughan, S., Young, S., Barth, A. J., Bentz, M. C., Brewer, B. J., Crenshaw, D. M., Dalla Bontà, E., De Lorenzo-Cáceres, A., Denney, K. D., Dietrich, M., Ely, J., Fausnaugh, M. M., Grier, C. J., Hall, P. B., Kaastra, J., Kelly, B. C., Korista, K. T., Lira, P., Mathur, S., Netzer, H., Pancoast, A., Pei, L., Pogge, R. W., Schimoia, J. S., Treu, T., Vestergaard, M., Villforth, C., Yan, H., and Zu, Y. (2015). Space Telescope and

Optical Reverberation Mapping Project. II. Swift and HST Reverberation Mapping of the Accretion Disk of NGC 5548. *ApJ*, 806:129.

Edelson, R., Koratkar, A., Nandra, K., Goad, M., Peterson, B. M., Collier, S., Krolik, J., Malkan, M., Maoz, D., O'Brien, P., Shull, J. M., Vaughan, S., and Warwick, R. (2000). Intensive HST, RXTE, and ASCA Monitoring of NGC 3516: Evidence against Thermal Reprocessing. *ApJ*, 534:180–188.

Edelson, R., Turner, T. J., Pounds, K., Vaughan, S., Markowitz, A., Marshall, H., Dobbie, P., and Warwick, R. (2002). X-Ray Spectral Variability and Rapid Variability of the Soft X-Ray Spectrum Seyfert 1 Galaxies Arakelian 564 and Ton S180. *ApJ*, 568:610–626.

Edelson, R. A. and Krolik, J. H. (1988). The discrete correlation function - A new method for analyzing unevenly sampled variability data. *ApJ*, 333:646–659.

Edelson, R. A., Krolik, J. H., and Pike, G. F. (1990). Broad-Band Properties of the CfA Seyfert Galaxies. III. Ultraviolet Variability. *ApJ*, 359:86.

Edwin, P. M. and Roberts, B. (1983). Wave propagation in a magnetic cylinder. , 88:179–191.

Emmanoulopoulos, D., McHardy, I. M., and Papadakis, I. E. (2011). Negative X-ray reverberation time delays from MCG-6-30-15 and Mrk 766. *MNRAS*, 416:L94–L98.

Emmanoulopoulos, D., Papadakis, I. E., Dovčiak, M., and McHardy, I. M. (2014). General relativistic modelling of the negative reverberation X-ray time delays in AGN. *MNRAS*, 439:3931–3950.

Esin, A. A., McClintock, J. E., and Narayan, R. (1997). Advection-Dominated Accretion and the Spectral States of Black Hole X-Ray Binaries: Application to Nova Muscae 1991. *ApJ*, 489:865–889.

Evans, P. A., Beardmore, A. P., Page, K. L., Osborne, J. P., O'Brien, P. T., Willingale, R., Starling, R. L. C., Burrows, D. N., Godet, O., Vetere, L., Racusin, J., Goad, M. R., Wiersema, K., Angelini, L., Capalbi, M., Chincarini, G., Gehrels, N., Kennea, J. A., Margutti, R., Morris, D. C., Mountford, C. J., Pagani, C., Perri, M., Romano, P., and Tanvir, N. (2009). Methods and results of an automatic analysis of a complete sample of Swift-XRT observations of GRBs. *MNRAS*, 397:1177–1201.

Evans, P. A., Beardmore, A. P., Page, K. L., Tyler, L. G., Osborne, J. P., Goad, M. R., O'Brien, P. T., Vetere, L., Racusin, J., Morris, D., Burrows, D. N., Capalbi, M., Perri, M., Gehrels, N., and Romano, P. (2007). An online repository of Swift/XRT light curves of γ-ray bursts. *AAP*, 469:379–385.

Event Horizon Telescope Collaboration, Akiyama, K., Alberdi, A., Alef, W., Asada, K., Azulay, R., Baczko, A.-K., Ball, D., Baloković, M., and Barrett, J. (2019). First M87 Event Horizon Telescope Results. I. The Shadow of the Supermassive Black Hole. *ApJ*, 875(1):L1.

Fabian, A. C., Iwasawa, K., Reynolds, C. S., and Young, A. J. (2000). Broad Iron Lines in Active Galactic Nuclei. *PASP*, 112:1145–1161.

Fabian, A. C., Kara, E., Walton, D. J., Wilkins, D. R., Ross, R. R., Lozanov, K., Uttley, P., Gallo, L. C., Zoghbi, A., Miniutti, G., Boller, T., Brandt, W. N., Cackett, E. M., Chiang, C.-Y., Dwelly, T., Malzac, J., Miller, J. M., Nardini, E., Ponti, G., Reis, R. C., Reynolds, C. S., Steiner, J. F., Tanaka, Y., and Young, A. J. (2013). Long XMM observation of the narrow-line Seyfert 1 galaxy IRAS 13224-3809: rapid variability, high spin and a soft lag. *MNRAS*, 429:2917–2923.

Fabian, A. C., Lohfink, A., Belmont, R., Malzac, J., and Coppi, P. (2017). Properties of AGN coronae in the NuSTAR era - II. Hybrid plasma. *MNRAS*, 467:2566–2570.

Fabian, A. C., Lohfink, A., Kara, E., Parker, M. L., Vasudevan, R., and Reynolds, C. S. (2015). Properties of AGN coronae in the NuSTAR era. *MNRAS*, 451:4375–4383.

Fabian, A. C., Rees, M. J., Stella, L., and White, N. E. (1989). X-ray fluorescence from the inner disc in Cygnus X-1. *MNRAS*, 238:729–736.

Fabian, A. C. and Ross, R. R. (2010). X-ray Reflection. *SSR*, 157:167–176.

Fabian, A. C. and Vaughan, S. (2003). The iron line in MCG-6-30-15 from XMM-Newton: evidence for gravitational light bending? *MNRAS*, 340:L28–L32.

Fabian, A. C., Zoghbi, A., Ross, R. R., Uttley, P., Gallo, L. C., Brandt, W. N., Blustin, A. J., Boller, T., Caballero-Garcia, M. D., Larsson, J., Miller, J. M., Miniutti, G., Ponti, G., Reis, R. C., Reynolds, C. S., Tanaka, Y., and Young, A. J. (2009). Broad line emission from iron K- and L-shell transitions in the active galaxy 1H0707-495. *Nature*, 459:540–542.

Fabian, A. C., Zoghbi, A., Wilkins, D., Dwelly, T., Uttley, P., Schartel, N., Miniutti, G., Gallo, L., Grupe, D., Komossa, S., and Santos-Lleó, M. (2012). 1H 0707-495 in 2011: an X-ray source within a gravitational radius of the event horizon. *MNRAS*, 419:116–123.

Farinelli, R., Titarchuk, L., Paizis, A., and Frontera, F. (2008). A New Comptonization Model for Weakly Magnetized, Accreting Neutron Stars in Low-Mass X-Ray Binaries. *ApJ*, 680(1):602–614.

Fausnaugh, M. M., Denney, K. D., Barth, A. J., Bentz, M. C., Bottorff, M. C., Carini, M. T., Croxall, K. V., De Rosa, G., Goad, M. R., Horne, K., Joner, M. D., Kaspi, S., Kim, M., Klimanov, S. A., Kochanek, C. S., Leonard, D. C., Netzer, H., Peterson, B. M., Schnülle, K., Sergeev, S. G., Vestergaard, M., Zheng, W.-K., Zu, Y., Anderson, M. D., Arévalo, P., Bazhaw, C., Borman, G. A., Boroson, T. A., Brandt, W. N., Breeveld, A. A., Brewer, B. J., Cackett, E. M., Crenshaw, D. M., Dalla Bontà, E., De Lorenzo-Cáceres, A., Dietrich, M., Edelson, R., Efimova, N. V., Ely, J., Evans, P. A., Filippenko, A. V., Flatland, K., Gehrels, N., Geier, S., Gelbord, J. M., Gonzalez, L., Gorjian, V., Grier, C. J., Grupe, D., Hall, P. B., Hicks, S., Horenstein, D., Hutchison, T., Im, M., Jensen, J. J., Jones, J., Kaastra, J., Kelly, B. C., Kennea, J. A., Kim, S. C., Korista, K. T., Kriss, G. A., Lee, J. C., Lira, P., MacInnis, F., Manne-Nicholas, E. R., Mathur, S., McHardy, I. M., Montouri, C., Musso, R., Nazarov, S. V., Norris, R. P., Nousek, J. A., Okhmat, D. N., Pancoast, A., Papadakis, I., Parks, J. R., Pei, L., Pogge, R. W., Pott, J.-U., Rafter, S. E., Rix, H.-W., Saylor, D. A., Schimoia, J. S., Siegel, M., Spencer, M., Starkey, D., Sung, H.-I., Teems, K. G., Treu, T., Turner, C. S., Uttley, P., Villforth, C., Weiss, Y., Woo, J.-H., Yan, H., and Young, S. (2016). Space Telescope and Optical Reverberation Mapping Project. III. Optical Continuum Emission and Broadband Time Delays in NGC 5548. *ApJ*, 821:56.

Fender, R. (2010). *'Disc-Jet' Coupling in Black Hole X-Ray Binaries and Active Galactic Nuclei*, volume 794, page 115.

Ferrarese, L. and Merritt, D. (2000). A Fundamental Relation between Supermassive Black Holes and Their Host Galaxies. *ApJL*, 539(1):L9–L12.

Fiori, M., Zampieri, L., Burtovoi, A., Naletto, G., Barbieri, C., Ochner, P., Umbriaco, G., Barbieri, M., and Casella, P. (2018). Other low-frequency optical QPO-like features in MAXI J1820+070 detected with IFI+IQUEYE@Galileo. *The Astronomer's Telegram*, 11824.

Foreman-Mackey, D., Hogg, D. W., Lang, D., and Goodman, J. (2013). emcee: The MCMC Hammer. *PASP*, 125:306.

Fragile, P. C., Blaes, O. M., Anninos, P., and Salmonson, J. D. (2007). Global General Relativistic Magnetohydrodynamic Simulation of a Tilted Black Hole Accretion Disk. *ApJ*, 668:417–429.

Francis, P. J., Hewett, P. C., Foltz, C. B., Chaffee, F. H., Weymann, R. J., and Morris, S. L. (1991). A high signal-to-noise ratio composite quasar spectrum. *ApJ*, 373:465–470.

Fürst, F., Grinberg, V., Tomsick, J. A., Bachetti, M., Boggs, S. E., Brightman, M., Christensen, F. E., Craig, W. W., Gandhi, P., Grefenstette, B., Hailey, C. J., Harrison, F. A., Madsen, K. K., Parker, M. L., Pottschmidt, K., Stern, D., Walton, D. J., Wilms, J., and Zhang, W. W. (2016a). Spectro-Timing Study of GX 339-4 in a Hard Intermediate State. *ApJ*, 828:34.

Fürst, F., Müller, C., Madsen, K. K., Lanz, L., Rivers, E., Brightman, M., Arevalo, P., Baloković, M., Beuchert, T., Boggs, S. E., Christensen, F. E., Craig, W. W., Dauser, T., Farrah, D., Graefe, C., Hailey, C. J., Harrison, F. A., Kadler, M., King, A., Krauß, F., Madejski, G., Matt, G., Marinucci, A., Markowitz, A., Ogle, P., Ojha, R., Rothschild, R., Stern, D., Walton, D. J., Wilms, J., and Zhang, W. (2016b). NuSTAR and XMM-Newton Observations of the Hard X-Ray Spectrum of Centaurus A. *ApJ*, 819:150.

Gandhi, P., Rao, A., Johnson, M. A. C., Paice, J. A., and Maccarone, T. J. (2018). Gaia DR2 Distances and Peculiar Velocities for Galactic Black Hole Transients. *ArXiv e-prints*.

García, J., Dauser, T., Lohfink, A., Kallman, T. R., Steiner, J. F., McClintock, J. E., Brenneman, L., Wilms, J., Eikmann, W., Reynolds, C. S., and Tombesi, F. (2014). Improved Reflection Models of Black Hole Accretion Disks: Treating the Angular Distribution of X-Rays. *ApJ*, 782:76.

García, J., Dauser, T., Reynolds, C. S., Kallman, T. R., McClintock, J. E., Wilms, J., and Eikmann, W. (2013). X-Ray Reflected Spectra from Accretion Disk Models. III. A Complete Grid of Ionized Reflection Calculations. *ApJ*, 768:146.

García, J. A., Dauser, T., Steiner, J. F., McClintock, J. E., Keck, M. L., and Wilms, J. (2015). On Estimating the High-energy Cutoff in the X-Ray Spectra of Black Holes via Reflection Spectroscopy. *ApJL*, 808:L37.

García, J. A., Fabian, A. C., Kallman, T. R., Dauser, T., Parker, M. L., McClintock, J. E., Steiner, J. F., and Wilms, J. (2016). The effects of high density on the X-ray spectrum reflected from accretion discs around black holes. *MNRAS*, 462:751–760.

García, J. A., Kallman, T. R., Bautista, M., Mendoza, C., Deprince, J., Palmeri, P., and Quinet, P. (2018). The Problem of the High Iron Abundance in Accretion Disks around Black Holes. In *Workshop on Astrophysical Opacities*, volume 515 of *Astronomical Society of the Pacific Conference Series*, page 282.

Gardner, E. and Done, C. (2017). The origin of the UV/optical lags in NGC 5548. *MNRAS*, 470:3591–3605.

Gaskell, C. M. and Klimek, E. S. (2003). Variability of Active Galactic Nuclei from Optical to X-ray Regions. *Astronomical and Astrophysical Transactions*, 22:661–680.

Gaskell, C. M. and Peterson, B. M. (1987). The accuracy of cross-correlation estimates of quasar emission-line region sizes. *ApJS*, 65:1–11.

Gaskell, C. M. and Sparke, L. S. (1986). Line variations in quasars and Seyfert galaxies. *ApJ*, 305:175–186.

Gehrels, N., Chincarini, G., Giommi, P., Mason, K. O., Nousek, J. A., Wells, A. A., White, N. E., Barthelmy, S. D., Burrows, D. N., Cominsky, L. R., Hurley, K. C., Marshall, F. E., Mészáros, P., Roming, P. W. A., Angelini, L., Barbier, L. M., Belloni, T., Campana, S., Caraveo, P. A., Chester, M. M., Citterio, O., Cline, T. L., Cropper, M. S., Cummings, J. R., Dean, A. J., Feigelson, E. D., Fenimore, E. E., Frail, D. A., Fruchter, A. S., Garmire, G. P., Gendreau, K., Ghisellini, G., Greiner, J., Hill, J. E., Hunsberger, S. D., Krimm, H. A., Kulkarni, S. R., Kumar, P., Lebrun, F., Lloyd-Ronning, N. M., Markwardt, C. B., Mattson, B. J., Mushotzky, R. F., Norris, J. P., Osborne, J., Paczynski, B., Palmer, D. M., Park, H.-S., Parsons, A. M., Paul, J., Rees, M. J., Reynolds, C. S., Rhoads, J. E., Sasseen, T. P., Schaefer, B. E., Short, A. T., Smale, A. P., Smith, I. A., Stella, L., Tagliaferri, G., Takahashi, T., Tashiro, M., Townsley, L. K., Tueller, J., Turner, M. J. L., Vietri, M., Voges, W., Ward, M. J., Willingale, R., Zerbi, F. M., and Zhang, W. W. (2004). The Swift Gamma-Ray Burst Mission. *ApJ*, 611:1005–1020.

Gendreau, K. C., Arzoumanian, Z., Adkins, P. W., Albert, C. L., Anders, J. F., Aylward, A. T., Baker, C. L., Balsamo, E. R., Bamford, W. A., Benegalrao, S. S., Berry, D. L., Bhalwani, S., Black, J. K., Blaurock, C., Bronke, G. M., Brown, G. L., Budinoff, J. G., Cantwell, J. D., Cazeau, T., Chen, P. T., Clement, T. G., Colangelo, A. T., Coleman, J. S., Coopersmith, J. D., Dehaven, W. E., Doty, J. P., Egan, M. D., Enoto, T., Fan, T. W., Ferro, D. M., Foster, R., Galassi, N. M., Gallo, L. D., Green, C. M., Grosh, D., Ha, K. Q., Hasouneh, M. A., Heefner, K. B., Hestnes, P., Hoge, L. J., Jacobs, T. M., Jørgensen, J. L., Kaiser, M. A., Kellogg, J. W., Kenyon, S. J., Koenecke, R. G., Kozon, R. P., LaMarr, B., Lambertson, M. D., Larson, A. M., Lentine, S., Lewis, J. H., Lilly, M. G., Liu, K. A., Malonis, A., Manthripragada, S. S., Markwardt, C. B., Matonak, B. D., Mcginnis, I. E., Miller, R. L., Mitchell, A. L., Mitchell, J. W., Mohammed, J. S., Monroe, C. A., Montt de Garcia, K. M., Mulé, P. D., Nagao, L. T., Ngo, S. N., Norris, E. D., Norwood, D. A., Novotka, J., Okajima, T., Olsen, L. G., Onyeachu, C. O., Orosco, H. Y., Peterson, J. R., Pevear, K. N., Pham, K. K., Pollard, S. E., Pope, J. S., Powers, D. F., Powers, C. E., Price, S. R., Prigozhin, G. Y., Ramirez, J. B., Reid, W. J., Remillard, R. A., Rogstad, E. M., Rosecrans, G. P., Rowe, J. N., Sager, J. A., Sanders, C. A., Savadkin, B., Saylor, M. R., Schaeffer, A. F., Schweiss, N. S., Semper, S. R., Serlemitsos, P. J., Shackelford, L. V., Soong, Y., Struebel, J., Vezie, M. L., Villasenor, J. S., Winternitz, L. B., Wofford, G. I., Wright, M. R., Yang, M. Y., and Yu, W. H. (2016). The Neutron star Interior Composition Explorer (NICER):

design and development. In *Space Telescopes and Instrumentation 2016: Ultraviolet to Gamma Ray*, volume 9905 of *Society of Photo-Optical Instrumentation Engineers (SPIE) Conference Series*, page 99051H.

George, I. M. and Fabian, A. C. (1991). X-ray reflection from cold matter in active galactic nuclei and X-ray binaries. *MNRAS*, 249:352–367.

Giacchè, S., Gilli, R., and Titarchuk, L. (2014). Analysis of X-ray spectral variability and black hole mass determination of the NLS1 galaxy Mrk 766. *AAP*, 562:A44.

Gibson, R. R., Brandt, W. N., and Schneider, D. P. (2008). Are Optically Selected Quasars Universally X-Ray Luminous? X-Ray-UV Relations in Sloan Digital Sky Survey Quasars. *ApJ*, 685:773–786.

Gierliński, M. and Done, C. (2004). Black hole accretion discs: reality confronts theory. *MNRAS*, 347:885–894.

Gilfanov, M. (2010). X-Ray Emission from Black-Hole Binaries. In Belloni, T., editor, *Lecture Notes in Physics, Berlin Springer Verlag*, volume 794 of *Lecture Notes in Physics, Berlin Springer Verlag*, page 17.

Gillessen, S., Eisenhauer, F., Trippe, S., Alexander, T., Genzel, R., Martins, F., and Ott, T. (2009). Monitoring Stellar Orbits Around the Massive Black Hole in the Galactic Center. *ApJ*, 692:1075–1109.

Gliozzi, M., Papadakis, I. E., Grupe, D., Brinkmann, W. P., and Räth, C. (2017). Long-term monitoring of Ark 120 with Swift. *MNRAS*, 464:3955–3964.

Gondoin, P., Aschenbach, B. R., Beijersbergen, M. W., Egger, R., Jansen, F. A., Stockman, Y., and Tock, J.-P. (1998a). Calibration of the first XMM flight mirror module: I. Image quality. In Hoover, R. B. and Walker, A. B., editors, *X-Ray Optics, Instruments, and Missions*, volume 3444 of *Society of Photo-Optical Instrumentation Engineers (SPIE) Conference Series*, pages 278–289.

Gondoin, P., Aschenbach, B. R., Beijersbergen, M. W., Egger, R., Jansen, F. A., Stockman, Y., and Tock, J.-P. (1998b). Calibration of the first XXM flight mirror module: II. Effective area. In Hoover, R. B. and Walker, A. B., editors, *X-Ray Optics, Instruments, and Missions*, volume 3444 of *Society of Photo-Optical Instrumentation Engineers (SPIE) Conference Series*, pages 290–301.

González-Martín, O. and Vaughan, S. (2012). X-ray variability of 104 active galactic nuclei. XMM-Newton power-spectrum density profiles. *AAP*, 544:A80.

Grupe, D., Komossa, S., Gallo, L. C., Lia Longinotti, A., Fabian, A. C., Pradhan, A. K., Gruberbauer, M., and Xu, D. (2012). A Remarkable Long-term Light Curve and Deep, Low-state Spectroscopy: Swift and XMM-Newton Monitoring of the NLS1 Galaxy Mkn 335. *ApJS*, 199:28.

Grupe, D., Komossa, S., Leighly, K. M., and Page, K. L. (2010). The Simultaneous Optical-to-X-Ray Spectral Energy Distribution of Soft X-Ray Selected Active Galactic Nuclei Observed by Swift. *ApJS*, 187:64–106.

Guainazzi, M. and Bianchi, S. (2007). On the origin of soft X-rays in obscured AGN: answers from high-resolution spectroscopy with XMM-Newton. *MNRAS*, 374:1290–1302.

Guilbert, P. W., Fabian, A. C., and Rees, M. J. (1983). Spectral and variability constraints on compact sources. *MNRAS*, 205:593–603.

Haardt, F. and Maraschi, L. (1991). A two-phase model for the X-ray emission from Seyfert galaxies. *ApJL*, 380:L51–L54.

Haardt, F. and Maraschi, L. (1993). X-ray spectra from two-phase accretion disks. *ApJ*, 413:507–517.

Halpern, J. P. (1984). Variable X-ray absorption in the QSO MR 2251-178. *ApJ*, 281:90–94.

Harrison, F. A., Craig, W. W., Christensen, F. E., Hailey, C. J., Zhang, W. W., Boggs, S. E., Stern, D., Cook, W. R., Forster, K., Giommi, P., Grefenstette, B. W., Kim, Y., Kitaguchi, T., Koglin, J. E., Madsen, K. K., Mao, P. H., Miyasaka, H., Mori, K., Perri, M., Pivovaroff, M. J., Puccetti, S., Rana, V. R., Westergaard, N. J., Willis, J., Zoglauer, A., An, H., Bachetti, M., Barrière, N. M., Bellm, E. C., Bhalerao, V., Brejnholt, N. F., Fuerst, F., Liebe, C. C., Markwardt, C. B., Nynka, M., Vogel, J. K., Walton, D. J., Wik, D. R., Alexander, D. M., Cominsky, L. R., Hornschemeier, A. E., Hornstrup, A., Kaspi, V. M., Madejski, G. M., Matt, G., Molendi, S., Smith, D. M., Tomsick, J. A., Ajello, M., Ballantyne, D. R., Baloković, M., Barret, D., Bauer, F. E., Blandford, R. D., Brandt, W. N., Brenneman, L. W., Chiang, J., Chakrabarty, D., Chenevez, J., Comastri, A., Dufour, F., Elvis, M., Fabian, A. C., Farrah, D., Fryer, C. L., Gotthelf, E. V., Grindlay, J. E., Helfand, D. J., Krivonos, R., Meier, D. L., Miller, J. M., Natalucci, L., Ogle, P., Ofek, E. O., Ptak, A., Reynolds, S. P., Rigby, J. R., Tagliaferri, G., Thorsett, S. E., Treister, E., and Urry, C. M. (2013). The Nuclear Spectroscopic Telescope Array (NuSTAR) High-energy X-Ray Mission. *ApJ*, 770:103.

Hawking, S. W. (1974). Black hole explosions? *Nature*, 248(5443):30–31.

Hitomi Collaboration, Aharonian, F., Akamatsu, H., Akimoto, F., Allen, S. W., Angelini, L., Audard, M., Awaki, H., Axelsson, M., Bamba, A., Bautz, M. W., Blandford, R., Brenneman, L. W., Brown, G. V., Bulbul, E., Cackett, E. M., Canning, R. E. A., Chernyakova, M., Chiao, M. P., Coppi, P. S., Costantini, E., de Plaa, J., de Vries, C. P., den Herder, J.-W., Done, C., Dotani, T., Ebisawa, K., Eckart, M. E., Enoto, T., Ezoe, Y., Fabian, A. C., Ferrigno, C., Foster, A. R., Fujimoto, R., Fukazawa, Y., Furuzawa, A., Galeazzi, M., Gallo, L. C., Gandhi, P., Giustini, M., Goldwurm, A., Gu, L., Guainazzi, M., Haba, Y., Hagino, K., Hamaguchi, K., Harrus, I. M., Hatsukade, I., Hayashi, K., Hayashi, T., Hayashi, T., Hayashida, K., Hiraga, J. S., Hornschemeier, A., Hoshino, A., Hughes, J. P., Ichinohe, Y., Iizuka, R., Inoue, H., Inoue, S., Inoue, Y., Ishida, M., Ishikawa, K., Ishisaki, Y., Iwai, M., Kaastra, J., Kallman, T., Kamae, T., Kataoka, J., Katsuda, S., Kawai, N., Kelley, R. L., Kilbourne, C. A., Kitaguchi, T., Kitamoto, S., Kitayama, T., Kohmura, T., Kokubun, M., Koyama, K., Koyama, S., Kretschmar, P., Krimm, H. A., Kubota, A., Kunieda, H., Laurent, P., Lee, S.-H., Leutenegger, M. A., Limousin, O., Loewenstein, M., Long, K. S., Lumb, D., Madejski, G., Maeda, Y., Maier, D., Makishima, K., Markevitch, M., Matsumoto, H., Matsushita, K., McCammon, D., McNamara, B. R., Mehdipour, M., Miller, E. D., Miller, J. M., Mineshige, S., Mitsuda, K., Mitsuishi, I., Miyazawa, T., Mizuno, T., Mori, H., Mori, K., Mukai, K., Murakami, H., Mushotzky, R. F., Nakagawa, T., Nakajima, H., Nakamori,

T., Nakashima, S., Nakazawa, K., Nobukawa, K. K., Nobukawa, M., Noda, H., Odaka, H., Ohashi, T., Ohno, M., Okajima, T., Ota, N., Ozaki, M., Paerels, F., Paltani, S., Petre, R., Pinto, C., Porter, F. S., Pottschmidt, K., Reynolds, C. S., Safi-Harb, S., Saito, S., Sakai, K., Sasaki, T., Sato, G., Sato, K., Sato, R., Sawada, M., Schartel, N., Serlemtsos, P. J., Seta, H., Shidatsu, M., Simionescu, A., Smith, R. K., Soong, Y., Stawarz, Ł., Sugawara, Y., Sugita, S., Szymkowiak, A., Tajima, H., Takahashi, H., Takahashi, T., Takeda, S., Takei, Y., Tamagawa, T., Tamura, T., Tanaka, K., Tanaka, T., Tanaka, Y., Tanaka, Y. T., Tashiro, M. S., Tawara, Y., Terada, Y., Terashima, Y., Tombesi, F., Tomida, H., Tsuboi, Y., Tsujimoto, M., Tsunemi, H., Tsuru, T. G., Uchida, H., Uchiyama, H., Uchiyama, Y., Ueda, S., Ueda, Y., Uno, S., Urry, C. M., Ursino, E., Wang, Q. H. S., Watanabe, S., Werner, N., Wilkins, D. R., Williams, B. J., Yamada, S., Yamaguchi, H., Yamaoka, K., Yamasaki, N. Y., Yamauchi, M., Yamauchi, S., Yaqoob, T., Yatsu, Y., Yonetoku, D., Zhuravleva, I., and Zoghbi, A. (2018). Atmospheric gas dynamics in the Perseus cluster observed with Hitomi. *PASJ*, 70(2):9.

Hjorth, J., Vestergaard, M., Sorensen, A. N., and Grundahl, F. (1995). Detection of a Faint Optical Jet in 3C 120. *ApJL*, 452:L17.

Holczer, T., Behar, E., and Arav, N. (2010). X-ray Absorption Analysis of MCG -6-30-15: Discerning Three Kinematic Systems. *ApJ*, 708:981–994.

Homan, J., Altamirano, D., Arzoumanian, Z., Buisson, D., Eikenberry, S., Fabian, A. C., Gendreau, K., Kara, E., Ludlam, R., Neilsen, J., Ray, P. S., Remillard, R., Steiner, J., Uttley, P., and Nicer Team (2018). NICER observations of MAXI J1820+070: Continuing evolution of X-ray variability properties. *The Astronomer's Telegram*, 11576.

Homan, J., Wijnands, R., van der Klis, M., Belloni, T., van Paradijs, J., Klein-Wolt, M., Fender, R., and Méndez, M. (2001). Correlated X-Ray Spectral and Timing Behavior of the Black Hole Candidate XTE J1550-564: A New Interpretation of Black Hole States. *ApJS*, 132:377–402.

Houck, J. C. and Denicola, L. A. (2000). ISIS: An Interactive Spectral Interpretation System for High Resolution X-Ray Spectroscopy. In Manset, N., Veillet, C., and Crabtree, D., editors, *Astronomical Data Analysis Software and Systems IX*, volume 216 of *Astronomical Society of the Pacific Conference Series*, page 591.

Ingram, A. and Done, C. (2011). A physical model for the continuum variability and quasi-periodic oscillation in accreting black holes. *MNRAS*, 415:2323–2335.

Ingram, A., Done, C., and Fragile, P. C. (2009). Low-frequency quasi-periodic oscillations spectra and Lense-Thirring precession. *MNRAS*, 397:L101–L105.

Ingram, A. and van der Klis, M. (2015). Phase-resolved spectroscopy of low-frequency quasi-periodic oscillations in GRS 1915+105. *MNRAS*, 446:3516–3525.

Ingram, A., van der Klis, M., Middleton, M., Altamirano, D., and Uttley, P. (2017). Tomographic reflection modelling of quasi-periodic oscillations in the black hole binary H 1743-322. *MNRAS*, 464(3):2979–2991.

Ingram, A., van der Klis, M., Middleton, M., Done, C., Altamirano, D., Heil, L., Uttley, P., and Axelsson, M. (2016). A quasi-periodic modulation of the iron line centroid energy in the black hole binary H1743-322. *MNRAS*, 461(2):1967–1980.

Inoue, H. (2003). The Astro-E mission. *Advances in Space Research*, 32:2089–2090.

Israel, W. (1967). Event Horizons in Static Vacuum Space-Times. *Physical Review*, 164:1776–1779.

Israel, W. (1968). Event horizons in static electrovac space-times. *Communications in Mathematical Physics*, 8:245–260.

Jansen, F., Lumb, D., Altieri, B., Clavel, J., Ehle, M., Erd, C., Gabriel, C., Guainazzi, M., Gondoin, P., Much, R., Munoz, R., Santos, M., Schartel, N., Texier, D., and Vacanti, G. (2001). XMM-Newton observatory. I. The spacecraft and operations. *AAP*, 365:L1–L6.

Jebsen, J. T. (1921). On the General Spherically Symmetric Solutions of Einstein's Gravitational Equations in Vacuo. *Arkiv for Matematik, Astronomi och Fysik*, 15(18):18.

Jeffery, G. B. (1921). The Field of an Electron on Einstein's Theory of Gravitation. *Proceedings of the Royal Society of London Series A*, 99:123–134.

Jiang, J., Fabian, A. C., Wang, J., Walton, D. J., García, J. A., Parker, M. L., Steiner, J. F., and Tomsick, J. A. (2019). High-density reflection spectroscopy: I. A case study of GX 339-4. *MNRAS*, 484:1972–1982.

Jiang, J., Parker, M. L., Fabian, A. C., Alston, W. N., Buisson, D. J. K., Cackett, E. M., Chiang, C. Y., Dauser, T., Gallo, L. C., García, J. A., Harrison, F. A., Lohfink, A. M., De Marco, B., Kara, E., Miller, J. M., Miniutti, G., Pinto, C., Walton, D. J., and Wilkins, D. R. (2018). The 1.5 Ms observing campaign on IRAS 13224-3809 - I. X-ray spectral analysis. *MNRAS*, 477(3):3711–3726.

Joinet, A., Kalemci, E., and Senziani, F. (2008). Hard X-Ray Emission of the Microquasar GRO J1655-40 during the Rise of Its 2005 Outburst. *ApJ*, 679:655–663.

Just, D. W., Brandt, W. N., Shemmer, O., Steffen, A. T., Schneider, D. P., Chartas, G., and Garmire, G. P. (2007). The X-Ray Properties of the Most Luminous Quasars from the Sloan Digital Sky Survey. *ApJ*, 665:1004–1022.

Kaastra, J. S., Mewe, R., and Nieuwenhuijzen, H. (1996). SPEX: a new code for spectral analysis of X UV spectra. In Yamashita, K. and Watanabe, T., editors, *UV and X-ray Spectroscopy of Astrophysical and Laboratory Plasmas*, pages 411–414.

Kalberla, P. M. W., Burton, W. B., Hartmann, D., Arnal, E. M., Bajaja, E., Morras, R., and Pöppel, W. G. L. (2005). The Leiden/Argentine/Bonn (LAB) Survey of Galactic HI. Final data release of the combined LDS and IAR surveys with improved stray-radiation corrections. *AAP*, 440:775–782.

Kallman, T. and Bautista, M. (2001). Photoionization and High-Density Gas. *ApJS*, 133:221–253.

Kara, E., Alston, W., and Fabian, A. (2016a). A global look at X-ray time lags in Seyfert galaxies. *Astronomische Nachrichten*, 337:473.

Kara, E., Alston, W. N., Fabian, A. C., Cackett, E. M., Uttley, P., Reynolds, C. S., and Zoghbi, A. (2016b). A global look at X-ray time lags in Seyfert galaxies. *MNRAS*, 462:511–531.

Kara, E., Cackett, E. M., Fabian, A. C., Reynolds, C., and Uttley, P. (2014a). The curious time lags of PG 1244+026: discovery of the iron K reverberation lag. *MNRAS*, 439:L26–L30.

Kara, E., Fabian, A. C., Cackett, E. M., Miniutti, G., and Uttley, P. (2013a). Revealing the X-ray source in IRAS 13224-3809 through flux-dependent reverberation lags. *MNRAS*, 430:1408–1413.

Kara, E., Fabian, A. C., Cackett, E. M., Steiner, J. F., Uttley, P., Wilkins, D. R., and Zoghbi, A. (2013b). The closest look at 1H0707-495: X-ray reverberation lags with 1.3 Ms of data. *MNRAS*, 428:2795–2804.

Kara, E., Fabian, A. C., Cackett, E. M., Uttley, P., Wilkins, D. R., and Zoghbi, A. (2013c). Discovery of high-frequency iron K lags in Ark 564 and Mrk 335. *MNRAS*, 434:1129–1137.

Kara, E., Fabian, A. C., Cackett, E. M., Uttley, P., Wilkins, D. R., and Zoghbi, A. (2013d). Discovery of high-frequency iron K lags in Ark 564 and Mrk 335. *MNRAS*.

Kara, E., Fabian, A. C., Lohfink, A. M., Parker, M. L., Walton, D. J., Boggs, S. E., Christensen, F. E., Hailey, C. J., Harrison, F. A., Matt, G., Reynolds, C. S., Stern, D., and Zhang, W. W. (2015). The Compton hump and variable blue wing in the extreme low-flux NuSTAR observations of 1H0707-495. *MNRAS*, 449:234–242.

Kara, E., Fabian, A. C., Marinucci, A., Matt, G., Parker, M. L., Alston, W., Brenneman, L. W., Cackett, E. M., and Miniutti, G. (2014b). The changing X-ray time lag in MCG-6-30-15. *MNRAS*, 445:56–65.

Kara, E., Garcia, J. A., Lohfink, A., Fabian, A. C., Reynolds, C. S., Tombesi, F., and Wilkins, D. R. (2017). The high-Eddington NLS1 Ark 564 has the coolest corona. *ArXiv e-prints*.

Kara, E., Steiner, J. F., Fabian, A. C., Cackett, E. M., Uttley, P., Remillard, R. A., Gendreau, K. C., Arzoumanian, Z., Altamirano, D., Eikenberry, S., Enoto, T., Homan, J., Neilsen, J., and Stevens, A. L. (2019). The corona contracts in a black-hole transient. *Nature*, 565:198–201.

Kawamuro, T., Negoro, H., Yoneyama, T., Ueno, S., Tomida, H., Ishikawa, M., Sugawara, Y., Isobe, N., Shimomukai, R., Mihara, T., Sugizaki, M., Nakahira, S., Iwakiri, W., Yatabe, F., Takao, Y., Matsuoka, M., Kawai, N., Sugita, S., Yoshii, T., Tachibana, Y., Harita, S., Morita, K., Yoshida, A., Sakamoto, T., Serino, M., Kawakubo, Y., Kitaoka, Y., Hashimoto, T., Tsunemi, H., Nakajima, M., Kawase, T., Sakamaki, A., Maruyama, W., Ueda, Y., Hori, T., Tanimoto, A., Oda, S., Morita, T., Yamada, S., Tsuboi, Y., Nakamura, Y., Sasaki, R., Kawai, H., Sato, T., Yamauchi, M., Hanyu, C., Hidaka, K., Yamaoka, K., and Shidatsu, M. (2018). MAXI/GSC detection of a probable new X-ray transient MAXI J1820+070. *The Astronomer's Telegram*, 11399.

Kelly, B. C., Sobolewska, M., and Siemiginowska, A. (2011). A Stochastic Model for the Luminosity Fluctuations of Accreting Black Holes. *ApJ*, 730:52.

Kerr, R. P. (1963). Gravitational Field of a Spinning Mass as an Example of Algebraically Special Metrics. *Physical Review Letters*, 11:237–238.

King, A. L., Lohfink, A., and Kara, E. (2017). AGN Coronae through a Jet Perspective. *ApJ*, 835:226.

King, A. R., Pringle, J. E., West, R. G., and Livio, M. (2004). Variability in black hole accretion discs. *MNRAS*, 348:111–122.

Kishimoto, M., Hönig, S. F., Antonucci, R., Millour, F., Tristram, K. R. W., and Weigelt, G. (2011). Mapping the radial structure of AGN tori. *AAP*, 536:A78.

Kokubun, M., Abe, K., Ezoe, Y., Fukazawa, Y., Hong, S., Inoue, H., Itoh, T., Kamae, T., Kasama, D., Kawaharada, M., Kawano, N., Kawashima, K., Kawasoe, S., Kobayashi, Y., Kotoku, J., Kouda, M., Kubota, A., Madejski, G. M., Makishima, K., Mitani, T., Miyasaka, H., Miyawaki, R., Mori, K., Mori, M., Murakami, T., Murashima, M. M., Nakazawa, K., Niko, H., Nomachi, M., Ohno, M., Okada, Y., Oonuki, K., Sato, G., Suzuki, M., Takahashi, H., Takahashi, I., Takahashi, T., Tamura, K., Tanaka, T., Tashiro, M., Terada, Y., Tominaga, S., Watanabe, S., Yamaoka, K., Yanagida, T., and Yonetoku, D. (2004). Improvements of the Astro-E2 Hard X-Ray Detector (HXD-II). *IEEE Transactions on Nuclear Science*, 51:1991–1996.

Komossa, S. (2008). Narrow-line Seyfert 1 Galaxies. In *Revista Mexicana de Astronomia y Astrofisica Conference Series*, volume 32 of *Revista Mexicana de Astronomia y Astrofisica, vol. 27*, pages 86–92.

Korista, K. T. and Goad, M. R. (2001). The Variable Diffuse Continuum Emission of Broad-Line Clouds. *ApJ*, 553:695–708.

Kormendy, J. and Ho, L. C. (2013). Coevolution (Or Not) of Supermassive Black Holes and Host Galaxies. *ARAA*, 51(1):511–653.

Kormendy, J. and Richstone, D. (1995). Inward Bound—The Search For Supermassive Black Holes In Galactic Nuclei. *ARAA*, 33:581.

Koyama, K., Tsunemi, H., Dotani, T., Bautz, M. W., Hayashida, K., Tsuru, T. G., Matsumoto, H., Ogawara, Y., Ricker, G. R., Doty, J., Kissel, S. E., Foster, R., Nakajima, H., Yamaguchi, H., Mori, H., Sakano, M., Hamaguchi, K., Nishiuchi, M., Miyata, E., Torii, K., Namiki, M., Katsuda, S., Matsuura, D., Miyauchi, T., Anabuki, N., Tawa, N., Ozaki, M., Murakami, H., Maeda, Y., Ichikawa, Y., Prigozhin, G. Y., Boughan, E. A., Lamarr, B., Miller, E. D., Burke, B. E., Gregory, J. A., Pillsbury, A., Bamba, A., Hiraga, J. S., Senda, A., Katayama, H., Kitamoto, S., Tsujimoto, M., Kohmura, T., Tsuboi, Y., and Awaki, H. (2007). X-Ray Imaging Spectrometer (XIS) on Board Suzaku. *PASJ*, 59:23–33.

Krimm, H. A., Holland, S. T., Corbet, R. H. D., Pearlman, A. B., Romano, P., Kennea, J. A., Bloom, J. S., Barthelmy, S. D., Baumgartner, W. H., Cummings, J. R., Gehrels, N., Lien, A. Y., Markwardt, C. B., Palmer, D. M., Sakamoto, T., Stamatikos, M., and Ukwatta, T. N. (2013). The Swift/BAT Hard X-Ray Transient Monitor. *ApJS*, 209:14.

Kriss, G. A., Peterson, B. M., Crenshaw, D. M., and Zheng, W. (2000). A High Signal-to-Noise Ultraviolet Spectrum of NGC 7469: New Support for Reprocessing of Continuum Radiation. *ApJ*, 535:58–72.

Krolik, J. H. and Kallman, T. R. (1988). The effects of thermal accretion disk spectra on the emission lines from active galactic nuclei. *ApJ*, 324:714–720.

Laha, S., Guainazzi, M., Dewangan, G. C., Chakravorty, S., and Kembhavi, A. K. (2014). Warm absorbers in X-rays (WAX), a comprehensive high-resolution grating spectral study of a sample of Seyfert galaxies - I. A global view and frequency of occurrence of warm absorbers. *MNRAS*, 441:2613–2643.

Lamb, P. and Sanford, P. W. (1979). Compton scattering effects observed in Sco X-1 and similar sources. *MNRAS*, 188:555–563.

Laor, A. (1991). Line profiles from a disk around a rotating black hole. *ApJ*, 376:90–94.

Lee, J. C., Ogle, P. M., Canizares, C. R., Marshall, H. L., Schulz, N. S., Morales, R., Fabian, A. C., and Iwasawa, K. (2001). Revealing the Dusty Warm Absorber in MCG -6-30-15 with the Chandra High-Energy Transmission Grating. *ApJL*, 554(1):L13–L17.

Leighly, K. M. (2004). Hubble Space Telescope STIS Ultraviolet Spectral Evidence of Outflow in Extreme Narrow-Line Seyfert 1 Galaxies. II. Modeling and Interpretation. *ApJ*, 611:125–152.

Leighly, K. M. and Moore, J. R. (2004). Hubble Space Telescope STIS Ultraviolet Spectral Evidence of Outflow in Extreme Narrow-Line Seyfert 1 Galaxies. I. Data and Analysis. *ApJ*, 611:107–124.

Li, L.-X., Zimmerman, E. R., Narayan, R., and McClintock, J. E. (2005). Multitemperature Blackbody Spectrum of a Thin Accretion Disk around a Kerr Black Hole: Model Computations and Comparison with Observations. *ApJS*, 157(2):335–370.

Liebmann, A. C., Haba, Y., Kunieda, H., Tsuruta, S., Takahashi, M., and Takahashi, R. (2014). Dynamical Behavior of X-Ray Spectra from Markarian 766. *ApJ*, 780:35.

Lightman, A. P. and White, T. R. (1988). Effects of cold matter in active galactic nuclei - A broad hump in the X-ray spectra. *ApJ*, 335:57–66.

Lira, P., Arévalo, P., Uttley, P., McHardy, I. M. M., and Videla, L. (2015). Long-term monitoring of the archetype Seyfert galaxy MCG-6-30-15: X-ray, optical and near-IR variability of the corona, disc and torus. *MNRAS*, 454:368–379.

Lobban, A., Porquet, D., Reeves, J., Markowitz, A., Nardini, E., and Grosso, N. (2017). A deep X-ray view of the bare AGN Ark 120. III. X-ray timing analysis and multiwavelength variability. *ArXiv e-prints*.

Lobban, A. P., Vaughan, S., Pounds, K., and Reeves, J. N. (2016). X-ray timing analysis of the quasar PG 1211+143. *MNRAS*, 457:38–50.

Lohfink, A. M., Reynolds, C. S., Vasudevan, R., Mushotzky, R. F., and Miller, N. A. (2014). The Fast UV Variability of the Active Galactic Nucleus in Fairall 9. *ApJ*, 788:10.

Lubiński, P., Beckmann, V., Gibaud, L., Paltani, S., Papadakis, I. E., Ricci, C., Soldi, S., Türler, M., Walter, R., and Zdziarski, A. A. (2016). A comprehensive analysis of the hard X-ray spectra of bright Seyfert galaxies. *MNRAS*, 458:2454–2475.

Lubiński, P., Zdziarski, A. A., Walter, R., Paltani, S., Beckmann, V., Soldi, S., Ferrigno, C., and Courvoisier, T. J.-L. (2010). Extreme flux states of NGC 4151 observed with INTEGRAL. *MNRAS*, 408:1851–1865.

Lusso, E. and Risaliti, G. (2016). The Tight Relation between X-Ray and Ultraviolet Luminosity of Quasars. *ApJ*, 819:154.

Lynden-Bell, D. (1964). On Large-Scale Instabilities during Gravitational Collapse and the Evolution of Shrinking Maclaurin Spheroids. *ApJ*, 139:1195.

Lynden-Bell, D. (1969). Galactic Nuclei as Collapsed Old Quasars. *Nature*, 223:690–694.

Lyubarskii, Y. E. (1997). Flicker noise in accretion discs. *MNRAS*, 292:679.

Maccarone, T. J. and Coppi, P. S. (2002). Higher order variability properties of accreting black holes. *MNRAS*, 336(3):817–825.

Maccarone, T. J. and Schnittman, J. D. (2005). The bicoherence as a diagnostic for models of high-frequency quasi-periodic oscillations. *MNRAS*, 357(1):12–16.

Madsen, K. K., Beardmore, A. P., Forster, K., Guainazzi, M., Marshall, H. L., Miller, E. D., Page, K. L., and Stuhlinger, M. (2017). IACHEC Cross-calibration of Chandra, NuSTAR, Swift, Suzaku, XMM-Newton with 3C 273 and PKS 2155-304. *AJ*, 153:2.

Madsen, K. K., Harrison, F. A., Markwardt, C. B., An, H., Grefenstette, B. W., Bachetti, M., Miyasaka, H., Kitaguchi, T., Bhalerao, V., Boggs, S., Christensen, F. E., Craig, W. W., Forster, K., Fuerst, F., Hailey, C. J., Perri, M., Puccetti, S., Rana, V., Stern, D., Walton, D. J., Jørgen Westergaard, N., and Zhang, W. W. (2015). Calibration of the NuSTAR High-energy Focusing X-ray Telescope. *ApJS*, 220:8.

Magdziarz, P. and Zdziarski, A. A. (1995). Angle-dependent Compton reflection of X-rays and gamma-rays. *MNRAS*, 273:837–848.

Magorrian, J., Tremaine, S., Richstone, D., Bender, R., Bower, G., Dressler, A., Faber, S. M., Gebhardt, K., Green, R., Grillmair, C., Kormendy, J., and Lauer, T. (1998). The Demography of Massive Dark Objects in Galaxy Centers. *AJ*, 115(6):2285–2305.

Malizia, A., Molina, M., Bassani, L., Stephen, J. B., Bazzano, A., Ubertini, P., and Bird, A. J. (2014). The INTEGRAL High-energy Cut-off Distribution of Type 1 Active Galactic Nuclei. *ApJL*, 782:L25.

Maoz, D., Edelson, R., and Nandra, K. (2000). A Possible 100 Day X-Ray-to-Optical Lag in the Variations of the Seyfert 1 Nucleus NGC 3516. *AJ*, 119:119–125.

Maoz, D., Markowitz, A., Edelson, R., and Nandra, K. (2002). X-Ray versus Optical Variations in the Seyfert 1 Nucleus NGC 3516: A Puzzling Disconnectedness. *AJ*, 124:1988–1994.

Marinucci, A., Matt, G., Miniutti, G., Guainazzi, M., Parker, M. L., Brenneman, L., Fabian, A. C., Kara, E., Arevalo, P., Ballantyne, D. R., Boggs, S. E., Cappi, M., Christensen, F. E., Craig, W. W., Elvis, M., Hailey, C. J., Harrison, F. A., Reynolds, C. S., Risaliti, G., Stern, D. K., Walton, D. J., and Zhang, W. (2014). The Broadband Spectral Variability of MCG-6-30-15 Observed by NuSTAR and XMM-Newton. *ApJ*, 787:83.

Markoff, S., Nowak, M. A., and Wilms, J. (2005). Going with the Flow: Can the Base of Jets Subsume the Role of Compact Accretion Disk Coronae? *ApJ*, 635:1203–1216.

Markowitz, A. (2009). The X-Ray Power Spectral Density Function and Black Hole Mass Estimate for the Seyfert Active Galactic Nucleus IC 4329a. *ApJ*, 698:1740–1748.

Marshall, F. E., Boldt, E. A., Holt, S. S., Mushotzky, R. F., Rothschild, R. E., Serlemitsos, P. J., and Pravdo, S. H. (1979). New hard X-ray sources observed with HEAO A-2. *ApJS*, 40:657–665.

Marshall, K., Ryle, W. T., and Miller, H. R. (2008). Correlated X-Ray and Optical Variability in Markarian 509. *ApJ*, 677:880–883.

Marziani, P., Calvani, M., and Sulentic, J. W. (1992). Twin peaks - IC 4329A and Arakelian 120. *ApJ*, 393:658–665.

Masetti, N., Palazzi, E., Bassani, L., Malizia, A., and Stephen, J. B. (2004). Unveiling the nature of three INTEGRAL sources through optical spectroscopy. *AAP*, 426:L41–L44.

Mason, K. O., Breeveld, A., Much, R., Carter, M., Cordova, F. A., Cropper, M. S., Fordham, J., Huckle, H., Ho, C., Kawakami, H., Kennea, J., Kennedy, T., Mittaz, J., Pandel, D., Priedhorsky, W. C., Sasseen, T., Shirey, R., Smith, P., and Vreux, J.-M. (2001). The XMM-Newton optical/UV monitor telescope. *AAP*, 365:L36–L44.

Mason, K. O., McHardy, I. M., Page, M. J., Uttley, P., Córdova, F. A., Maraschi, L., Priedhorsky, W. C., Puchnarewicz, E. M., and Sasseen, T. (2002). XMM-Newton Observations of a Possible Light Echo in the Seyfert 1 Nucleus of NGC 4051. *ApJL*, 580:L117–L120.

Matsumoto, H., Koyama, K., Tsuru, T. G., Nakajima, H., Yamaguchi, H., Tsunemi, H., Hayashida, K., Miyata, E., Torii, K., Namiki, M., Dotani, T., Ozaki, M., Murakami, H., Anabuki, N., Kitamoto, S., Awaki, H., Kohmura, T., Katayama, H., Bamba, A., Bautz, M. W., Doty, J. P., Ricker, G. R., Foster, R. F., Prigozhin, G. Y., Kissel, S. E., Burke, B. E., Pillsbury, A. D., and Lamarr, B. (2005). X-ray imaging spectrometers (XIS) of Astro-E2. *Nuclear Instruments and Methods in Physics Research A*, 541:357–364.

Matsuoka, M., Kawasaki, K., Ueno, S., Tomida, H., Kohama, M., Suzuki, M., Adachi, Y., Ishikawa, M., Mihara, T., Sugizaki, M., Isobe, N., Nakagawa, Y., Tsunemi, H., Miyata, E., Kawai, N., Kataoka, J., Morii, M., Yoshida, A., Negoro, H., Nakajima, M., Ueda, Y., Chujo, H., Yamaoka, K., Yamazaki, O., Nakahira, S., You, T., Ishiwata, R., Miyoshi, S., Eguchi, S., Hiroi, K., Katayama, H., and Ebisawa, K. (2009). The MAXI Mission on the ISS: Science and Instruments for Monitoring All-Sky X-Ray Images. *PASJ*, 61:999–1010.

McHardy, I. (2010). *X-Ray Variability of AGN and Relationship to Galactic Black Hole Binary Systems*, volume 794, page 203.

McHardy, I. M. (2013). Short time-scale AGN X-ray variability with EXOSAT: black hole mass and normalized variability amplitude. *MNRAS*, 430:L49–L53.

McHardy, I. M., Connolly, S. D., Horne, K., Cackett, E. M., Gelbord, J., Peterson, B. M., Pahari, M., Gehrels, N., Goad, M., Lira, P., Arevalo, P., Baldi, R. D., Brandt, N., Breedt, E., Chand, H., Dewangan, G., Done, C., Elvis, M., Emmanoulopoulos, D., Fausnaugh, M. M., Kaspi, S., Kochanek, C. S., Korista, K., Papadakis, I. E., Rao, A. R., Uttley, P., Vestergaard, M., and Ward, M. J. (2018). X-ray/UV/optical variability of NGC 4593 with Swift: reprocessing of X-rays by an extended reprocessor. *MNRAS*, 480(3):2881–2897.

McHardy, I. M., Connolly, S. D., Peterson, B. M., Bieryla, A., Chand, H., Elvis, M. S., Emmanoulopoulos, D., Falco, E., Gandhi, P., Kaspi, S., Latham, D., Lira, P., McCully, C., Netzer, H., and Uemura, M. (2016). The origin of UV-optical variability in AGN and test of disc models: XMM-Newton and ground-based observations of NGC 4395. *Astronomische Nachrichten*, 337:500.

Mehdipour, M., Branduardi-Raymont, G., Kaastra, J. S., Petrucci, P. O., Kriss, G. A., Ponti, G., Blustin, A. J., Paltani, S., Cappi, M., Detmers, R. G., and Steenbrugge, K. C. (2011). Multiwavelength campaign on Mrk 509. IV. Optical-UV-X-ray variability and the nature of the soft X-ray excess. *AAP*, 534:A39.

Meléndez, M., Kraemer, S. B., Weaver, K. A., and Mushotzky, R. F. (2011). Uncovering the Spectral Energy Distribution in Active Galaxies Using High-ionization Mid-infrared Emission Lines. *ApJ*, 738:6.

Mereminskiy, I. A., Grebenev, S. A., Molkov, S. V., Zaznobin, I. A., Khorunzhev, G. A., Burenin, R. A., and Eselevich, M. V. (2018). Low-frequency QPOs in MAXI J1820+070 as seen by INTEGRAL/SPI. *The Astronomer's Telegram*, 11488.

Merloni, A. and Fabian, A. C. (2003). Iron Kα line profiles and the inner boundary condition of accretion flows. *MNRAS*, 342:951–961.

Miller, L., Turner, T. J., and Reeves, J. N. (2008). An absorption origin for the X-ray spectral variability of MCG-6-30-15. *AAP*, 483:437–452.

Miller, L., Turner, T. J., Reeves, J. N., George, I. M., Kraemer, S. B., and Wingert, B. (2007). The variable X-ray spectrum of Markarian 766. I. Principal components analysis. *AAP*, 463:131–143.

Miniutti, G. and Fabian, A. C. (2004). A light bending model for the X-ray temporal and spectral properties of accreting black holes. *MNRAS*, 349:1435–1448.

Miniutti, G., Fabian, A. C., Anabuki, N., Crummy, J., Fukazawa, Y., Gallo, L., Haba, Y., Hayashida, K., Holt, S., Kunieda, H., Larsson, J., Markowitz, A., Matsumoto, C., Ohno, M., Reeves, J. N., Takahashi, T., Tanaka, Y., Terashima, Y., Torii, K., Ueda, Y., Ushio, M., Watanabe, S., Yamauchi, M., and Yaqoob, T. (2007). Suzaku Observations of the Hard X-Ray Variability of MCG -6-30-15: the Effects of Strong Gravity around a Kerr Black Hole. *PASJ*, 59:315–325.

Mitsuda, K., Bautz, M., Inoue, H., Kelley, R. L., Koyama, K., Kunieda, H., Makishima, K., Ogawara, Y., Petre, R., Takahashi, T., Tsunemi, H., White, N. E., Anabuki, N., Angelini, L., Arnaud, K., Awaki, H., Bamba, A., Boyce, K., Brown, G. V., Chan, K.-W., Cottam, J., Dotani, T., Doty, J., Ebisawa, K., Ezoe, Y., Fabian, A. C., Figueroa, E., Fujimoto, R., Fukazawa, Y., Furusho, T., Furuzawa, A., Gendreau, K., Griffiths, R. E., Haba, Y., Hamaguchi, K., Harrus, I., Hasinger, G., Hatsukade, I., Hayashida, K., Henry, P. J., Hiraga, J. S., Holt, S. S., Hornschemeier, A., Hughes, J. P., Hwang, U., Ishida, M., Ishisaki, Y., Isobe, N., Itoh, M., Iyomoto, N., Kahn, S. M., Kamae, T., Katagiri, H., Kataoka, J., Katayama, H., Kawai, N., Kilbourne, C., Kinugasa, K., Kissel, S., Kitamoto, S., Kohama, M., Kohmura, T., Kokubun, M., Kotani, T., Kotoku, J., Kubota, A., Madejski, G. M., Maeda, Y., Makino, F., Markowitz, A., Matsumoto, C., Matsumoto, H., Matsuoka, M., Matsushita, K., McCammon, D., Mihara, T., Misaki, K., Miyata, E., Mizuno, T., Mori, K.,

Mori, H., Morii, M., Moseley, H., Mukai, K., Murakami, H., Murakami, T., Mushotzky, R., Nagase, F., Namiki, M., Negoro, H., Nakazawa, K., Nousek, J. A., Okajima, T., Ogasaka, Y., Ohashi, T., Oshima, T., Ota, N., Ozaki, M., Ozawa, H., Parmar, A. N., Pence, W. D., Porter, F. S., Reeves, J. N., Ricker, G. R., Sakurai, I., Sanders, W. T., Senda, A., Serlemitsos, P., Shibata, R., Soong, Y., Smith, R., Suzuki, M., Szymkowiak, A. E., Takahashi, H., Tamagawa, T., Tamura, K., Tamura, T., Tanaka, Y., Tashiro, M., Tawara, Y., Terada, Y., Terashima, Y., Tomida, H., Torii, K., Tsuboi, Y., Tsujimoto, M., Tsuru, T. G., Turner, M. J. L. ., Ueda, Y., Ueno, S., Ueno, M., Uno, S., Urata, Y., Watanabe, S., Yamamoto, N., Yamaoka, K., Yamasaki, N. Y., Yamashita, K., Yamauchi, M., Yamauchi, S., Yaqoob, T., Yonetoku, D., and Yoshida, A. (2007). The X-Ray Observatory Suzaku. *PASJ*, 59:S1–S7.

Miyoshi, M., Moran, J., Herrnstein, J., Greenhill, L., Nakai, N., Diamond, P., and Inoue, M. (1995). Evidence for a black hole from high rotation velocities in a sub-parsec region of NGC4258. *Nature*, 373(6510):127–129.

Molina, M., Giroletti, M., Malizia, A., Landi, R., Bassani, L., Bird, A. J., Dean, A. J., de Rosa, A., Fiocchi, M., and Panessa, F. (2007). Broad-band X-ray spectrum of the newly discovered broad-line radio galaxy IGR J21247+5058. *MNRAS*, 382:937–943.

Morgan, C. W., Kochanek, C. S., Morgan, N. D., and Falco, E. E. (2010). The Quasar Accretion Disk Size-Black Hole Mass Relation. *ApJ*, 712:1129–1136.

Motta, S., Belloni, T., and Homan, J. (2009). The evolution of the high-energy cut-off in the X-ray spectrum of GX 339-4 across a hard-to-soft transition. *MNRAS*, 400:1603–1612.

Mushotzky, R. F., Done, C., and Pounds, K. A. (1993). X-ray spectra and time variability of active galactic nuclei. *ARAA*, 31:717–761.

Mushotzky, R. F., Marshall, F. E., Boldt, E. A., Holt, S. S., and Serlemitsos, P. J. (1980). HEAO 1 spectra of X-ray emitting Seyfert 1 galaxies. *ApJ*, 235:377–385.

Nandra, K., Clavel, J., Edelson, R. A., George, I. M., Malkan, M. A., Mushotzky, R. F., Peterson, B. M., and Turner, T. J. (1998). New Constraints on the Continuum Emission Mechanism of Active Galactic Nuclei: Intensive Monitoring of NGC 7469 in the X-Ray and Ultraviolet. *ApJ*, 505:594–606.

Nandra, K., George, I. M., Mushotzky, R. F., Turner, T. J., and Yaqoob, T. (1997a). ASCA Observations of Seyfert 1 Galaxies. I. Data Analysis, Imaging, and Timing. *ApJ*, 476:70–82.

Nandra, K., George, I. M., Mushotzky, R. F., Turner, T. J., and Yaqoob, T. (1997b). ASCA Observations of Seyfert 1 Galaxies. II. Relativistic Iron Kα Emission. *ApJ*, 477:602–622.

Nandra, K., O'Neill, P. M., George, I. M., and Reeves, J. N. (2007). An XMM-Newton survey of broad iron lines in Seyfert galaxies. *MNRAS*, 382:194–228.

Nardini, E., Reeves, J. N., Gofford, J., Harrison, F. A., Risaliti, G., Braito, V., Costa, M. T., Matzeu, G. A., Walton, D. J., Behar, E., Boggs, S. E., Christensen, F. E., Craig, W. W., Hailey, C. J., Matt, G., Miller, J. M., O'Brien, P. T., Stern, D., Turner, T. J., and Ward, M. J. (2015). Black hole feedback in the luminous quasar PDS 456. *Science*, 347:860–863.

Newman, E. T., Couch, E., Chinnapared, K., Exton, A., Prakash, A., and Torrence, R. (1965). Metric of a Rotating, Charged Mass. *Journal of Mathematical Physics*, 6:918–919.

Noda, H., Minezaki, T., Watanabe, M., Kokubo, M., Kawaguchi, K., Itoh, R., Morihana, K., Saito, Y., Nakao, H., Imai, M., Moritani, Y., Takaki, K., Kawabata, M., Nakaoka, T., Uemura, M., Kawabata, K., Yoshida, M., Arai, A., Takagi, Y., Morokuma, T., Doi, M., Itoh, Y., Yamada, S., Nakazawa, K., Fukazawa, Y., and Makishima, K. (2016). X-ray and Optical Correlation of Type I Seyfert NGC 3516 Studied with Suzaku and Japanese Ground-Based Telescopes. *ArXiv e-prints*.

Nordström, G. (1918). On the Energy of the Gravitation field in Einstein's Theory. *Koninklijke Nederlandse Akademie van Wetenschappen Proceedings Series B Physical Sciences*, 20:1238–1245.

Novikov, I. D. and Thorne, K. S. (1973). Astrophysics of black holes. In Dewitt, C. and Dewitt, B. S., editors, *Black Holes (Les Astres Occlus)*, pages 343–450.

Nowak, M. A., Vaughan, B. A., Wilms, J., Dove, J. B., and Begelman, M. C. (1999). Rossi X-Ray Timing Explorer Observation of Cygnus X-1. II. Timing Analysis. *ApJ*, 510(2):874–891.

O'Donnell, J. E. (1994). R_{nu}-dependent optical and near-ultraviolet extinction. *ApJ*, 422:158–163.

Oh, K., Koss, M., Markwardt, C. B., Schawinski, K., Baumgartner, W. H., Barthelmy, S. D., Cenko, S. B., Gehrels, N., Mushotzky, R., Petulante, A., Ricci, C., Lien, A., and Trakhtenbrot, B. (2018). The 105-Month Swift-BAT All-sky Hard X-Ray Survey. *ApJS*, 235:4.

Olive, J. F., Barret, D., Boirin, L., Grindlay, J. E., Swank, J. H., and Smale, A. P. (1998). RXTE observation of the X-ray burster 1E 1724-3045. I. Timing study of the persistent X-ray emission with the PCA. *AAP*, 333:942–951.

Pal, M. and Naik, S. (2017). Correlated X-ray/UV/optical emission and short term variability in a Seyfert 1 galaxy NGC 4593. *ArXiv e-prints*.

Pan, H.-W., Yuan, W., Yao, S., Zhou, X.-L., Liu, B., Zhou, H., and Zhang, S.-N. (2016). Detection of a Possible X-Ray Quasi-periodic Oscillation in the Active Galactic Nucleus 1H 0707-495. *ApJL*, 819:L19.

Papadakis, I. E., Nicastro, F., and Panagiotou, C. (2016). Modelling the variable broad-band optical/UV/X-ray spectrum of PG1211+143: implications for the ionized outflow. *AAP*, 591:A102.

Park, S. Q., Miller, J. M., McClintock, J. E., Remillard, R. A., Orosz, J. A., Shrader, C. R., Hunstead, R. W., Campbell-Wilson, D., Ishwara-Chandra, C. H., Rao, A. P., and Rupen, M. P. (2004). Spectral and Timing Evolution of the Black Hole X-Ray Nova 4U 1543-47 during Its 2002 Outburst. *ApJ*, 610:378–389.

Parker, M. L., Alston, W. N., Buisson, D. J. K., Fabian, A. C., Jiang, J., Kara, E., Lohfink, A., Pinto, C., and Reynolds, C. S. (2017a). Revealing the ultrafast outflow in IRAS 13224-3809 through spectral variability. *MNRAS*, 469:1553–1558.

Parker, M. L., Buisson, D. J. K., Tomsick, J. A., Fabian, A. C., Madsen, K. K., Walton, D. J., and Fürst, F. (2019). XRB continuum fitting with sensitive high-energy X-ray detectors. *MNRAS*, 484(1):1202–1212.

Parker, M. L., Fabian, A. C., Matt, G., Koljonen, K. I. I., Kara, E., Alston, W., Walton, D. J., Marinucci, A., Brenneman, L., and Risaliti, G. (2015a). Revealing the X-ray variability of AGN with principal component analysis. *MNRAS*, 447:72–96.

Parker, M. L., Marinucci, A., Brenneman, L., Fabian, A. C., Kara, E., Matt, G., and Walton, D. J. (2014a). Principal component analysis of MCG-06-30-15 with XMM-Newton. *MNRAS*, 437:721–729.

Parker, M. L., Miller, J. M., and Fabian, A. C. (2018). X-ray reflection from the inner disc of the AGN Ton S180. *MNRAS*, 474:1538–1544.

Parker, M. L., Pinto, C., Fabian, A. C., Lohfink, A., Buisson, D. J. K., Alston, W. N., Kara, E., Cackett, E. M., Chiang, C.-Y., Dauser, T., De Marco, B., Gallo, L. C., Garcia, J., Harrison, F. A., King, A. L., Middleton, M. J., Miller, J. M., Miniutti, G., Reynolds, C. S., Uttley, P., Vasudevan, R., Walton, D. J., Wilkins, D. R., and Zoghbi, A. (2017b). The response of relativistic outflowing gas to the inner accretion disk of a black hole. *Nature*, 543:83–86.

Parker, M. L., Tomsick, J. A., Miller, J. M., Yamaoka, K., Lohfink, A., Nowak, M., Fabian, A. C., Alston, W. N., Boggs, S. E., Christensen, F. E., Craig, W. W., Fürst, F., Gandhi, P., Grefenstette, B. W., Grinberg, V., Hailey, C. J., Harrison, F. A., Kara, E., King, A. L., Stern, D., Walton, D. J., Wilms, J., and Zhang, W. W. (2015b). NuSTAR and Suzaku Observations of the Hard State in Cygnus X-1: Locating the Inner Accretion Disk. *ApJ*, 808:9.

Parker, M. L., Wilkins, D. R., Fabian, A. C., Grupe, D., Dauser, T., Matt, G., Harrison, F. A., Brenneman, L., Boggs, S. E., Christensen, F. E., Craig, W. W., Gallo, L. C., Hailey, C. J., Kara, E., Komossa, S., Marinucci, A., Miller, J. M., Risaliti, G., Stern, D., Walton, D. J., and Zhang, W. W. (2014b). The NuSTAR spectrum of Mrk 335: extreme relativistic effects within two gravitational radii of the event horizon? *MNRAS*, 443:1723–1732.

Pei, Y. C. (1992). Interstellar dust from the Milky Way to the Magellanic Clouds. *ApJ*, 395:130–139.

Perola, G. C., Matt, G., Cappi, M., Fiore, F., Guainazzi, M., Maraschi, L., Petrucci, P. O., and Piro, L. (2002). Compton reflection and iron fluorescence in BeppoSAX observations of Seyfert type 1 galaxies. *AAP*, 389:802–811.

Peterson, B. M. (2008). The central black hole and relationships with the host galaxy. , 52(6):240–252.

Peterson, B. M., Ferrarese, L., Gilbert, K. M., Kaspi, S., Malkan, M. A., Maoz, D., Merritt, D., Netzer, H., Onken, C. A., Pogge, R. W., Vestergaard, M., and Wandel, A. (2004). Central Masses and Broad-Line Region Sizes of Active Galactic Nuclei. II. A Homogeneous Analysis of a Large Reverberation-Mapping Database. *ApJ*, 613:682–699.

Peterson, B. M., McHardy, I. M., Wilkes, B. J., Berlind, P., Bertram, R., Calkins, M., Collier, S. J., Huchra, J. P., Mathur, S., Papadakis, I., Peters, J., Pogge, R. W., Romano, P., Tokarz, S., Uttley, P., Vestergaard, M., and Wagner, R. M. (2000). X-Ray and Optical Variability in NGC 4051 and the Nature of Narrow-Line Seyfert 1 Galaxies. *ApJ*, 542:161–174.

Peterson, B. M., Wanders, I., Horne, K., Collier, S., Alexander, T., Kaspi, S., and Maoz, D. (1998). On Uncertainties in Cross-Correlation Lags and the Reality of Wavelength-dependent Continuum Lags in Active Galactic Nuclei. *PASP*, 110:660–670.

Petrucci, P. O., Haardt, F., Maraschi, L., Grandi, P., Malzac, J., Matt, G., Nicastro, F., Piro, L., Perola, G. C., and De Rosa, A. (2001). Testing Comptonization Models Using BeppoSAX Observations of Seyfert 1 Galaxies. *ApJ*, 556:716–726.

Phillips, M. M., Feldman, F. R., Marshall, F. E., and Wamsteker, W. (1979). ESO 103-G35 - A new Seyfert galaxy and possible X-ray source. *AAP*, 76:L14–L17.

Pinto, C., Middleton, M. J., and Fabian, A. C. (2016). Resolved atomic lines reveal outflows in two ultraluminous X-ray sources. *Nature*, 533:64–67.

Polletta, M. and Courvoisier, T. J.-L. (1999). ISOPHOT observations of narrow line Seyfert 1 galaxies. *AAP*, 350:765–776.

Ponti, G., Gallo, L. C., Fabian, A. C., Miniutti, G., Zoghbi, A., Uttley, P., Ross, R. R., Vasudevan, R. V., Tanaka, Y., and Brandt, W. N. (2010). Relativistic disc reflection in the extreme NLS1 IRAS13224-3809. *MNRAS*, 406:2591–2604.

Ponti, G., Papadakis, I., Bianchi, S., Guainazzi, M., Matt, G., Uttley, P., and Bonilla, N. F. (2012). CAIXA: a catalogue of AGN in the XMM-Newton archive. III. Excess variance analysis. *AAP*, 542:A83.

Poole, T. S., Breeveld, A. A., Page, M. J., Landsman, W., Holland, S. T., Roming, P., Kuin, N. P. M., Brown, P. J., Gronwall, C., Hunsberger, S., Koch, S., Mason, K. O., Schady, P., vanden Berk, D., Blustin, A. J., Boyd, P., Broos, P., Carter, M., Chester, M. M., Cucchiara, A., Hancock, B., Huckle, H., Immler, S., Ivanushkina, M., Kennedy, T., Marshall, F., Morgan, A., Pandey, S. B., de Pasquale, M., Smith, P. J., and Still, M. (2008). Photometric calibration of the Swift ultraviolet/optical telescope. *MNRAS*, 383:627–645.

Pounds, K. A., Nandra, K., Stewart, G. C., George, I. M., and Fabian, A. C. (1990). X-ray reflection from cold matter in the nuclei of active galaxies. *Nature*, 344:132.

Pounds, K. A., Reeves, J. N., Page, K. L., Wynn, G. A., and O'Brien, P. T. (2003). Fe K emission and absorption features in XMM-Newton spectra of Markarian 766: evidence for reprocessing in flare ejecta. *MNRAS*, 342:1147–1155.

Poutanen, J., Zdziarski, A. A., and Ibragimov, A. (2008). Superorbital variability of X-ray and radio emission of Cyg X-1 - II. Dependence of the orbital modulation and spectral hardness on the superorbital phase. *MNRAS*, 389:1427–1438.

Priestley, M. (1981). *Spectral Analysis and Time Series*. Academic Press, London.

Pringle, J. E. (1981). Accretion discs in astrophysics. *ARAA*, 19:137–162.

Protassov, R., van Dyk, D. A., Connors, A., Kashyap, V. L., and Siemiginowska, A. (2002). Statistics, Handle with Care: Detecting Multiple Model Components with the Likelihood Ratio Test. *ApJ*, 571:545–559.

Recondo-Gonzalez, M. C., Wamsteker, W., Clavel, J., Rodriguez-Pascual, P. M., Vio, R., Ting-Gui, W., Santos-Lleo, M., and Makino, F. (1997). Ultraviolet variability of the Seyfert 1 galaxy Fairall 9. *AAPS*, 121.

Reis, R. C., Fabian, A. C., and Miller, J. M. (2010). Black hole accretion discs in the canonical low-hard state. *MNRAS*, 402:836–854.

Reis, R. C. and Miller, J. M. (2013). On the Size and Location of the X-Ray Emitting Coronae around Black Holes. *ApJL*, 769:L7.

Reis, R. C., Miller, J. M., Reynolds, M. T., Fabian, A. C., Walton, D. J., Cackett, E., and Steiner, J. F. (2013). Evidence of Light-bending Effects and Its Implication for Spectral State Transitions. *ApJ*, 763:48.

Reissner, H. (1916). Über die Eigengravitation des elektrischen Feldes nach der Einsteinschen Theorie. *Annalen der Physik*, 355:106–120.

Remillard, R. A. and McClintock, J. E. (2006). X-Ray Properties of Black-Hole Binaries. *ARAA*, 44:49–92.

Remillard, R. A., Muno, M. P., McClintock, J. E., and Orosz, J. A. (2002). Evidence for Harmonic Relationships in the High-Frequency Quasi-periodic Oscillations of XTE J1550-564 and GRO J1655-40. *ApJ*, 580:1030–1042.

Reynolds, C. S. and Nowak, M. A. (2003). Fluorescent iron lines as a probe of astrophysical black hole systems. , 377:389–466.

Ribo, M., Combi, J. A., and Mirabel, I. F. (2004). A radio galaxy as possible counterpart of IGR J21247+5058. *The Astronomer's Telegram*, 235.

Ricci, C., Ho, L. C., Fabian, A. C., Trakhtenbrot, B., Koss, M. J., Ueda, Y., Lohfink, A., Shimizu, T., Bauer, F. E., Mushotzky, R., Schawinski, K., Paltani, S., Lamperti, I., Treister, E., and Oh, K. (2018). BAT AGN Spectroscopic Survey - XII. The relation between coronal properties of active galactic nuclei and the Eddington ratio. *MNRAS*, 480:1819–1830.

Ricci, C., Trakhtenbrot, B., Koss, M. J., Ueda, Y., Del Vecchio, I., Treister, E., Schawinski, K., Paltani, S., Oh, K., Lamperti, I., Berney, S., Gandhi, P., Ichikawa, K., Bauer, F. E., Ho, L. C., Asmus, D., Beckmann, V., Soldi, S., Baloković, M., Gehrels, N., and Markwardt, C. B. (2017). BAT AGN Spectroscopic Survey. V. X-Ray Properties of the Swift/BAT 70-month AGN Catalog. *ApJS*, 233:17.

Risaliti, G., Braito, V., Laparola, V., Bianchi, S., Elvis, M., Fabbiano, G., Maiolino, R., Matt, G., Reeves, J., Salvati, M., and Wang, J. (2009). A Strong Excess in the 20-100 keV Emission of NGC 1365. *ApJL*, 705:L1–L5.

Risaliti, G., Harrison, F. A., Madsen, K. K., Walton, D. J., Boggs, S. E., Christensen, F. E., Craig, W. W., Grefenstette, B. W., Hailey, C. J., Nardini, E., Stern, D., and Zhang, W. W. (2013). A rapidly spinning supermassive black hole at the centre of NGC1365. *Nature*, 494:449–451.

Risaliti, G., Nardini, E., Salvati, M., Elvis, M., Fabbiano, G., Maiolino, R., Pietrini, P., and Torricelli-Ciamponi, G. (2011). X-ray absorption by broad-line region clouds in Mrk 766. *MNRAS*, 410:1027–1035.

Robertson, D. R. S., Gallo, L. C., Zoghbi, A., and Fabian, A. C. (2015). Searching for correlations in simultaneous X-ray and UV emission in the narrow-line Seyfert 1 galaxy 1H 0707-495. *MNRAS*, 453:3455–3460.

Rodriguez, J., Durouchoux, P., Mirabel, I. F., Ueda, Y., Tagger, M., and Yamaoka, K. (2002). Energy dependence of a low frequency QPO in GRS 1915+105. *AAP*, 386:271–279.

Roming, P. W. A., Kennedy, T. E., Mason, K. O., Nousek, J. A., Ahr, L., Bingham, R. E., Broos, P. S., Carter, M. J., Hancock, B. K., Huckle, H. E., Hunsberger, S. D., Kawakami, H., Killough, R., Koch, T. S., McLelland, M. K., Smith, K., Smith, P. J., Soto, J. C., Boyd, P. T., Breeveld, A. A., Holland, S. T., Ivanushkina, M., Pryzby, M. S., Still, M. D., and Stock, J. (2005). The Swift Ultra-Violet/Optical Telescope. *SSR*, 120:95–142.

Roques, J.-P. and Jourdain, E. (2018). On the high-energy emissions of compact objects observed with INTEGRAL SPI: Event selection impact on source spectra and scientific results for the bright sources Crab Nebula, GS2023+338 and MAXI J1820+070. *arXiv e-prints*.

Ross, R. R. and Fabian, A. C. (1993). The effects of photoionization on X-ray reflection spectra in active galactic nuclei. *MNRAS*, 261:74–82.

Rybicki, G. B. and Lightman, A. P. (1979). *Radiative processes in astrophysics*.

Sako, M., Kahn, S. M., Behar, E., Kaastra, J. S., Brinkman, A. C., Boller, T., Puchnarewicz, E. M., Starling, R., Liedahl, D. A., Clavel, J., and Santos-Lleo, M. (2001). Complex resonance absorption structure in the X-ray spectrum of <ASTROBJ>IRAS 13349+2438</ASTROBJ>. *AAP*, 365:L168–L173.

Sako, M., Kahn, S. M., Branduardi-Raymont, G., Kaastra, J. S., Brinkman, A. C., Page, M. J., Behar, E., Paerels, F., Kinkhabwala, A., Liedahl, D. A., and den Herder, J. W. (2003). Can a Dusty Warm Absorber Model Reproduce the Soft X-Ray Spectra of MCG -6-30-15 and Markarian 766? *ApJ*, 596:114–128.

Salpeter, E. E. (1964). Accretion of Interstellar Matter by Massive Objects. *ApJ*, 140:796–800.

Schneider, D. P., Schmidt, M., and Gunn, J. E. (1991). Moderate resolution spectrophotometry of high redshift quasars. *AJ*, 101:2004–2016.

Schwarzschild, K. (1916). Über das Gravitationsfeld eines Massenpunktes nach der Einsteinschen Theorie. *Sitzungsberichte der Königlich Preußischen Akademie der Wissenschaften (Berlin), 1916, Seite 189-196*.

Shakura, N. I. and Sunyaev, R. A. (1973). Black holes in binary systems. Observational appearance. *AAP*, 24:337–355.

Shappee, B. J., Prieto, J. L., Grupe, D., Kochanek, C. S., Stanek, K. Z., De Rosa, G., Mathur, S., Zu, Y., Peterson, B. M., Pogge, R. W., Komossa, S., Im, M., Jencson, J., Holoien, T. W.-S., Basu, U., Beacom, J. F., Szczygieł, D. M., Brimacombe, J., Adams, S., Campillay, A., Choi, C., Contreras, C., Dietrich, M., Dubberley, M., Elphick, M., Foale, S., Giustini, M., Gonzalez, C., Hawkins, E., Howell, D. A., Hsiao, E. Y., Koss, M., Leighly, K. M., Morrell, N., Mudd, D., Mullins, D., Nugent, J. M., Parrent, J., Phillips, M. M., Pojmanski, G., Rosing, W., Ross, R., Sand, D., Terndrup, D. M., Valenti, S., Walker, Z., and Yoon, Y. (2014). The Man behind the Curtain: X-Rays Drive the UV through NIR Variability in the 2013 Active Galactic Nucleus Outburst in NGC 2617. *ApJ*, 788:48.

Shemmer, O., Brandt, W. N., Netzer, H., Maiolino, R., and Kaspi, S. (2008). The Hard X-Ray Spectrum as a Probe for Black Hole Growth in Radio-Quiet Active Galactic Nuclei. *ApJ*, 682:81–93.

Shemmer, O., Romano, P., Bertram, R., Brinkmann, W., Collier, S., Crowley, K. A., Detsis, E., Filippenko, A. V., Gaskell, C. M., George, T. A., Gliozzi, M., Hiller, M. E., Jewell, T. L., Kaspi, S., Klimek, E. S., Lannon, M. H., Li, W., Martini, P., Mathur, S., Negoro, H., Netzer, H., Papadakis, I., Papamastorakis, I., Peterson, B. M., Peterson, B. W., Pogge, R. W., Pronik, V. I., Rumstay, K. S., Sergeev, S. G., Sergeeva, E. A., Stirpe, G. M., Taylor, C. J., Treffers, R. R., Turner, T. J., Uttley, P., Vestergaard, M., von Braun, K., Wagner, R. M., and Zheng, Z. (2001). Multiwavelength Monitoring of the Narrow-Line Seyfert 1 Galaxy Arakelian 564. III. Optical Observations and the Optical-UV-X-Ray Connection. *ApJ*, 561:162–170.

Shemmer, O., Uttley, P., Netzer, H., and McHardy, I. M. (2003). Complex optical-X-ray correlations in the narrow-line Seyfert 1 galaxy NGC 4051. *MNRAS*, 343:1341–1347.

Shidatsu, M., Nakahira, S., Yamada, S., Kawamuro, T., Ueda, Y., Negoro, H., Murata, K. L., Itoh, R., Tachibana, Y., Adachi, R., Yatsu, Y., Kawai, N., Hanayama, H., Horiuchi, T., Akitaya, H., Saito, T., Takayama, M., Ohshima, T., Katoh, N., Takahashi, J., Nagayama, T., Yamanaka, M., Kawabata, M., Nakaoka, T., Takagi, S., Morokuma, T., Morihana, K., Maehara, H., and Sekiguchi, K. (2018). X-Ray, Optical, and Near-infrared Monitoring of the New X-Ray Transient MAXI J1820+070 in the Low/Hard State. *ApJ*, 868:54.

Shull, J. M., Stevans, M., and Danforth, C. W. (2012). HST-COS Observations of AGNs. I. Ultraviolet Composite Spectra of the Ionizing Continuum and Emission Lines. *ApJ*, 752:162.

Silk, J. and Rees, M. J. (1998). Quasars and galaxy formation. *AAP*, 331:L1–L4.

Smith, R. and Vaughan, S. (2007). X-ray and optical variability of Seyfert 1 galaxies as observed with XMM-Newton. *MNRAS*, 375:1479–1487.

Stahle, C. K., Allen, C. A., Boyce, K. R., Brekosky, R. P., Brown, G. V., Cottam, J., Figueroa-Feliciano, E., Galeazzi, M., Gygax, J. D., Jacobson, M. B., Kelley, R. L., Liu, D., McCammon, D., McClanahan, R. A., Moseley, S. H., Porter, F. S., Rocks, L. E., Szymkowiak, A. E., and Vaillancourt, J. E. (2004). The next-generation microcalorimeter array of XRS on Astro-E2. *Nuclear Instruments and Methods in Physics Research A*, 520:466–468.

Starkey, D., Horne, K., Fausnaugh, M. M., Peterson, B. M., Bentz, M. C., Kochanek, C. S., Denney, K. D., Edelson, R., Goad, M. R., De Rosa, G., Anderson, M. D., Arévalo, P., Barth, A. J., Bazhaw, C., Borman, G. A., Boroson, T. A., Bottorff, M. C., Brandt, W. N., Breeveld, A. A., Cackett, E. M., Carini, M. T., Croxall, K. V., Crenshaw, D. M., Dalla Bontà, E., De Lorenzo-Cáceres, A., Dietrich, M., Efimova, N. V., Ely, J., Evans, P. A., Filippenko, A. V., Flatland, K., Gehrels, N., Geier, S., Gelbord, J. M., Gonzalez, L., Gorjian, V., Grier, C. J., Grupe, D., Hall, P. B., Hicks, S., Horenstein, D., Hutchison, T., Im, M., Jensen, J. J., Joner, M. D., Jones, J., Kaastra, J., Kaspi, S., Kelly, B. C., Kennea, J. A., Kim, S. C., Kim, M., Klimanov, S. A., Korista, K. T., Kriss, G. A., Lee, J. C., Leonard, D. C., Lira, P., MacInnis, F., Manne-Nicholas, E. R., Mathur, S., McHardy, I. M., Montouri, C., Musso, R., Nazarov, S. V., Norris, R. P., Nousek, J. A., Okhmat, D. N., Pancoast, A., Parks, J. R., Pei, L., Pogge, R. W., Pott, J.-U., Rafter, S. E., Rix, H.-W., Saylor, D. A., Schimoia, J. S., Schnülle, K., Sergeev, S. G., Siegel, M. H., Spencer, M., Sung, H.-I., Teems, K. G., Turner, C. S., Uttley, P., Vestergaard, M., Villforth, C., Weiss, Y., Woo, J.-H., Yan, H., Young, S., Zheng, W., and Zu, Y. (2017). Space Telescope and Optical Reverberation Mapping Project.VI. Reverberating Disk Models for NGC 5548. *ApJ*, 835:65.

Steffen, A. T., Strateva, I., Brandt, W. N., Alexander, D. M., Koekemoer, A. M., Lehmer, B. D., Schneider, D. P., and Vignali, C. (2006). The X-Ray-to-Optical Properties of Optically Selected Active Galaxies over Wide Luminosity and Redshift Ranges. *AJ*, 131:2826–2842.

Steiner, J. F., McClintock, J. E., Remillard, R. A., Gou, L., Yamada, S., and Narayan, R. (2010). The Constant Inner-disk Radius of LMC X-3: A Basis for Measuring Black Hole Spin. *ApJL*, 718:L117–L121.

Stella, L. and Vietri, M. (1998). Lense-Thirring Precession and Quasi-periodic Oscillations in Low-Mass X-Ray Binaries. *ApJL*, 492:L59–L62.

Stella, L., Vietri, M., and Morsink, S. M. (1999). Correlations in the Quasi-periodic Oscillation Frequencies of Low-Mass X-Ray Binaries and the Relativistic Precession Model. *ApJL*, 524:L63–L66.

Strateva, I. V., Brandt, W. N., Schneider, D. P., Vanden Berk, D. G., and Vignali, C. (2005). Soft X-Ray and Ultraviolet Emission Relations in Optically Selected AGN Samples. *AJ*, 130:387–405.

Strüder, L., Briel, U., Dennerl, K., Hartmann, R., Kendziorra, E., Meidinger, N., Pfeffermann, E., Reppin, C., Aschenbach, B., Bornemann, W., Bräuninger, H., Burkert, W., Elender, M., Freyberg, M., Haberl, F., Hartner, G., Heuschmann, F., Hippmann, H., Kastelic, E., Kemmer, S., Kettenring, G., Kink, W., Krause, N., Müller, S., Oppitz, A., Pietsch, W., Popp, M., Predehl, P., Read, A., Stephan, K. H., Stötter, D., Trümper, J., Holl, P., Kemmer, J., Soltau, H., Stötter, R., Weber, U., Weichert, U., von Zanthier, C., Carathanassis, D., Lutz, G., Richter, R. H., Solc, P., Böttcher, H., Kuster, M., Staubert, R., Abbey, A., Holland, A., Turner, M., Balasini, M., Bignami, G. F., La Palombara, N., Villa, G., Buttler, W., Gianini, F., Lainé, R., Lumb, D., and Dhez, P. (2001). The European Photon Imaging Camera on XMM-Newton: The pn-CCD camera. *AAP*, 365:L18–L26.

Sunyaev, R. A. and Titarchuk, L. G. (1980). Comptonization of X-rays in plasma clouds - Typical radiation spectra. *AAP*, 86:121–138.

Sunyaev, R. A. and Truemper, J. (1979). Hard X-ray spectrum of CYG X-1. *Nature*, 279:506–508.

Svensson, R. (1982). Electron-Positron Pair Equilibria in Relativistic Plasmas. *ApJ*, 258:335.

Svensson, R. (1984). Steady mildly relativistic thermal plasmas - Processes and properties. *MNRAS*, 209:175–208.

Svensson, R. and Zdziarski, A. A. (1994). Black hole accretion disks with coronae. *ApJ*, 436:599–606.

Takahashi, T., Abe, K., Endo, M., Endo, Y., Ezoe, Y., Fukazawa, Y., Hamaya, M., Hirakuri, S., Hong, S., Horii, M., Inoue, H., Isobe, N., Itoh, T., Iyomoto, N., Kamae, T., Kasama, D., Kataoka, J., Kato, H., Kawaharada, M., Kawano, N., Kawashima, K., Kawasoe, S., Kishishita, T., Kitaguchi, T., Kobayashi, Y., Kokubun, M., Kotoku, J., Kouda, M., Kubota, A., Kuroda, Y., Madejski, G., Makishima, K., Masukawa, K., Matsumoto, Y., Mitani, T., Miyawaki, R., Mizuno, T., Mori, K., Mori, M., Murashima, M., Murakami, T., Nakazawa, K., Niko, H., Nomachi, M., Okada, Y., Ohno, M., Oonuki, K., Ota, N., Ozawa, H., Sato, G., Shinoda, S., Sugiho, M., Suzuki, M., Taguchi, K., Takahashi, H., Takahashi, I., Takeda, S., Tamura, K.-I., Tamura, T., Tanaka, T., Tanihata, C., Tashiro, M., Terada, Y., Tominaga, S., Uchiyama, Y., Watanabe, S., Yamaoka, K., Yanagida, T., and Yonetoku, D. (2007). Hard X-Ray Detector (HXD) on Board Suzaku. *PASJ*, 59:35–51.

Tanaka, Y., Nandra, K., Fabian, A. C., Inoue, H., Otani, C., Dotani, T., Hayashida, K., Iwasawa, K., Kii, T., Kunieda, H., Makino, F., and Matsuoka, M. (1995). Gravitationally redshifted emission implying an accretion disk and massive black hole in the active galaxy MCG-6-30-15. *Nature*, 375:659–661.

Tazaki, F., Ueda, Y., Ishino, Y., Eguchi, S., Isobe, N., Terashima, Y., and Mushotzky, R. F. (2010). Suzaku Observation of the Brightest Broad-line Radio Galaxy 4C 50.55 (IGR J21247+5058). *ApJ*, 721:1340–1347.

Telfer, R. C., Zheng, W., Kriss, G. A., and Davidsen, A. F. (2002). The Rest-Frame Extreme-Ultraviolet Spectral Properties of Quasi-stellar Objects. *ApJ*, 565:773–785.

Thorne, K. S. (1974). Disk-Accretion onto a Black Hole. II. Evolution of the Hole. *ApJ*, 191:507–520.

Thorne, K. S. and Price, R. H. (1975). Cygnus X-1 - an interpretation of the spectrum and its variability. *ApJL*, 195:L101–L105.

Timmer, J. and Koenig, M. (1995). On generating power law noise. *AAP*, 300:707.

Titarchuk, L. (1994). Generalized Comptonization models and application to the recent high-energy observations. *ApJ*, 434:570–586.

Titarchuk, L. and Osherovich, V. (2000). The Global Normal Disk Oscillations and the Persistent Low-Frequency Quasi-periodic Oscillations in X-Ray Binaries. *ApJL*, 542:L111–L114.

Tombesi, F., Cappi, M., Reeves, J. N., Palumbo, G. G. C., Yaqoob, T., Braito, V., and Dadina, M. (2010). Evidence for ultra-fast outflows in radio-quiet AGNs. I. Detection and statistical incidence of Fe K-shell absorption lines. *AAP*, 521:A57.

Tomsick, J. A., Parker, M. L., García, J. A., Yamaoka, K., Barret, D., Chiu, J.-L., Clavel, M., Fabian, A., Fürst, F., Gandhi, P., Grinberg, V., Miller, J. M., Pottschmidt, K., and Walton, D. J. (2018). Alternative Explanations for Extreme Supersolar Iron Abundances Inferred from the Energy Spectrum of Cygnus X-1. *ApJ*, 855:3.

Tomsick, J. A., Yamaoka, K., Corbel, S., Kaaret, P., Kalemci, E., and Migliari, S. (2009). Truncation of the Inner Accretion Disk Around a Black Hole at Low Luminosity. *ApJL*, 707:L87–L91.

Tortosa, A., Marinucci, A., Matt, G., Bianchi, S., La Franca, F., Ballantyne, D. R., Boorman, P. G., Fabian, A. C., Farrah, D., Fuerst, F., Gandhi, P., Harrison, F. A., Koss, M. J., Ricci, C., Stern, D., Ursini, F., and Walton, D. J. (2017). Broad-band X-ray spectral analysis of the Seyfert 1 galaxy GRS 1734-292. *MNRAS*, 466:4193–4200.

Trevese, D., Perna, M., Vagnetti, F., Saturni, F. G., and Dadina, M. (2014). C IV and C III] Reverberation Mapping of the Luminous Quasar PG 1247+267. *ApJ*, 795:164.

Troyer, J., Starkey, D., Cackett, E. M., Bentz, M. C., Goad, M. R., Horne, K., and Seals, J. E. (2016). Correlated X-ray/ultraviolet/optical variability in NGC 6814. *MNRAS*, 456:4040–4050.

Tucker, M. A., Shappee, B. J., Holoien, T. W.-S., Auchettl, K., Strader, J., Stanek, K. Z., Kochanek, C. S., Bahramian, A., ASAS-SN, Dong, S., Prieto, J. L., Shields, J., Thompson, T. A., Beacom, J. F., Chomiuk, L., ATLAS, Denneau, L., Flewelling, H., Heinze, A. N., Smith, K. W., Stalder, B., Tonry, J. L., Weiland, H., Rest, A., Huber, M. E., Rowan, D. M., and Dage, K. (2018). ASASSN-18ey: The Rise of a New Black Hole X-Ray Binary. *ApJL*, 867:L9.

Turner, A. K., Fabian, A. C., Lee, J. C., and Vaughan, S. (2004). The soft X-ray absorption lines of the Seyfert 1 galaxy MCG-6-30-15. *MNRAS*, 353:319–328.

Turner, M. J. L., Abbey, A., Arnaud, M., Balasini, M., Barbera, M., Belsole, E., Bennie, P. J., Bernard, J. P., Bignami, G. F., Boer, M., Briel, U., Butler, I., Cara, C., Chabaud, C., Cole, R., Collura, A., Conte, M., Cros, A., Denby, M., Dhez, P., Di Coco, G., Dowson, J., Ferrando, P., Ghizzardi, S., Gianotti, F., Goodall, C. V., Gretton, L., Griffiths, R. G., Hainaut, O., Hochedez, J. F., Holland, A. D., Jourdain, E., Kendziorra, E., Lagostina, A., Laine, R., La Palombara, N., Lortholary, M., Lumb, D., Marty, P., Molendi, S., Pigot, C., Poindron, E., Pounds, K. A., Reeves, J. N., Reppin, C., Rothenflug, R., Salvetat, P., Sauvageot, J. L., Schmitt, D., Sembay, S., Short, A. D. T., Spragg, J., Stephen, J., Strüder, L., Tiengo, A., Trifoglio, M., Trümper, J., Vercellone, S., Vigroux, L., Villa, G., Ward, M. J., Whitehead, S., and Zonca, E. (2001). The European Photon Imaging Camera on XMM-Newton: The MOS cameras : The MOS cameras. *AAP*, 365:L27–L35.

Turner, T. J., Kraemer, S. B., Mushotzky, R. F., George, I. M., and Gabel, J. R. (2003). Elemental Abundances in NGC 3516. *ApJ*, 594:128–135.

Turner, T. J., Miller, L., Kraemer, S. B., Reeves, J. N., and Pounds, K. A. (2009). Suzaku Observation of a Hard Excess in 1H 0419 - 577: Detection of a Compton-Thick Partial-Covering Absorber. *ApJ*, 698:99–105.

Turner, T. J., Miller, L., Reeves, J. N., and Kraemer, S. B. (2007). The variable X-ray spectrum of Markarian 766. II. Time-resolved spectroscopy. *AAP*, 475:121–131.

Urry, C. M. and Padovani, P. (1995). Unified Schemes for Radio-Loud Active Galactic Nuclei. *PASP*, 107:803.

Uttley, P., Cackett, E. M., Fabian, A. C., Kara, E., and Wilkins, D. R. (2014). X-ray reverberation around accreting black holes. *AAPR*, 22:72.

Uttley, P., Edelson, R., McHardy, I. M., Peterson, B. M., and Markowitz, A. (2003). Correlated Long-Term Optical and X-Ray Variations in NGC 5548. *ApJL*, 584:L53–L56.

Uttley, P., McHardy, I. M., and Vaughan, S. (2005). Non-linear X-ray variability in X-ray binaries and active galaxies. *MNRAS*, 359:345–362.

Vagnetti, F., Antonucci, M., and Trevese, D. (2013). Variability and the X-ray/UV ratio of active galactic nuclei. II. Analysis of a low-redshift Swift sample. *AAP*, 550:A71.

Vagnetti, F., Turriziani, S., Trevese, D., and Antonucci, M. (2010). Variability and the X-ray/UV ratio of active galactic nuclei. *AAP*, 519:A17.

van den Eijnden, J., Ingram, A., Uttley, P., Motta, S. E., Belloni, T. M., and Gardenier, D. W. (2017). Inclination dependence of QPO phase lags in black hole X-ray binaries. *MNRAS*, 464:2643–2659.

van der Klis, M. (2006). *Rapid X-ray Variability*, pages 39–112.

Vanden Berk, D. E., Richards, G. T., Bauer, A., Strauss, M. A., Schneider, D. P., Heckman, T. M., York, D. G., Hall, P. B., Fan, X., Knapp, G. R., Anderson, S. F., Annis, J., Bahcall, N. A., Bernardi, M., Briggs, J. W., Brinkmann, J., Brunner, R., Burles, S., Carey, L., Castander, F. J., Connolly, A. J., Crocker, J. H., Csabai, I., Doi, M., Finkbeiner, D., Friedman, S., Frieman, J. A., Fukugita, M., Gunn, J. E., Hennessy, G. S., Ivezić, Ž., Kent, S., Kunszt, P. Z., Lamb, D. Q., Leger, R. F., Long, D. C., Loveday, J., Lupton, R. H., Meiksin, A., Merelli, A., Munn, J. A., Newberg, H. J., Newcomb, M., Nichol, R. C., Owen, R., Pier, J. R., Pope, A., Rockosi, C. M., Schlegel, D. J., Siegmund, W. A., Smee, S., Snir, Y., Stoughton, C., Stubbs, C., SubbaRao, M., Szalay, A. S., Szokoly, G. P., Tremonti, C., Uomoto, A., Waddell, P., Yanny, B., and Zheng, W. (2001). Composite Quasar Spectra from the Sloan Digital Sky Survey. *AJ*, 122:549–564.

Vasudevan, R. V. and Fabian, A. C. (2007). Piecing together the X-ray background: bolometric corrections for active galactic nuclei. *MNRAS*, 381:1235–1251.

Vasudevan, R. V. and Fabian, A. C. (2009). Simultaneous X-ray/optical/UV snapshots of active galactic nuclei from XMM-Newton: spectral energy distributions for the reverberation mapped sample. *MNRAS*, 392:1124–1140.

Vasudevan, R. V., Fabian, A. C., Gandhi, P., Winter, L. M., and Mushotzky, R. F. (2010). The power output of local obscured and unobscured AGN: crossing the absorption barrier with Swift/BAT and IRAS. *MNRAS*, 402:1081–1098.

Vasudevan, R. V., Fabian, A. C., Mushotzky, R. F., Meléndez, M., Winter, L. M., and Trippe, M. L. (2013). Three active galactic nuclei close to the effective Eddington limit for dusty gas. *MNRAS*, 431:3127–3138.

Vasudevan, R. V., Mushotzky, R. F., Reynolds, C. S., Fabian, A. C., Lohfink, A. M., Zoghbi, A., Gallo, L. C., and Walton, D. (2014). The Hard X-Ray Perspective on the Soft X-Ray Excess. *ApJ*, 785:30.

Vaughan, S., Edelson, R., Warwick, R. S., and Uttley, P. (2003a). On characterizing the variability properties of X-ray light curves from active galaxies. *MNRAS*, 345:1271–1284.

Vaughan, S., Fabian, A. C., and Nandra, K. (2003b). X-ray continuum variability of MCG-6-30-15. *MNRAS*, 339:1237–1255.

Vaughan, S., Uttley, P., Pounds, K. A., Nandra, K., and Strohmayer, T. E. (2011). The rapid X-ray variability of NGC 4051. *MNRAS*, 413:2489–2499.

Verner, D. A., Ferland, G. J., Korista, K. T., and Yakovlev, D. G. (1996). Atomic Data for Astrophysics. II. New Analytic FITS for Photoionization Cross Sections of Atoms and Ions. *ApJ*, 465:487.

Véron-Cetty, M.-P. and Véron, P. (2006). A catalogue of quasars and active nuclei: 12th edition. *AAP*, 455:773–777.

Vestergaard, M. (2002). Determining Central Black Hole Masses in Distant Active Galaxies. *ApJ*, 571:733–752.

Vignali, C., Brandt, W. N., and Schneider, D. P. (2003). X-Ray Emission from Radio-Quiet Quasars in the Sloan Digital Sky Survey Early Data Release: The α_{ox} Dependence upon Ultraviolet Luminosity. *AJ*, 125:433–443.

Volonteri, M., Madau, P., Quataert, E., and Rees, M. J. (2005). The Distribution and Cosmic Evolution of Massive Black Hole Spins. *ApJ*, 620(1):69–77.

Walton, D. J., Reis, R. C., and Fabian, A. C. (2010). Explaining the hard excesses in active galactic nuclei. *MNRAS*, 408:601–606.

Walton, D. J., Risaliti, G., Harrison, F. A., Fabian, A. C., Miller, J. M., Arevalo, P., Ballantyne, D. R., Boggs, S. E., Brenneman, L. W., Christensen, F. E., Craig, W. W., Elvis, M., Fuerst, F., Gandhi, P., Grefenstette, B. W., Hailey, C. J., Kara, E., Luo, B., Madsen, K. K., Marinucci, A., Matt, G., Parker, M. L., Reynolds, C. S., Rivers, E., Ross, R. R., Stern, D., and Zhang, W. W. (2014). NuSTAR and XMM-NEWTON Observations of NGC 1365: Extreme Absorption Variability and a Constant Inner Accretion Disk. *ApJ*, 788:76.

Wanders, I., Peterson, B. M., Alloin, D., Ayres, T. R., Clavel, J., Crenshaw, D. M., Horne, K., Kriss, G. A., Krolik, J. H., Malkan, M. A., Netzer, H., O'Brien, P. T., Reichert, G. A., Rodríguez-Pascual, P. M., Wamsteker, W., Alexander, T., Anderson, K. S. J., Benitez, E., Bochkarev, N. G., Burenkov, A. N., Cheng, F.-Z., Collier, S. J., Comastri, A., Dietrich,

M., Dultzin-Hacyan, D., Espey, B. R., Filippenko, A. V., Gaskell, C. M., George, I. M., Goad, M. R., Ho, L. C., Kaspi, S., Kollatschny, W., Korista, K. T., Laor, A., MacAlpine, G. M., Mignoli, M., Morris, S. L., Nandra, K., Penton, S., Pogge, R. W., Ptak, R. L., Rodríguez-Espinoza, J. M., Santos-Lleó, M., Shapovalova, A. I., Shull, J. M., Snedden, S. A., Sparke, L. S., Stirpe, G. M., Sun, W.-H., Turner, T. J., Ulrich, M.-H., Wang, T.-G., Wei, C., Welsh, W. F., Xue, S.-J., and Zou, Z.-L. (1997). Steps toward Determination of the Size and Structure of the Broad-Line Region in Active Galactic Nuclei. XI. Intensive Monitoring of the Ultraviolet Spectrum of NGC 7469. *ApJS*, 113:69–88.

Ward, M., Elvis, M., Fabbiano, G., Carleton, N. P., Willner, S. P., and Lawrence, A. (1987). The continuum of type 1 Seyfert galaxies. I - A single form modified by the effects of dust. *ApJ*, 315:74–91.

Warwick, R. S., Pounds, K. A., and Turner, T. J. (1988). Variable low-energy absorption in the X-ray spectrum of ESO 103-G35. *MNRAS*, 231:1145–1152.

Webster, B. L. and Murdin, P. (1972). Cygnus X-1-a Spectroscopic Binary with a Heavy Companion ? *Nature*, 235:37–38.

Weisskopf, M. C., Brinkman, B., Canizares, C., Garmire, G., Murray, S., and Van Speybroeck, L. P. (2002). An Overview of the Performance and Scientific Results from the Chandra X-Ray Observatory. *PASP*, 114:1–24.

Welsh, W. F. (1999). On the Reliability of Cross-Correlation Function Lag Determinations in Active Galactic Nuclei. *PASP*, 111:1347–1366.

Wijnands, R., Homan, J., and van der Klis, M. (1999). The Complex Phase-Lag Behavior of the 3-12 HZ Quasi-Periodic Oscillations during the Very High State of XTE J1550-564. *ApJL*, 526:L33–L36.

Wilkes, B. J., Mathur, S., Fiore, F., Antonelli, A., and Nicastro, F. (2001). BeppoSAX Observations of the Maser Seyfert 2 Galaxy ESO 103-G35. *ApJ*, 549:248–253.

Wilkins, D. R., Cackett, E. M., Fabian, A. C., and Reynolds, C. S. (2016). Towards modelling X-ray reverberation in AGN: piecing together the extended corona. *MNRAS*, 458:200–225.

Wilkins, D. R. and Fabian, A. C. (2011). Determination of the X-ray reflection emissivity profile of 1H 0707-495. *MNRAS*, 414:1269–1277.

Wilkins, D. R. and Fabian, A. C. (2012). Understanding X-ray reflection emissivity profiles in AGN: locating the X-ray source. *MNRAS*, 424:1284–1296.

Wilkins, D. R. and Gallo, L. C. (2015). Driving extreme variability: the evolving corona and evidence for jet launching in Markarian 335. *MNRAS*, 449:129–146.

Wilms, J., Allen, A., and McCray, R. (2000). On the Absorption of X-Rays in the Interstellar Medium. *ApJ*, 542:914–924.

Winkler, C., Courvoisier, T. J.-L., Di Cocco, G., Gehrels, N., Giménez, A., Grebenev, S., Hermsen, W., Mas-Hesse, J. M., Lebrun, F., Lund, N., Palumbo, G. G. C., Paul, J., Roques, J.-P., Schnopper, H., Schönfelder, V., Sunyaev, R., Teegarden, B., Ubertini, P., Vedrenne, G., and Dean, A. J. (2003). The INTEGRAL mission. *AAP*, 411:L1–L6.

Winter, L. M., Lewis, K. T., Koss, M., Veilleux, S., Keeney, B., and Mushotzky, R. F. (2010). Optical Spectral Properties of Swift Burst Alert Telescope Hard X-Ray-Selected Active Galactic Nuclei Sources. *ApJ*, 710:503–539.

Xu, Y., García, J. A., Fürst, F., Harrison, F. A., Walton, D. J., Tomsick, J. A., Bachetti, M., King, A. L., Madsen, K. K., Miller, J. M., and Grinberg, V. (2017). Spectral and Timing Properties of IGR J17091-3624 in the Rising Hard State During Its 2016 Outburst. *ApJ*, 851(2):103.

Xu, Y.-D. (2011). The Relation of Optical/Ultraviolet and X-Ray Emission in Low-luminosity Active Galactic Nuclei. *ApJ*, 739:64.

Young, A. J., Crawford, C. S., Fabian, A. C., Brandt, W. N., and O'Brien, P. T. (1999). The optical variability of the narrow-line Seyfert 1 galaxy IRAS 13224-3809. *MNRAS*, 304:L46–L52.

Yu, W., Lin, J., Mao, D., Zhang, J., Yan, Z., and Bai, J. (2018a). Further detection of the optical low frequency QPO in the black hole transient MAXI J1820+070. *The Astronomer's Telegram*, 11591.

Yu, W., Zhang, J., Yan, Z., Wang, X., and Bai, J. (2018b). Detection of optical and X-ray QPOs at similar frequencies in MAXI J1820+070. *The Astronomer's Telegram*, 11510.

Zampieri, L., Fiori, M., Burtovoi, A., Naletto, G., Barbieri, C., Ochner, P., Umbriaco, G., and Barbieri, M. (2018). Low-frequency optical QPO in MAXI J1820+070 detected with IFI+IQUEYE@Galileo. *The Astronomer's Telegram*, 11723.

Zdziarski, A. A. (1985). Power-law X-ray and gamma-ray emission from relativistic thermal plasmas. *ApJ*, 289:514–525.

Zdziarski, A. A. (2005). Energy-dependent variability from accretion flows. *MNRAS*, 360:816–824.

Zdziarski, A. A., Johnson, W. N., and Magdziarz, P. (1996). Broad-band γ-ray and X-ray spectra of NGC 4151 and their implications for physical processes and geometry. *MNRAS*, 283:193–206.

Zhou, X.-L. and Wang, J.-M. (2005). Narrow Iron Kα Lines in Active Galactic Nuclei: Evolving Populations? *ApJL*, 618:L83–L86.

Zoghbi, A., Fabian, A. C., Reynolds, C. S., and Cackett, E. M. (2012). Relativistic iron K X-ray reverberation in NGC 4151. *MNRAS*, 422:129–134.

Zoghbi, A., Fabian, A. C., Uttley, P., Miniutti, G., Gallo, L. C., Reynolds, C. S., Miller, J. M., and Ponti, G. (2010). Broad iron L line and X-ray reverberation in 1H0707-495. *MNRAS*, 401:2419–2432.

Życki, P. T., Done, C., and Smith, D. A. (1999). The 1989 May outburst of the soft X-ray transient GS 2023+338 (V404 Cyg). *MNRAS*, 309:561–575.

Appendix A

Ultraviolet and X-ray variability of active galactic nuclei with *Swift* – further figures

A.1 Lightcurves

Lightcurves for each source in our sample in each band. Rates are given in cts s^{-1}; X-rays are measured over 0.3-10 keV

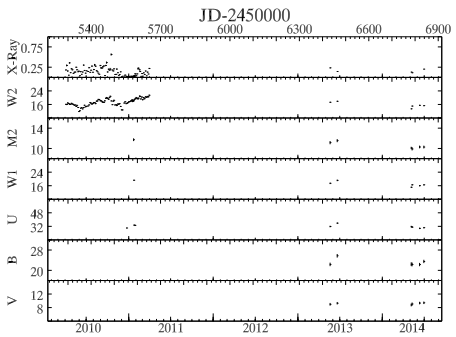

Fig. A.1 1H 0707–495

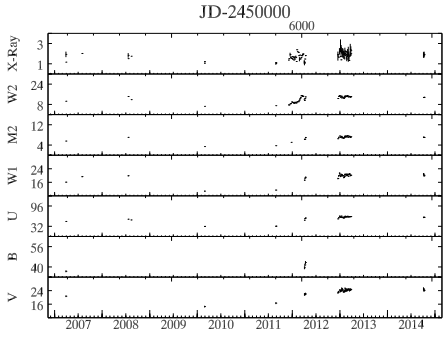

Fig. A.2 3C 120

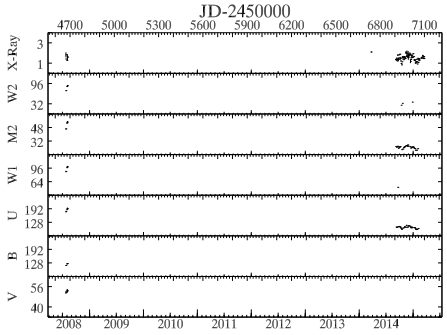

Fig. A.3 ARK 120

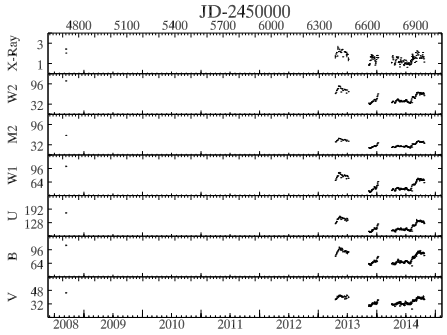

Fig. A.4 Fairall 9

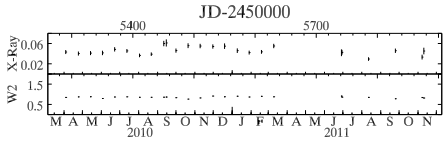

Fig. A.5 H 0557–385

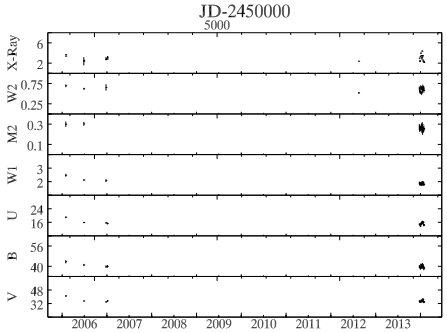

Fig. A.6 IC 4329A

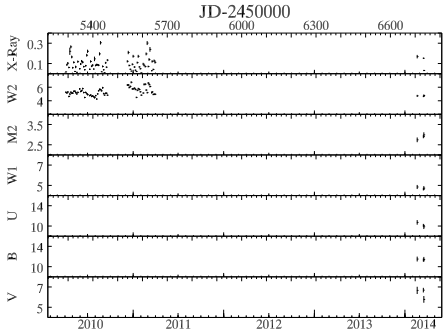

Fig. A.7 IRAS 13224-3809

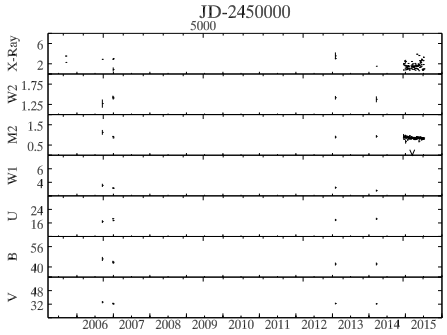

Fig. A.8 MCG–6-30-15

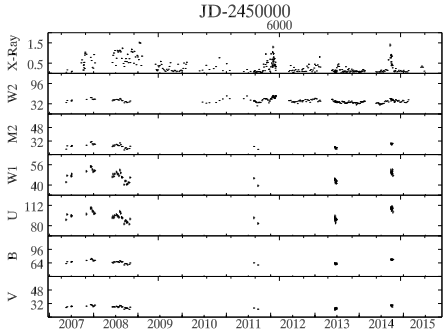

Fig. A.9 MRK 335

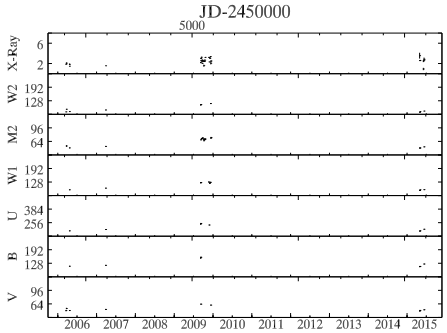

Fig. A.10 MRK 509

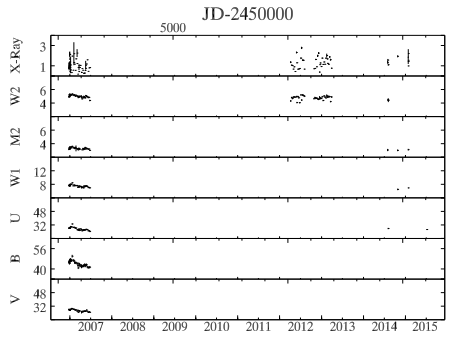

Fig. A.11 MRK 766

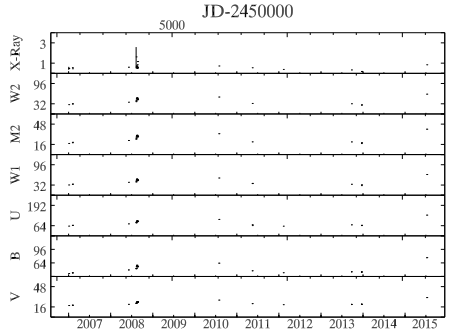

Fig. A.12 MRK 841

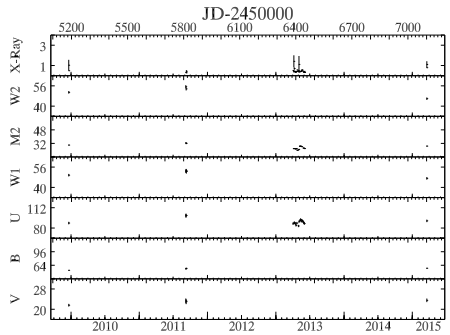

Fig. A.13 MRK 1383

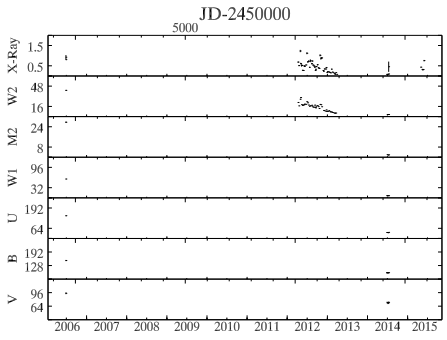

Fig. A.14 NGC 3516

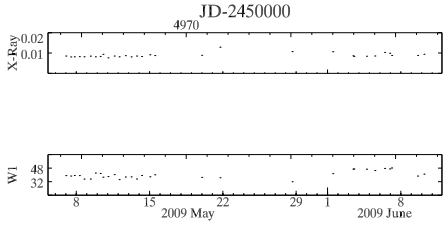

Fig. A.15 NGC 4051

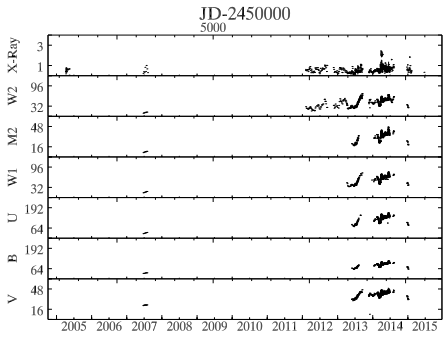

Fig. A.16 NGC 5548

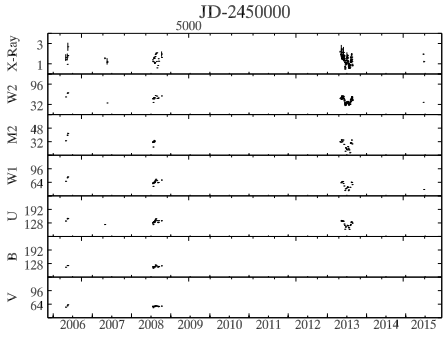

Fig. A.17 NGC 7469

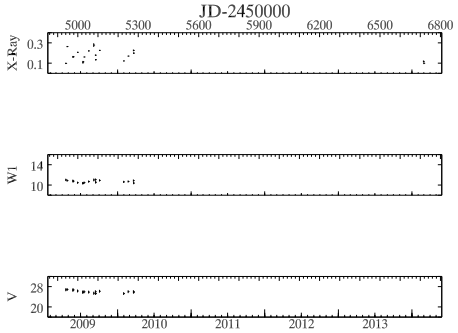

Fig. A.18 PDS 456

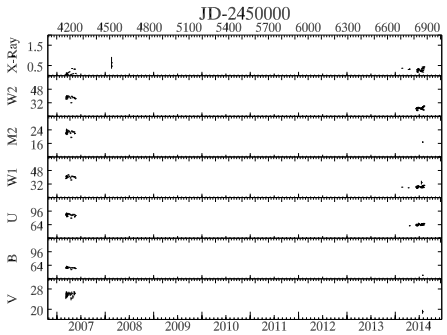

Fig. A.19 PG 1211+143

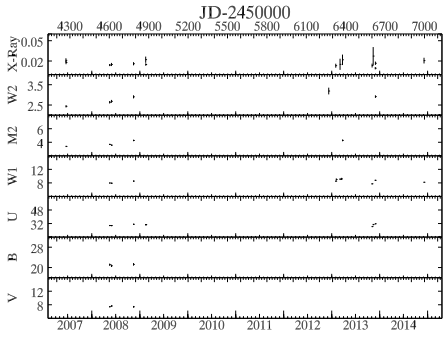

Fig. A.20 PG 1247+267

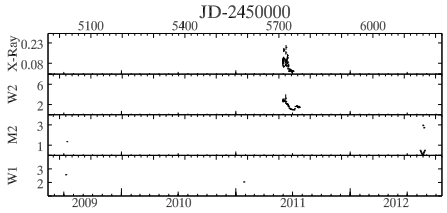

Fig. A.21 Zw229-15

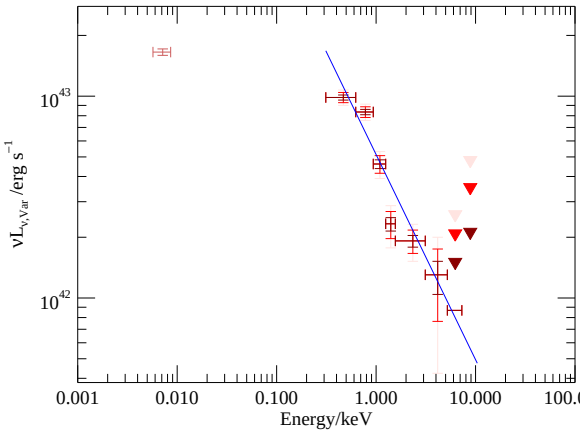

Fig. A.22 1H 0707–495

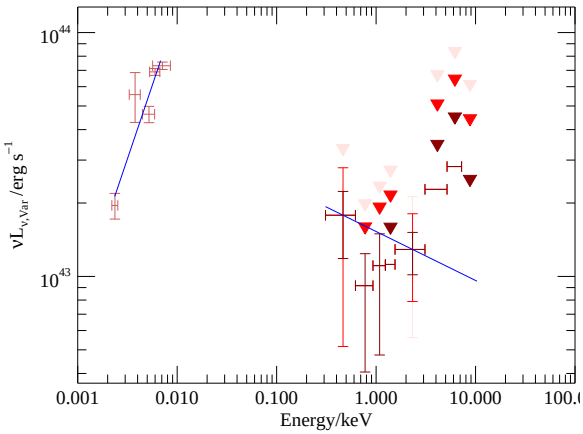

Fig. A.23 3C 120

A.2 Broadband Variability Spectra

Energies are given in the source frame. UV errors are shown at 1-σ. 1,2 and 3-σ X-ray errors are shown in maroon, red and pink respectively; triangles represent upper limits. Blue lines show powerlaw fits to UV and X-ray bands separately; those for X-rays only include points detected at 2-σ.

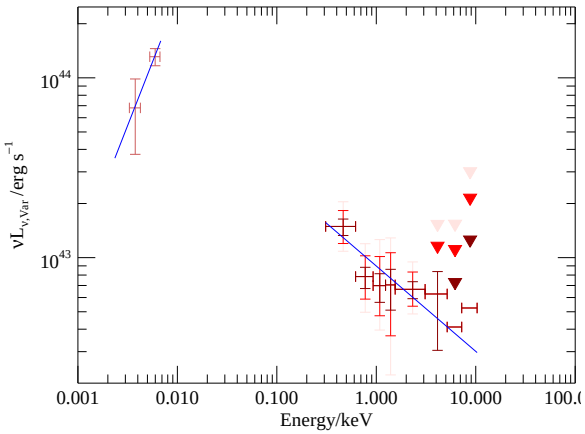

Fig. A.24 ARK 120

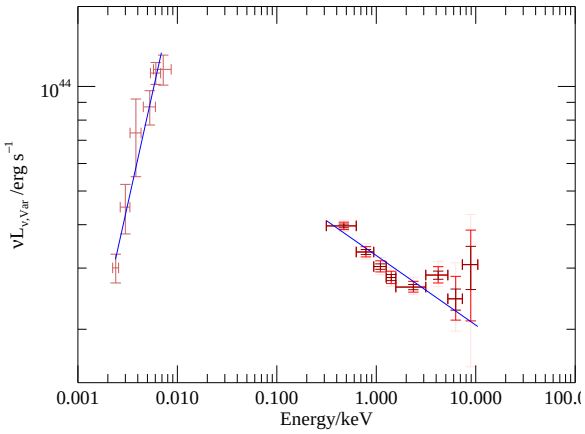

Fig. A.25 Fairall 9

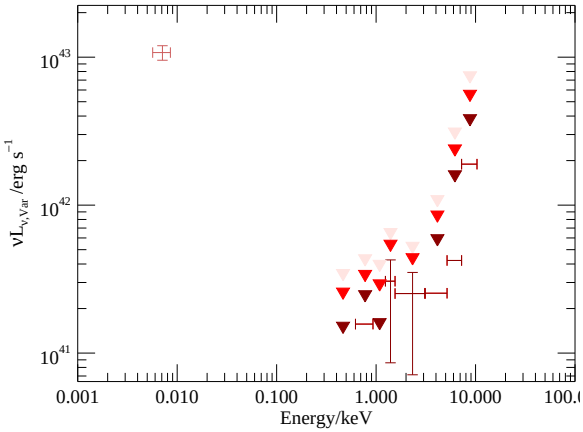

Fig. A.26 H 0557–385

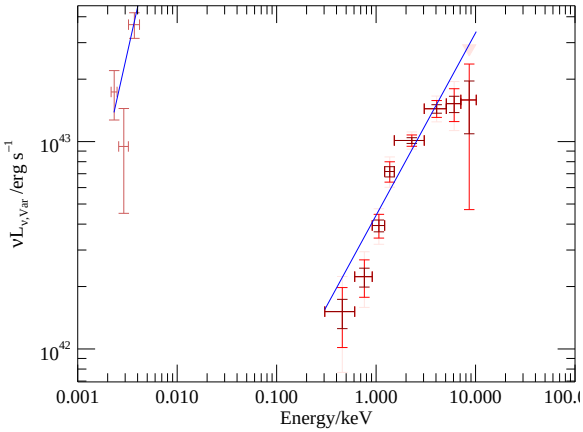

Fig. A.27 IC 4329A

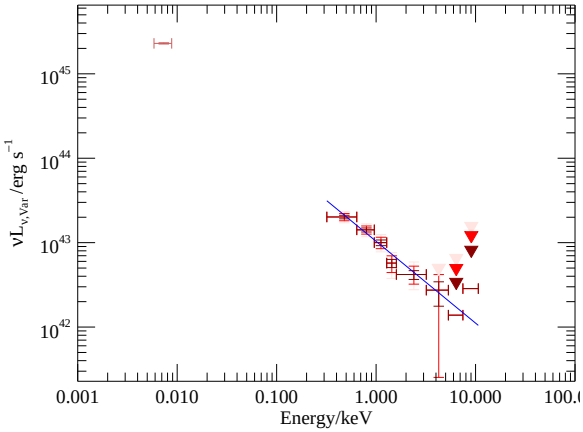

Fig. A.28 IRAS 13224-3809

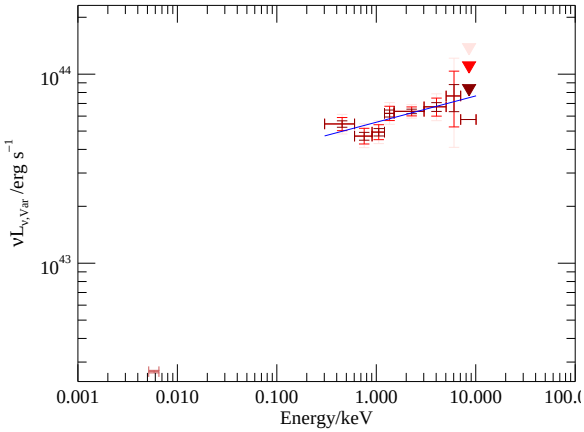

Fig. A.29 MCG–6-30-15

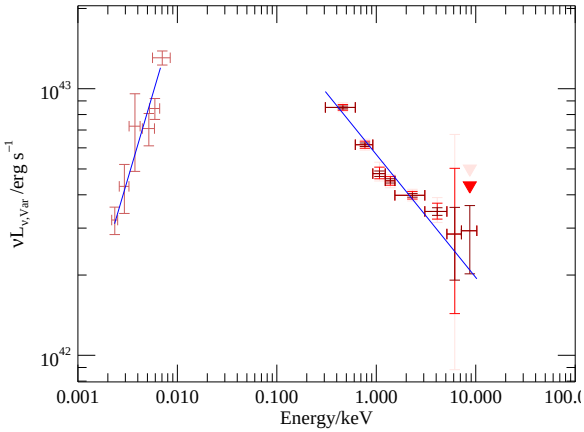

Fig. A.30 MRK 335

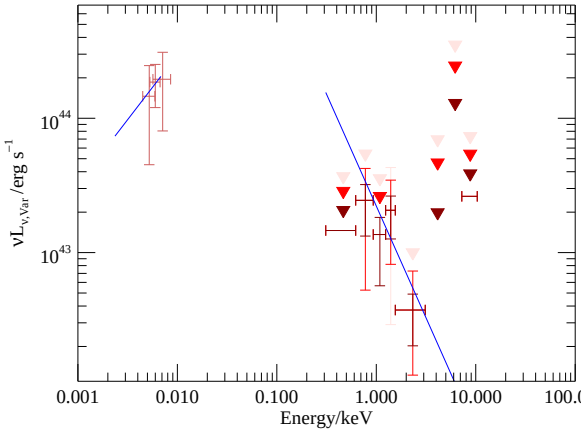

Fig. A.31 MRK 509

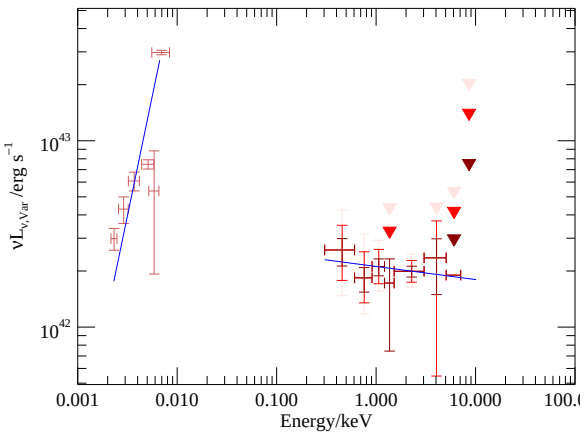

Fig. A.32 MRK 766

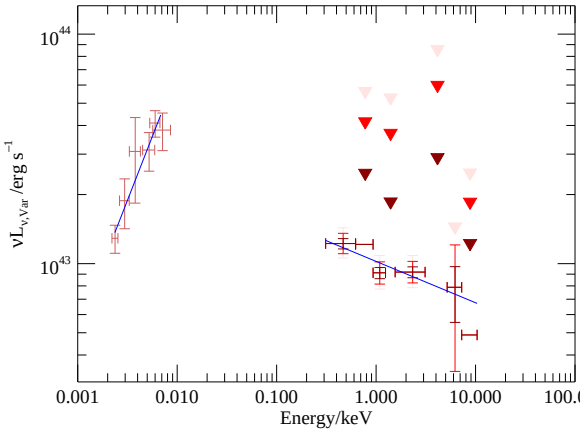

Fig. A.33 MRK 841

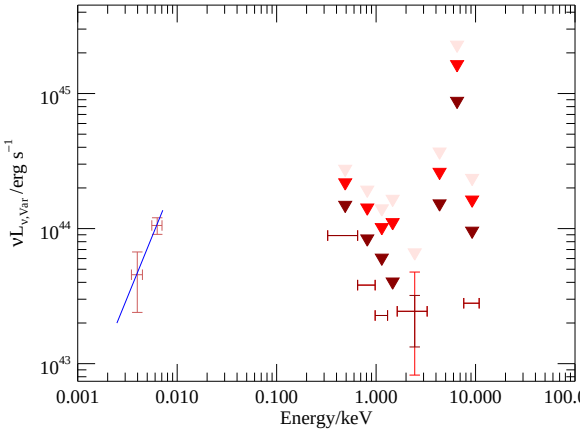

Fig. A.34 MRK 1383

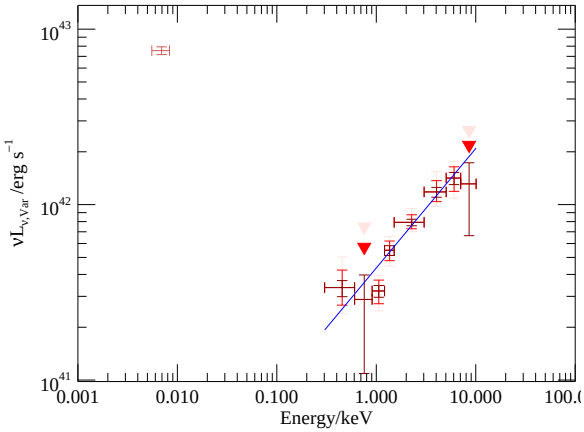

Fig. A.35 NGC 3516

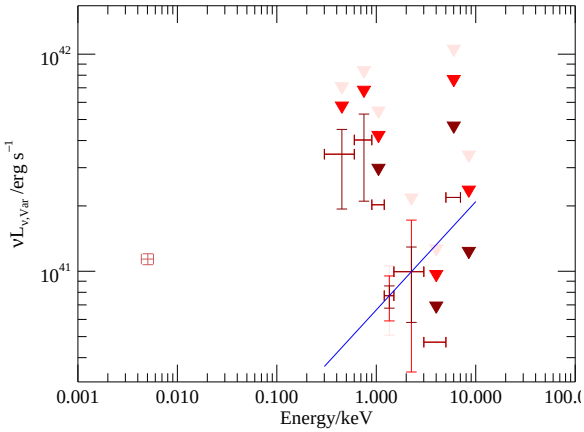

Fig. A.36 NGC 4051

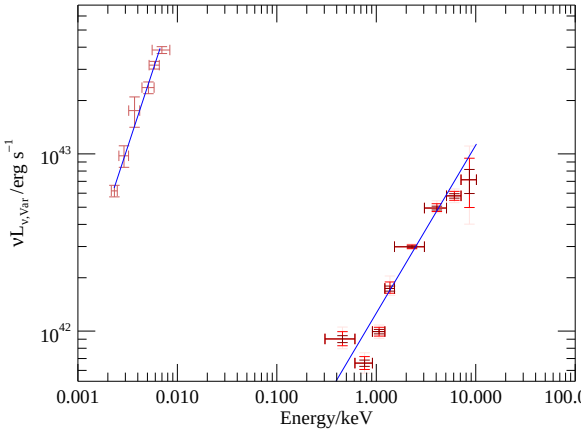

Fig. A.37 NGC 5548

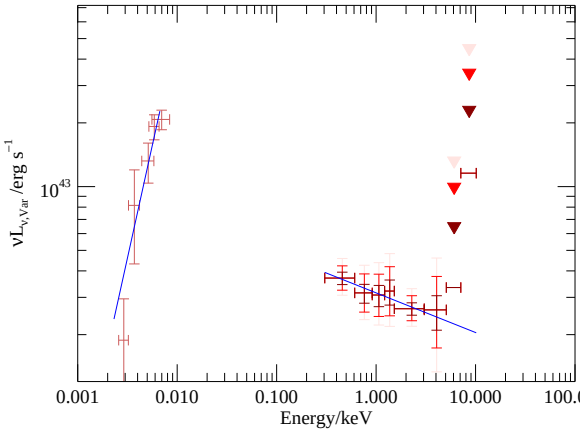

Fig. A.38 NGC 7469

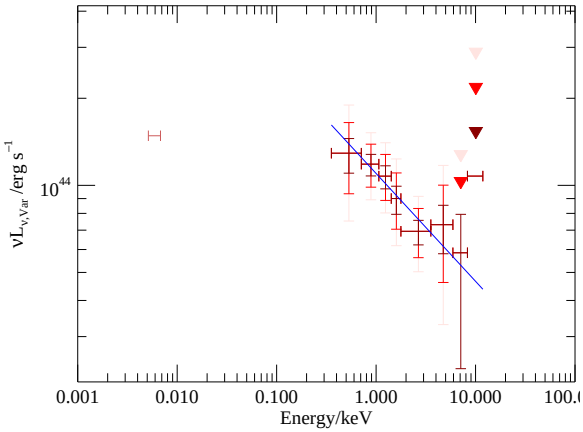

Fig. A.39 PDS 456

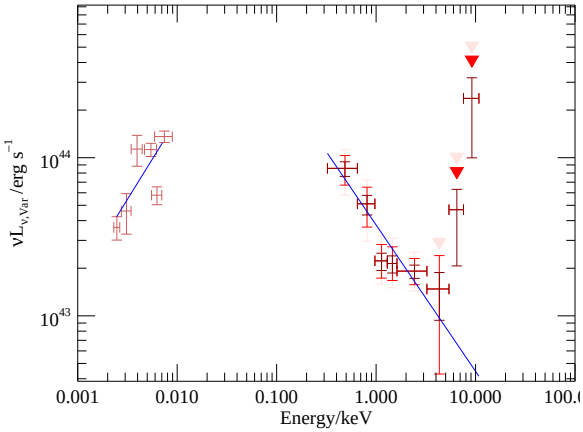

Fig. A.40 PG 1211+143

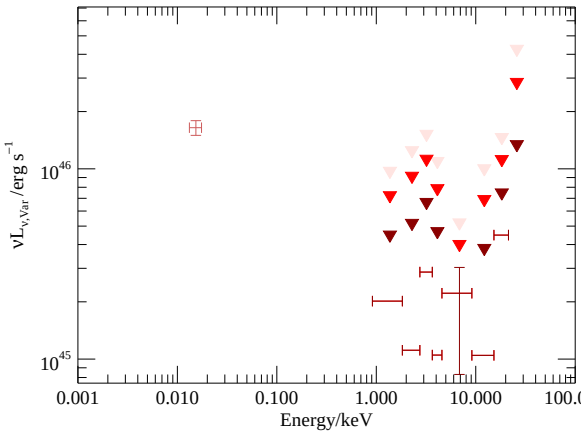

Fig. A.41 PG 1247+267

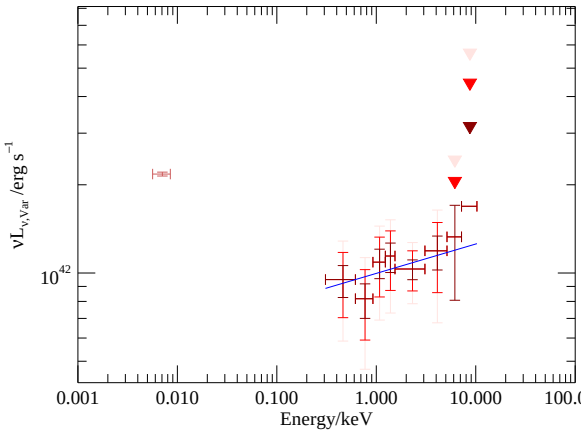

Fig. A.42 Zw 229-15

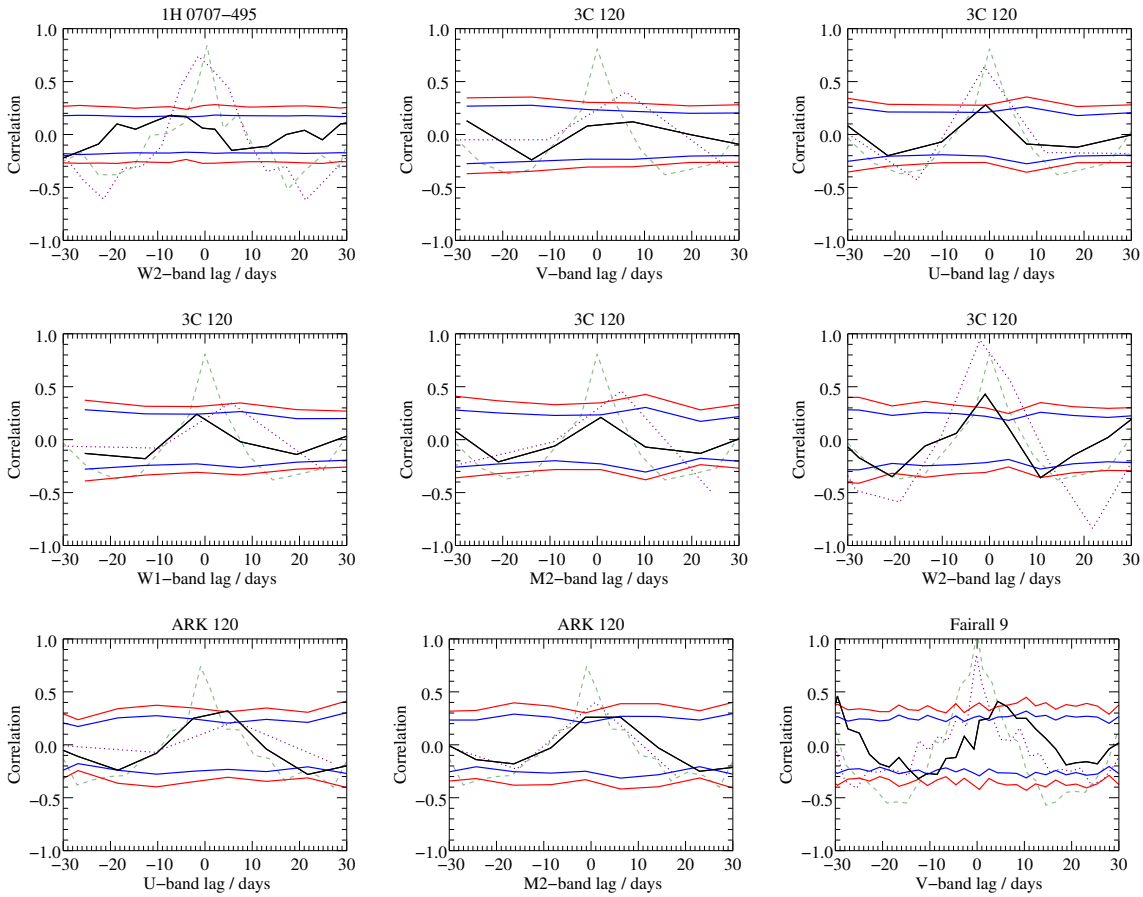

A.3 DCFs

Discrete correlation function (black) of given band relative to X-rays. Positive lag indicates UV variations occurring after X-ray variations. 95 and 99% confidence intervals are shown in blue and red respectively. The ACF of the X-rays and UV are shown in green dashed and purple dotted lines respectively. Plots with fewer than 3 DCF bins are not shown.

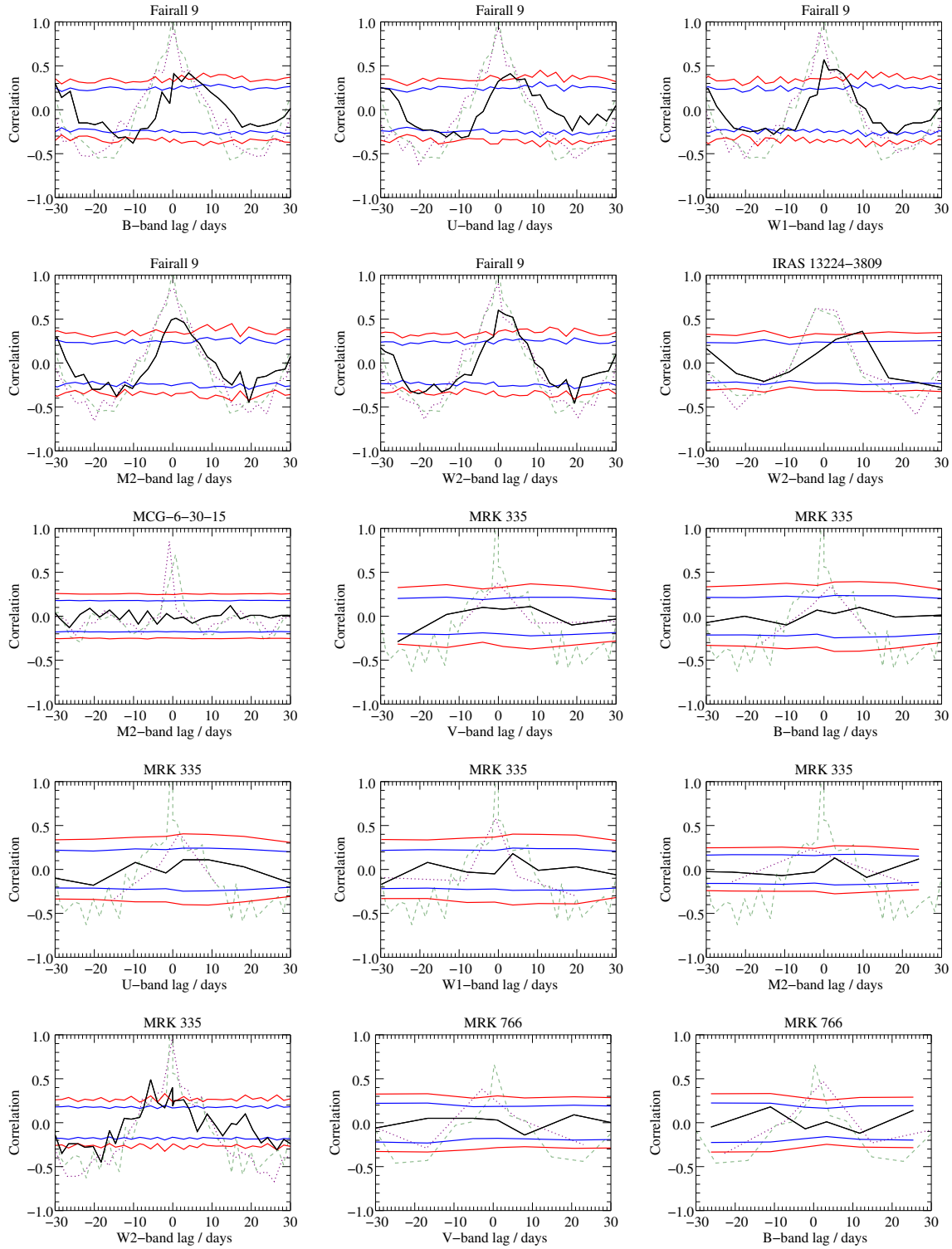
Fairall 9
Correlation
B−band lag / days
Fairall 9
U−band lag / days
Fairall 9
W1−band lag / days
Fairall 9
M2−band lag / days
Fairall 9
W2−band lag / days
IRAS 13224−3809
W2−band lag / days
MCG−6−30−15
M2−band lag / days
MRK 335
V−band lag / days
MRK 335
B−band lag / days
MRK 335
U−band lag / days
MRK 335
W1−band lag / days
MRK 335
M2−band lag / days
MRK 335
W2−band lag / days
MRK 766
V−band lag / days
MRK 766
B−band lag / days

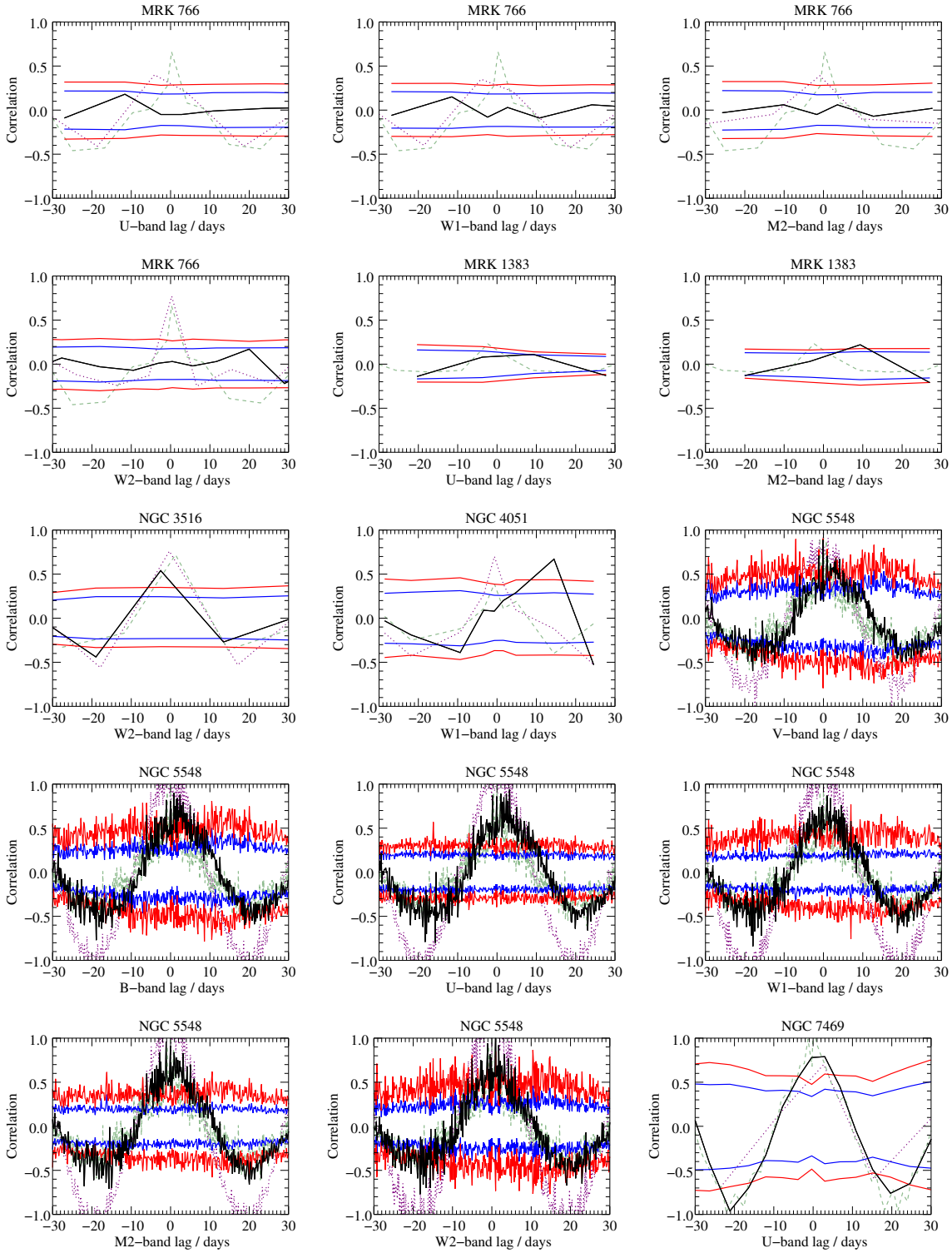
MRK 766
U−band lag / days
MRK 766
W1−band lag / days
MRK 766
M2−band lag / days
MRK 766
W2−band lag / days
MRK 1383
U−band lag / days
MRK 1383
M2−band lag / days
NGC 3516
W2−band lag / days
NGC 4051
W1−band lag / days
NGC 5548
V−band lag / days
NGC 5548
B−band lag / days
NGC 5548
U−band lag / days
NGC 5548
W1−band lag / days
NGC 5548
M2−band lag / days
NGC 5548
W2−band lag / days
NGC 7469
U−band lag / days
Correlation

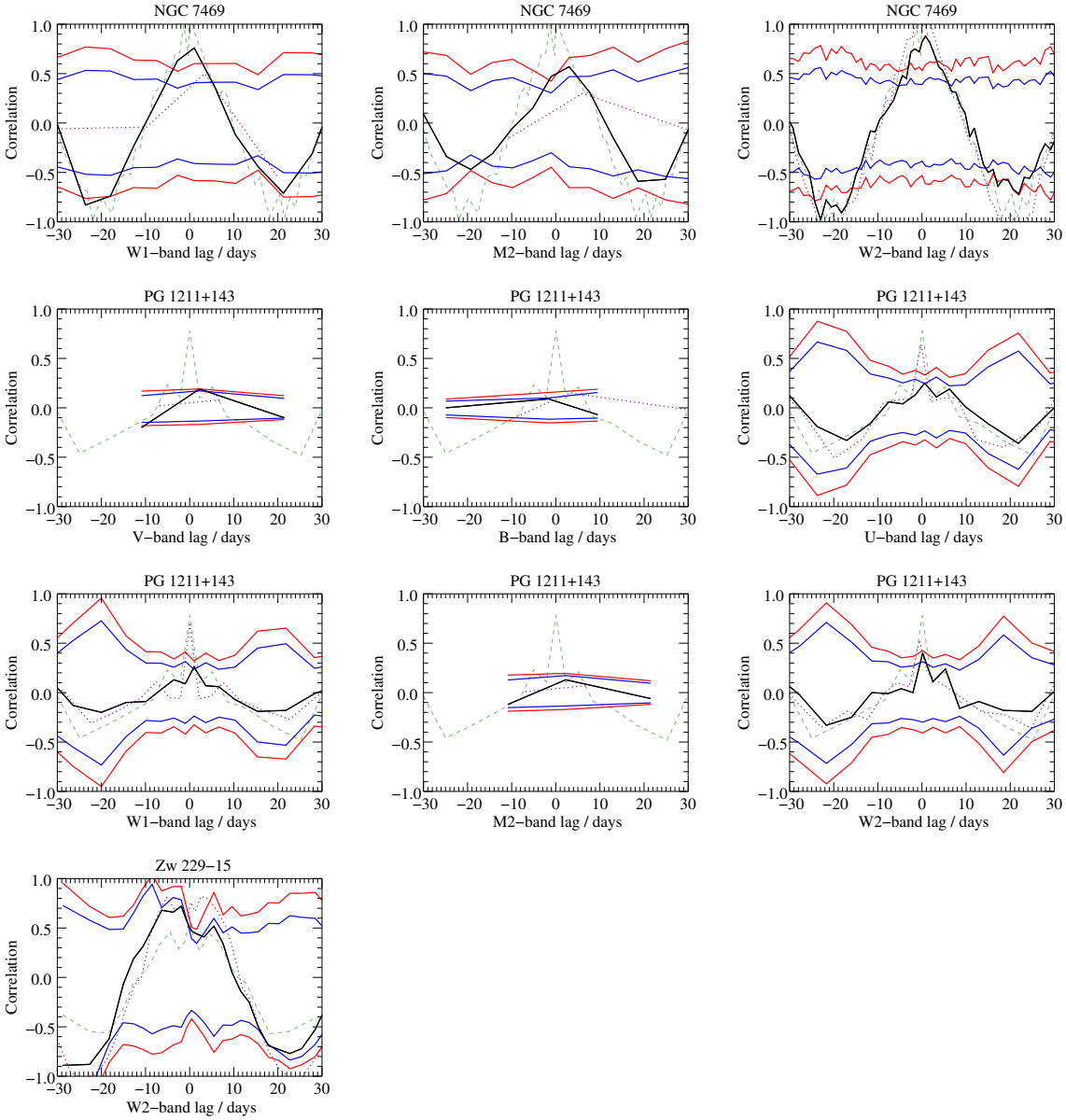
NGC 7469
Correlation
W1−band lag / days
NGC 7469
Correlation
M2−band lag / days
NGC 7469
Correlation
W2−band lag / days
PG 1211+143
Correlation
V−band lag / days
PG 1211+143
Correlation
B−band lag / days
PG 1211+143
Correlation
U−band lag / days
PG 1211+143
Correlation
W1−band lag / days
PG 1211+143
Correlation
M2−band lag / days
PG 1211+143
Correlation
W2−band lag / days
Zw 229−15
Correlation
W2−band lag / days

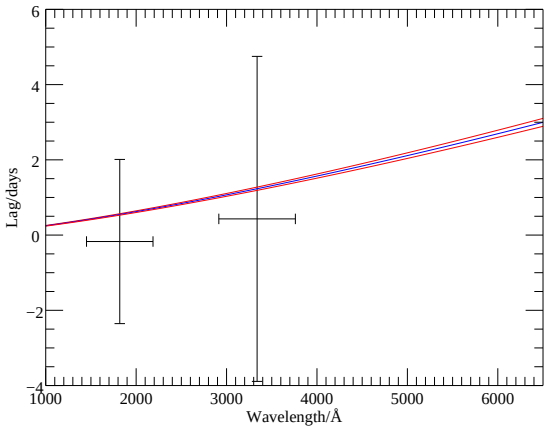

Fig. A.43 3C 120

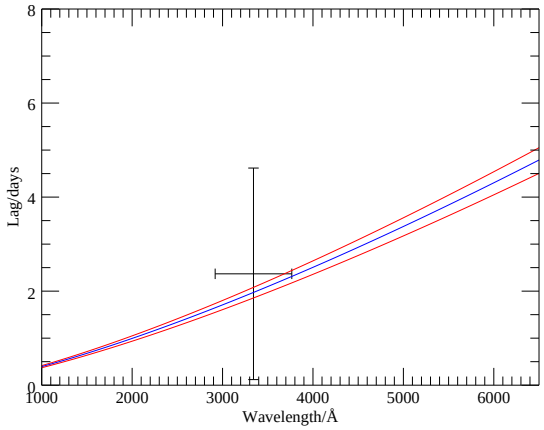

Fig. A.44 ARK 120

A.4 lags

For each source with UV/X-ray correlations detected at 99% confidence, the lags are shown as a function of wavelength. These are compared to the predictions for a thin disc (blue) and 1-σ errors (red).

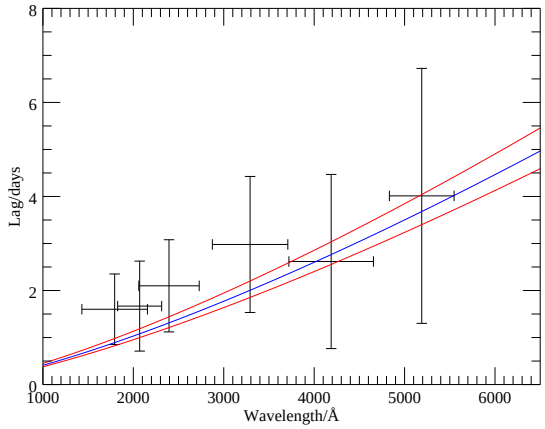

Fig. A.45 Fairall 9

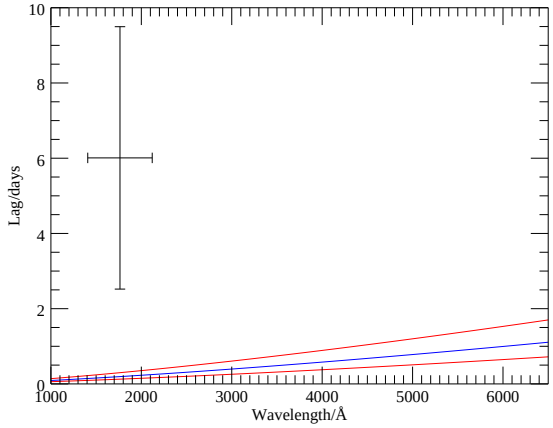

Fig. A.46 IRAS 13224-3809

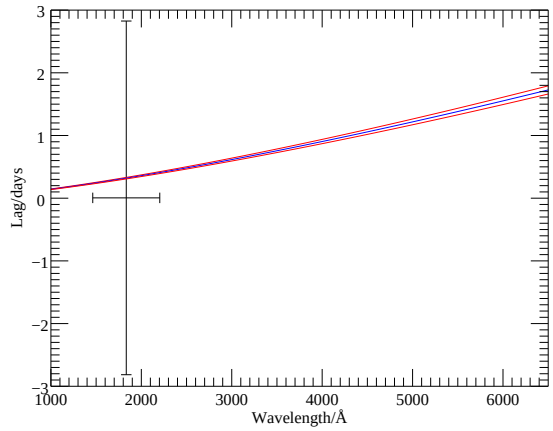

Fig. A.47 MRK 335

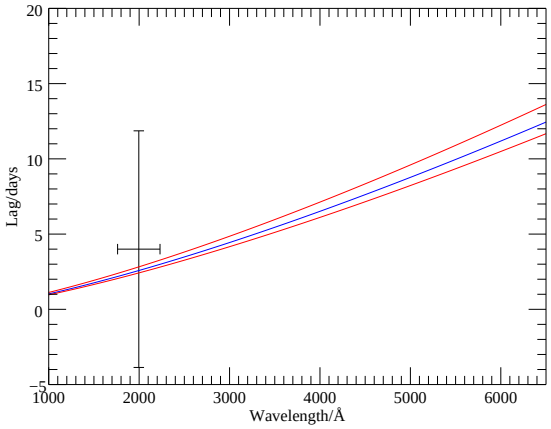

Fig. A.48 MRK 1383

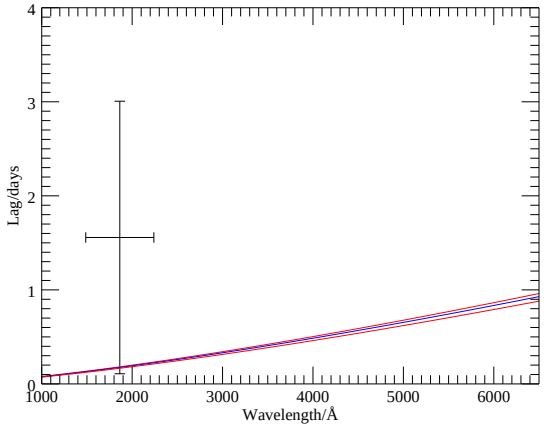

Fig. A.49 NGC 3516

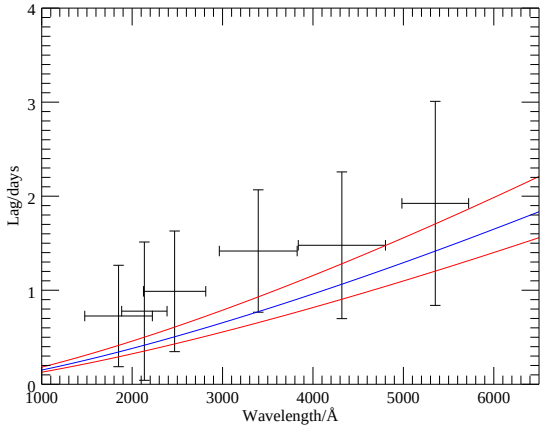

Fig. A.50 NGC 5548

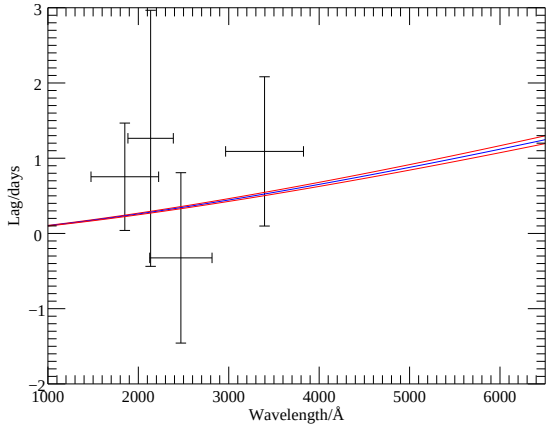

Fig. A.51 NGC 7469